



**HAL**  
open science

## Plasma deposition at atmospheric pressure and characterization of nanostructures

Hande Yavuz

► **To cite this version:**

Hande Yavuz. Plasma deposition at atmospheric pressure and characterization of nanostructures. Other. Ecole Centrale Paris, 2012. English. NNT : 2012ECAP0008 . tel-00685122

**HAL Id: tel-00685122**

**<https://theses.hal.science/tel-00685122>**

Submitted on 4 Apr 2012

**HAL** is a multi-disciplinary open access archive for the deposit and dissemination of scientific research documents, whether they are published or not. The documents may come from teaching and research institutions in France or abroad, or from public or private research centers.

L'archive ouverte pluridisciplinaire **HAL**, est destinée au dépôt et à la diffusion de documents scientifiques de niveau recherche, publiés ou non, émanant des établissements d'enseignement et de recherche français ou étrangers, des laboratoires publics ou privés.



**ÉCOLE CENTRALE DES ARTS  
ET MANUFACTURES  
« ÉCOLE CENTRALE PARIS »**

**THÈSE**

présentée par

**Hande YAVUZ**

pour l'obtention du

**GRADE DE DOCTEUR**

**Spécialité : Science des Matériaux**

**Laboratoire d'accueil : Laboratoire de Mécanique des Sols, Structures et Matériaux**

**Dépôt par plasma à pression atmosphérique et  
caractérisation des nano structures obtenues**

**Soutenue le 26 Janvier 2012 devant le jury composé de :**

<b>Christophe Laux</b>	<b>Professeur, Ecole Centrale Paris</b>	<b>Président</b>
<b>Marie-Geneviève Barthes-Labrousse</b>	<b>DR CNRS, Université Paris-Sud</b>	<b>Rapporteur</b>
<b>Fabien Miomandre</b>	<b>MdC HDR, ENS Cachan</b>	<b>Rapporteur</b>
<b>Thierry Sindzingre</b>	<b>Acxys</b>	<b>Examineur</b>
<b>Pascal Rumeau</b>	<b>IFTH</b>	<b>Examineur</b>
<b>Alain Sylvestre</b>	<b>MdC HDR, Université Joseph Fourier</b>	<b>Examineur</b>
<b>Jinbo Bai</b>	<b>DR CNRS</b>	<b>Directeur de thèse</b>

**2012ECAP0008**



## *Remerciements*

Le projet d'accomplir cette thèse est né en 2007 pendant une conférence à Budapest (Hongrie), au cours d'un échange partagé avec Dr. Jinbo Bai, Directeur de Recherche du CNRS au Laboratoire de Mécanique des Sols, Structures et Matériaux de l'Ecole Centrale de Paris, que je remercie sincèrement pour m'avoir offert cette occasion de relever ce défi. Je suis très reconnaissante à l'égard de Dr. Jean-Marie Fleureau, ancien Directeur du Laboratoire de Mécanique des Sols, Structures et Matériaux de l'Ecole Centrale de Paris et Fabien Miomandre, Directeur du département Chimie de l'Ecole Nationale Supérieure de Cachan qui ont bien voulu m'accorder leur confiance sur ce projet.

Je tiens à remercier profondément Nasser Darabiha, Directeur de l'Ecole Doctorale de l'ECP, ainsi que Hachmi Ben Dhia Directeur de Laboratoire MSSMat. Ils m'ont tous deux montré une exceptionnelle capacité d'analyse de ma situation et ont été capable de m'apporter un soutien pertinent et absolument essentiel à la réussite de ce travail.

Je remercie le Gouvernement Français et notamment la Direction de l'Ecole Centrale de Paris pour le soutien financier qui est la base de la réussite de ce travail.

J'exprime mes remerciements à Marie Geneviève Barthes-Labrousse, Directeur de Recherche du CNRS au Laboratoire LEHME-ICMMO de l'Université Paris-Sud 11, et encore une fois à Fabien Miomandre pour avoir accepté de participer au jury. Je tiens à leur exprimer ma reconnaissance pour avoir consacré une partie de leur temps à évaluer ce travail.

Je remercie à Christophe Laux, Professeur de l'ECP pour avoir accepté de présider ce jury et de m'avoir consacré une partie de son temps sur ce projet. J'exprime mes remerciements à Alain Sylvestre, Maître de Conférences à l'Université Joseph Fourier, Thierry Sindzingre, Directeur d'Acxys et Pascal Rumeau, responsable R&D à l'IFTH pour avoir fait partie de la commission d'examen. J'adresse mes remerciements encore à Thierry Sindzingre et Jérôme Dutroncy, responsable R&D à Acxys pour leur aide et leurs compétences m'ont été précieuses sur le plan technique.

Je tiens grande remercier à nombreuse collègues qui ont tous su partagé généreusement leur savoir dans tous les domaines : Farida Djebbari, Sylviane Bourgeois, Françoise Garnier, Sokona Konaté, Paul-Haghi Ashtiani,



Arnaud Brosseau, David Alamarguy, Marie-France Trichet et Rémy Pires. Merci pour leur appui lors des essais mécaniques, chimique et leur amitié. Je suis heureuse de connaître des collègues comme vous !

Finalement, un grand merci aux copains et copines d'avoir partagé des bons et des mauvais moments: Youqin, Hassan, Anthony, Jérôme, Youssef, Delong, Weilong, Johan, Jinkai, Shenghong, Weikang, Jing S, Jing Z et Simona.

Enfin, je souhaite exprimer mon infinie gratitude à ma mère, Hacer Yavuz, pour ses encouragements et son support absolument sans faille. L'accomplissement de ce travail doit beaucoup à la profondeur de son amour et de son immense dévouement maternel. Je souhaite aussi dire toute ma gratitude à Grégory Girard qui m'a communiqué son enthousiasme pour la Recherche, la physique des plasmas, et qui m'a prodigué de précieux conseils pour mener à bien cette thèse. Je lui suis surtout reconnaissante, pour toujours, pour sa confiance en moi, la sincérité et la profondeur de l'amour qu'il m'a témoigné. La chaleur de ces sentiments ont été une source permanente d'encouragements et m'ont considérablement aidé pour aller au terme de mon étude. Rien n'aurait été rédigé sur ce travail sans la vitalité de ces sentiments.

# Table of contents



Abbreviations

Symbols

General introduction

**Chapter I: Literature review**

Introduction.....	13
1. Composites.....	14
1.1. Carbon fibers (CFs).....	19
1.2. Carbon nanotubes (CNTs) .....	22
1.3. Epoxy resins.....	27
1.4. The interfacial properties of composites.....	29
1.5. Use of carbon fiber composites in aviation industry.....	32
2. Plasma application for material processing.....	37
2.1. Plasma.....	37
2.2. Plasma discharge.....	41
2.2.1. DC discharge.....	42
2.2.2. Dielectric barrier discharge (DBD).....	43
2.3. Plasma process.....	45
2.4. The effect of plasma on the surface of CNTs and CFs.....	47
2.5. Forth generation of polymers: electrically conducting polymers.....	52
2.5.1. Polypyrrole (PPy).....	53
2.5.2. Plasma polymerized polypyrrole (PPPy).....	56
3. Conclusion.....	60

**Chapter II: Experimental**

Introduction.....	63
1. Plasma system.....	64
2. Experimental procedure.....	67
3. Apparatus.....	68
3.1. X-ray photoelectron spectroscopy (XPS).....	68
3.2. Scanning electron microscopy (SEM).....	69
3.3. Atomic force microscopy (AFM).....	69
3.4. Thermogravimetric analysis (TGA).....	70
3.5. Optical microscopy.....	70
4. Materials.....	70
5. Composite sample preparation.....	71
6. Electrical property evaluations.....	72
6.1. Electrical measurement procedure for fibers.....	72
6.2. Electrical measurement procedure for fiber/epoxy composites.....	74
7. Mechanical property evaluations.....	76
8. Conclusion.....	79

**Chapter III: Statistical experimental design on plasma polypyrrole deposition**

Introduction.....	82
1. Experimental design on plasma polypyrrole deposition.....	83
1.1. Experimental design on plasma polypyrrole deposition in the absence of dopant.....	86
1.1.1. Model equation and comparison of predicted and actual values of electrical resistivity.....	87
1.1.2. Response surface plots and optimum conditions for electrical resistivity.....	89

1.2. Experimental design on plasma polypyrrole deposition in the presence of dopant.....	90
1.2.1. Model equation and comparison of predicted and actual values of electrical resistivity.....	93
1.2.2. Response surface plots and optimum conditions for electrical resistivity.....	95
2. Conclusion.....	98
3. Supplementary information.....	99
<b><u>Chapter IV: Characterization of plasma polypyrrole deposited fibers</u></b>	
Introduction.....	112
1. Surface properties of plasma treated T700/CNT and AS4 fibers.....	114
1.1. Results of XPS.....	114
1.2. Results of SEM.....	134
1.3. Results of AFM.....	143
1.4. Thermogravimetric analysis (TGA).....	147
2. Conclusion.....	149
<b><u>Chapter V: Characterization of plasma treated carbon fiber/epoxy composites</u></b>	
Introduction.....	152
1. Mechanical properties of plasma treated fiber epoxy composites.....	153
2. Results of SEM.....	156
3. Electrical resistivity of plasma treated carbon fiber epoxy composites.....	168
4. Conclusion.....	175
General conclusion and perspectives.....	176
References.....	180

## Abbreviations and symbols



## Abbreviations

<b>AC</b>	Alternative Current
<b>AFM</b>	Atomic Force Microscopy
<b>BAM</b>	Bulylamine
<b>B.E.</b>	Binding Energy
<b>CAP</b>	Competitive Ablation Polymerization
<b>CFs</b>	Carbon fibers
<b>CNTs</b>	Carbon nanotubes
<b>CVD</b>	Chemical Vapor Deposition
<b>DBD</b>	Dielectric Barrier Discharge
<b>DC</b>	Direct Current
<b>DOE</b>	Design of Experiment
<b>E</b>	Exposure time
<b>EBSA</b>	4-ethylbenzene sulfonic acid
<b>EE</b>	Second-order coefficient for factor E
<b>EF</b>	Interaction effect for factors E and F
<b>XPS</b>	X-ray Photoelectron Spectroscopy
<b>E.R.</b>	Electrical Resistivity
<b>F</b>	Flow ratio of dopant to pyrrole
<b>FF</b>	Second-order coefficient for factor F
<b>Fig.</b>	Figure
<b>FTIR</b>	Fourier-Transform Infrared
<b>FWHM</b>	Full-width Half Maximum
<b>HRTEM</b>	High Resolution Transmission Electron Microscopy
<b>ILSS</b>	Interlaminar Shear Strength
<b>LDPE</b>	Low-density polyethylene
<b>MWNTs</b>	Multi-walled carbon nanotubes
<b>P</b>	Power
<b>P.A.</b>	Peak assignment (for XPS)
<b>PAN</b>	Polyacrylonitrile
<b>PBO</b>	Poly(p-phenylene-2,6-benzobisoxazole)
<b>PE</b>	Interaction effect for factors P and E
<b>PF</b>	Interaction effect for factors P and F
<b>PP</b>	Second-order coefficient for factor P
<b>PPy</b>	Polypyrrole
<b>PPPy</b>	Plasma polypyrrole
<b>PPTA</b>	Poly(p-phenylene terephthalamide)
<b>pTSA.H<sub>2</sub>O</b>	para-toluene sulfonic acid monohydrate
<b>R<sub>a</sub></b>	Arithmetic Mean (for AFM)
<b>R.A.</b>	Relative Area (for XPS)
<b>RF</b>	Radio-frequency
<b>RH</b>	Relative Humidity
<b>RMS</b>	Root-mean Square (for AFM)



<b>SAS</b>	Statistical Analysis System
<b>SEM</b>	Scanning Electron Microscopy
<b>SWNTs</b>	Single-walled carbon nanotubes
<b>TGA</b>	Thermogravimetric Analysis
<b>T700/CNT</b>	Carbon nanotubes grafted on T700 carbon fibers

### *Symbols*

$\beta_i$	Linear coefficient of response function (i.e. electrical resistivity)
$\beta_{ii}$	Quadratic coefficient of response function
$\beta_{ij}$	Cross-product coefficient of response function
<b>b</b>	Width [cm] or [m]
<b>h</b>	Thickness [cm] or [m]
<b>l</b>	Length [cm]
<b>E</b>	Young modulus [GPa]
$E_f$	Flexural modulus [GPa]
<b>F</b>	Load [kg.m s <sup>-2</sup> ]
<b>L</b>	Span [m]
<b>R</b>	Resistance [ohm]
<b>R<sub>c</sub></b>	Sum of contact resistance [ohm]
$S_f$	Flexural strength [MPa]
$t_{13}$	Interlaminar shear strength [GPa]
$\rho_l$	Longitudinal electrical resistivity [ohm.cm]
$\rho_{tt}$	Through-thickness electrical resistivity [ohm.cm]
$\rho_{tw}$	Through-width electrical resistivity [ohm.cm]

# General introduction

## *General introduction*

Carbon nanotubes (CNTs) have drawn great attention in both academic and industrial research teams in the recent years due to discovery of their wide range of special functional properties. Their unique intrinsic properties such as high electrical (1000 S/cm) and thermal (3000 W/mK) conductive capabilities, unprecedented mechanical properties ( $E=1000$  GPa) make them especially desirable in the fields of aerospace, automobile, defense, and sport industries.

Due to the superb functional properties, these carbon tubules have found great potential to be used as a reinforcement material in the novel polymer matrix composites. Moreover, grafting CNTs on carbon fibers (CNTs-CF) have a potential to heal some of the critical weaknesses of the conventional carbon fiber composites. In principle, there are a large number of parameters such as nanotube grafting density, length, diameter, alignment and crystallinity, which can be adjusted during the grafting process of CNTs onto carbon fibers (e.g. CVD process), have great impact on the properties of the resultant composites. Besides, the surface chemistry of such hybrid systems is especially needed to be modified in order to enhance compatibility between CNT-CF reinforcements and polymer matrix. For this purpose, the interaction between two phases could be enhanced by high polarity group integration onto the outer surfaces of CNTs-CF by the surface treatment methods. Among these methods, plasma processing can be considered as a promising tool in materials surface treatment because of the comparatively straightforward scale-up to larger dimensions, possibility of in-line surface treatment and compatibility of any type of substrate. Further, with the well-designed plasma conditions it is also possible to deposit functional structures on materials in a very short time.

In the frame of this work, we adapt a dielectric barrier discharge technique for in-line plasma polypyrrole deposition on the surface CFs and CNTs-CF. The aim of this study is not only to enhance the interfacial properties of CF and CNTs-CF composites and to retain the intrinsic properties of those materials but also to provide valuable alternatives to previous polymer deposition methods existed in the literature.

# Chapter I

## Literature review



## *Introduction*

This chapter gives an overview of two major subjects of the study: (1) composites and their applications, (2) plasma application for materials processing. First part of this chapter reviews the composites and the properties of their constituents including the functional properties of novel reinforcements (CNTs) in such composites as well as the recent developments of these materials in the use of aviation industry. Second part covers the theory of plasma, principles of plasma discharge processes and the effect of non-polymer forming plasma deposition on CNTs and carbon fibers. Additionally, conducting polymers, particularly plasma polypyrrole deposition on different substrates are also included in order to demonstrate the effect of polymer-forming plasmas on such substrates.

## 1 Composites

Composites are multifunctional materials having unique mechanical and physical properties that can be tailored to meet the requirements of a particular application. They are strongly heterogeneous materials; their properties vary considerably from point to point in the material, depending on which material phase the point is located in [1].

Composite materials can either be natural or artificial. Biologically structural materials such as wood, bamboo, bone and shell occurring in nature are some examples of natural composites. Straw-reinforced mud bricks are one of the first artificial composites. Today, artificial composites, simply composites, made from the physical combination of two or more constituent materials, one of which is called reinforcement and the other is matrix. The reinforcements used in composite materials are usually in the form of continuous or discontinuous fibers, whiskers (e.g. elongated single crystals of SiC, Al<sub>2</sub>O<sub>3</sub>, etc), particles (e.g. roughly equal dimensional SiC, Al<sub>2</sub>O<sub>3</sub>, etc), nanoparticles (carbon nanotubes, nanofibers, nanoclays, etc) and numerous forms of fibrous architectures produced by textile technology (e.g. fabrics and braids) (Fig. 1.1). The four major classes of matrix used in the composites are polymers (thermosets and thermoplastics), metals (alloys of aluminum, titanium, iron, etc), ceramics (silicon carbide, alumina, silicon nitride, etc), and carbon (lubricants, diamonds, structural fibers, etc). Among these constituents, reinforcements provide strength and stiffness to composite while matrix gives rigidity and environmental resistance and hold the reinforcement together [1].

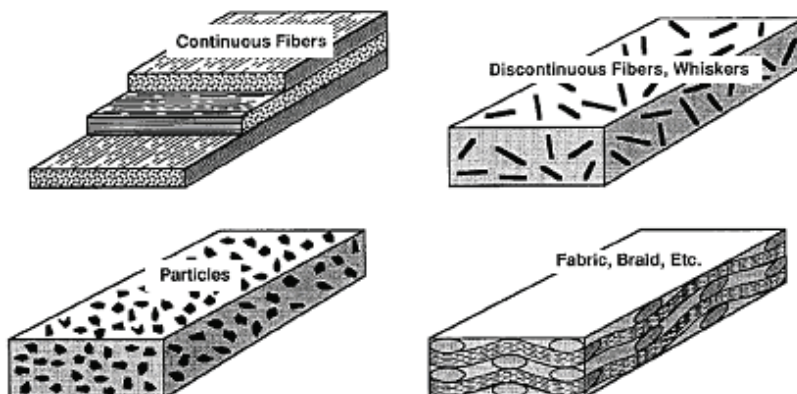


Figure 1.1 Composites with different reinforcement forms [1]

One of the largest class of composite materials used in structural applications are carbon fiber epoxy matrix composites. The attractiveness of carbon fiber/epoxy composites over conventional engineering materials such as glass/epoxy composite, steel, aluminum and wood can be seen when specific properties compared, as in Fig. 1.2. For composite materials, specific fatigue resistance is three times higher than that of aluminum alloys and two times higher than for high strength steel and titanium alloys because the fatigue resistance is equal to 90% of the static fracture strength for a composite, instead of 35% for aluminum alloys and 50% for steels and titanium alloys. With respect to these fundamental characteristics, within a wide temperature range (e.g. from  $-60\text{ }^{\circ}\text{C}$  to  $+200\text{ }^{\circ}\text{C}$ ), they are superior to aluminum, titanium alloys and steel under certain conditions [2] (Fig.1.3).

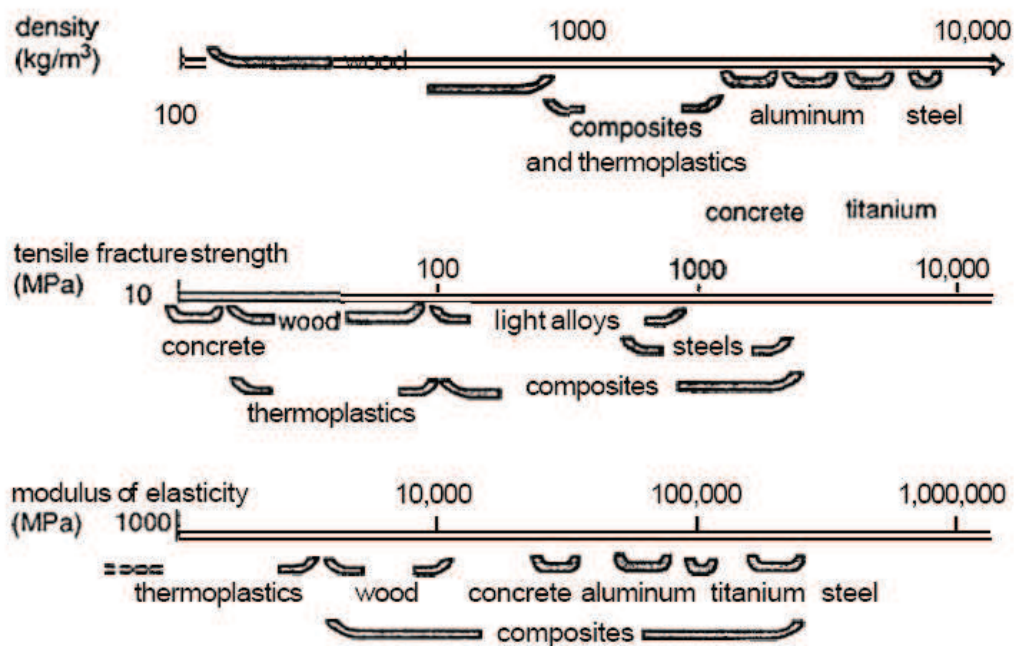


Figure 1.2 *Properties of commonly used engineering materials and carbon fiber/epoxy composites* [3]



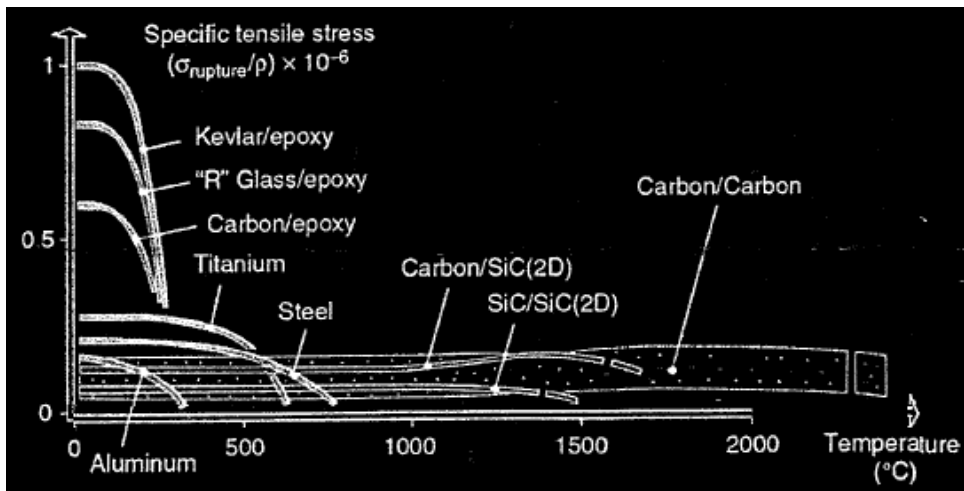


Figure 1.3 Specific strength of different composites depending on temperature [3]

Surely, the level those properties of fiber/matrix composites depends on several parameters such as orientation, length, shape and composition of fibers; mechanical properties of matrix as well as the proportion of fiber to matrix and the integrity of the bond between fiber and matrix (interphase). Of these, fiber orientation determines the mechanical strength of the composite and the direction of greatest strength. Fiber orientation can be one dimensional, planar (two-dimensional), or multi-dimensional (e.g. three-dimensional) (Fig. 1.4) [3, 4].

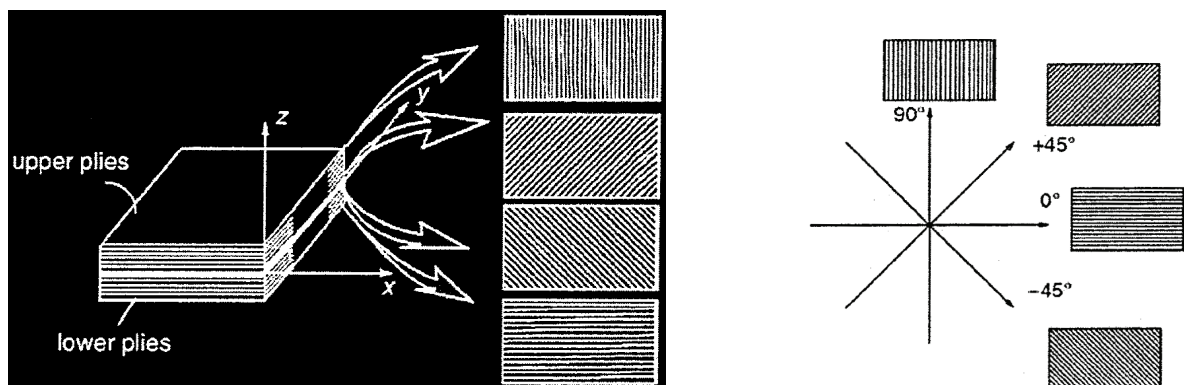


Figure 1.4 Common ply orientations in a fiber reinforced composite [3]

The one-dimensional type has the maximum composite strength and modulus in the direction of the fiber axis. The two-dimensional type exhibits different strengths in each direction of fiber orientation due to anisotropy and the three-dimensional type is isotropic but has greatly decreased reinforcing values [4]. As the fiber orientation becomes more random, the mechanical properties (e.g. tensile properties) in any one direction become lower (Figure 1.5). Hence, the superiority of reinforcing fibers strength characteristics is mainly seen in properties of unidirectional composites [2].

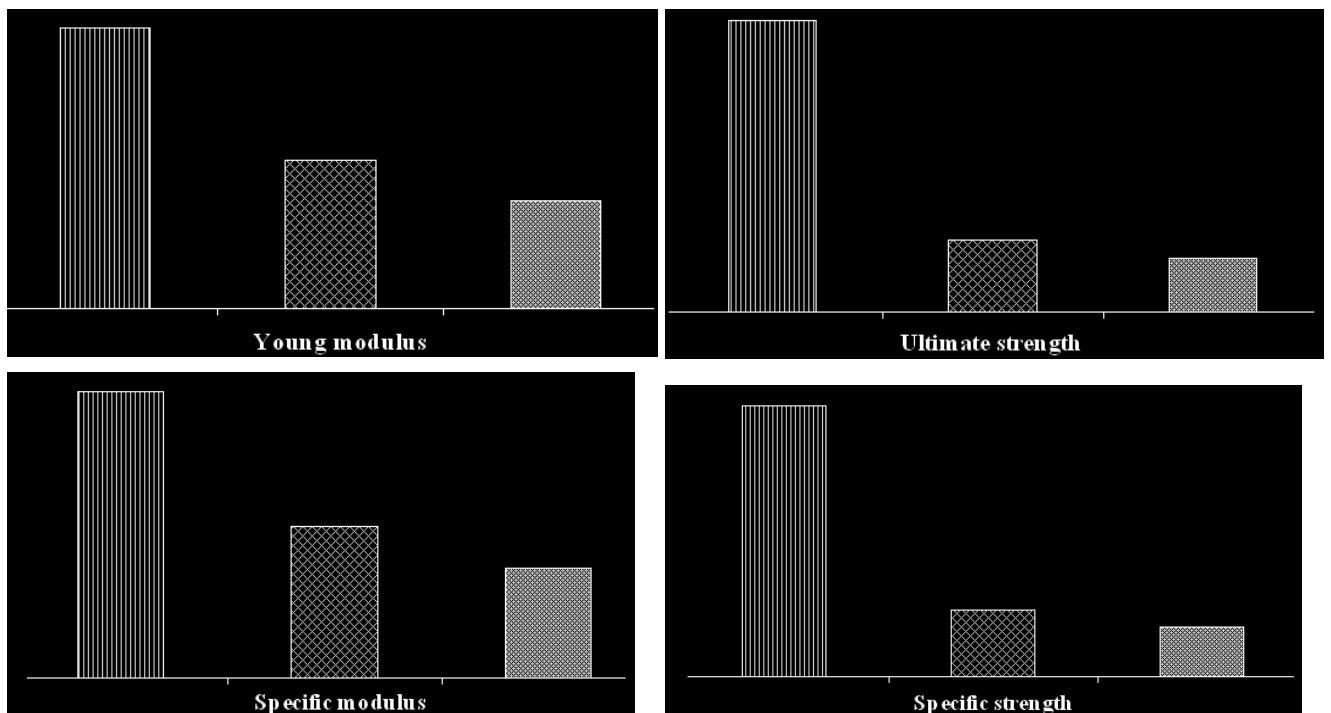


Figure 1.5 Tensile properties of continuous carbon fiber epoxy composites [4]

(Note:  Unidirectional,  Cross-ply,  Quasi-isotropic)

The mechanical properties are also affected by the proportion between fiber and matrix through the direction in which fiber is oriented. Thus, there must be a substantial volume fraction (i.e. >10 %) of the fiber reinforcement to the matrix in order to provide fiber phase that is stiffer and stronger than matrix. Besides, fiber length (continuous or short) impacts mechanical properties; further it has a bearing on the processibility of the composite. For example, composites made from short fibers,

if they could be properly oriented, could have substantially greater strengths than those made from continuous fibers (e.g. whiskers [4]).

Mechanical properties of epoxy matrix are also decisive for such properties of composites like shear load capability, buckling behavior, impact resistance and maximum use temperature [2]. Voids (air pockets) in the matrix due to poor processing and/or excess moisture or resin-lean (or rich) areas have detrimental effect on such properties of composites (Fig. 1.6). Under load, a fiber passing through such void may buckle and transfer stress to the resin, which then readily cracks [4].

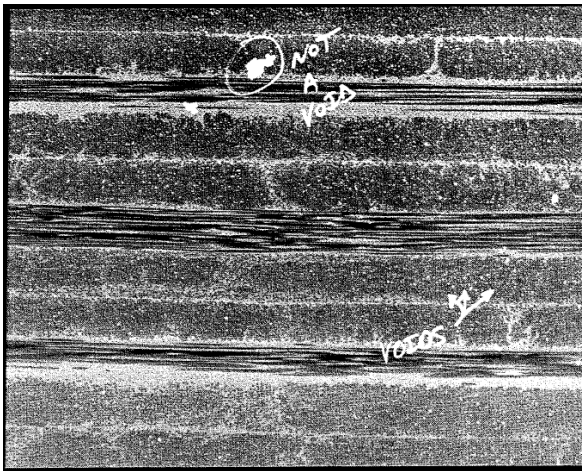


Figure 1.6 *Cross-section of a lamina with voids* [4]

There are several formulations of thermostable epoxy matrices that have been carried out to provide the highest post-cure characteristics, to ensure good adhesion to fibers and to improve mechanical characteristics within a wide temperature range [2]. Further, thanks to new generation epoxies, it is possible to cure them at relatively low temperatures and pressures with minimal shrinkage which has also great impact on processing cost [5].

Fiber composites are able to withstand higher stresses than their individual constituents because the fibers and matrix interact, resulting in redistribution of the stresses. The ability of constituents to exchange stresses depends on the effectiveness of the coupling or bonding between them. Bonding can sometimes be achieved by direct contact of the two phases, but usually a specially treated fiber must be used to ensure a receptive adherent surface [4]. This is especially required for high-strength and high-modulus carbon fibers for use in load-carrying structures. Because under

load, the fiber–matrix bond is often in a state of shear, therefore compatible surface treatments must be utilized to strengthen these bonds against shear forces. This requirement has led to the development of fiber finishes such as surface treatments including sizing and oxidation. However, it should be kept in mind that if the interfacial bond strength is too high, tensile strength will produce a brittle composite which is likely to be flaw sensitive and have a lower mechanical performance [6]. If the interfacial bond strength is too low, interfacial bond strength will produce poor shear and tensile strengths, and can be easily delaminated [6]. For this reason, optimization of wettability of fibers with various binders is needed in order to provide necessary adhesion between fiber and matrix. This ensures the composite from early failure when under load [2]. An important property of a composite is its resistance to failure. Failure may occur separately or a combination of several effects (Fig. 1.7): fiber rupture, matrix rupture, separation plies from each-other (e.g. due to fiber buckling) [3].

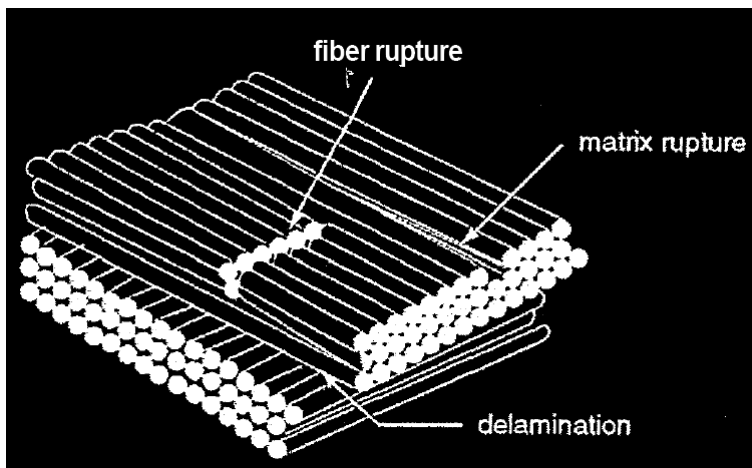


Fig 1.7 Different modes of failure in a carbon fiber reinforced composite [3]

### 1.1 Carbon fibers (CFs)

Carbon fibers are composed of at least 92 wt.% carbon in composition [7]. Like all fiber reinforcements (glass, aramid, boron or ceramic), they can be continuous or discontinuous. Continuous fiber composites contain fiber reinforcements with high aspect ratio (length-to-diameter); discontinuous fiber composites are composed of short fibers.

It is generally agreed that carbon fibers are composed of two-dimensional turbostratic graphitic crystallites oriented preferentially parallel to the fiber axis and have two-phase structure (i.e. crystalline and amorphous phases) and needle-shaped microvoids [8]. The illustrations of such phases as well as microstructure of carbon fiber are represented in Figs. 1.8, 1.9 respectively. Crystalline structure (graphite) consists of  $sp^2$  hybridized carbon atoms arranged two-dimensionally in a honeycomb structure in the x-y plane. Partly crystalline structures composed of well developed carbon layers and parallel to one another but have no particular stacking sequence [7].

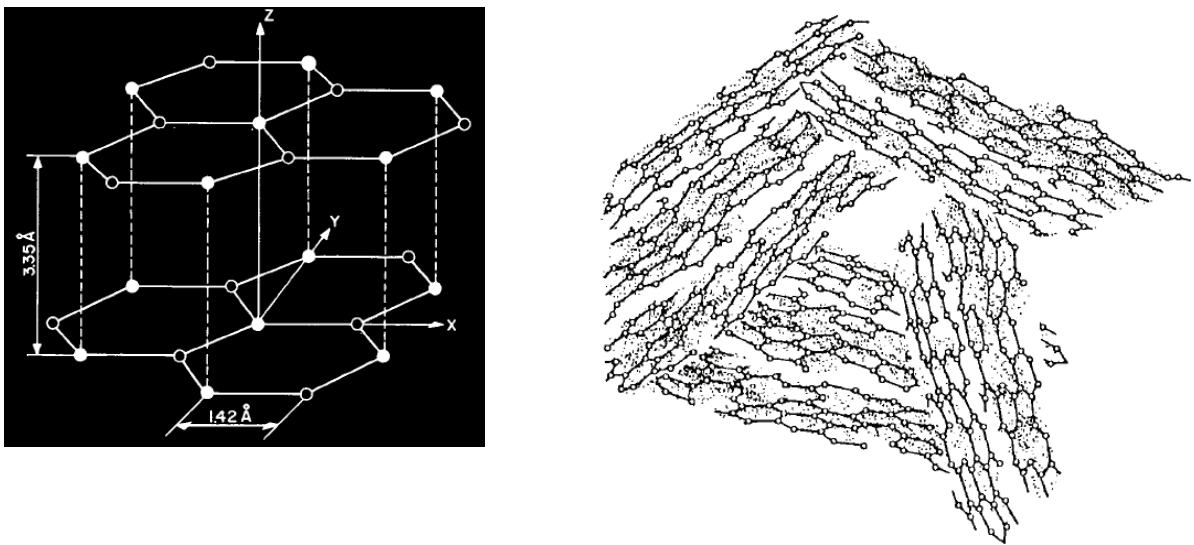


Figure 1.8 Structures of carbon fibers, a) graphitic structure (crystalline), b) amorphous structure [7,9]

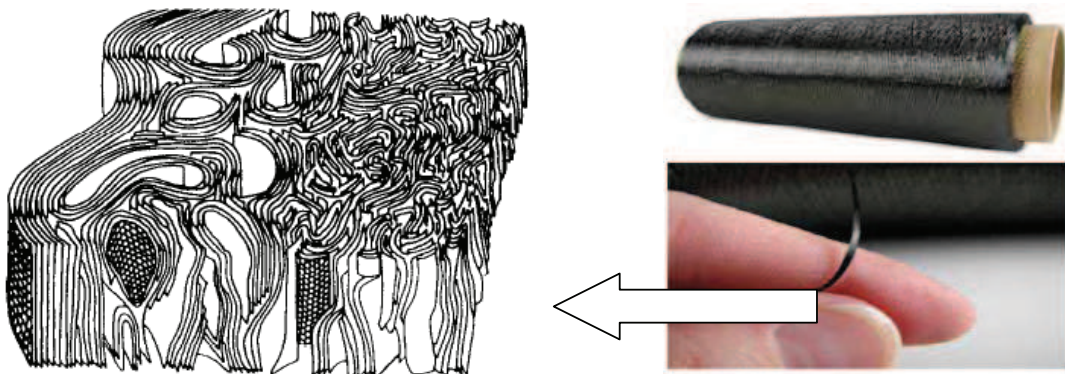


Figure 1.9 The microstructure of carbon fiber [10, 11]

There are vast grades of carbon fibers. In general, commercial carbon fibers are available in three categories: general-purpose, high-performance (high strength or high modulus), and activated carbon fibers. Those commercial carbon fibers are fabricated by using pitch (from coal or petroleum) or polyacrylonitrile (PAN) as the precursor. At the end of the fabrication process of fibers, oxidation treatment may use to develop fiber adhesion and to increase laminar shear strength when used in composite structures. An illustration of structure of carbon fiber prior to functionalization and after oxidation is given in Fig 1.10 [12]. Furthermore, different plasma treatments of carbon fibers are also discussed in the Section 2.4.

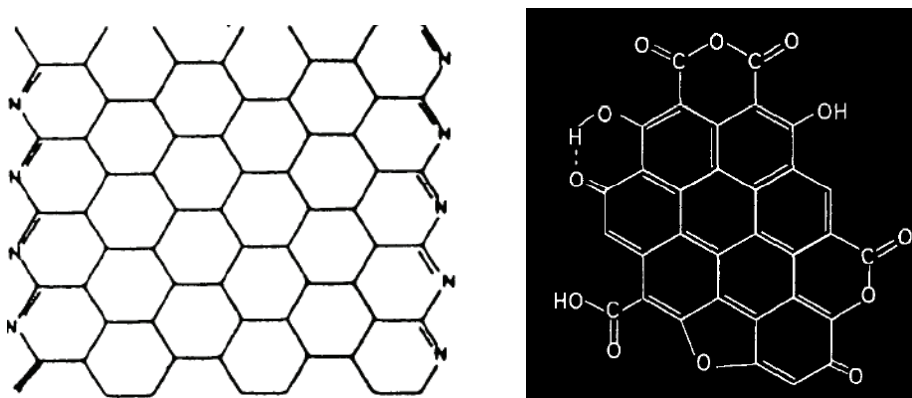


Figure 1.10 Structure of carbon fiber, a) prior to functionalization (after carbonization) [7], b) Functional groups on carbon fiber after oxidation [12]

Table 1.1 shows selected mechanical and physical properties of some high performance PAN (manufacturer: Toray and Hercules) and Pitch (manufacturer: DuPont) based carbon fibers on the market. Among the high-performance fibers, PAN based carbon fibers can attain a higher tensile strength and greater elongation than those based on pitch, because (1) shear is easier between the carbon layers in a graphitized fiber, (2) pitch is more graphitizable than PAN, and (3) the oriented graphitic structure causes the fibers to be more sensitive to surface defects and structural flaws. On the other hand, among the high-performance carbon fibers, those based on pitch can attain a higher modulus than those based on PAN, because pitch is more graphitizable than PAN. The higher the proportion of graphite and the greater the degree of alignment of carbon layers parallel to fiber axis, the greater the density, the carbon content, and the fiber's tensile modulus, electrical conductivity, and



thermal conductivity parallel to the fiber axis; the smaller the fiber's coefficient of thermal expansion and internal shear strength [7].

Table 1.1 Properties of various carbon fibers [7]

Fiber designation	Tensile strength (MPa)	Tensile modulus (GPa)	Diameter ( $\mu\text{m}$ )
Toray T300	3530	230	7.0
Toray T700	4900	230	7.0
Toray T1000	7060	294	5.3
Hercules AS1	3105	228	8.0
Hercules AS4	3795	235	8.0
Hercules AS6	4140	242	5.0
DuPont E35	2800	241	9.6
DuPont E75	3100	516	9.4
DuPont E130	3900	894	9.2

## 1.2 Carbon nanotubes (CNTs)

Carbon nanotubes vary in their morphology and their structural characteristics. Resulting from these properties; chiral angle, tube diameter, C–C bond length of the hexagonal lattice, tube length, tube-end configuration (end-caps), as well as the nanotube wall structure are treated as important parameters to characterize the nanotubes [13, 15]. Since the discovery of these tiny tubules by Iijima in 1991, two limiting configurations (i.e. armchair nanotubes and zigzag nanotubes, Figure 1.11) were offered to identify the structure of multi-walled carbon nanotubes (MWNTs), single-walled carbon nanotubes (SWNTs), single-crystal nanosized fibers and fullerene tubes (Figure 1.12).

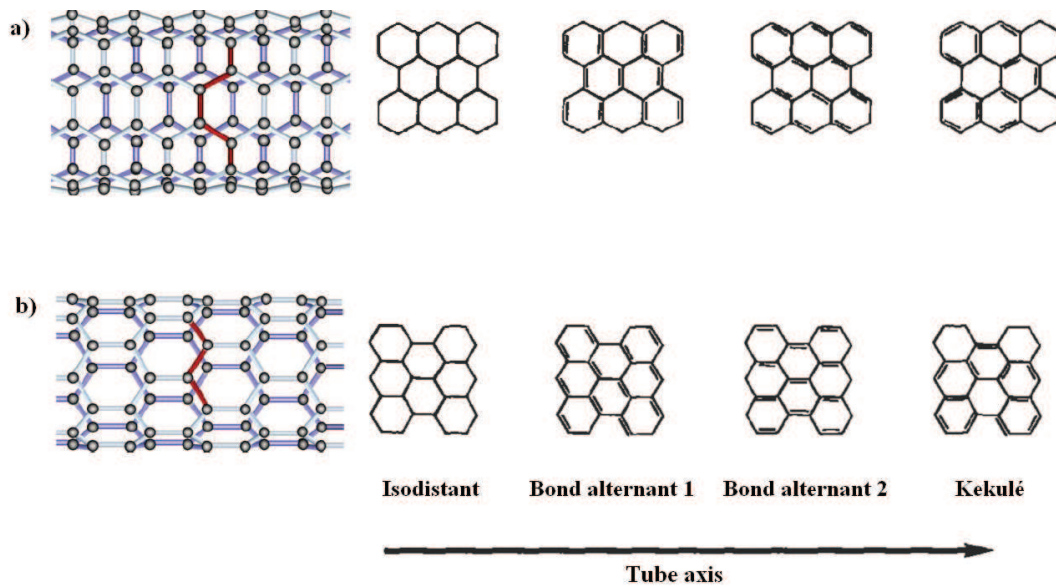


Figure 1.11 Outlook of CNT structures according to bond alternation, a) armchair, b) zigzag [13, 14]

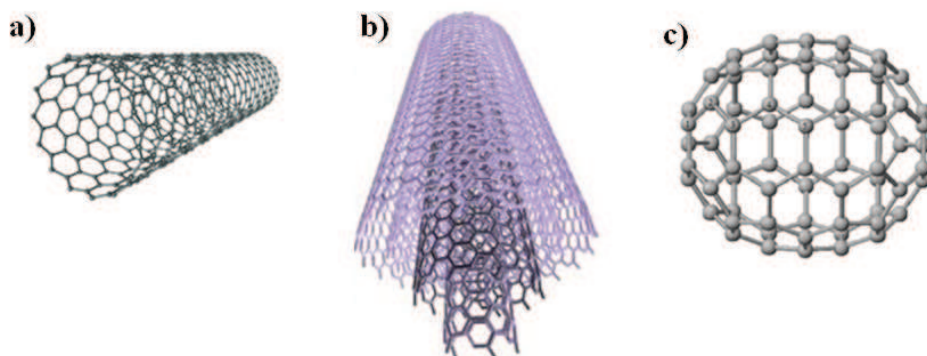


Figure 1.12 Different forms of carbon nanotubes, a) SWNT, b) MWNT, c) Fullerene C70

Regarding their chiral angle and diameter (configuration) these nanotubes can possess different level of metallization (i.e. metallic, semi-metallic or semi-conducting). Due to their tunable band-gap, they can produce conductive capabilities which have been characterized by several techniques [16-18]. Carbon nanotubes can also ensure high elastic and strength properties [13, 19]. Because of C-C covalent bonding and seamless hexagonal network architecture, carbon nanotubes can possess



higher Young modulus (1 TPa) than aluminum (70 GPa) and carbon fiber (700 GPa) [20]. Strength to weight ratio 500 times higher than that of aluminum whereas one order of magnitude improvement can also be achieved over carbon fiber/epoxy composites [20]. It has been found that when uniform forces are applied on the outer layer of MWNTs, the inner layer exhibits small axial displacements which reveal that the force acting on the outer layer is transferred to the inner layer through long range intermolecular Van der Waals interactions [13].

Thanks to the unprecedented mechanical and electrical properties of CNTs, they have found a great potential to be embedded in a wide variety of applications and even these tiny straight tubules projected to replace a certain number of conventional materials with themselves [21]. The replacement of Kevlar (PPTA), Zylon (PBO), and carbon fibers with CNTs is expected to have a great impact on a wide range of structural applications in order to obtain high performance, multifunctional, and lightweight reinforcements in polymer matrix composites [21, 22]. They also provide key solutions to several sorts of multi-functional applications. They can be used as field emitting devices for flat panel displays, conductive flexible sheets and coatings for electronic displays and touch screens, microelectrodes for electrocatalytic reactions, supporting media for heterogenous catalysis, anode for lithium ion batteries, nanoprobe for AFM (Figure 1.13), biomedical ablation agents for the investigation of cancer and plaques, supercapacitors for energy applications, and ballistic electrical conductors for nearly lossless power transmission over 1000 km [19, 21, 22].

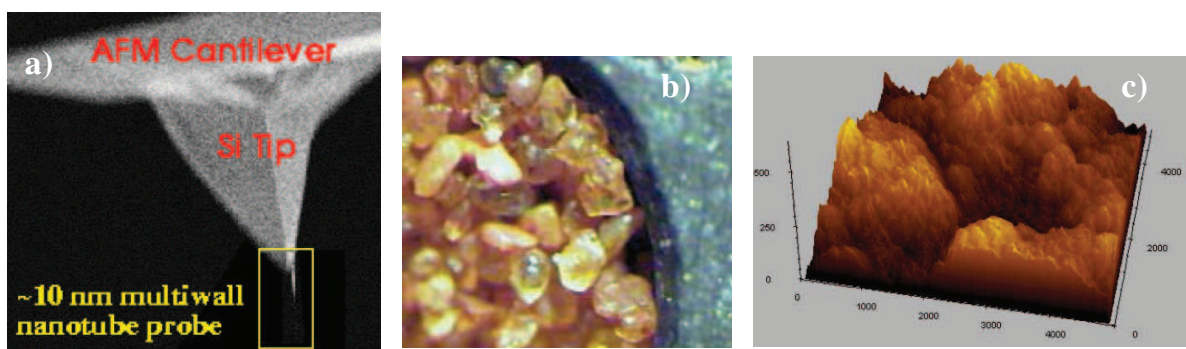


Figure 1.13 Application of MWNT probe, a) 10 nm MWNT AFM probe, b) Optical image of Red Dune Sand, c) AFM image of Red Dune Sand using MWNT tip [20]

One of the most frequent applications of these straight carbon tubules is considered as a reinforcement component in advanced polymer matrix composites [21]. However, in order to obtain more advanced CNT polymer composites, there are several indispensable points that researchers take into account during the processing period of these materials. It is well known that the resultant CNT polymer composites affected by the production process and pretreatment of CNT, matrix type and nanocomposite preparation technique [21]. Firstly, CNT production processes conducted by electric arc discharge, laser ablation or chemical vapor deposition can influence the structural (i.e. aspect ratio, surface area, purity, uniformity, alignment) and surface properties (e.g. molecular interactions) of CNTs. Among these processes, electric arc discharge may cause bundles during the preparation of CNT which may in turn cause undesirable and poor mechanical properties [21]. Other than these CNT production methods, the content of CNT in the matrix also plays a very important role in the quality of the final material. Secondly, several pretreatments such as purification, disentangling, and activation are needed before functionalization (Figure 1.14) in order to overcome the different formations of CNT (e.g. ropes, bundles, spheroid fullerenes, impurities) [19, 21]. Thirdly, polymeric matrices provide rigidity, environmental resistance, and shape to the structure. For example, epoxy, poly(methyl methacrylate), poly(vinyl chloride), polypropylene, polyethylene, and polystyrene when used in nanocomposite preparations, not only affect the cost, manufacturing, chemical, thermal, and electrical properties of composites but also directly change the ductility, toughness of the structure, wear resistance, and failure mode of the structure. Finally, the preparation of nanocomposites may be explained in three groups: solution or melt mixing and in-situ polymerization [19, 21]. Generally, in solution mixing, CNTs are introduced into the prepared polymer matrix solution by mechanical mixing, magnetic agitation or high-energy sonication. In melt mixing, nanocomposites can be prepared by using a twin-screw extruder. For in-situ polymerization, CNT are firstly mixed with monomers and then CNT reinforced polymer composites can be obtained by polymerizing the monomers under specific conditions. After the completion of mixing process, casting of nanocomposites onto suitable molding plates can also be performed by compression or injection molding which can give possibility to prepare these materials into the appropriate dimension for the testing of those nanomaterials [21].

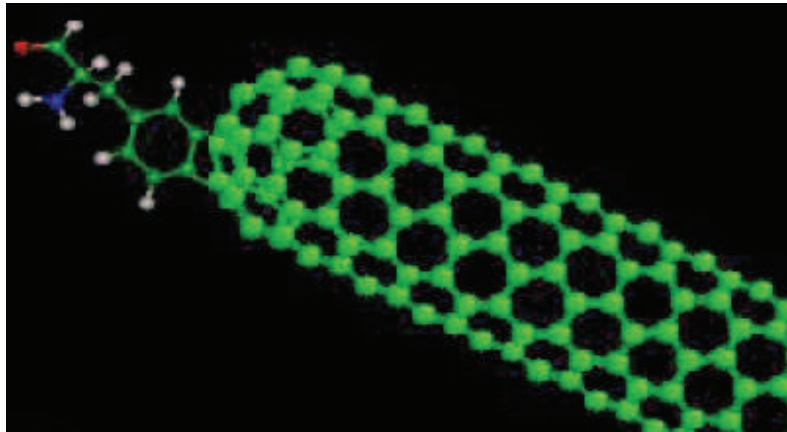


Figure 1.14 *Functionalization of carbon nanotubes* [20]

Several methods can be embedded in the current procedures in order to obtain more advanced CNT reinforced composites. While these methods are being employed, the most important criterions are: to disperse CNTs in polymer matrix uniformly without random orientations, to align CNTs in polymer matrix in order to overcome anisotropic nature of CNT, to weaken the Van der Waals forces between CNTs in order to overcome their entangled form, to reduce the defected sites in composite caused by agglomeration and entanglement of CNTs, as well as to increase the adhesion capability of CNTs in order to ensure the effective stress transfer from matrix to CNTs [21]. This knowledge and know-how has been greatly enhanced due to the fact that several researchers have developed many processes to prepare more advanced composites. In order to enhance the interfacial strength between the CNTs and polymer matrix, the amount of good bonding between CNTs and polymer matrix must be reached. Therefore, the integration of functional groups such as hydroxyl, carboxyl, nitrogen or fluorine based groups on the outer layers of CNTs by plasma modification [23-35] is one of the novel process which may give possibility to render the interfacial adhesion between matrix and CNTs. The effect of plasma treatment on carbon nanotubes including mechanical properties is discussed in the Section 2.4.

### 1.3 Epoxy resins

Epoxy resins are widely used than all other thermoset matrices in advanced composite materials. They can be considered as a reference matrix material in most of polymer composites especially for structural aerospace applications due to their desirable physical and mechanical properties over the other thermosets like phenolics, polyesters (Table 1.2).

Epoxy resins are manufactured from bisphenol A and epichlorohydrin and contain one or more epoxy groups (i.e. oxirane) per molecule (Fig. 1.15). They can be cured into the finished product by a catalyst or with hardeners containing acids or amines at ambient or elevated temperatures, depending on the type of curative. The level of their performance can be adjusted by varying the basic reactions with different chemicals or different catalysts, or both, by combination with other resins, or by cross-linking with organic acids, amines, etc. By using a polyamide curing agent, an epoxy can be made water emulsifiable for use in waterbased paints. Thermostable epoxy matrices with maximum use temperature of 150-160 °C can be based on epoxy/novolac polyfunctional epoxy resins to be cured with amines. Such catalysts made it possible to derive epoxy/novolac matrices for prepregs with a room temperature lifetime over a year [2]. Moreover, an epoxy resin with 19% bromine in the molecule is flame-resistant whereas with 49% bromine, it become semisolid and used for heat-resistant adhesives and coatings [36].

The large databases exist for epoxy systems used in military and civil aircraft showed that the first generation epoxy systems are brittle and limited to relatively low design strain levels. This, coupled with the vulnerability of these materials to foreign object impact damage, defines the need for improved toughened composites. Therefore new composite systems were needed to be developed in order to improve toughness characteristics.

Table 1.2 Properties of selected thermoset resins [3]

Resin	Density (kg/m <sup>3</sup> )	Elastic modulus (MPa)	Shear modulus (MPa)	Tensile strength (MPa)	Useful temperature limit (°C)
Epoxy	1200	4500	1600	130	90-200
Phenolic	1300	3000	1100	70	120-200
Polyester	1200	4000	1400	80	60-200
Polyimide	1400	4000 to 19000	1100	70	250-300

The new generation epoxy systems, mix of epoxy and a thermoplastic (binary-matrix), may improve toughness properties of composites [5]. Owing to new formulations exceedingly high moduli and strengths may be obtained probably due to the enhanced compatibility between carbon fibers and the elimination of many interface problems. These epoxy composites are also resistant to aircraft fluids such as jet fuel or hydraulic fluid. Such composites are of importance in aerospace applications where high ratios of a property to density are desired, as well as in such domestic applications as sports equipment.

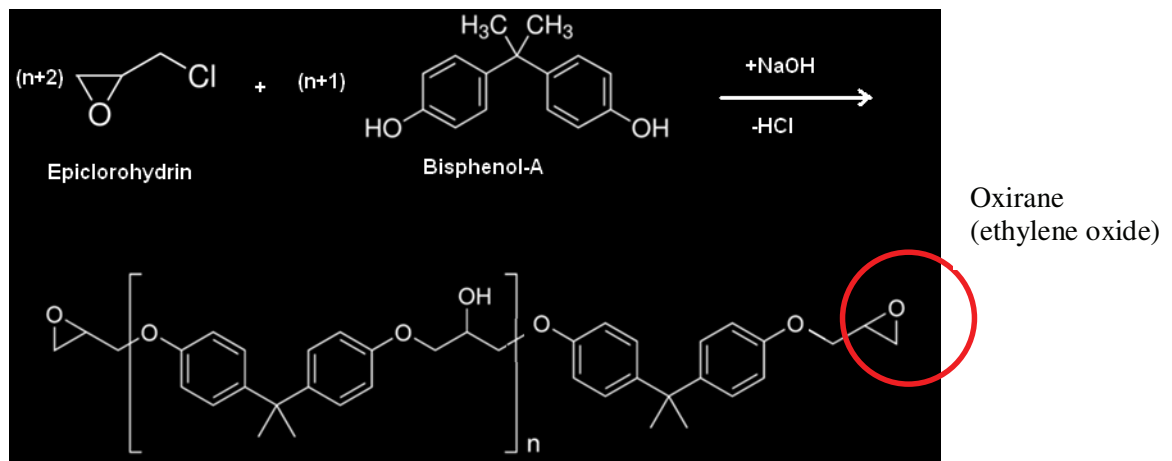


Figure 1.15 Manufacturing scheme of epoxy resin

### 1.4 The interfacial properties of composites

The properties of interphase and interface in a composite as well as the adhesion between the constituents of a composite play important role on the performance of a composite. Interfaces in composites are the zones of compositional, structural, and property gradients, typically varying in width from a single atom layer to micrometers. Interphase in composites is a physical entity with a finite thickness which depends upon the cause of the structural difference from the fiber or matrix [37, 38] (Fig. 1.16). Thermodynamic and kinetic effects can contribute to interphase formation. Thermodynamic features establish the intensity of the driving force and provide the necessary conditions for interphase formation; kinetic factors such as diffusion, nucleation and reaction of the components determine the time scale (relative to processing times) that is required to achieve interphase structures; thus providing the sufficient conditions for interphase formation [37, 38].

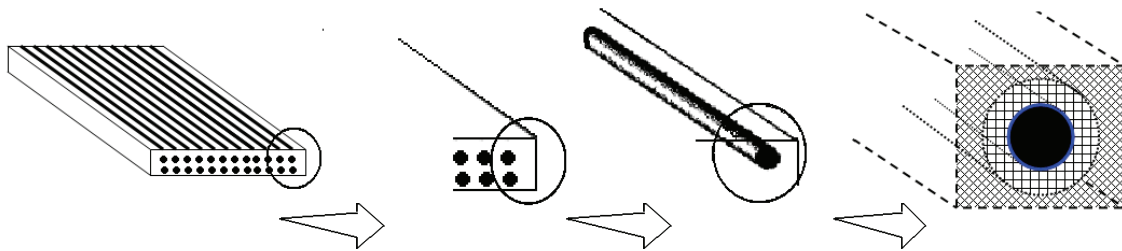






Fig 1.16 Breakdown of a fiber composite showing interphase and interface

(Note:  Matrix,  Interphase,  Interface,  Fiber)

Adhesion usually refers to the sticking together of solid surfaces by molecular attraction across common interface [39]. A schematic illustration was given in Figure 1.17 in order to describe the mechanism of adhesion. For the maximum adhesion, the adhesive (epoxy) must come into complete intimate contact with the surface of the adherent (carbon fiber); the adhesive must completely wet the adherent. Wetting is considered to be maximized when the intermolecular forces are the same forces as are normally considered in intermolecular interactions such as the Van der Waals. When adhesion is considered, the mechanism of adhesion, the natural roughness or etching of the fiber surface causing interlocking may form a mechanical bond between the fiber and matrix. Reaction bonding is where atoms or molecules of the fiber and the

matrix diffuse into each other at the interface. The importance of the fiber matrix interface bond is demonstrated by the direct relationship between compressive strength and interlaminar shear strength that has been seen for some materials [40]. The formation of chemical bonds at the interface is not considered to be of primary importance for achieving maximum wetting, but in many cases it is considered important in achieving durable adhesive bonds. If the situation is such that the adhesive completely wets the adherent, the strength of the adhesive joint depends on the design of the joint, the physical properties of the adherents, and, most importantly, the physical properties of the adhesive [36].

Besides adhesion phenomena, for higher ductility and toughness, and better transfer of loads from the matrix to fiber, composites require larger surface area of the fiber-matrix interface. For the same volume fraction of fibers in a composite, the area of the fiber-matrix interface is inversely proportional to the diameter of the fiber [4].

Proper characterization of composite interfaces, whether it is for chemical or mechanical properties, is extremely difficult because most interfaces are buried inside the material [41]. Because of this reason, there is a lack of understanding of processes occurring at the atomic level of interfaces, and how these processes influence the global material behavior. Therefore new material combinations or substitutions for existing reinforcing fibers, adherents or epoxy matrices are difficult to achieve. This lack of ability to a priori select surface and interfacial conditions is due to the lack of understanding of the structure and composition of the fiber-matrix interface itself [42].



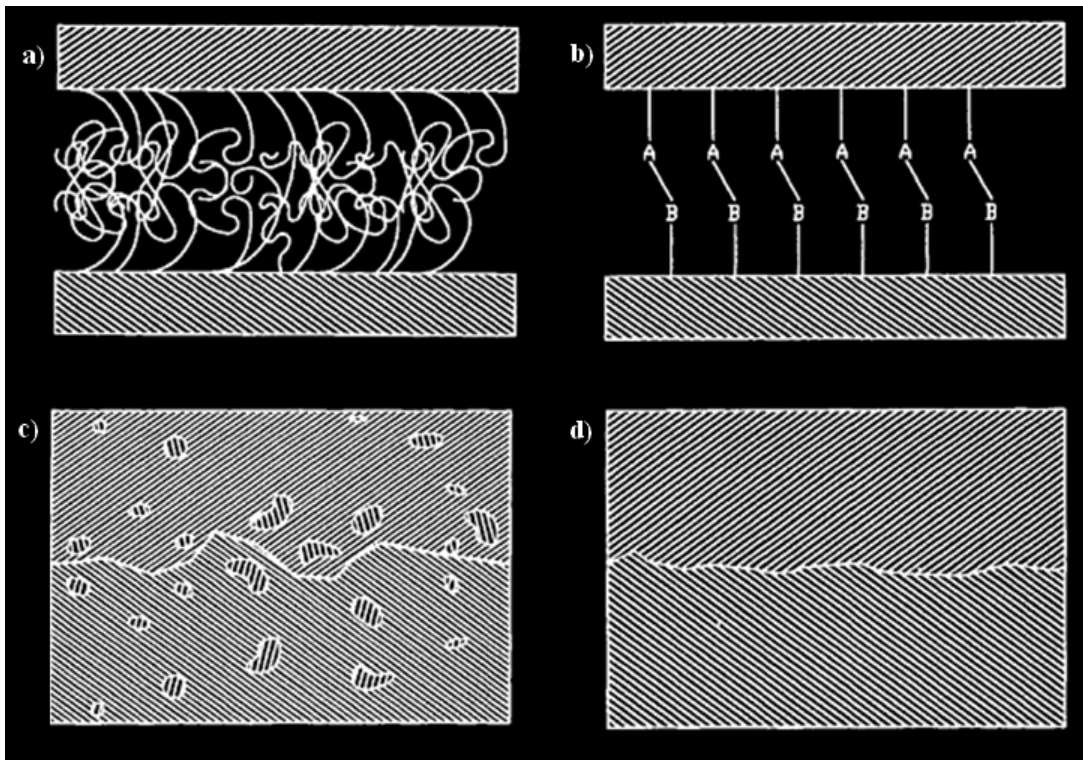


Figure 1.17 Schematic illustration of mechanism of adhesion, a) molecular entanglement, b) chemical bonding, c) interdiffusion of elements, d) mechanical interlocking [39, 41]



### 1.5 Use of carbon fiber composites in aviation industry

Composite materials were developed because no single, homogenous structural material could be found that had all the desired attributes for a given application. Owing to new inherent potentials of composites a tendency to a changeover in aviation materials utilization breakdown can be noted, as Fig. 1.18 represents [2]. The fraction of aluminum alloys is reduced noticeably from 70% to 30%; the composites fraction is increased from 8 to 50%. It can be said that aerospace industry composites use moves from secondary structure to primary structure [43].

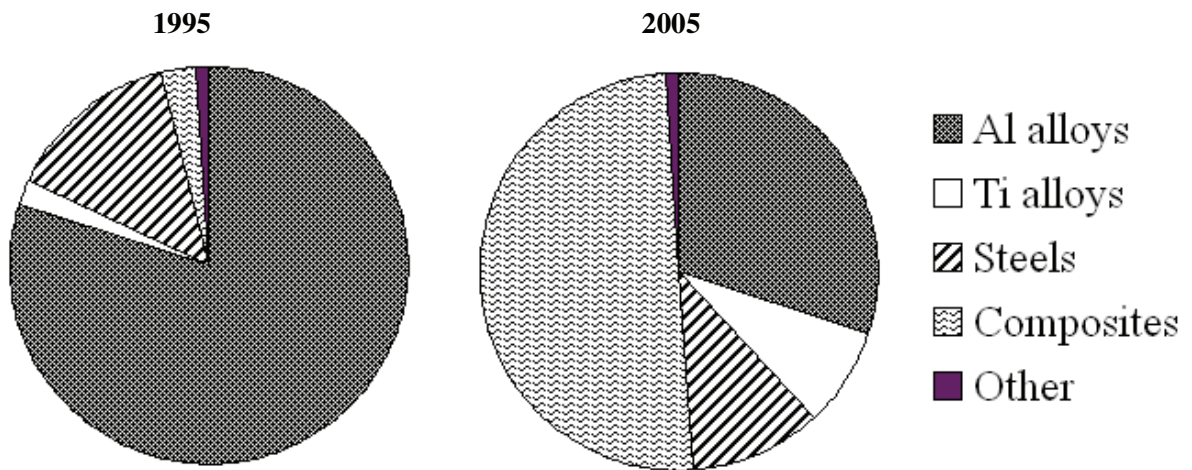


Figure 1.18 *Materials used in airframes* [2]

Many fiber reinforced composites compare well with metallic alloys; their practical efficiency due to unprecedented characteristics such as great resistance to high-temperature corrosion, oxidation and wear [44]. Aluminum alloys, which provide high strength and fairly high stiffness at low weight, have provided good performance and have been the main material used in aircraft structures over the years. However, both corrosion and fatigue in aluminum alloys have produced problems such as high maintenance costs. Especially in the 1940s a need for materials with improved structural properties were gained acceleration. For example short glass fibers impregnated with thermosetting resins (i.e. fiberglass) were employed in filament wound rocket motors. Composite materials were put into broader use in the 1950s, and initially seemed to be the only viable approach for the elimination of

corrosion and crack formation in high performance structures. For many decades, lightweight composites have been replacing traditional aluminum structures in a wide variety of aircraft types. As it can be seen from Figure 1.19 the use of such composites in aircrafts is rapidly increasing since 1975. Especially, the new Boeing B787 and Airbus A350XWB are seen as an indication of a step change in the use of composites (around 50%) as a primary structure in commercial aviation (Figure 1.20) [44, 46]. This is due to the cost and weight savings (fuel saving) that materials such as glass/phenolic and carbon/epoxy offer aircraft manufacturers over aluminium, while maintaining or surpassing its strength and durability.

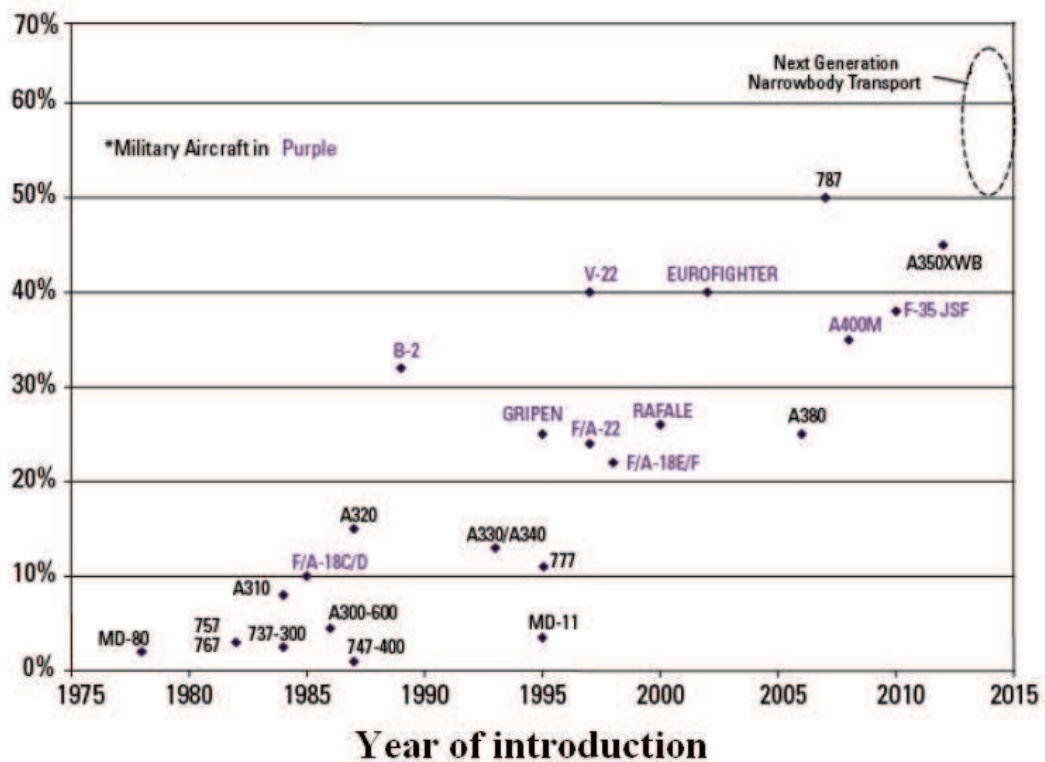


Figure 1.19 The growth of composite structure on major aircraft programs (1975-2010) as a percentage of weight [45]

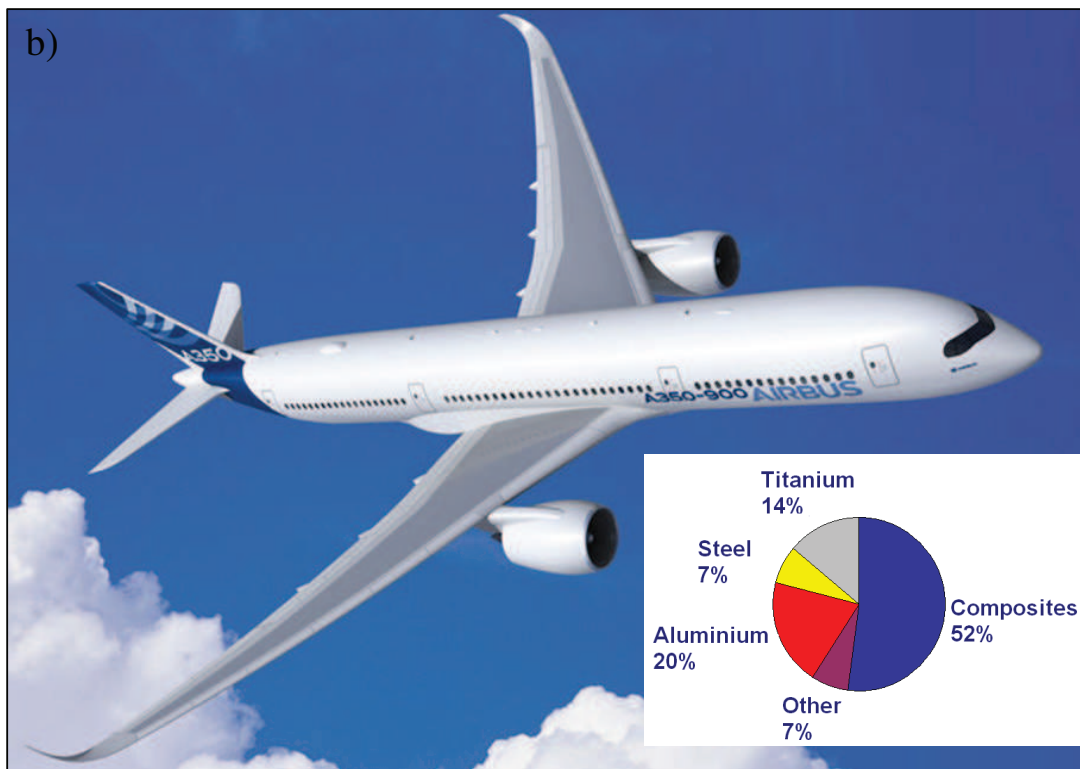
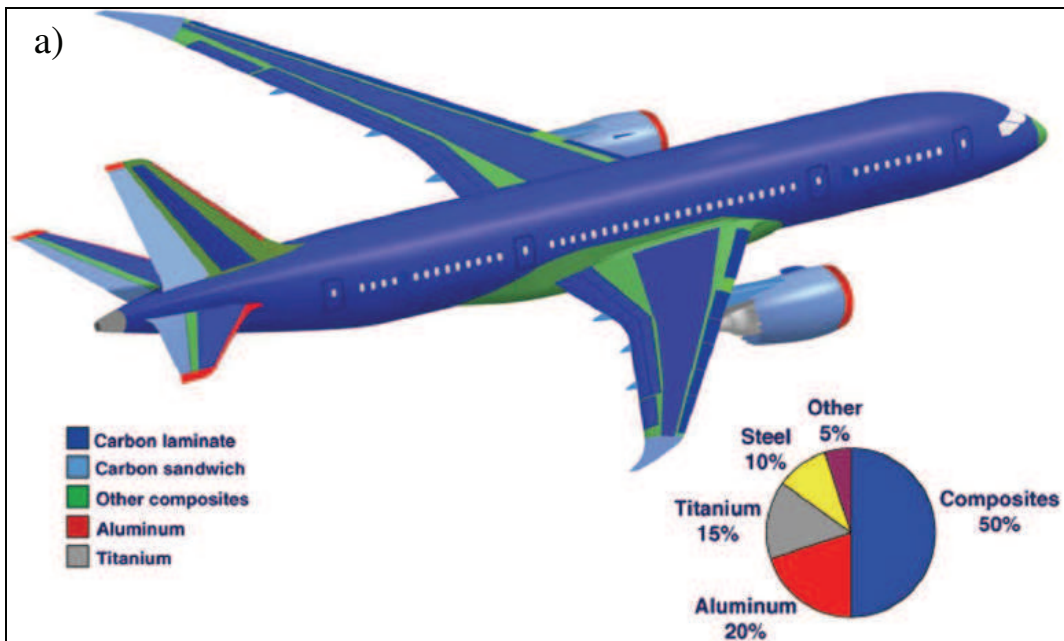


Figure 1.20 The Boeing 787(a) and Airbus 350 XWB (b) use significant amount of composite materials on their primary structure

Composites are important materials that are used widely, not only in the aerospace industry, but also in a large and increasing number of commercial engineering applications such as internal combustion engines; machine components; thermal control and electronic packaging; automobile (Figure 1.21), train, mechanical components, such as brakes, drive shafts, flywheels, tanks, and pressure vessels; dimensionally stable components; process industries equipment requiring resistance to high-temperature corrosion, oxidation, and wear; offshore and onshore oil exploration and production; marine structures; sports and leisure equipment; and biomedical devices [47].



Figure 1.21 McLaren MP4-12C uses lightweight carbon fiber reinforced composite structures (marked with an arrow) for highest power to weight ratio

However, there is a lot of conflicting or incorrect information in the aviation community about the safety and capability of fiber composite materials. Of these, mechanical failure such as delamination (subsurface damage) which may go undetected for a long period as well as lightning strike to aircraft poses an appreciable threat to flight safety. It was stated that about ninety percent of the lightning discharges to aircraft are the aircraft themselves [48]. The initiation apparently involves a bidirectional leader whose positive and negative parts develop from opposite sides of the aircraft (Fig. 1.22). In order to avoid such lightning damage to aircraft nonconductors at the exterior of the aircraft may be connected with diverter

strips to divert strike to nearby conductive structure, in case if there is no conducting surface on exterior of aircraft. Another possibility to achieve conductivity across joints by mating surfaces with carbon fiber reinforced composites [20]. Since the electrical conductivity is explained by transversal and longitudinal directions, while the two-dimensional carbon fibers exhibit high conductivity in longitudinal direction, they demonstrate low conductivity in transversal directions compared to longitudinal directions [20]. Therefore, three-dimensional structures are needed in order to overcome the low conductivity of the material in the transverse directions. So grafting carbon nanotubes on the carbon fibers may be a potential solution for this purpose.

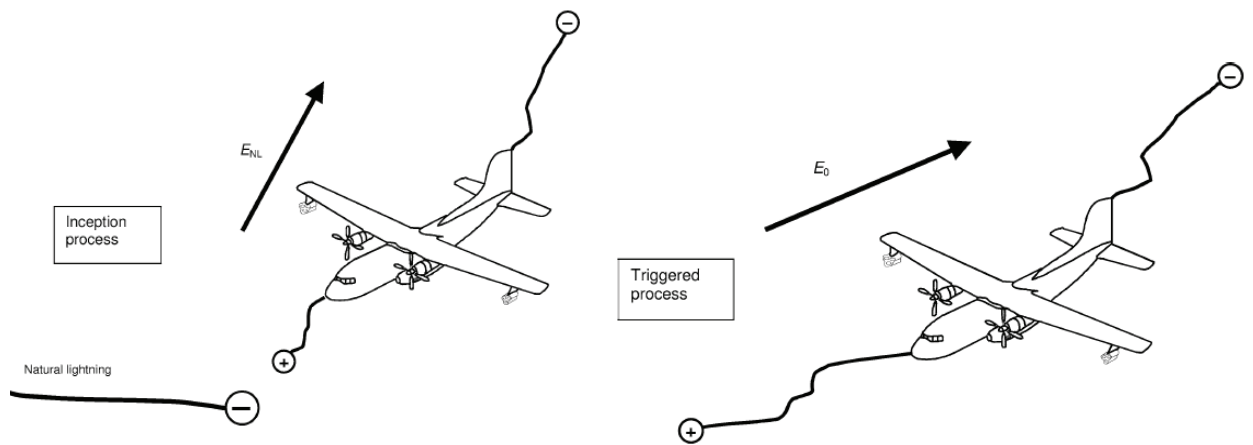


Figure 1.22 *The two different processes that lead to a lightning strike to an aircraft through a bi-leader process. Left: the interception by the aircraft of a natural lightning discharge. Right: the aircraft itself triggers the lightning discharge. The aircraft-triggered process is the more common one [49]*



## 2 *Plasma application for material processing*

A rich variety of plasma applications are employed in material processing and are offered many advantages over conventional techniques. In metal industry, plasma jet generated by electric arc can be used for welding, melting and/or vaporization of metals and ceramics because they can be employed between 6500 K and 30,000 K whereas combustion flame temperatures lies around 3300 K. In electronics industry, the manufacture of electronic components with the advent of nanostructured metals, nanopowder production and in-situ coating of these nanoparticles can be accomplished with plasma assisted material processing. In coatings industry, plasma process can provide the deposition of complex alloys, elemental materials, composites, and ceramics for wear- and heat-resistant applications. The surface of chemically inert materials can also be modified by plasma processing to promote adhesion, wettability and processability of those materials for printing, painting, and metallization in which wetting and adhesion are critical issues [50].

### 2.1 *Plasma*

The plasma term was firstly introduced into physics literature by Langmuir in 1929 to denote an electrically neutral region of a gas discharge that is not influenced by its boundaries [51]. Plasma is often referred as the fourth state of matter. As temperature increases, molecules become more energetic and transform in the sequence: solid, liquid, gas, and plasma (Fig. 1.23). In the latter stages, molecules in the gas dissociate to form a gas of atoms and then a gas of freely moving charged particles, electrons, and positive ions (i.e. plasma state) [50].

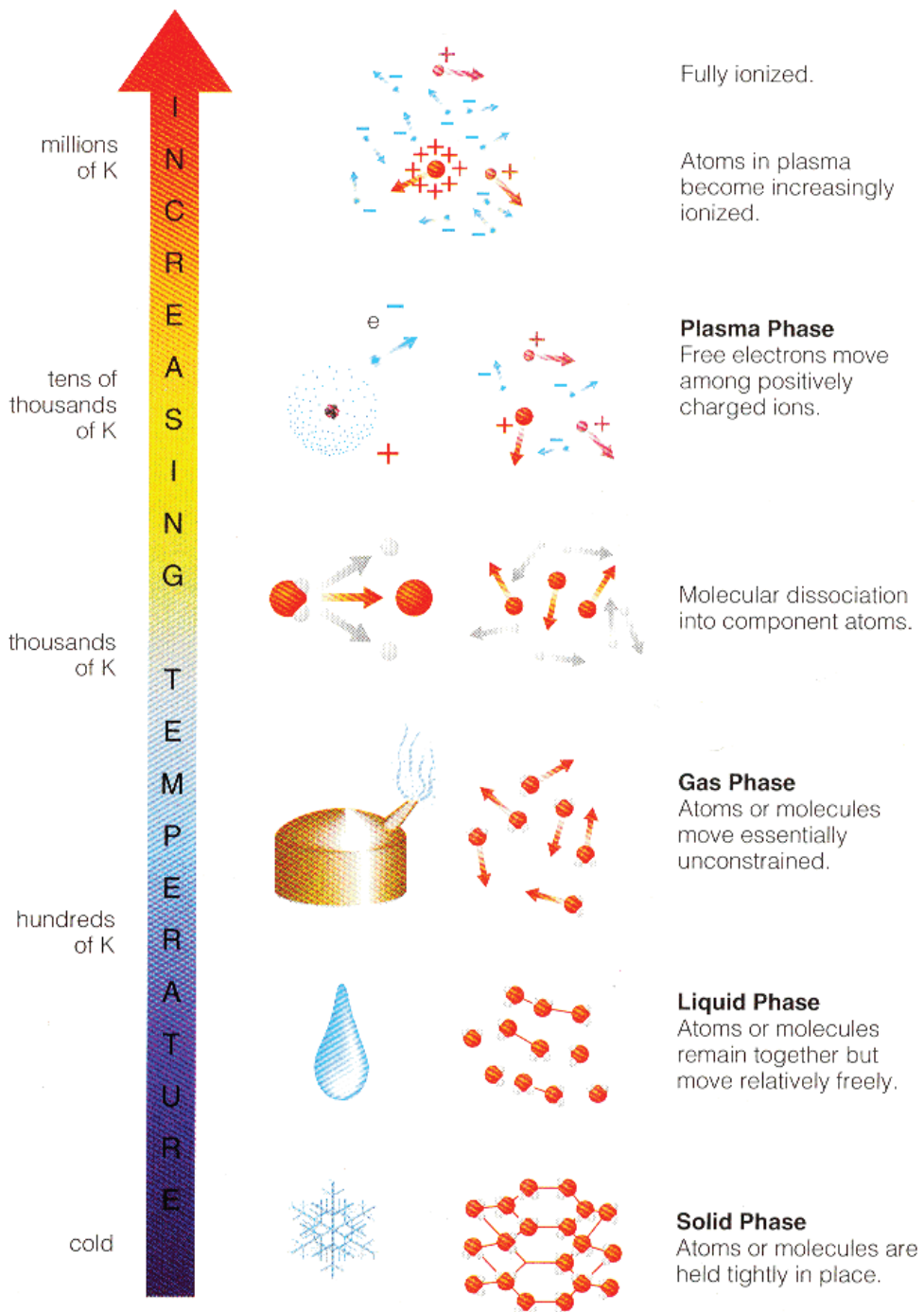


Figure 1.23 General progression of phase change

Plasmas can exist in nature or can be manmade. Either natural or manmade plasmas can be thermal and non-thermal and are classified in terms of electron temperatures and electron densities as shown in Fig. 1.24. In this figure, electron temperature is expressed in eV ( $1 \text{ eV} \approx 11,600 \text{ K}$ ); electron density in  $1/\text{cm}^3$ . Generally, thermal plasmas have very energetic heavy particles ( $10^6 - 10^8 \text{ K}$ ) and thermally in equilibrium with electrons, thus called thermal plasma [53]. In non-thermal plasmas the temperature of heavy particles can be as low as room temperature while electrons can reach  $10^3 - 10^4 \text{ K}$ , because electrons and heavy particles can not reach thermal equilibrium they so-called non-thermal plasma [53].

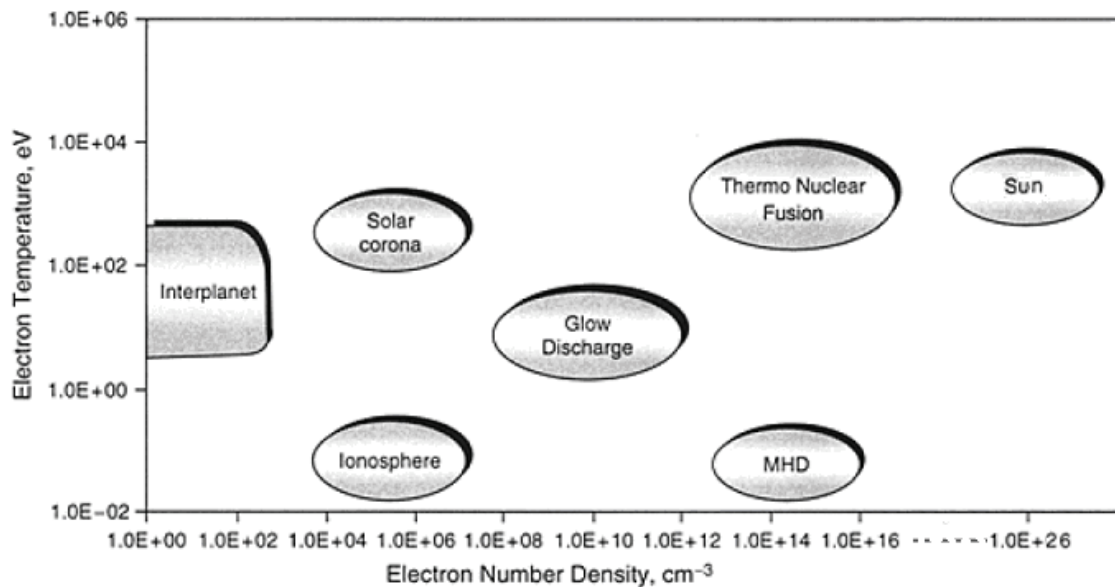


Figure 1.24 Operating regions of natural and manmade plasmas

The most common natural plasma observed on Earth are lightning and Aurora Borealis [50]. The characteristics of these plasmas are strongly dependent on pressure. Lightning occurs at relatively high pressures, it consists of a narrow, highly luminous channel with numerous branches; Aurora Borealis occurs at low pressures, it exhibits low-luminosity, diffuse event [50]. Manmade plasmas, which can be generated under controlled laboratory conditions, is defined the process of a discharge of a capacitor into a circuit containing a gas gap between two electrodes. If the voltage between the electrodes is sufficiently large, electrical breakdown occurs in the gap and the gas becomes conductor, and the capacitor discharges [50]. Under the influence of an



electric field between the electrodes, electric charges can move through the gas, acquire energy and promote several plasma reactions (Fig. 1.25): elementary plasma reactions (e.g. ionization of atoms and molecules by electron impact, electron attachment to atoms or molecules, ion-molecular reactions, etc) and recombination reactions (e.g. recombination of charged particles or neutral species) as well as dissociation of neutral species by electron impact; relaxation of excited species (e.g. relaxation of electronically excited atoms and molecules; vibrationally excited molecules; and rotationally excited molecules); electron detachment and destruction of negative ions; photochemical processes [50].

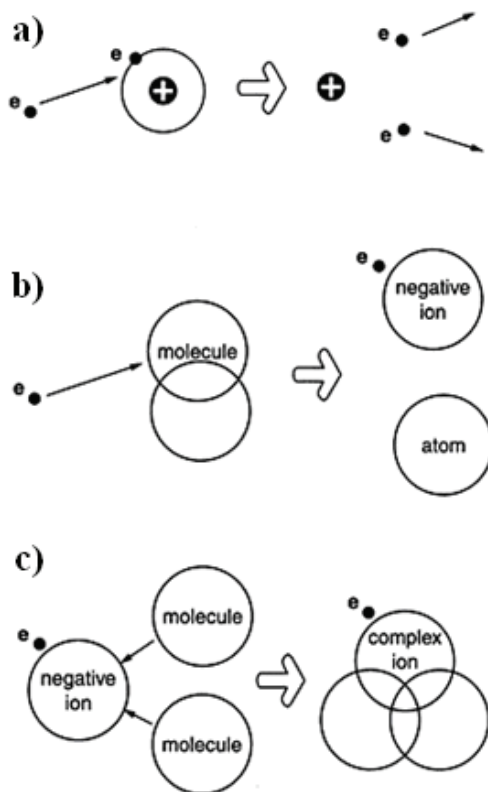


Figure 1.25 *Elementary plasma processes a) simplest ionization mechanism, b) dissociative attachment and formation of a negative ion, c) complex ion formation*

## 2.2 Plasma discharge

According to their physical features and peculiarities, plasma discharges can be classified in three different ways: (1) thermal or non-thermal discharges, (2) high pressure-discharges or low-pressure discharges, and (3) DC or non-DC discharges.

The thermal discharges are hot while the non-thermal discharges operate close to room temperature. The difference between these two qualitatively different types of electric discharges is primarily related to different ionization mechanisms. Ionization in non-thermal discharges is mostly provided by direct electron impact (electron collisions with “cold” non-excited atoms and molecules), in contrast to thermal discharges where ionization is due to electron collisions with preliminary excited hot atoms and molecules [50]. Thermal discharges (e.g. electric arc) are usually powerful and easily sustained at high pressures, but operate close to thermodynamic equilibrium ( $T_{\text{electron}}=T_{\text{ion}}\approx 10,000$  K) and are not chemically selective. The non-thermal discharges (e.g. glow discharges) are very selective with respect to plasma chemical reactions. The non-thermal discharges can operate very far from thermodynamic equilibrium ( $T_{\text{electron}}=10,000-100,000$  K,  $T_{\text{ion}}=300-1000$  K) with very high energy efficiency, but usually with limited power. Typically in thermal plasmas, electron density varies between  $10^{21}$  and  $10^{26}$  m<sup>-3</sup>; non-thermal plasmas usually lower than  $10^{19}$  m<sup>-3</sup> [54].

Low-pressure discharges are usually cold and not very powerful, while high pressure discharges can be very hot and powerful (electric arc) as well as cold and weak (corona). The characteristic difference between high and low pressure manmade plasmas is the collision frequency. In short, the higher the pressure, the higher the collision frequency and the lower the electron mean free path between collisions [50].

The DC discharges can have constant current (arc, glow) or can be sustained in pulse-periodic regime (pulsed corona). The pulsed periodic regime permits providing higher power in cold discharges at atmospheric pressure. Non-DC discharges can be low or high frequencies (including radio frequency and microwave). Further properties of these discharges are explored in the following section.

### 2.2.1 DC discharge

DC discharges are non-thermal and generally created in closed discharge chambers using interior electrodes. Different types of discharges and plasmas can be obtained depending on the applied voltage and the discharge current, as shown in Fig. 1.26 [55]. The dark Townsend discharge corresponds to the first plateau in Figure 1.26. In dark Townsend discharge, the discharge current is low (about  $10^{-10}$  to  $10^{-5}$  A); the electron and ion densities are negligible which means perturbations of the external electric field in plasma can be neglected. Moreover, the voltage necessary to sustain this discharge does not depend on current and coincides with the breakdown voltage. Transition from dark to glow discharge occurs when discharge current increase (plasma density increase) and reconstruction of electric field reduces voltage. Further decreases in voltage result in second plateau which corresponds to the normal glow discharge. This discharge exists over a range of currents ( $10^{-4}$  to 0.1 A) and current density on the cathode is fixed in normal glow discharges. Abnormal glow discharge occurs only when the current is so large that no additional free surface remains on the cathode does further current growth, thus it requires a voltage increase to provide higher values of current density. At very high currents, the discharge undergoes an irreversible transition down into an arc [50, 55].

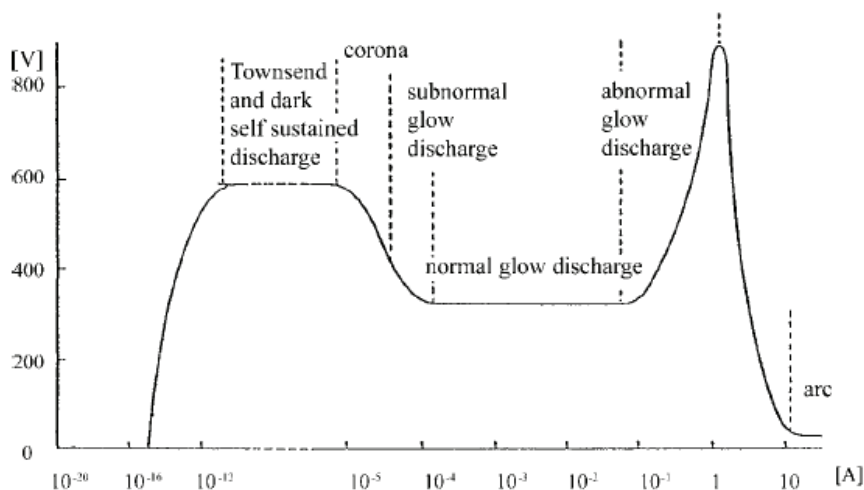


Figure 1.26 The dependence of voltage upon current for various kinds of DC discharges

In addition to the continuous DC discharge, pulsed-DC discharges are also used in plasma applications. As it can be understood from the name, pulse is a variation of a voltage or current normally having a constant. Pulsed regime provides advantages over continuous DC sources such as operation at higher power, additional performance control by a variable duty cycle of active plasma regime and plasma afterglow, prevent or minimize inhomogeneous thin film due to pulsed operation in conjunction with rapid gas exchange between pulses [55].

### 2.2.2 Dielectric barrier discharge (DBD)

Dielectric barrier discharge (DBD) is a non-DC (AC), non-thermal plasma, and operable either in closed or open-air systems (0.1–10 bar). In 1857, Siemens used this type of discharge for the generation of ozone from air or oxygen. Deeper studies of numerous high-voltage engineers were provided new insights into the understanding the characteristics of DBD. In 1932, Buss observed air breakdown with a number of individual tiny breakdown channels in a kind of DBD reactor [56]. Later much information about these current channels (microdischarges) collected by many scientists [56]. Further studies on DBD systems provide necessary information to control, to model and consequently to optimize such systems for many applications. Today, these DBDs are being used for plasma displays (miniature excimer fluorescent lamp), ozone generation for water treatment (20-50 mm-diameter, 1-2 m-long glass tubes) [56] or oxidation of volatile organic contaminants [57]. In addition, due to their numerous advantages over other discharges such as the option to work with non-thermal plasma at atmospheric pressure and the comparatively straightforward scale-up to larger dimensions make them also promising tool in continuous surface treatments [54, 58-61].

DBD is generated between two metal electrodes of which at least one is coated with a dielectric material (Fig. 1.27). In such DBD systems, the presence of the dielectric(s) precludes DC operation. For atmospheric pressure discharges, the gas-filled gap is small (a few millimeters), thus requiring alternating driving voltages with amplitudes of typically 10 kV or higher. The presence of dielectric material limits the current between the electrodes. The charge carriers streaming from the plasma to the dielectric remain on the surface of the dielectric and compensate the external electric

field. The current density in the filaments is  $100\text{--}1000\text{ A cm}^{-2}$ , the electron density is  $10^{14}\text{--}10^{15}\text{ cm}^{-3}$  and typical electron energies are in the range  $1\text{--}10\text{ eV}$  [55].

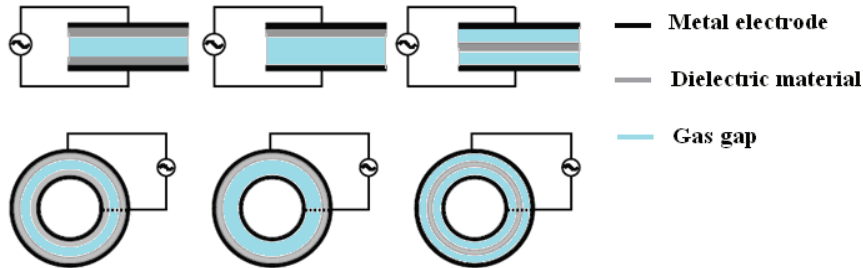


Figure 1.27 Common DBD configurations [62]

By exploring voltage-current signals of DBD systems, it is possible to have the details of the discharge characteristics (Fig. 1.28). Shortly, in filamentary mode, the alternative current signal is changed the cycle of the discharge and streamers formation is repeated with the largest probability to start from the place of the surface with some charge not being transfer during previous current half period. In glow discharge mode large numbers of streamers start in the whole inter electrode space at the same time interval, therefore homogeneous diffuse discharge is obtained [62].

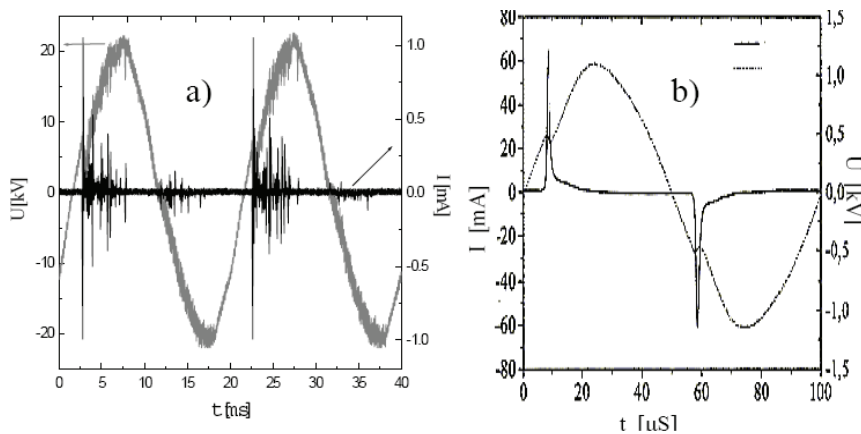


Figure 1.28 Voltage and current signals, a) filamentary mode with water as a barrier electrode, b) glow discharge mode [62]

### 2.3 Plasma process

Plasma processes includes vast number of complex reactions, therefore they can not be explained by a single approximation. For this reason, plasma reactions should be categorized in order to provide a clear physical picture for an appropriate analysis (e.g. quantum mechanical analysis). These reactions are: (1) ionization reactions, (2) electron-ion recombination reactions, (3) electron losses due to formation of negative ions, (4) ion-ion recombination reactions, (5) ion-molecular reactions, (6) elementary process of excited molecules and atoms [50] can be taken into account while performing reaction analysis. A scheme is given in Fig. 1.29 to demonstrate the possible reactions in a plasma environment.

Ionization reactions can be further divided into five subcategories: direct ionization, stepwise ionization, ionization by collision with heavy particles, photo-ionization and surface ionization. First, direct ionization of neutral species (e.g. preliminary not excited atoms, radicals or molecules) by electron impact are the most important processes in cold or non-thermal discharges in which electric fields and thus electron energies are quite high (provide ionization in one collision), but the level of excitation of neutral species is relatively moderate. Second, stepwise ionization of preliminary excited neutral species by electron are important mainly in thermal or energy-intense discharges, when the degree of ionization (ratio of number densities of electrons and neutrals) and the concentration of highly excited neutral species are quite large. Third, ionization by collision with heavy particles can take place during ion-molecular or ion-atomic collisions, as well as in collisions of electronically or vibrationally excited species, when the total energy of the collision partners exceeds the ionization potential. The chemical energy of the colliding neutral species can be contributed into ionization also via the so-called processes of associative ionization. Forth, photo-ionization processes are the formation of electron-ion pair by neutral species and photons collisions. This is mainly important in thermal plasmas and some propagation mechanisms of propagation of non-thermal discharges. Fifth, surface ionization (i.e. electron emission) provided by electron, ion, and photon collisions, or just by surface heating can be considered in heterogeneous systems [50].

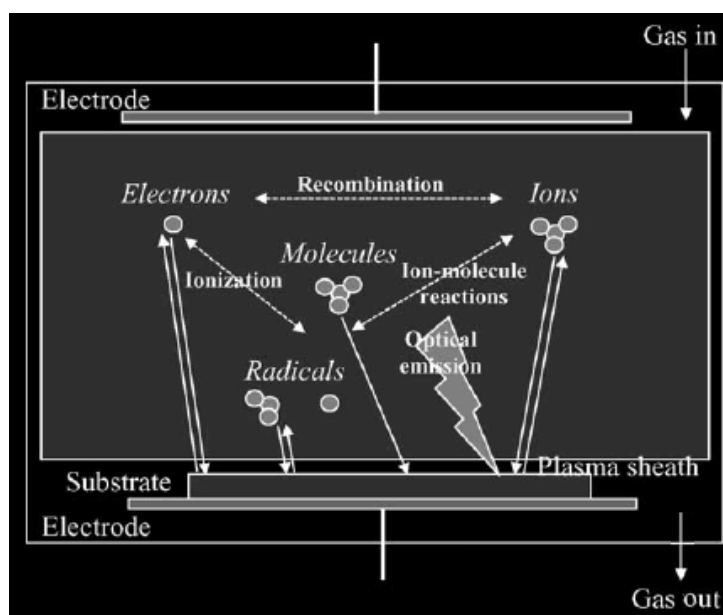


Figure 1.29 Interactions of plasma-generated species with the substrate [63]

When a non-polymer forming (e.g. hydrogen, nitrogen, oxygen, argon) or a polymer forming precursor (e.g. organic gases or vapors of organic liquids) introduced in glow discharge plasma, additional plasma reactions take place beside the above listed plasma reactions. These reactions are: (1) dissociation of precursor(s) with the collisions of energetic species (i.e. energetic species have 1-10 eV energies, thus have sufficient energy to break bonds) (Table 1.3), (2) fragment-recombination reactions initiated by the plasma-created and surface-attached active species [63]. Further, in the case of the injection of such precursors in post-discharge region (afterglow), mostly metastables and radicals can interact either physically or chemically with the substrate surface than that of electrons and ions [86, 87]. Because, unlike glow discharge plasma, many energetic species do not have lifetimes long enough to be present in the downstream from the discharge due to ambipolar diffusion and recombination reactions at the walls of the plasma chamber (i.e. the density of ions and electrons decrease rapidly with the distance from plasma) [86, 87]. Therefore, the functionalization process may take place as a result of the interaction between long-lived energetic species and surface, and/or the surface may degrade due to the removal of surface material (etching) [88].

Table 1.3 Some typical bond dissociation energies [63]

Species	Energy (eV)	Energy (kJ/mol)
C-H	3.3	318.6
C-N	7.8	753.2
C=O	11.2	1081.5
C-C	6.3	608.3
C=C	7.6	733.9
C≡C	10.0	965.6
·CH·	6.1	589.0
·CH <sub>2</sub> ·	4.4	424.9
CH <sub>3</sub> ·	1.5	144.8
NH·	3.6	347.6

(1 eV= 23.1 kcal/mole=96.56 kJ/mole)

#### 2.4 The effect of plasma on the surface of CNTs and CFs

In this section, different combinations of non-polymer forming plasma process and their effect on carbon nanotubes and carbon fibers are reviewed. Polymer-forming plasma process (particularly pyrrole) is taken into account in the Section 2.5.2. Particularly pyrrole plasma polymerization on different substrates is reviewed. The identification of reaction mechanism is not aimed in this study; the resultant effect of plasma treatments on such materials is explored rather than the reaction mechanism. In this way, one can have accurate information on which manner and at which extent a plasma process alter the surface properties of CNTs and carbon fibers.

R. Ionescu et al. examined the oxygen functionalization of MWNTs (deposited onto sensor substrates) by using inductively coupled RF plasma (13.56 MHz) and their possible use in gas sensors [23]. After 10 and 30 min O<sub>2</sub> plasma (30 W), oxygen content on MWNTs was increased from 0 to 10 and 20 at.%, respectively. Hydroxyl, carbonyl, carboxyl groups on MWNTs obtained indicated that nitrogen dioxide sensitivity was increased and the detection limit was decreased to 500 ppb. T. Xu et



al. worked on the surface modification and purification of multi-walled carbon nanotubes by O<sub>2</sub> inductively coupled RF plasma [24]. According to their results, the direct discharge could result in not only a quick grafting of polar functional groups but also an easy damage of MWNTs after longer time (30 min), particularly under intensive power (800 W). Also, they realized that the carbon nanotubes clearly seen after the 30 min plasma treatment and the amorphous parts and the impurities were removed due to the ion beam irradiation to MWNTs surface. J.A. Kim et al. worked on the O<sub>2</sub>/Ar plasma surface modification of acid treated MWNTs and examined the mechanical and rheological properties of CNT/epoxy nanocomposites [25]. They have found that plasma treated CNTs have the characteristic oxygen peak of carbonyl group (C=O) and improved interfacial bonding and dispersion of nanotubes in the epoxy matrix. H. Bubert et al. worked on modification of CNTs with Ar/O<sub>2</sub> argon and Ar/CO<sub>2</sub> plasma by using low-pressure 27.12 MHz plasma reactors [26]. They found that the modified layers consisted of hydroxide, carbonyl and carboxyl groups (14.5 at. % oxygen content) and the thicknesses were approximately 1–2 nm after a short time of oxygen plasma exposure and could not be enlarged with further treatment. The author stated that the most polar surface was obtained when carbon dioxide used as plasma (80 W, 3-5 min.). G. Kalita et al. worked on multi-walled carbon nanotubes (MWNTs) functionalization with nitrogen (N<sub>2</sub>) and argon (Ar) microwave plasma for photovoltaic device fabrication [27]. It is indicated that on the side walls of the outer layer of MWNTs included imine, amine, nitride and amide groups. According to their results, the detected little defects on the outmost layer of MWNTs caused no destruction to multi-walled structure of the CNTs. They found that the functionalized MWNTs were well dispersed and well embedded within the polymer matrix, MWNTs functionalized composite film facilitated efficient holes transportation, suppressed the recombination of photo generated charges, namely, the treatment improved the device performance.

N.O.V. Plank and R. Cheung examined the modification mechanism of SWNTs with CF<sub>4</sub> and SF<sub>6</sub> plasma for 1 min with different bias voltage in order to examine the effect of bias on the subsequent bonding of fluorine to the SWNTs by reactive ion etching [28]. Their actinometry and ion current density measurements have shown that in a plasma environment with a greater atomic fluorine pressure, a more covalent C–F attachment observed after decomposition of the F1s spectra, as was the case for the SF<sub>6</sub> plasma in comparison to the CF<sub>4</sub> plasma over all bias

conditions. Y.W. Zhu et al. achieved surface functionalization of aligned MWNTs grown on iron-coated silicon substrates by  $\text{CF}_4$  plasma produced by reactive ion etching [29]. By exploring the field emission measurements, they found that only 2 min of plasma treatment helped to enhance the emission currents. Also, reactive sites of aligned CNTs (i.e. cylindrical walls of the CNTs near tips) were easily removed by less than 2 min plasma etching. However, over 2 min plasma treatments emission properties of films were found degraded. Except that, with  $\text{CF}_4$  treatment, the surface density of aligned CNTs became reduced due to the formation of CNT bundles. Y.C. Hong et al. treated MWNT powders by  $\text{CF}_4$  glow discharge plasma (20 kHz, 20 W) in order to obtain super-hydrophobic material [30]. After  $\text{CF}_4$  plasma treatment, C–F, C–F<sub>2</sub>, and C–F<sub>3</sub> were detected by XPS measurements. They observed solubility differences between unmodified and  $\text{CF}_4$  modified samples, and they found that modified CNTs were perfectly floated on water surface without aggregation for several months. However, unmodified samples were settled down easily due to the high surface energy of the graphitic surface of nanotubes. C. Bittencourt et al. prepared MWNTs by catalytic CVD, and then worked on the  $\text{CF}_4$  RF (13.56 MHz) plasma process of MWNTs which can lead to increase in the electrical resistance of CNTs [31]. They established that the fluorine atoms grafted onto MWNTs effectively. When they increased the plasma treatment time (5 to 600 s at 15 W), an increase in the semi-ionic/covalent ratio was observed. Besides, while observing the surface of CNTs by HRTEM, which can helped to evaluate the possible etching of CNT walls due to exposure to  $\text{CF}_4$  plasma, they found that plasma treatment led to the increase in active sites and did not etch the CNT surface significantly. L. Valentini et al. worked on the plasma (13.56 MHz) fluorination of SWNTs for the preparation of epoxy nanocomposites [32]. Their main purpose was to show how plasma fluorinated single-walled carbon nanotubes (SWNTs) reacted with a primary aliphatic amine (i.e. butylamine, BAM) and combined together to prepare crosslinked epoxy nanocomposite material. In this respect they investigated the cure reaction of diglycidyl ether of bisphenol A-based epoxy resin reacted with butylamine molecules anchored onto the fluorinated SWNTs obtained by plasma treatment. According to their results, BAM-SWNTs were acted as a strong catalyst during the cure reaction of epoxy and amino-functionalized SWNTs. They found that amino functionalized nanotubes have better dispersion in the polymer matrix, an also for the BAM-SWNTs based system, the tensile strength increases with respect to the neat system. On the

other hand, thermogravimetric measurements showed that after pyrolysis in nitrogen the weight loss of fluorinated SWNTs was higher than that observed for the untreated ones. Reason of that behavior was connected to the disordered graphene structure of the tubes by the presence of fluorine atoms.

W. J. Chou et al. synthesized MWNTs and grafted with maleic anhydride (mCNTs) in Ar RF (13.56 MHz) plasma [33]. That process was led to the outer layer functionalization of MWNTs and also the amount of maleic anhydride grafting percentage affected the resultant nanocomposite which was found as 6.4 wt.% by XPS. Results of mechanical tests are quiet important, because Young's modulus of the polyimide nanocomposites increased to 2.27 GPa when 0.05 wt.% MWNT was incorporated into the polyimide. The addition of 0.5 wt.% of the mCNT to the polyimide further increases the Young's modulus to 4.56 GPa, which was 110% higher than that of the neat polyimide. As a result, plasma modification was affected the interfacial interactions of MWNTs and polyimide matrix; thus the resultant material has less free volume and has improved elasticity because of better chemical bonding and good dispersion of mCNTs. On the other hand, large surface area of CNTs and strong Van der Waals forces of CNTs caused clusters in high loadings which may be the responsible of poor mechanical properties and unavoidable structural defects.

Donglu Shi et al. worked on CNTs as a substrate which is comprised of ropes of tubes held together by Van der Waals forces [34]. In their study, pyrrole was used as a monomer for the plasma polymerization (RF 13.56 MHz). Also, an ultrathin film of pyrrole was coated on both outer and inner surfaces. They detected an ultrathin amorphous film layer which has covered both the inner (1-3 nm) and outer (2-7 nm) surfaces of the nanotubes after plasma treatment. For the uncoated CNT composite, the strength of the composite shows a gradual decrease as the CNT concentration increases while the coated counterpart showed a significant increase in strength. The fracture surface of uncoated CNT composite was rather flat due to the nature of brittle fracture. Because of this reason they observed severe pullouts of CNTs from the surface of composite. However, the coated CNTs were well dispersed in the matrix with a wavy type of fracture surface morphology which exhibited few clusters and pullouts.

K. Yu et al. investigated the formation of the 3D multiple-way connected nanotube webs by hydrogen RF (13.56 MHz) plasma alternated at 250 W [35]. They

have found that during hydrogen plasma treatment, the amorphous structure was produced on the MWNT graphite layers due to the bombardment of high energetic ions formed in the plasma region. And, the large-scaled temperature dependence observed on electric resistance for the treated MWNT film due to the scattering of conduction electrons which was caused by the increased defect density and disorder in the nanotube graphite layers.

V. Brüser et al. treated carbon nanofibers (vapor grown carbon fibers, VGCF) with nitrogen and oxygen containing RF (13.56 MHz) plasma to enhance the wettability and thus to improve the bonding to the matrix in polymer composites [64]. The water contact angles of VGCF decrease with plasma treatments in  $\text{NH}_3$ ,  $\text{O}_2$ ,  $\text{CO}_2$ ,  $\text{H}_2\text{O}$  and formic acid. In the range of 0.01 to 1 mbar the water contact angle at treatments in  $\text{NH}_3$  increases with increasing pressure. However, using  $\text{O}_2$ ,  $\text{CO}_2$ ,  $\text{H}_2\text{O}$  and  $\text{HCOOH}$  the water contact angle decreases with increasing process pressure. By XPS measurements, they found that  $\text{O}_2$  and  $\text{CO}_2$  lead to the higher concentrations of  $\text{COOH}$  and  $\text{C:O}$  functional groups on the surface in comparison to  $\text{H}_2\text{O}$  and  $\text{HCOOH}$ .

G. Bogoeva-Gaceva et al. worked on the surface chemistry and morphology of high modulus carbon fibers, treated with pulse-voltage excited air, oxygen, nitrogen and acrylonitrile plasmas [65]. They found that oxygen- and nitrogen-containing species were generated on the surface under plasma treatment without significant changes in the fiber morphology. The highest value of interfacial shear strengths was determined for air-plasma-treated fibres. The overall changes in the shear strengths of model composites, caused by plasma treatment, were not higher than 10 MPa.

A. P. Kettle et al. explored the relationship between fiber surface chemistry and interfacial bond formation in carbon-fiber/epoxy composites with RF plasma radio frequency (13.56 MHz) [66]. They were performed direct copolymerisation of acrylic-acid/hexane, allyl-alcohol/hexane and allyl-amine/octadiene. The introduction of co-monomers, acrylic-acid, allyl-alcohol and allyl-amine individually to the plasma feed was resulted in increased levels of specific fiber surface functionalities and improvements in the level of adhesion. With an increase in adhesion the mode of interfacial failure was changed from debonding to matrix yielding and cracking. Carboxylic acid and amine groups are found more effective than hydroxyl groups, reflecting the generally recognized reactivity of these species towards epoxides.

K.K.C. Ho et al. worked on atmospheric pressure plasma fluorination (APF) with Freon 22: $\text{N}_2$  (1:70) of carbon fibers [67]. They were positioned the carbon fibre

roving at a distance of 15 mm from the tip of the plasma jet (efficient distance between the plasma jet and the substrate for atmospheric pressure plasma treatment is between 12 and 15 mm). A surface fluorine content after plasma fluorination was 4.9 at.% by using a continuous discharge. They concluded APF is a promising step for in-line carbon fiber/matrix interface tailoring during manufacturing of unidirectional fiber reinforced fluoro-polymer composites.

### 2.5 Forth generation of polymers: electrically conducting polymers

Saturated polymers are insulating due to their all four valence electrons of carbon are used up in covalent bonds. Conjugated polymers can be electrically conducting, because their chemical bondings lead to one unpaired electron ( $\Pi$ -electron) per carbon atom. Further,  $\Pi$ -bonding in which the carbon orbitals are  $sp^2p_z$  configuration and in which the orbitals of successive carbon atoms along the backbone overlap, leads to electron delocalization along the backbone of the polymer chain [68]. Electrical conductivity in such kind of conjugated polymer was first discovered by Heeger, MacDiarmid, Shirakawa and co-workers in 1976 [68]. In 2000, Nobel Prize in chemistry was awarded to group, recognizing their pathbreaking discovery of high conductivity in polyacetylene upon doping with iodine (Fig. 1.30) [69].

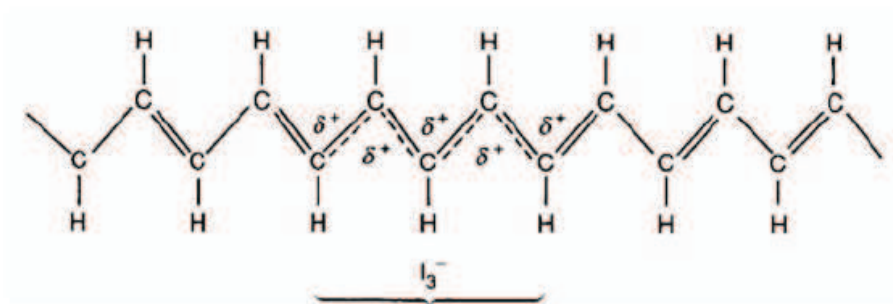


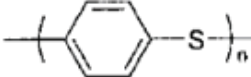
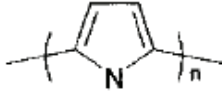
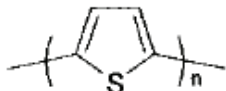
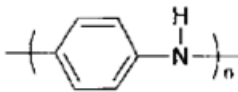


Figure 1.30 Doped polyacetylene structure (---: positive charge delocalization along polymer chain [70])

In spite of their short history electrically conducting polymers belonging to polyenes or polyaromatics such as polyacetylene, polyaniline, polypyrrole, polythiophene, poly(p-phenylene), and poly(phenylene vinylene) prepared either by chemical or electrochemical polymerization methods are some of the widely studied

classes due to the ability of electrical charge transfer to the same extent as an electrical conductor or a semiconductor (Table 1.4). Thus, they have been utilized in many technological applications like rechargeable batteries, conductive adhesives, chemical sensors, electromagnetic shielding, light emitting diodes, and electrochromic displays [71-76].

Table 1.4 Electrical conductivity of selected polymers prepared by conventional methods [77]

Polymer	Structure	Doping method
Polyacetylene		Chemical, electrochemical (dopant: AsF <sub>5</sub> , I <sub>2</sub> , Li or K)
Poly(p-phenylene)		Chemical (dopant: AsF <sub>5</sub> , Li or K)
Poly(phenylene sulphide)		Chemical (dopant: AsF <sub>5</sub> )
Polypyrrole		Chemical, electrochemical (dopant: BF <sub>4</sub> <sup>-</sup> , ClO <sub>4</sub> <sup>-</sup> or FeCl <sub>3</sub> )
Polythiophene		Chemical, electrochemical (dopant: BF <sub>4</sub> <sup>-</sup> , ClO <sub>4</sub> <sup>-</sup> or FeCl <sub>3</sub> )
Polyaniline		Chemical, electrochemical (dopant: HCl, FeCl <sub>3</sub> or (NH <sub>4</sub> ) <sub>2</sub> S <sub>2</sub> O <sub>8</sub> )

### 2.5.1 Polypyrrole (PPy)

Like other undoped  $\Pi$ -conjugated conducting polymers, polypyrrole polymers possess low electrical conductivity without doping. Therefore, partial charge extraction from PPy chain is required and can be achieved either by chemical or electrochemical processes (upon doping). The level of doping has a considerable

effect on the electronic and band structures of PPy, as shown in Figs. 1.31 and 1.32, respectively.

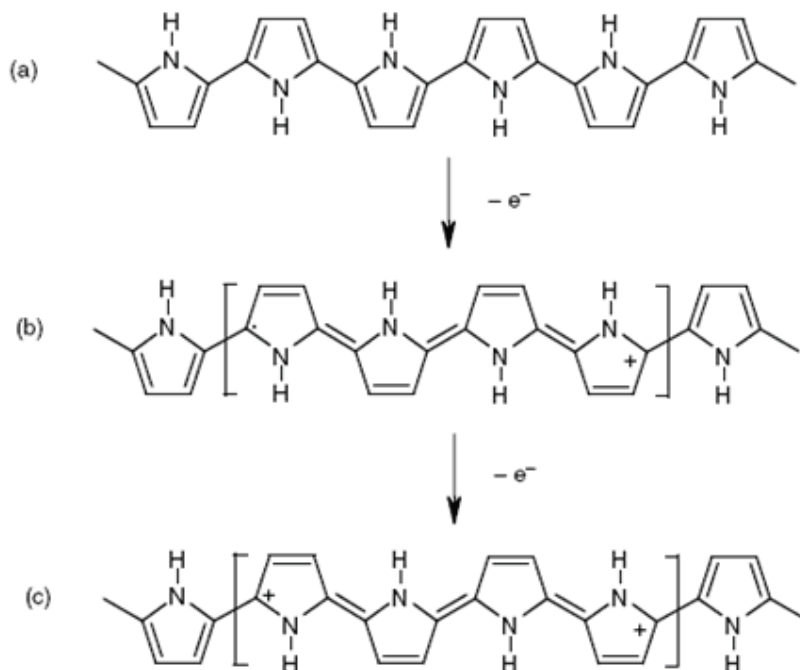


Fig. 1.31 *Electronic structure of a) neutral PPy, b) polaron in partially doped PPy, c) bipolaron in fully doped PPy [69]*

Neutral PPy (Fig. 1.31a) has benzenoid structure with a bandgap (gap between valence band and conductance band) of 3.16 eV, thus categorized as an insulator at room temperature. Upon doping (i.e. extraction of negative charge from a neutral segment of PPy), a local deformation occurs and quionoid structure of PPy forms (polaron) (Fig. 1.31b). Further oxidation leads more electron removal from PPy chain and forms bipolaron which extends over about four pyrrole rings (Fig. 1.31c). As the degree of oxidation increase, narrow intermediate band structures forms (Fig. 1.32). At higher doping levels, bipolarons become more dominant than polarons. Additionally, when PPy doped, counterions are also contributed to polymer chain to maintain the electrical neutrality of polymer. It has been reported that electron-rich heterocycle based polypyrrole is very stable in the p-doped form. Their stability is due to their lower polymer oxidation potentials. Also, good environmental stability and high electrical conductivity make them one of the most studied conducting polymers.

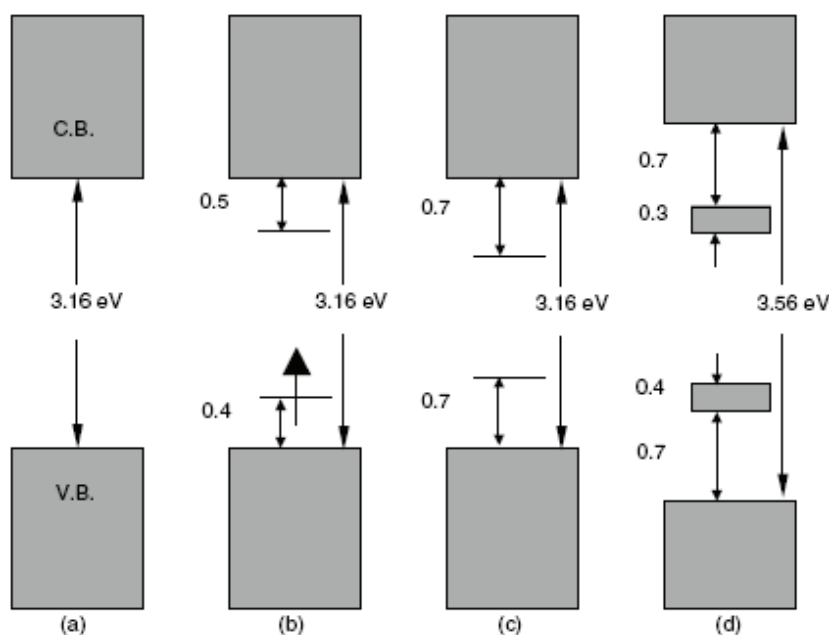


Figure 1.32 *Electronic energy diagrams for a) neutral PPy, b) polaron, c) bipolaron, and d) fully doped PPy* [69]

The charge mobility in conducting PPy greatly influences the electrical conductivity. Since the overall mobility of charge carriers depends on intrachain mobility (corresponds to charge transfer along the polymer chain) and interchain mobility (involves the hopping or tunneling of the charge from a chain to neighboring chains), low degree of polymer crystallinity and defects in polymer chains causes interruptions in charge mobility, thus lower the electrical conductivity. However a high degree of structural order can be achieved by doping PPy with hexafluorophosphate and by applying mechanical stretching [69].

PPy chains are intrinsically planar and linear; many conformational and structural defects can be formed during polymerization (Figure 1.33) [69]. The defects break the planarity and linearity of the PPy chain and reduce the extent of  $\Pi$ -orbital overlaps. The defects include conformational defects such as 2–2' coupling with non-regular  $180^\circ$  rotation of the alternating pyrrole unit, chemical defects and non-aromatic bonding and formation of carbonyl or hydroxyl groups in PPy chains due to over-oxidation [69].



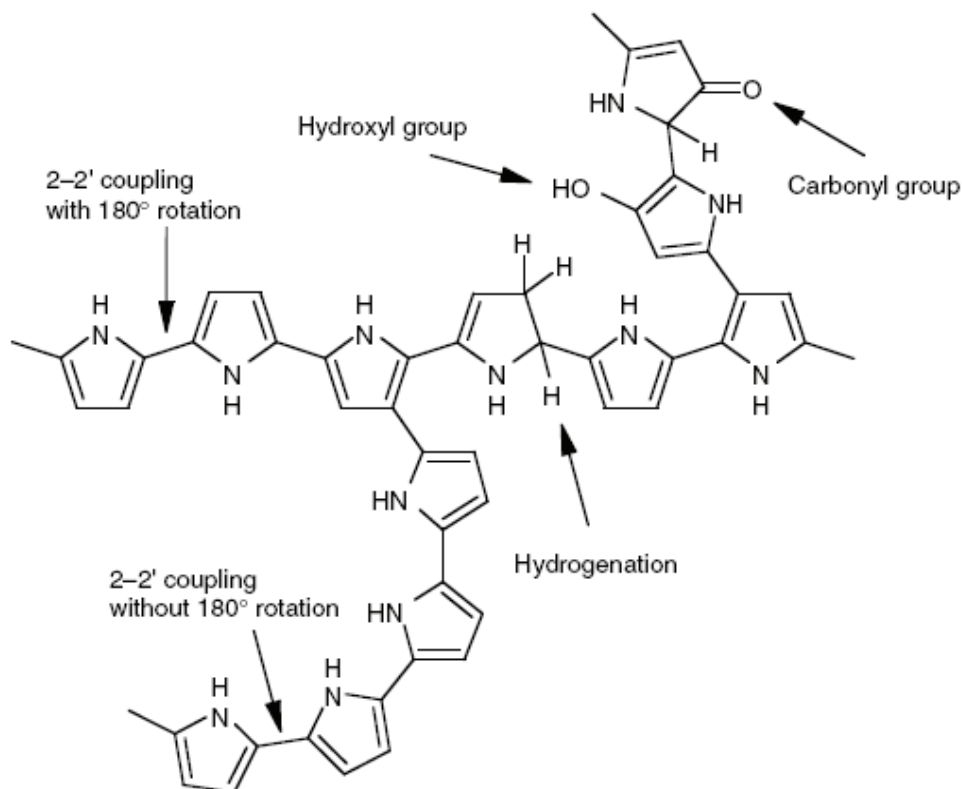


Figure 1.33 Chemical and conformational defects in PPy

### 2.5.2 Plasma polymerized polypyrrole (PPPy)

In this section, the effect of pyrrole plasma treatment on various substrates is reviewed. It has been observed that plasma conditions usually have a significant influence on the gas-phase molecular-fragmentation mechanisms and accordingly, on the nature of structures of the nascent macromolecular layers generated as a result of surface-mediated recombination of active species.

Yu Iriyama worked on the plasma polymerization (13.56 MHz capacitively coupled RF) of pyrrole, thiophene, and furan on low-density polyethylene (LDPE) film [78]. It was found that surface concentration of oxygen on the plasma polymerized pyrrole and thiophene films increased gradually with time. The increase rate of oxygen was higher when the films were stored in ambient air than in a desiccator. For pyrrole plasma treated LDPE film, nitrile group was formed, and could be hydrolyzed to form carboxyl group with the formation of ammonia.

K. Hosono et al. studied the structural and electrical properties of plasma polymerized polypyrrole (PPPy) films (RF 13.65 MHz) [79]. Doping process was also performed with 4-ethylbenzene sulfonic acid (EBSA) in a vacuum sealed and heat-treated glass tube. They found that the atomic ratio of C:H:N in the PPPy was calculated 2.21:2.66:1. This ratio was different than that for ideal PPy (C:H:N 4:3:1). Therefore, it was concluded that the pyrrole ring was decomposed to some extent in the PPPy films (Figure 1.34). The conductivity of EBSA treated PPPy was given  $4.8 \times 10^{-4} \text{ S.cm}^{-1}$  at 40 °C in the humidity of 60%.

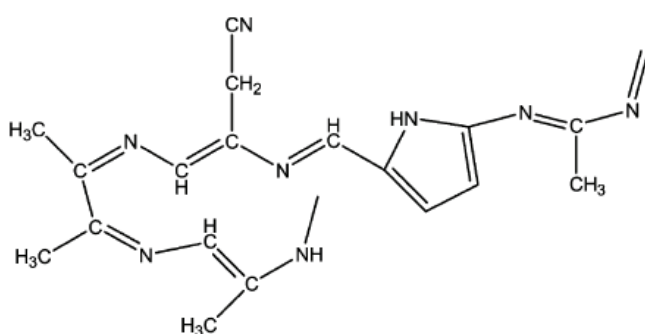


Figure 1.34 A structural model of PPPy

K. Hosono et al. discussed the effects of the discharge conditions on the structure and conductivity of the plasma polymerized polypyrrole films [80]. They found that the structure of polymer backbone of PPPy films depends on the discharge power. By FTIR, UV-vis and elemental measurements, they found that at low discharge powers (10 W) some pyrrole units were survived whereas almost all the pyrrole rings were cleaved in PPPy films prepared with the higher discharge power. Further at higher power (100 W) a three-dimensional crosslinked structure seems to have been formed. The electrical conductivity measured at room temperature in the humidity of ~40% for the 10 W-, 20 W-, 50 W and 100 W-PPPy/EBSA films were around  $4 \times 10^{-4}$ ,  $5 \times 10^{-8}$ ,  $2 \times 10^{-5}$  and  $3 \times 10^{-4} \text{ S.cm}^{-1}$ , respectively.

G.J. Cruz et al. presented the synthesis of polypyrrole films by plasma (13.5 MHz) and characterization of those films both undoped and doped in-situ with iodine [81]. It was demonstrated that both PPy and PPy-I<sub>2</sub> films exhibited a humidity related-behavior of conductivity characteristics. The undoped PPy films were obtained with thickness between 2.7-13.1  $\mu\text{m}$  and conductivity between  $10^{-12}$  (RH 30%) and  $10^{-9}$

S/cm (RH 90%). The thickness of the films doped with iodine was between 4.9-19.8  $\mu\text{m}$  and conductivity between  $10^{-10}$  (RH 30%) and  $10^{-3}$  S/cm (RH 92%). Besides, the probable ring opening reactions took place during the plasma polymerization because the existence of a strong absorption in the  $2932\text{ cm}^{-1}$  wavenumber region suggested that the deposited layers have dominant non-aromatic structures.

M. Vasquez et al. worked on the simultaneous plasma doping of (RF 13.5 MHz) pyrrole and thiophene with chloroform [82]. The electrical conductivity of chlorinated plasma polymers was increased by 5 orders of magnitude compared to undoped plasma polymers. Namely, conductivity of doped polymers was found between  $10^{-5}$  S/cm (RH 40%) and  $10^{-3}$  S/cm (RH 75%). It was indicated that the Cl atoms were combined with the structure of both polymers in a proportion of 4 or 5 equivalent monomer rings per Cl atom. The presence of each chlorine atom in the polymers expected to modify the electronic configuration in its neighborhood, because of the high electronegativity of Cl, in such a way that those sites could be negative to other parts of the chains. The possibilities of transporting electric charges along the polymers could also be linked to the presence of C=C bonds in similar patterns as those found in the heteroaromatic rings.

W. J van Ooij et al. studied DC-plasma polymerization of pyrrole and its characterization with different techniques [83]. According to their spectroscopic analyses, no pyrrole ring was found in the plasma polymerized polypyrrole. They concluded that the pressure has an impact on the structural properties of polypyrrole, thus at low pressure synthesized polypyrrole were less hydrogenated than those of high pressure. Electrical conductivity of films was found between  $10^{-3}$  and  $10^{-4}$  S/cm.

F. Fally et al. worked on the plasma polymerization of pyrrole in an inductively coupled RF (13.56 MHz) plasma [84]. At relatively low power level (i.e. low energy input) (3 W) pyrrole was polymerized whereas at high power (40W) ring opening and crosslinking reactions dominated, leading to a completely disordered structure.

P. Heyse et al. studied plasma polymerization of 22 different combinations of polymer forming and non-polymer forming precursors in a DBD reactor [85]. They used dielectric barrier discharge He and He:N<sub>2</sub> (1:1) as a carrier gas (non-polymer forming gas); pyrrole, allylamine, acetylene, ethylene, propylene, etc. as a polymer-forming precursor. Later they chose pyrrole and acetylene as two promising precursor for further investigation. According to their results, the acetylene polymer film shows

resemblance with its low-pressure plasma analogue, whereas polypyrrole coatings produced in vacuum and atmospheric plasmas are were found different due to the possible oxygenation of the polymer films initiated by their contact with air and water vapor, and also long term aging induce surface changes.

### 3 Conclusion

In this chapter, the fundamental properties of the composites, carbon fibers and carbon nanotubes, epoxy matrix and the principles of adhesion between fiber and matrix were reviewed in order to provide necessary background for the next chapters. Additionally, plasma processes including different types of plasma discharges, and their effect on fibers and carbon nanotubes were discussed in detail. Since the modification of any material by using dielectric barrier discharge at atmospheric pressure (continuous process) with polymer or non-polymer forming precursors is quite new process compared to RF discharge (batch process), there was not so much published work found in the literature. Therefore, mainly RF and DC discharge with non-polymer precursors such as O<sub>2</sub>, N<sub>2</sub>, Ar and polymer forming precursors particularly with pyrrole precursor were discussed by means of electrical, chemical, mechanical properties. Most of the authors stated that the pyrrole rings were cleaved during plasma polymerization; hence the obtained polymer was different than that of the chemically or electrochemically prepared polypyrrole. On the other hand, the highest electrical conductivity of such plasma polymerized pyrrole was reported around 10<sup>-3</sup> S/cm which is quite indicative that even the pyrrole rings were decomposed into several fragments; it can still possess conductive capability. Moreover, it can be said that plasma treatment with polymer or non-polymer forming precursors is capable of producing polar groups on fiber and carbon nanotubes surface which is expected to enhance the interfacial adhesion between fibers and carbon nanotubes. Moreover, the comparatively straightforward scale-up to larger dimensions, possibility of in-line surface treatment and compatibility of any type of substrate make DBD (at atmospheric pressure) a promising tool in continuous surface treatments.

# Chapter II

# Experimental



## *Introduction*

The purpose of this chapter is to present the experimental set-up of the plasma treatment process and the procedures of several sorts of characterization studies (e.g. chemical, electrical, and mechanical) which were used throughout the study. The corresponding literature survey to the experimental procedures is also embedded in this chapter. After the explanation of the experimental procedure which includes particularly the detailed design of “holder” for the post-discharge treatment of fibers, the properties of the apparatus used for the characterization studies are presented in general. In principle, the materials used in the study, the sample preparation for the several series of composite testing and their electrical and mechanical evaluations are explained in detail.



## 1 Plasma system

The plasma generation system used to treat AS4 and T700/CNT fibers is based on dielectric barrier discharge technique. It is developed by Acxys Technologies (France) and composed of plasma generator and plasma source (Figure 2.1). Plasma generator consists of electric supply, gas control and touch screen; plasma source consists of process gas distribution chamber and water cooled co-axial cylindrical electrodes. The atmospheric pressure glow discharge is produced between two co-axial water-cooled cylindrical electrodes located inside the source. The inner metal electrode is covered with a dielectric material (e.g. an insulator material) and surrounded by a cylindrical slotted metal electrode (Figure 2.2). The inner electrode is connected to a power supply consisting of a low frequency generator (120 kHz), a high voltage transformer (+/- 3.5 kV) and a power amplifier. The injected power can be adjusted between 1000 and 2000 W. Nitrogen is used as process gas, and flow is adjusted by a mass flow controller.

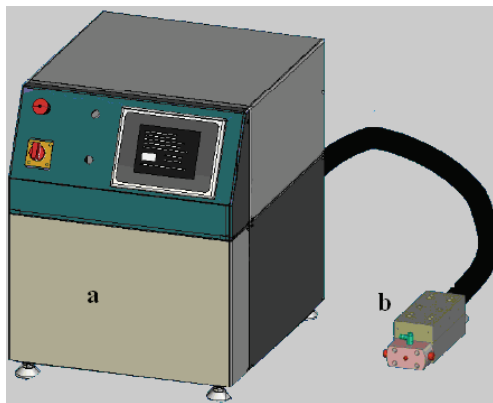


Figure 2.1 Acxys ULD120 dielectric barrier discharge system, a) generator part, b) plasma source [89]

We combined the as-mentioned plasma source with a suitable holder in order to treat the carbon fibers in the post-discharge zone (Figure 2.3). In the post-discharge zone, AS4 and T700/CNT fibers were treated with pyrrole (precursor) and p-toluene sulfonic acid monohydrate (dopant). In the presence of dopant, injection points of precursor and dopant were separated from each-other in order to avoid possible oxidation reactions between them. In each case, nitrogen was used to introduce the precursor and dopant

vapors into the post-discharge zone. Operating conditions for plasma deposition are based on the conditions for complete coverage of surfaces by plasma polymers. The plasma system except the generator was placed in a closed chamber and connected to a hood to provide a safe environment during the operation.

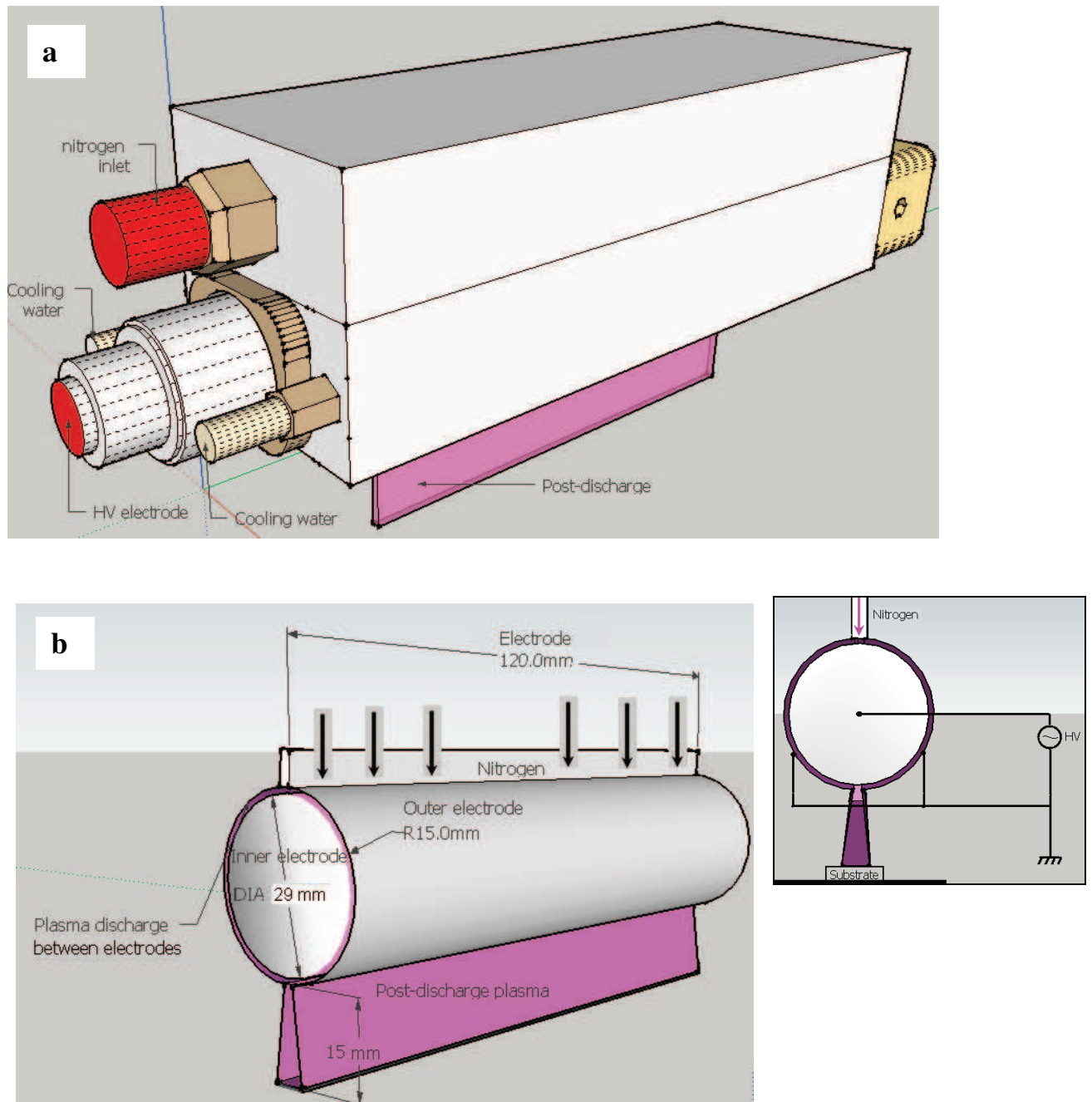


Figure 2.2 Plasma source used in the study, a) Configuration of source including gas inlet, cooling water, electrodes; b) Configuration of electrodes inside the source

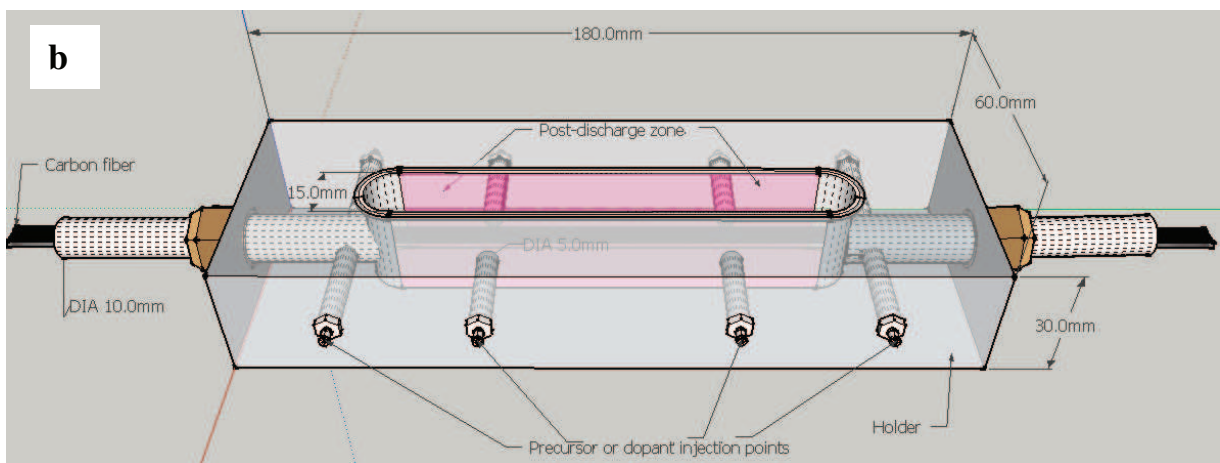
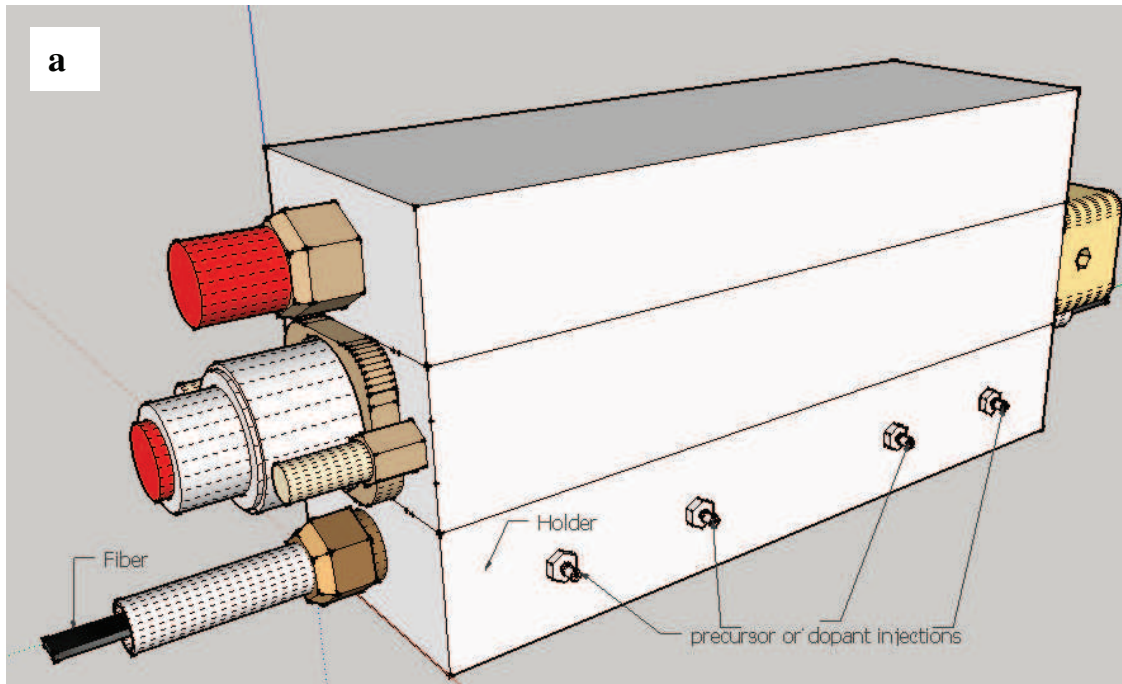


Figure 2.3 Plasma source with holder used for the fiber treatment, a) Configuration of the developed holder including precursor and dopant injection points; b) Detailed representation of the holder

## 2 Experimental procedure

The materials used in the study were AS4-12K (Hexcel), T700GC-12K (Toray), and T700/CNT carbon fibers. T700/CNT fibers were prepared by using a CVD reactor in MSSMat laboratory (Figure 2.4).

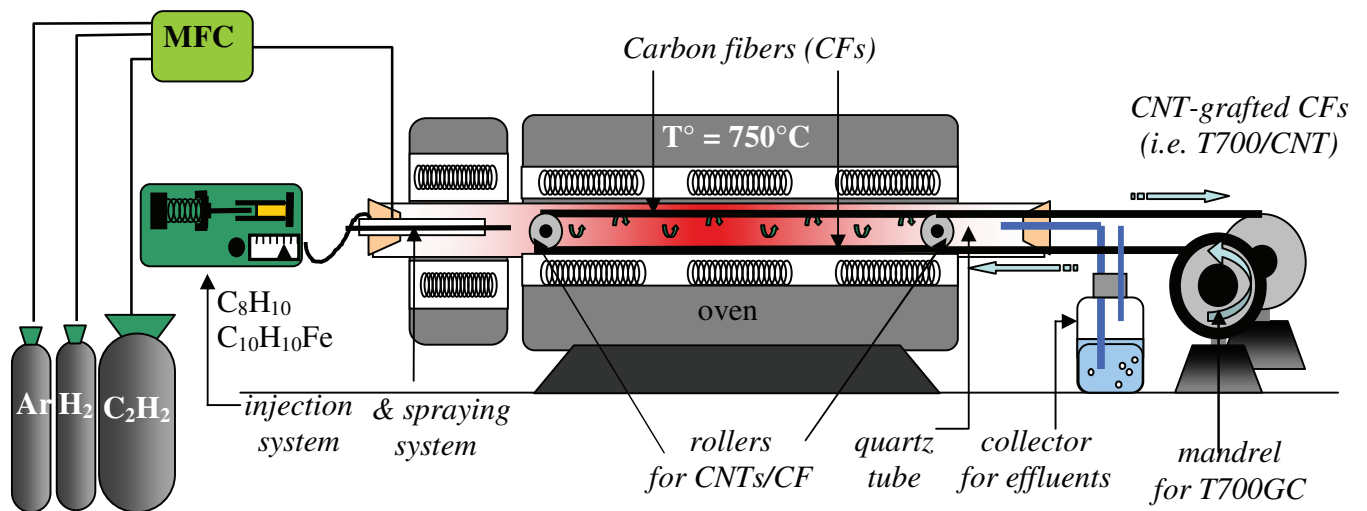


Figure 2.4 CVD reactor used in MSSMat laboratory for grafting the carbon nanotubes on carbon fibers (T700/CNT)

In general, two different experimental procedures were applied for the treatment of AS4 and T700/CNT carbon fibers: (1) static and (2) dynamic (Figure 2.5). In the static treatment, 120 mm-long multifilament carbon fibers were treated in the post-discharge zone simply by fixing a single bundle inside the holder. All the static treatment of carbon fibers were performed according to a statistical experimental design in order to predict the optimum plasma conditions for minimum electrical resistivity of the fibers (explained Chapter III). In the dynamic treatment, fiber tow (AS4 or T700/CNT) was placed in front of the plasma source and the treatment speed of fibers was adjusted according to the optimized static treatment time (~40 s). For this purpose, winding speed of fibers was adjusted to 0.2 m/min. After the experiments, plasma treated AS4 fibers were washed with acetonitrile (cas no. 75-05-8) and the solution was injected into a gas chromatograph in order to identify the solubility of the deposited layer. According to the results, no

peaks were observed except acetonitrile which was an indication of insolubility of coating in that solvent. All treated fibers were kept in the desiccators in order to avoid possible surface altering caused by air (e.g. water vapor).

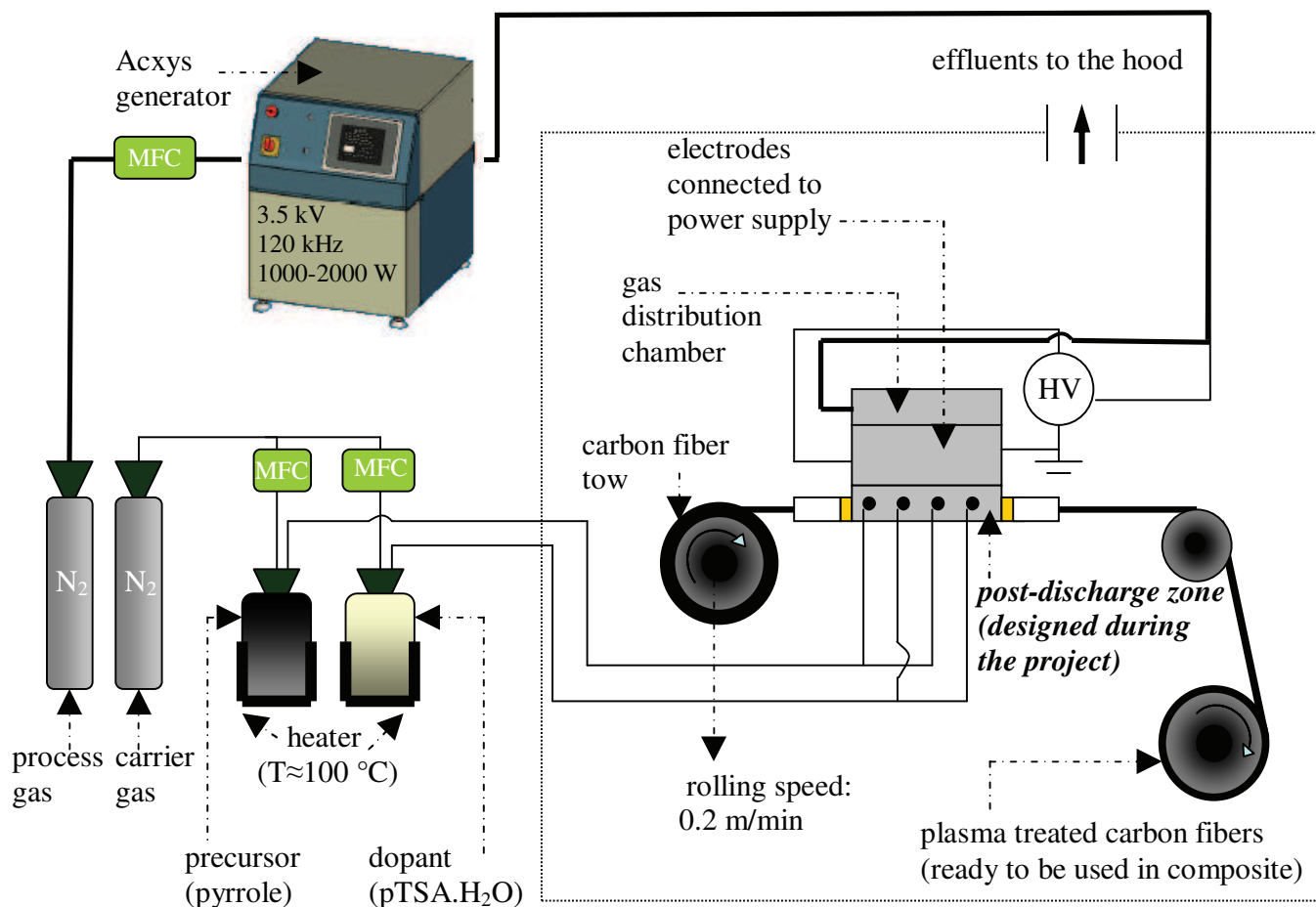


Figure 2.5 Plasma treatment system in MSSMat laboratory used for the polymer deposition on carbon fibers

### 3 Apparatus

#### 3.1 X-ray photoelectron spectroscopy (XPS)

The fiber surfaces were analyzed with the Physical Electronics PHI 5000 Versaprobe X-ray photoelectron spectrometer. The spectra were collected using a monochromatic Al K<sub>α</sub> X-ray source ( $h\nu = 1486.6$  eV) operated at 15 kV and 25 W. The

analysis chamber pressure was  $10^{-6}$  Pa. The electron analyzer was hemispheric with 16 channeltrons. The X-ray spot diameter was 200  $\mu\text{m}$ . The size of analyzed area was 560 x 560  $\mu\text{m}$ . The electron take off angle was  $45^\circ$ . The pass energy for collecting survey and high resolution spectra were 187.85 eV (step size = 0.4 eV, time/step=20 ms) and 29.35 eV (step size=0.1 eV, time/step=50 ms), respectively. A combination of 1 eV electrons and 6 eV  $\text{Ar}^+$  ions were used for the charge neutralization.

For calibration purposes, the C 1s electron binding energy was referenced at 284.8 eV. Curve fitting was performed using Multipak software (developed by Ulvac-Phi). The quantitative analysis of atomic surface composition of carbon fibers (C 1s, O 1s and N 1s photoelectron peaks) was calculated by integration of the peak areas with Shirley method on the basis of Wagner and Scofield sensitivity factors.

### 3.2 Scanning electron microscopy (SEM)

The topography of fracture surface of fiber/epoxy composites after three point bending test as well as the unsized and carbon nanotube grafted carbon fiber surfaces, before and after plasma deposition was examined by LEO Gemini 1530 scanning electron microscope. Fiber samples were fixed on aluminum holders without any metallization whereas the fracture surfaces of fiber/epoxy composites were sputtered with gold for few minutes prior to SEM analysis.

### 3.3 Atomic force microscopy (AFM)

The atomic force microscopy (AFM) measurements were performed using Veeco Explorer atomic force microscope operated in a tapping mode (non-contact mode) with silicon tips. In order to fix single fiber on a sample stub, a thin layer of melted Tempfix (Agar Scientific) was applied on a glass substrate and cured until it became tacky. Each single fiber held with tweezers and placed individually on the prepared glass plates. In this way, at least the half of the fiber diameter was remained above the surface of adhesive. The images were gathered at scanning areas 20 x 20 and 2 x 2  $\mu\text{m}$ . The used scan rate was  $1.18 \mu\text{m s}^{-1}$ .

### 3.4 Thermogravimetric analysis (TGA)

The TG thermograms were obtained from Perkin Elmer Pyris 6 model TGA thermal analyzer. Fiber samples were degraded in nitrogen atmosphere at a constant heating rate of 10 °C/min. Degradation kinetics and thermal stability of plasma deposited fibers were studied by TGA.

### 3.5 Optical microscopy

Leica Aristomet DC300 optical microscopy was used to observe the defects in the composites samples before and after the mechanical tests. In order to prepare the surface of composites for electrical measurements, samples were observed by optical microscope before and after the polishing of the exterior epoxy layer of composites.

## 4 Materials

PAN-based unsized AS4 and carbon nanotube deposited T700 fibers (T700/CNT) were used throughout the investigation. HexPly® M21 (Hexcel) epoxy resin with hardener provided on silicon paper was used as the matrix material.

Pyrrrole ( $C_4H_5N$ , 98+%, liquid at STP) and p-toluene sulfonic acid monohydrate ( $C_7H_8O_3S.H_2O$ , 98+%, solid at STP) were purchased from Sigma-Aldrich. Both precursor was heated prior to plasma treatment and was fed easily into the plasma post-discharge region in the vapor phase. Nitrogen (Alphagaz B50, 9.4 m<sup>3</sup>, 200 bar) which was used as a process gas for the initiation of plasma discharge and as a carrier gas for the feeding of precursors contains the following impurities:

$H_2O < 3$  ppm,

$O_2 < 2$  ppm,

$C_nH_n < 0.5$  ppm.



## 5 Composite sample preparation

AS4 and T700/CNT fibers were coated with different plasma polymers in continuous plasma post-discharge. Then these fibers were rolled on an epoxy-hardener casted silicon paper (Hexply M21) in the unidirectional alignment (Fig. 2.6).

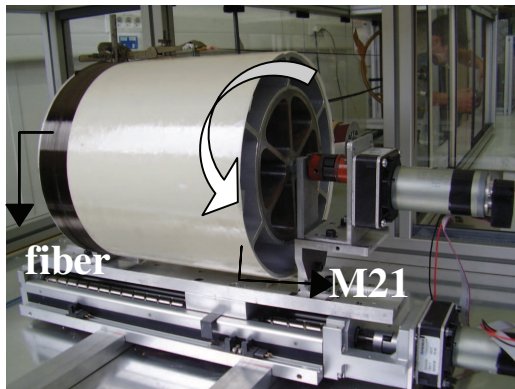


Figure 2.6 A drum used to prepare preregs

After rolling fibers, silicon paper was released from epoxy-hardener simply by ironing. Later, obtained preregs were laid-up in  $0^\circ$  alignment sequence and placed in a mold with dimensions of 40 x 40 cm and separated from each other by using a silicon spacer (Fig. 2.7). Vacuum bagging method was used for the composite fabrication. Primary vacuum was applied where the preregs placed, then the mold was compressed in a hot press at 7 bars and kept at  $180^\circ\text{C}$  for 2 hours as it was recommended by the manufacturer (Hexcel). Then it was left in the press until it has cooled down to room temperature.

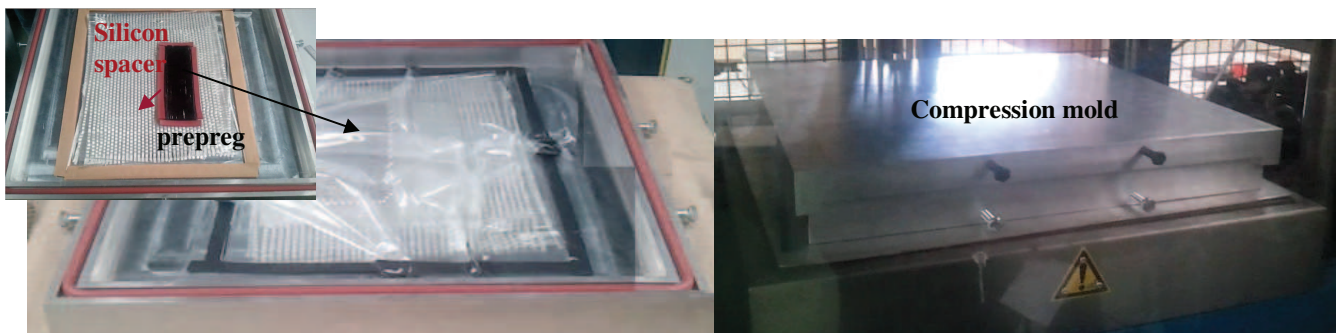


Figure 2.7 Compression mold used in fabrication of composites



### Fiber volume measurements

Fiber volume fraction was calculated from the following equation:

$$\text{Fiber volume fraction} = \frac{\text{number of filaments} * \text{plies} * \text{cross section filament area}}{\text{depth} * \text{width of sample}}$$

According to the given formula, the fiber volume fraction of samples was calculated around 60 %.

TABLE 2.1 Specifications of carbon fibers used in the study

	Density (g/cm <sup>3</sup> )	dtex (g/m)	Number of filaments	Cross-sectional area of fiber (μm <sup>2</sup> )	Mean diameter (μm)
AS4	1.79	0.858	12000	37.4	6.9
T700GC	1.80	0.800	12000	33.2	6.5

## 6 Electrical property evaluations

### 6.1 Electrical measurement procedure for fibers

Electrical resistivity (DC,  $\omega=0$ ) measurement of fibers was performed by Keithley Multimeter equipped with two copper electrodes. In order to adjust the proper distance, both electrodes were fastened with a double sided sticky tape under a ruler (Fig. 2.8). The oxidation effect of the copper electrodes was minimized by polishing their surface before the beginning of each measurement.

Fibers were prepared in different lengths in order to find out the contact resistance ( $R_c$ ) by the extrapolation of the experimental data to length=0 (Fig. 2.9). Contact resistance mainly includes the resistance of wires, the contact resistance between wires and the electrodes and the contact resistance between electrodes and the sample [90].

Electrical resistivity of a material is an intensive property (like temperature, specific volume, specific weight, specific enthalpy, surface energy, etc); that is, it does not depend on the size (extent) of material [91]. From this point of view, after excluding

the contact resistance as given in Eq. (2.1), electrical resistivity of a fiber should not be varied at different lengths of the same fiber.

The electrical resistivity of fibers excluding this constant can be calculated according to equation given below. Here, the approximate width and thickness of fibers were taken 0.6 and 0.0137 cm, respectively.

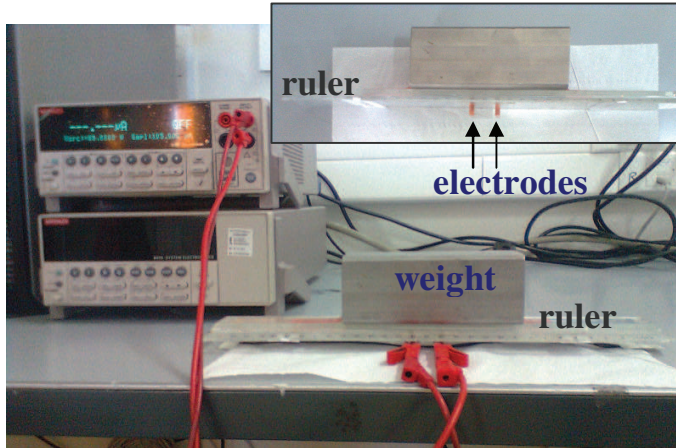


Figure 2.8 *Electrical resistivity (DC) measurement device used in MSSMat laboratory*

$$R = \frac{\rho_l}{bh} l + R_c \Rightarrow \rho_l = (R - R_c) \frac{bh}{l} \dots\dots\dots \text{Eq. (2.1)}$$

where  $\rho_l$  is electrical resistivity ( $\Omega \cdot \text{cm}$ )

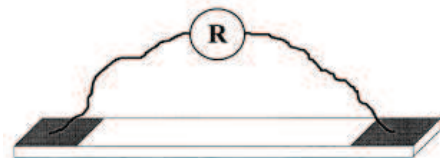
$R$  is electrical resistance ( $\Omega$ )

$R_c$  is sum of contact resistance ( $\Omega$ )

$l$  is distance between electrodes ( $\text{cm}$ )

$b$  is width ( $\text{cm}$ )

$h$  is thickness ( $\text{cm}$ )



The electrical resistivity of fibers was also measured by applying silver paste on the fibers where they come into contact with copper electrodes. It was found that the values obtained by this method were not largely different than that of the values predicted by the previous method (i.e. difference between the electrical resistivity is ~2 %).

Therefore, it can be concluded that the application of silver paste on AS4 and/or T700/CNT fibers provides no effect on the electrical resistivity of those fibers.

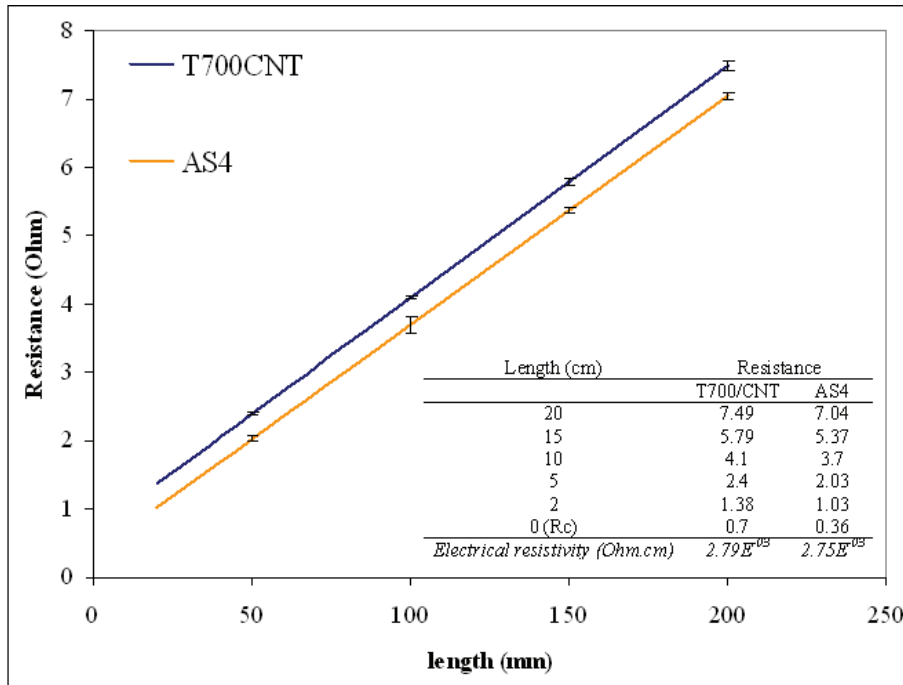


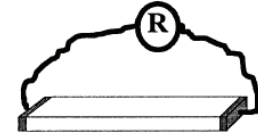
Figure 2.9 Resistance versus the length of fiber bundle

## 6.2 Electrical measurement procedure for fiber/epoxy composites

Electrical resistivity (DC,  $\omega=0$ ) of fiber/epoxy composites was measured by Keithley Multimeter equipped with two copper electrodes. A digital micrometer was used to fix and to measure the dimensions' of the composites between the electrodes. The longitudinal, transversal-through width and transversal-through thickness electrical resistivities were measured according to the following procedures [90]:

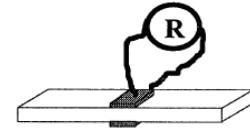
- Longitudinal electrical resistivity: 1 to 5 cm-long composites were cut, polished and silver paste was applied on the both ends of the composites where they come into contact with the electrodes. Longitudinal electrical resistivity of composites was calculated from the following equation and configuration:

$$R = \frac{\rho_l}{bh} l + R_c \Rightarrow \rho_l = (R - R_c) \frac{bh}{l}$$



- Transversal-through thickness electrical resistivity: 1 to 2 cm-long composites were cut, polished and observed under optical microscope in order to control the thickness of polished layer. Then, silver paste was applied on the both surfaces of the composites where they come in contact with the copper electrodes. Transversal-through thickness electrical resistivity of composites was calculated from the following equation and configuration:

$$R = \frac{\rho_{tt}}{bl} h + R_c \Rightarrow \rho_{tt} = (R - R_c) \frac{bl}{h}$$



- Transversal-through width electrical resistivity: 1 to 2 cm-long composites were cut, polished and silver paste was applied on the both sides of the composites where they come in contact with the electrodes. Transversal-through width electrical resistivity of composites was calculated from the following equation and configuration:

$$R = \frac{\rho_{tw}}{hl} b + R_c \Rightarrow \rho_{tw} = (R - R_c) \frac{hl}{b}$$



where  $\rho_l$  is longitudinal,  $\rho_{tt}$  is through thickness,  $\rho_{tw}$  is through width electrical resistivity ( $\Omega.cm$ )

$R$  is electrical resistance ( $\Omega$ )

$R_c$  is sum of contact resistance ( $\Omega$ )

$l$  is distance between electrodes ( $cm$ )

$b$  is width ( $cm$ )

$h$  is thickness ( $cm$ )

## 7 Mechanical property evaluations of composite

Interlaminar shear strength (ILSS) and flexural strength were measured to characterize the mechanical properties of fiber composites. Primarily due to its simplicity, three point bending test was used in this study in order to determine whether a treatment enhances fiber/matrix bonding. The samples were cut parallel to fiber orientation from unidirectional composite samples containing 60 % in volume of fibers which were fabricated using epoxy matrix with hardener. The ILSS of unidirectional fiber reinforced composites (the strength of the composite under shear stress acting parallel to the fiber axis) is often measured in the three point bending test. In this test a short rectangular bar shaped samples having a span (L) to depth (h) was subjected to symmetric three point bending as shown in Fig. 2.10.

Under a three point loading, a beam fails in tension on the bottom, in compression on the top face, or by interlaminar shear. The mode of failure depends on the span to depth ratio (or aspect ratio, L/h). The beam was loaded until fracture occurs, and the fracture load was interpreted as a measure of the shear strength of the material.

For ILSS tests, samples were tested according to the EN ISO 14125 standard where span to depth ratio is given as  $L/h \leq 5$ . Crosshead speed was constant at 1 mm/min. Overall dimensions of samples were approximately 30x1.8x10 mm. In order to calculate the average value of ILSS, 3 to 6 samples tests was conducted in this study.

ILSS was calculated from

$$t_{13} = \frac{3F}{4bh}$$

where  $t_{13}$  is interlaminar shear strength (GPa)

F is load  $\left( \frac{kg \ m}{s^2} \right)$

b is width (m)

h is thickness (m)

In the case of flexural strength, the dimensions of the samples were approximately 100x1.8x10 mm and span to depth ratio was  $L/h \leq 40$ . Similar to ILSS test, 10 cm-long rectangular bar shaped samples having a span (L) to depth (h) was subjected to symmetric three point bending as shown in Fig. 2.11. Crosshead speed was constant at 2 mm/min. At least 3 samples were used in the flexural strength tests.

Flexural strength was calculated from

$$s_f = -\frac{3FL}{2bh^2}$$

Flexural modulus was calculated from

$$E_f = \frac{FL^3}{4bh^3}$$

where  $s_f$  is flexural strength (MPa) and  $E_f$  is flexural modulus (GPa)

F is load  $\left(\frac{kg \ m}{s^2}\right)$

L is span (m)

b is width (m)

h is thickness (m)

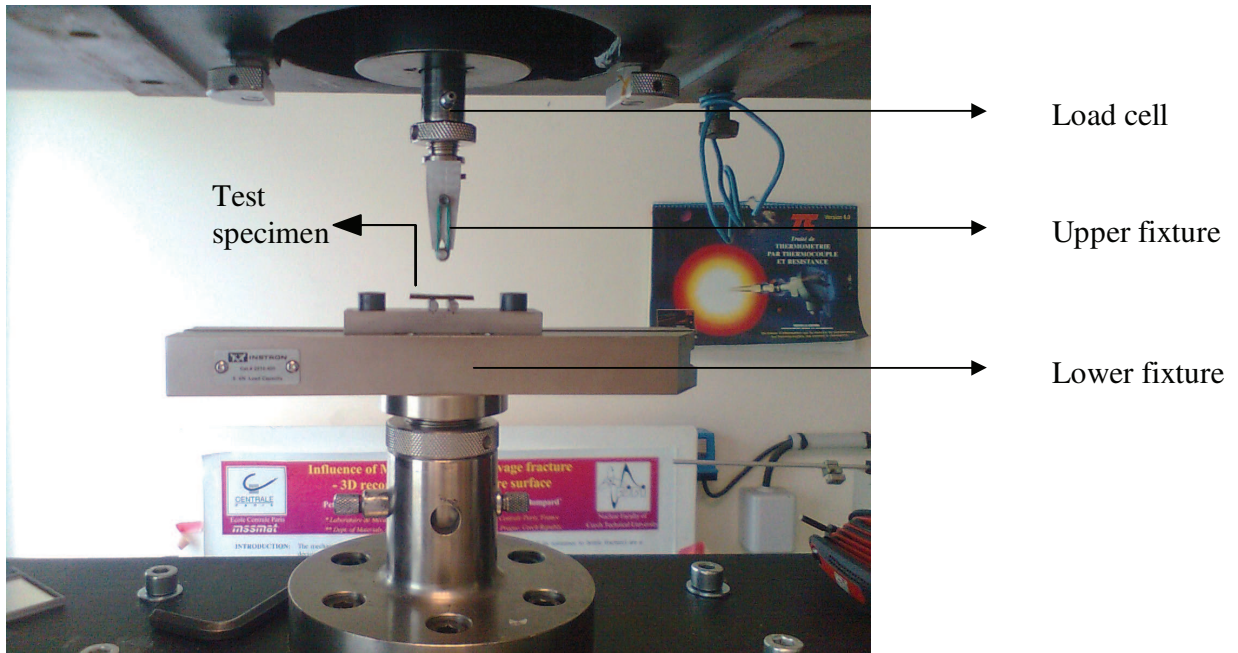


Figure 2.10 Three point bending fixture for ILSS test

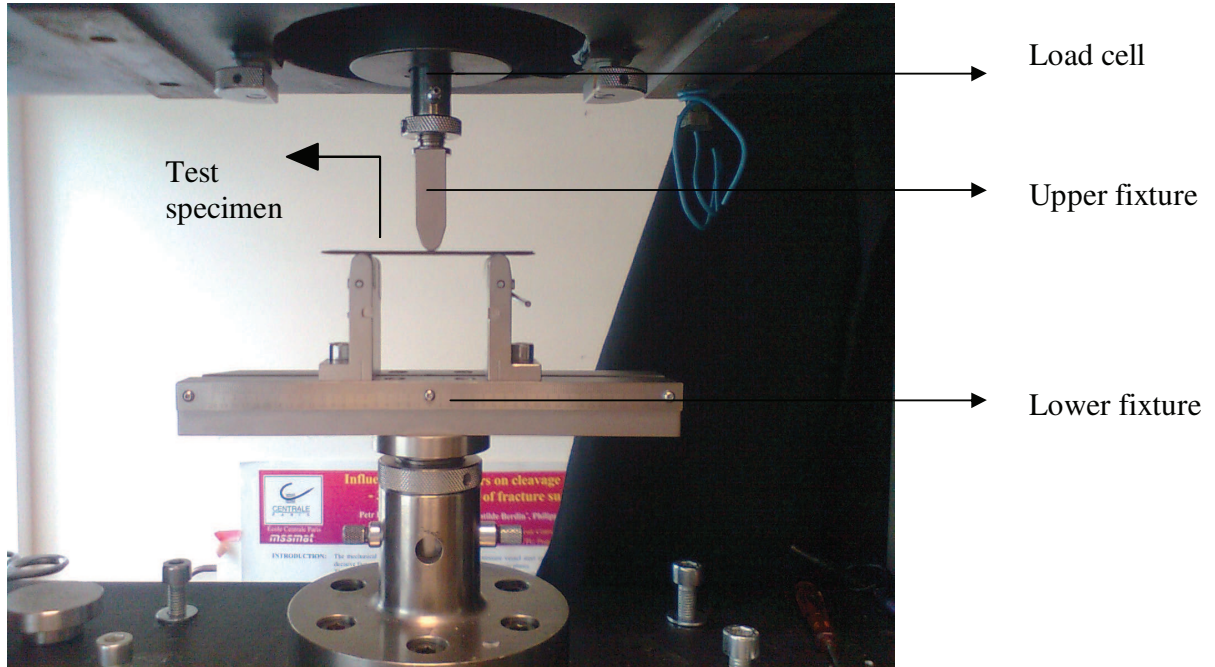


Figure 2.11 Three point bending fixture for flexural strength test

## *8 Conclusion*

This chapter was focused on the preparation and the physical-chemical characterization methods of plasma-modified carbon fiber (AS4) and carbon nanotube grafted carbon fibers (T700/CNT) and their composites. Depending on the purpose, those composites can be integrated into structural and functional applications in the fields of aerospace, automobile, defense, and sport industries.

In the experimental procedure, plasma deposition of a semi-conducting polymer, particularly polypyrrole, on both types of carbon fibers was explained in detail. The objective of the plasma deposition was not only to keep carbon nanotubes on the carbon fiber surface for safety reasons, but also to improve both electrical conductivity and mechanical interlocking of hybrid reinforcements in their composites.



## Chapter III

# Statistical experimental design on plasma polypyrrole deposition



## *Introduction*

The multidimensional combination of variables implies the need for extensive use of design of experiment (DOE, e.g. response surface design) to map the interactions between the different process parameters and to see which variable (or factor) have the greatest effect on the results of a process.

Response surface experiments (e.g. Box-Wilson and Box-Behnken designs) traditionally involve a small number (generally 2 to 5) of continuous factors. Each factor in these designs is set at three or five levels to economize on the number of runs needed, and response measurements are taken for only a fraction of the possible combinations of levels. Thus, compared to factorial designs, response surface designs require fewer experimental runs, which is why they provide a relatively inexpensive and efficient way to improve a process. Besides, these designs are a prelude to further experiments. So that it can provide a guide to further studies.

One of the most important differences between Box-Wilson and Box-Behnken designs is the axial scaling of design. Axial scaling value controls how far out the axial points are. In Box-Behnken design, axial value placed on the face of the cube (i.e. equal to one), therefore it leaves the axial points at the end of the -1 and +1 ranges. In Box-Wilson designs, rotatable axe makes the variance of prediction depend only on the scaled distance from the center of the design which causes the axial points to be more extreme than the range of the factor. In these designs, axial value is not constant; it depends on the number of independent variables (or factors).

The current optimization studies involve three major steps: performing the statistical design experiments according to Box-Wilson and Box-Behnken method, estimating the coefficients in the mathematical models, and predicting the response of the process (i.e. electrical resistivity of AS4 and T700/CNT type fibers), and then checking the adequacy of the model. In this respect, the main factors that influence the electrical resistivity of both types of the treated carbon fibers are investigated first using the as-described statistical analyses. The relationship between the chemical structure and physical properties and further mechanical properties of their composites are then discussed in Chapter IV and V, respectively.

## *1 Experimental design on plasma polypyrrole deposition*

The response surface methodology was used to create a predictive model of the relationship between the factors (variables) and the response which allows finding better operating settings for the process [92]. In this respect, Box-Wilson experimental design method was preferred to identify two selected process parameters (independent variables or factors) that influenced the electrical resistivity of AS4 and T700/CNT fibers in the absence of dopant. Similar to Box-Wilson empirical modeling technique, Box-Behnken experimental design method was used to determine the effects of the three major process parameters on the electrical resistivity of AS4 and T700/CNT fibers in the presence of dopant. Both empirical modeling techniques can also provide the interaction between the process parameters upon the electrical resistivity of the fibers.

Box-Wilson designs consist of two factor-five level statistical analysis system (SAS), whereas Box-Behnken designs have three factor-three level SAS. The two most important independent variables chosen in the Box-Wilson designs were input plasma power ( $X_1$ ) and plasma exposure time ( $X_2$ ) whereas dopant to precursor ratio ( $X_3$ ) was added beside these variables in the Box-Behnken designs. The definitions and different levels of factors either with coded and natural units for AS4 and T700/CNT fibers are tabulated in Table 3.1 and 3.2, respectively. It should be noted that, all experimental runs were based on the same amount of precursor flow rate. When the dopant to precursor flow ratio was equal to zero (in the Box-Behnken designs), the only feeding was pyrrole vapor. The rest of other experimental runs that existed in the same column was arranged by keeping precursor flow rate same and changing the dopant flow rate as what it was set in the related experimental run.

The Box-Wilson experimental design consists of four factorial (each run was repeated two times), four axial (each run was repeated two times) and center points. The Box-Behnken experimental design consists of 12 factorial (each run was repeated one time) and center points. The center points were repeated five times and thirty experimental runs were done for both analyses. Experimental conditions and responses based on the data given in Table 3.1 and 3.2 are reported in the same order in Table 3.3 and 3.4. The presented responses in Table 3.3 and 3.4 were the electrical resistivity of

plasma polymer deposited AS4 and T700/CNT fibers, respectively. The electrical resistivity measurement procedure for fibers has already been explained in Chapter II. According to given calculations in Chapter II, electrical resistivity of untreated AS4 fibers and T700/CNT fibers was found  $2.75 \times 10^{-3}$  and  $2.79 \times 10^{-3}$  ohm.cm, respectively.

TABLE 3.1. Levels of factors for both fiber types in the absence of dopant

Fiber	Factor	Symbol	Coded level				
			lowest (a)	low (-1)	middle (0)	high (+1)	highest (A)
AS4 T700/CNT	Power ( $X_1$ )	P	1000	1200	1400	1600	1800
AS4 T700/CNT			1200	1400	1600	1800	2000
AS4 T700/CNT	Exposure time ( $X_2$ )	E	20	30	45	60	70

TABLE 3.2. Levels of factors for both fiber types in the presence of dopant

Fiber	Factor	Symbol	Coded level		
			low (-1)	middle (0)	high (+1)
AS4 T700/CNT	Power ( $X_1$ )	P	1200	1400	1600
AS4 T700/CNT			1400	1600	1800
AS4 T700/CNT	Exposure time ( $X_2$ )	E	30	45	60
AS4 T700/CNT			Dopant to precursor flow ratio ( $X_3$ )	F	0

For both statistical modeling technique, linear (coefficient of main factor), cross-product (coefficient of two factor interaction) and quadratic coefficients (coefficient of curvature) of second-order polynomial model (Eq. 3.1) were calculated with a multiple linear regression using the JMP (SAS Institute) software [93].

$$Y = \beta_0 + \sum_{i=1}^k \beta_i X_i + \sum_{i=1}^k \beta_{ii} X_i^2 + \sum_{i=1}^{k-1} \sum_{j=i+1}^k \beta_{ij} X_i X_j \quad \dots\dots\dots \text{Eq. (3.1)}$$

where  $Y$  is the electrical resistivity of fibers (i.e. response variable),  $X_i$  is the processing factor (e.g. power, exposure time, etc) and  $\beta_i$ ,  $\beta_{ii}$ ,  $\beta_{ij}$  are the coefficients. The Student's t-test was used to examine the performance of data fitting and its weighting factors. p-values in the Student's t-test were used to determine the statistical significance of the process parameter effects. The determination coefficient ( $R^2$ ) was applied to evaluate the data fitting.

TABLE 3.3 Experimental conditions for both fiber types in the absence of dopant

Run	Coded value		Response	
	P	E	ER (AS4)	ER (T700/CNT)
1	-1	-1	0.00326	0.00327
2	-1	-1	0.00319	0.00338
3	-1	-1	0.00337	0.00345
4	-1	+1	0.00384	0.00366
5	-1	+1	0.00394	0.00358
6	-1	+1	0.00395	0.00377
7	+1	-1	0.00337	0.00399
8	+1	-1	0.00339	0.00385
9	+1	-1	0.00339	0.00394
10	+1	+1	0.00369	0.00539
11	+1	+1	0.00375	0.00518
12	+1	+1	0.00385	0.00517
13	a	0	0.00434	0.00335
14	a	0	0.00416	0.00334
15	a	0	0.00416	0.00335
16	A	0	0.00416	0.00565
17	A	0	0.00406	0.00537
18	A	0	0.00433	0.00545
19	0	a	0.00334	0.00354
20	0	a	0.00355	0.00357
21	0	a	0.00341	0.00348
22	0	A	0.00438	0.00525
23	0	A	0.00418	0.005
24	0	A	0.00431	0.00507
25	0	0	0.00315	0.00371
26	0	0	0.00308	0.00347
27	0	0	0.00306	0.00359
28	0	0	0.00308	0.00364
29	0	0	0.00302	0.00349
30	0	0	0.00301	0.00349

TABLE 3.4 Experimental conditions for both fiber types in the presence of dopant

Run	Coded value			Response	
	P	E	F	ER (AS4)	ER (T700/CNT)
1	-1	-1	0	0.00293	0.00309
2	-1	-1	0	0.00294	0.00308
3	-1	+1	0	0.00295	0.00334
4	-1	+1	0	0.00312	0.00345
5	+1	-1	0	0.0034	0.00403
6	+1	-1	0	0.00331	0.00398
7	0	0	0	0.00372	0.00438
8	0	0	0	0.00378	0.00427
9	0	-1	-1	0.00323	0.00402
10	0	-1	-1	0.0034	0.00411
11	0	-1	+1	0.0035	0.00381
12	0	-1	+1	0.00331	0.00413
13	0	+1	-1	0.00405	0.00441
14	0	+1	-1	0.00402	0.00429
15	0	+1	+1	0.00286	0.00387
16	0	+1	+1	0.00303	0.00411
17	-1	0	-1	0.00377	0.00358
18	-1	0	-1	0.00365	0.00370
19	+1	0	-1	0.00428	0.00329
20	+1	0	-1	0.00437	0.00334
21	-1	0	+1	0.0033	0.00448
22	-1	0	+1	0.00321	0.00468
23	+1	0	+1	0.00377	0.00464
24	+1	0	+1	0.00369	0.00440
25	0	0	0	0.0029	0.00325
26	0	0	0	0.00289	0.00323
27	0	0	0	0.00284	0.00317
28	0	0	0	0.00279	0.00317
29	0	0	0	0.00284	0.00314
30	0	0	0	0.00284	0.00314

### 1.1 Experimental design on plasma polypyrrole deposition in the absence of dopant

The methodology used in plasma polypyrrole deposition in the absence of dopant was based on the Box-Wilson response surface method. The independent variables (factors) were plasma power and plasma exposure time and they were symbolized as P and E, respectively. The response variable was the electrical resistivity (ER) of treated AS4 and T700/CNT type fibers. The Student's t-test was used to examine the performance of data fitting and its weighting factors. p-values in the Student's t-test were used to determine the statistical significance of the process parameter effects. Full report of the modeling results for AS4 and T700/CNT are given in Supplementary information, Table 3.1 and 3.2, respectively.

Fig. 3.1 shows the calculated profiles for the electrical resistivity of AS4 and T700/CNT as a function of the process parameters listed in Table 3.1 using Eq. (3.1) with coefficients listed in Table 3.5 and 3.6, respectively.

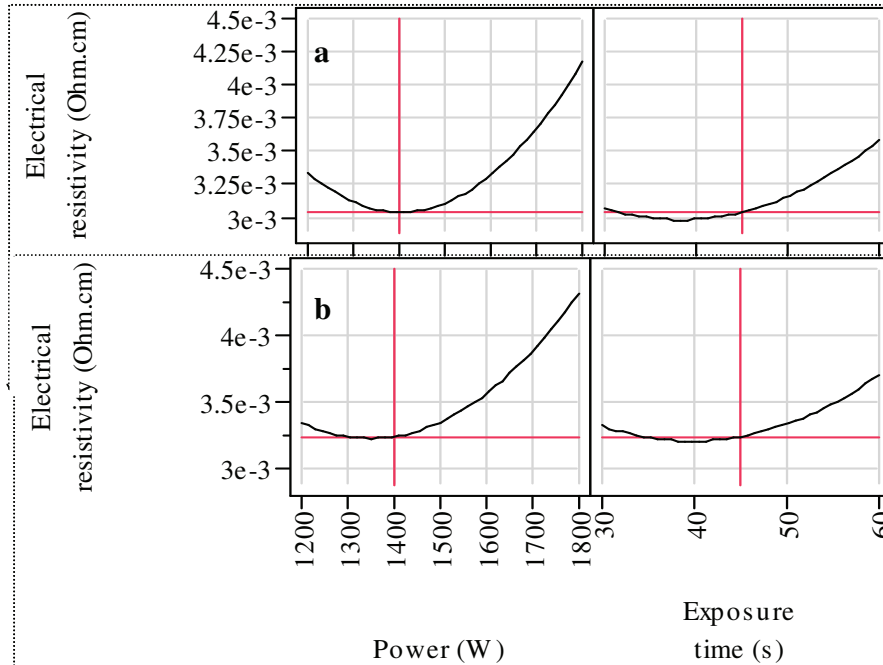


Figure 3.1 Calculated profiles of the electrical resistivity as a function of the process parameters for a) for AS4 fibers, b) for T700/CNT fibers

For both type of fibers, electrical resistivity increased drastically after 1400 W plasma power. Since the electrical properties depend highly on the characteristics of the material, it is observed that at 1400 W and higher plasma power, the deposited plasma polymer on the fiber surface exhibited less and less electrically conductive properties. As the plasma power increased, the electrons and/or the metastables can initiate more polymerization radicals and the ion-surface bombardment may induce more cross-linked or etched layer. This could be the reason of more defected polymer chain and less conducting pathway formations at higher powers which cause in further an increase in electrical resistivity. However, at 1400 W and lower plasma power, the electrical resistivity of fibers were remained approximately unchanged for T700/CNT type fibers. It could be due to the structural similarities that existed in the deposited layer at these conditions. In other words, the electrical properties of polymer deposited T700/CNT fibers were less destroyed and less differentiated from each-other at low plasma powers.

When plasma exposure time increased from forty to sixty seconds, an increase was observed in electrical resistivity of both types of fibers. This could be due to the fact that the plasma polymerization may less propagated at shorter exposure time, and then less polymer layer may formed, thus the electrical conductivity of AS4 and T700/CNT fibers were remained lower than that of longer exposure times. Nevertheless, when the AS4 type fibers treated for ninety seconds; it was observed that the deposited layer was detached from the fiber surface (further discussed in Chapter IV). Therefore plasma exposure range was chosen for the most stable plasma polymer deposition in the system.

### *1.1.1 Model equation and comparison of predicted and actual values of electrical resistivity*

Table 3.5 and 3.6 are the statistical calculations of the process parameter effect on the electrical resistivity of AS4 and T700/CNT fibers, respectively. The estimated coefficients of the polynomial model (Eq. 3.1) and the statistical significance of these coefficients (p-values) can be depicted in these tables. In order to assess the statistically significant responses to the electrical resistivity of fibers, p-value of the coefficients should be less than 0.05 (i.e. 95% confidence level). According to this information, all



coefficients in Table 3.5, the coefficients for factors E, PE, PP and EE in Table 3.6 were found statistically significant responses to the electrical resistivity of the T700/CNT and AS4 type fibers, respectively.

TABLE 3.5 The statistical calculations and the coefficients in the model equation (AS4)

Term	Coefficient	p-value
Intercept	0.003042	<0.0001
<b>P</b>	<b>-9.17E-06</b>	<b>0.5234</b>
E	0.000256	<0.0001
PE	-6.42E-05	0.0151
PP	0.000286	<0.0001
EE	0.000287	<0.0001

TABLE 3.6 The statistical calculations and the coefficients in the model equation (T700/CNT)

Term	Coefficient	p-value
Intercept	0.003566	<0.0001
P	0.000535	<0.0001
E	0.000445	<0.0001
PE	0.000254	<0.0001
PP	0.000213	<0.0001
EE	0.000271	<0.0001

In the case of AS4 type fibers, the second-order coefficients for P and E and the first-order coefficient for E showed the most significant response. The interaction effect for factor PE was also significant because of its low p-value (i.e. 0.0151). The first-order coefficient for P had no statistically significant impact on the electrical resistivity of AS4 fibers. In this respect, the electrical resistivity for AS4 fibers ( $ER_{AS4}$ ) was modeled using the following equation:

$$ER_{AS4} = 0.00304 + 0.000256E - 6.42e^{-5}PE + 0.000286PP + 0.000287EE \dots\dots\text{Eq. (3.2)}$$

For this model, the determination coefficient was 0.972 and the adjusted determination coefficient was 0.966. This good fit to the actual values (measured electrical resistivity) can be seen in graphically in Fig. 3.2(a).

In the case of T700/CNT type fibers, the second-order and first-order coefficients for P and E, and also the interaction effect for factor PE were significant because of their

low p-value (i.e.  $<0.05$ ). On the basis of these findings, the electrical resistivity for T700/CNT fibers ( $ER_{T700/CNT}$ ) was modeled as shown below:

$$ER_{T700/CNT} = 0.00356 + 0.000535P + 0.000445E + 0.000254PE + 0.000213PP + 0.000271EE$$

.....Eq. (3.3)

For this model, the determination coefficient was 0.988 and the adjusted determination coefficient was 0.985. Therefore, the proposed second-order polynomial models were proven successful in describing the electrical resistivity of fibers. Because the mean line (red line) was fallen inside the bounds of the 95% confidence curves (red-dotted lines) in Fig. 3.2(b), it can be said that the model was significant.

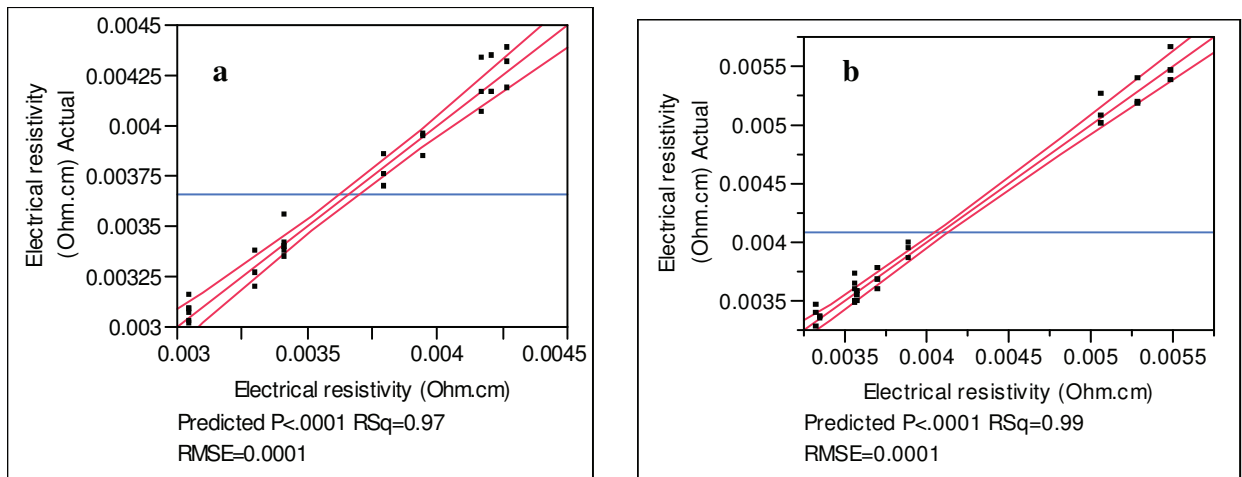


Figure 3.2 Comparison of the experimentally found (actual) electrical resistivity and the electrical resistivity predicted using a) Eq. (3.2) for AS4, b) Eq. (3.3) for T700/CNT

### 1.1.2 Response surface plots and optimum conditions for electrical resistivity

The contour profiler shows response contours for two factors at a time. Fig. 3.3 (a) and (b) show the response surface contours of AS4 and T700/CNT for the electrical resistivity as a function of factor PE, respectively. The response surface contours obtained for AS4 fibers showed a minimum electrical resistivity ( $2.98 \times 10^{-3}$  ohm.cm) at

1393 W and thirty-eight seconds. Compared to lower plasma power and shorter exposure times, stronger plasma power and longer exposure times caused a rapid increase in the electrical resistivity of AS4 fibers. It shows that the increase in power at higher levels affected the electrical resistivity more than that of lower plasma power levels.

It was observed from the response surface contours that at higher power and at longer exposure time, electrical resistivity of T700/CNT fibers increased monotonically. As the power decreased to 1387 W and the exposure time reduced to forty seconds electrical resistivity was reached to its lowest value. Namely, the predicted electrical resistivity at the optimum conditions was found  $3.21 \times 10^{-3}$  ohm.cm. The minimum electrical resistivity of both type of fibers were obtained approximately at the same conditions (i.e. 1400 W and 40 s).

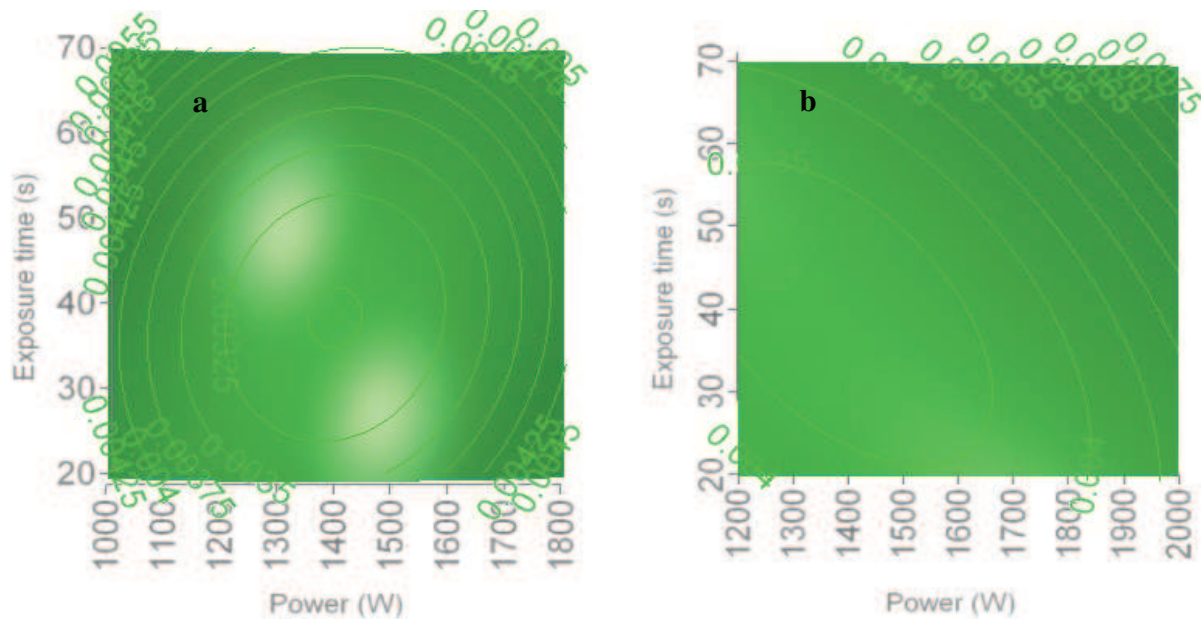


Figure 3.3 The response surface contours for the electrical resistivity as a function of factor PE a) for AS4, b) for T700/CNT

### 1.2 Experimental design on plasma polypyrrole deposition in the presence of dopant

The methodology used in plasma polypyrrole deposition in the presence of dopant was based on the Box-Behnken experimental design method. The independent variables

(factors) were plasma power, plasma exposure time and dopant to precursor flow ratio, and they were symbolized as P, E and F, respectively. The response variable was the electrical resistivity (ER) of treated AS4 and T700/CNT type fibers. The Student's t-test was used to examine the performance of data fitting and its weighting factors. p-values in the Student's t-test were used to determine the statistical significance of the process parameter effects. Full report of the modeling results for AS4 and T700/CNT are given in Supplementary information, Table 3.3 and 3.4, respectively.

Fig. 3.4 shows the calculated profiles for the electrical resistivity of AS4 and T700/CNT as a function of the process parameters listed in Table 3.2 using Eq. (3.1) with coefficients listed in Table 3.7 and 3.8, respectively.

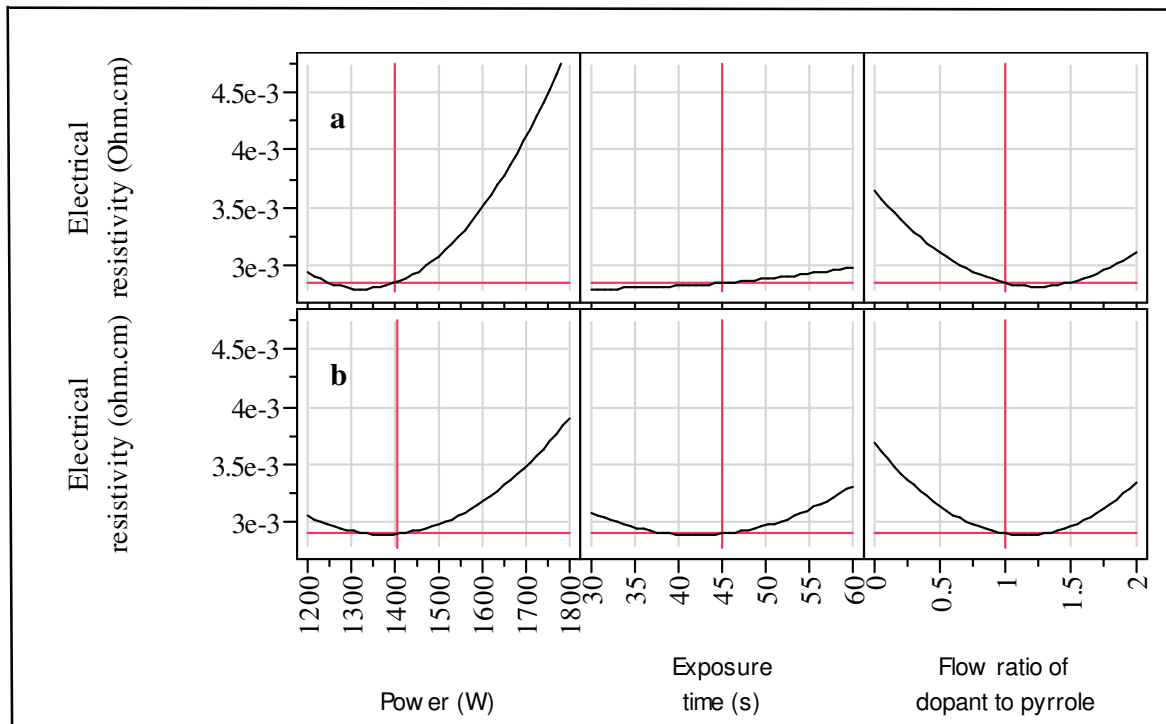


Figure 3.4 Calculated profiles of the electrical resistivity as a function of the process parameters for a) for AS4 fibers, b) for T700/CNT fibers

It can be clearly seen from Fig. 3.4 that the high plasma power was affected the electrical resistivity of both type of fibers than that of relatively low plasma powers. As the higher plasma powers were increased the formation of radicals and ion-surface

bombardment reactions, the both fiber surface may coated with more cross-linked and etched layer or may have short conjugation lengths in the polymer chain, which may cause a decrease in the conductivity, so that the electrical resistivity of both type of fibers were increased rapidly from 1400 to 1800 W. This finding was also observed in the previous Box-Wilson design which was performed in the absence of dopant. According to these results, it could be concluded that the both versions of experimental designs have verified each-other since the effect of plasma power on the electrical resistivity was remained nearly the same.

Since the aim of feeding dopant is to dope the polymer to facilitate the pass of current in the polymer, it was observed that when the dopant vapor was fed simultaneously with precursor pyrrole, the change observed in electrical resistivity from lowest to highest value of exposure time was not as large as the change observed in the case of power. The cause of this small difference observed in electrical resistivity of both type of fibers could be related to the two reasons: the doping with p-toluene sulfonic acid monohydrate was not effective enough to provide an increase in the conductivity of fibers between thirty to sixty seconds or the values chosen as a constraint for the exposure time was too narrow to observe the substantial difference. On the other hand, once the exposure time increased from seventy to one hundred and twenty seconds, not the layer only detached from the surface of AS4 fibers, but also another polymer deposits were formed partly on these fiber surfaces especially where the coating was fully detached from the surface of these fibers. Therefore, it was indicated that the constraints of exposure time has to be chosen as narrow as possible in order to provide stable conditions for the plasma polypyrrole deposition in the presence of dopant. Thus the lowest and the highest value of exposure time were chosen thirty and sixty seconds, respectively.

As it is seen from dopant to precursor flow vs electrical resistivity curve, the presence of dopant was provided a decrease in the electrical resistivity for both fibers. The most effective flow rate ratio was obtained when the dopant to precursor flow was equal to each-other. At higher dopant to precursor flow, electrical resistivity tends to increase to the higher values. This could be due to the negative effect of dopant on the polymer when it was fed more than the precursor into the discharge zone.

### 1.2.1 Model equation and comparison of predicted and actual values of electrical resistivity

Table 3.7 and 3.8 are the statistical calculations of the process parameter effect on the electrical resistivity of AS4 and T700/CNT fibers, respectively. The estimated coefficients of the polynomial model Eq. (3.1) and the statistical significance of these coefficients (p-values) are expressed in these tables. In order to assess the statistically significant responses to the electrical resistivity of fibers, p-value of the coefficients should be less than 0.05 (i.e. 95% confidence level). According to this information, the coefficients of factors except PE and EE in Table 3.7 and the coefficients of factors except PE, PF and EF for factors in Table 3.8 were found statistically significant responses to the electrical resistivity of the T700/CNT and AS4 type fibers, respectively.

TABLE 3.7. The statistical calculations and the coefficients in the model equation (AS4)

Term	Coefficient	p-value
Intercept	0.00285	<.0001
P	0.0002781	<.0001
E	9.4375e-5	<.0001
F	-0.000256	<.0001
PE	7.375e-5	0.0105
<b>PF</b>	<b>-0.000035</b>	<b>0.1953</b>
EF	-0.000295	<.0001
PP	0.0003744	<.0001
<b>EE</b>	<b>4.4375e-5</b>	<b>0.1183</b>
FF	0.0005306	<.0001

TABLE 3.8. The statistical calculations and the coefficients in the model equation (T700/CNT)

Term	Coefficient	p-value
Intercept	0.0031833	<.0001
P	0.0004994	<.0001
E	0.0001169	0.0003
F	-0.000105	0.0007
<b>PE</b>	<b>0.0000025</b>	<b>0.9472</b>
<b>PF</b>	<b>6.625e-5</b>	<b>0.0905</b>
<b>EF</b>	<b>-6.625e-5</b>	<b>0.0905</b>
PP	0.0002196	<.0001
EE	0.0002996	<.0001
FF	0.0006108	<.0001

In the case of AS4 type fibers, the second-order coefficients for P and F, the first-order coefficient for P, E and F showed the most significant response. The interaction effect for factors PE and EF were also significant because of their low p-value (i.e.

0.0105 and  $10^{-4}$ ). The interaction effect for factor PF and second-order coefficient for E had no statistically significant impact on the electrical resistivity of AS4 fibers. In this respect, the electrical resistivity for AS4 fibers ( $ER_{AS4}$ ) can be modeled using the following equation:

$$ER_{AS4} = 0.00285 + 0.0002781P + 9.43e^{-5}E - 0.000256F + 7.37e^{-5}PE - 0.000295EF + 0.0003744PP + 0.00053FF$$

.....Eq. (3.4)

For this model, the determination coefficient was found 0.982 and the adjusted determination coefficient was predicted 0.974. This good fit to the actual values (i.e. experimentally found electrical resistivity) can be seen in graphically in Fig. 3.5a.

In the case of T700/CNT type fibers, the second-order and first-order coefficients for P and E were significant because of their low p-value (i.e. <0.05). None of the interaction coefficients of the factors were found significant. On the basis of these findings, the electrical resistivity for T700/CNT fibers ( $ER_{T700/CNT}$ ) can be modeled as shown below:

$$ER_{T700/CNT} = 0.00318 + 0.000499P + 0.000117E - 0.000105F + 0.000219PP + 0.000299EE + 0.00061FF$$

.....Eq. (3.5)

For this model, the determination coefficient was found 0.972 and the adjusted determination coefficient was predicted 0.960. Therefore, the proposed second-order polynomial models were proven successful in describing the electrical resistivity of fibers. Because the mean line (red line) was fallen inside the bounds of the 95% confidence curves (red-dotted lines) in Fig 3.5b, it is told that the model was significant.

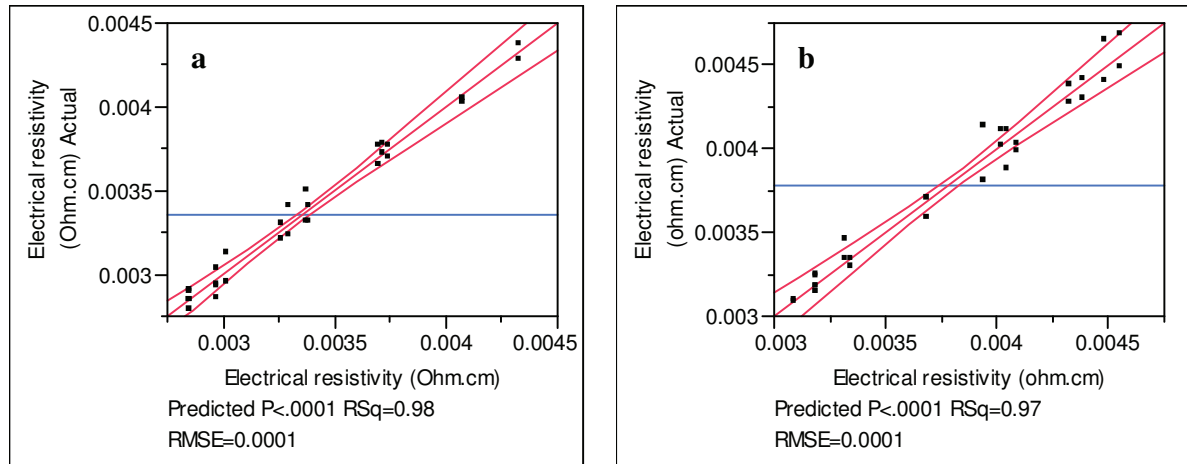


Figure 3.5 Comparison of the experimentally found (actual) electrical resistivity and the electrical resistivity predicted using a) Eq. (3.4) for AS4, b) Eq. (3.5) for T700/CNT

### 1.2.2 Response surface plots and optimum conditions for electrical resistivity

Fig. 3.6 (a) and (b) show the response surface contours of AS4 and T700/CNT for the electrical resistivity as a function of factor PE (holding flow ratio constant), respectively. The effects of operating variables on the electrical resistivity of AS4 and T700/CNT fibers were determined by obtaining projections of the response surface functions on certain planes of known parameters.

The response surface contours obtained for AS4 fibers showed a minimum electrical resistivity ( $2.77 \times 10^{-3}$  ohm.cm) around 1330 W, forty-four seconds and dopant to precursor flow ratio of (1.2:1). Compared to lower plasma power and shorter exposure times, higher plasma power and longer exposure times were caused higher electrical resistivity. It shows that a small increase at high plasma powers can affect the electrical resistivity more than that of lower plasma power. It was observed from the response surface contours that at higher power and at longer exposure time, electrical resistivity of T700/CNT fibers increased monotonically. As the power decreased to 1369 W, the exposure time reduced to forty-two seconds and when the dopant to precursor flow ratio was (1.1:1), the electrical resistivity was reached to its lowest value. Namely, the



predicted electrical resistivity at the optimum conditions was  $2.87 \times 10^{-3}$  ohm.cm for T700/CNT fibers.

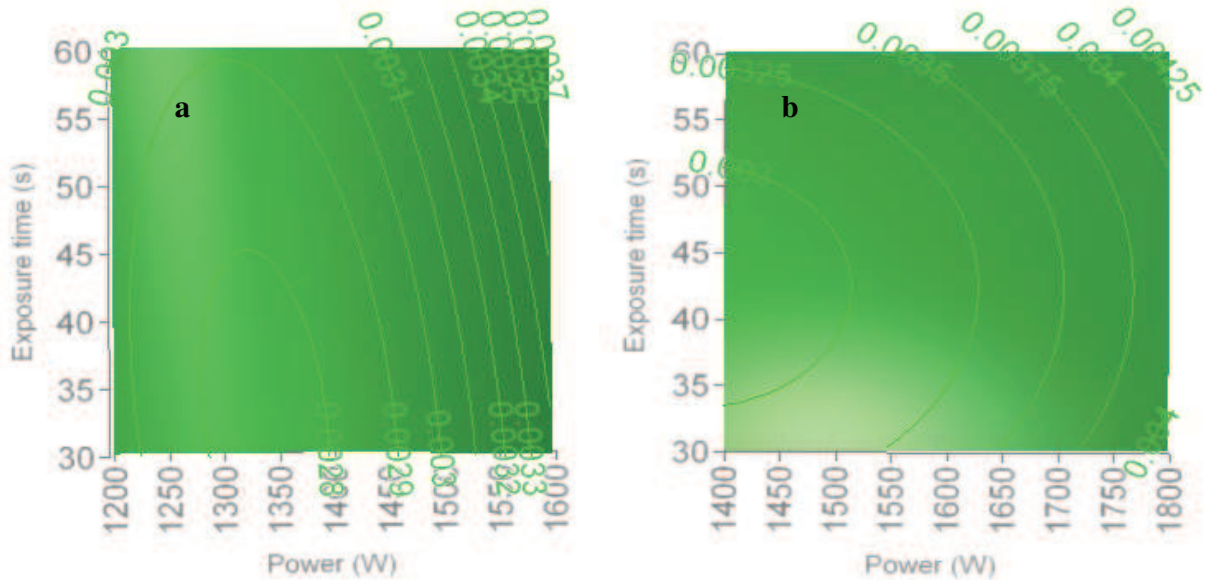


Figure 3.6 The response surface contours for the electrical resistivity as a function of factor PE a) for AS4, b) for T700/CNT

Keeping exposure time constant, the contour surface for electrical resistivity response of AS4 and T700/CNT fibers by the factor PF are shown in Fig. 3.7 (a) and (b), respectively. In the similar manner, the contour surface for response of AS4 and T700/CNT fibers by the factor EF are presented (holding power constant) in Fig. 3.8 (a) and (b), respectively. It was observed that the electrical resistivity of both fiber types tend to minimize around 1350 W, 40 s and 1:1 flow ratio (dopant : precursor). Comparing the values of electrical resistivity in the absence and in the presence of dopant, introduce of dopant simultaneously with precursor was provided a positive influence on the conductivity of both fibers. When the dopant was contributed to the reaction, the decrease in electrical resistivity for AS4 and T700/CNT was found around 7 and 11%, respectively.

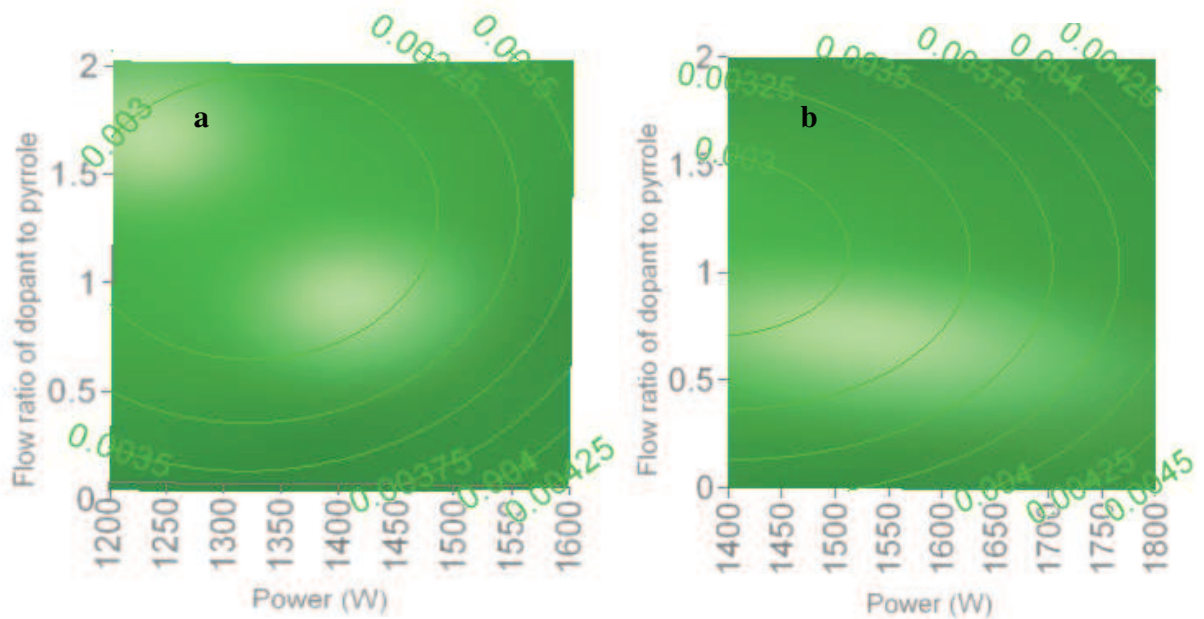


Figure 3.7 The response surface contours for the electrical resistivity as a function of factor PF a) for AS4, b) for T700/CNT

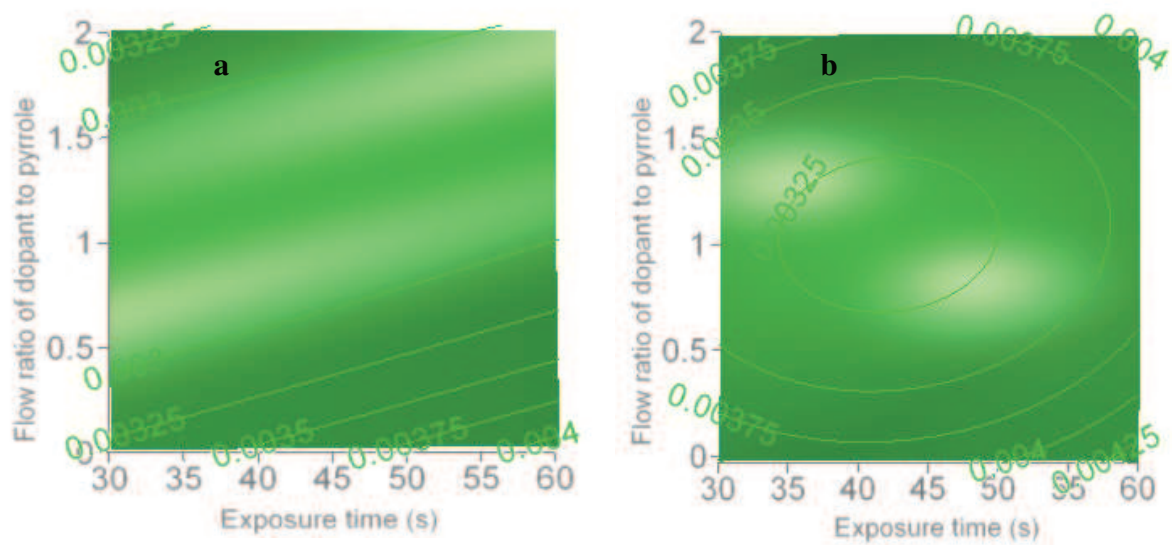


Figure 3.8 The response surface contours for the electrical resistivity as a function of factor EF a) for AS4, b) for T700/CNT

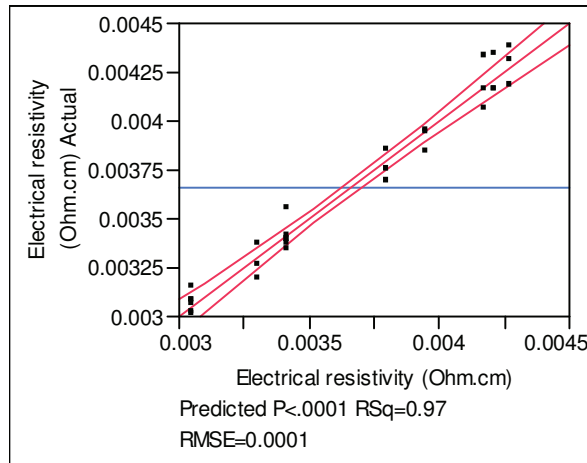
## *2 Conclusion*

In this chapter, the effect of double (power, exposure time) and triple (power, exposure time, dopant to precursor flow) varied process parameters were evaluated on electrical resistivity of CFs and CNTs-CF by response surface methodology. It was found that those parameters were strong and consistent enough to describe the response (electrical resistivity) of the process. The variation in response for replicate samples was also critical for assessing how much of the response is due to the statistically varied process conditions. Therefore, not only the mid-point of each design was repeated for five times, but also the factorial and axial points were repeated one or two times depending on the type of the design. The properties of plasma deposited fibers strongly dependent on process parameters such as power, duration of the experiment, and combination of precursor to dopant. A relatively low plasma power and a moderate exposure time are required for low electrical resistivity, because higher plasma powers and longer exposure times reduce electrical conductivity.

### 3 Supplementary information

**TABLE 1 Full report of Box-Wilson experimental design for AS4 type fibers**

**Response Electrical resistivity (Ohm.cm)  
Actual by Predicted Plot**



#### Summary of Fit

RSquare	0.972384
RSquare Adj	0.966631
Root Mean Square Error	0.000085
Mean of Response	0.003659
Observations (or Sum Wgts)	30

#### Analysis of Variance

Source	DF	Sum of Squares	Mean Square	F Ratio
Model	5	6.09633e-6	1.2193e-6	169.0127
Error	24	1.73137e-7	7.2141e-9	<b>Prob &gt; F</b>
C. Total	29	6.26947e-6		<.0001

#### Lack Of Fit

Source	DF	Sum of Squares	Mean Square	F Ratio
Lack Of Fit	3	2.08706e-8	6.9569e-9	0.9595
Pure Error	21	1.52267e-7	7.2508e-9	<b>Prob &gt; F</b>
Total Error	24	1.73137e-7		0.4302
				<b>Max RSq</b>
				0.9757

**Parameter Estimates**

<b>Term</b>	<b>Estimate</b>	<b>Std Error</b>	<b>t Ratio</b>	<b>Prob&gt; t </b>
Intercept	0.0030417	3.14e-5	96.88	<.0001
Power (W)(1200,1600)	-9.167e-6	1.416e-5	-0.65	0.5234
Exposure time (s)(30,60)	0.0002558	1.586e-5	16.13	<.0001
Power (W)*Exposure time (s)	-6.417e-5	2.452e-5	-2.62	0.0151
Power (W)*Power (W)	0.000286	1.219e-5	23.47	<.0001
Exposure time (s)*Exposure time (s)	0.0002869	1.765e-5	16.26	<.0001

**Effect Tests**

<b>Source</b>	<b>Nparm</b>	<b>DF</b>	<b>Sum of Squares</b>	<b>F Ratio</b>	<b>Prob &gt; F</b>
Power (W)(1200,1600)	1	1	3.025e-9	0.4193	0.5234
Exposure time (s)(30,60)	1	1	1.87597e-6	260.0437	<.0001
Power (W)*Exposure time (s)	1	1	4.94083e-8	6.8489	0.0151
Power (W)*Power (W)	1	1	3.97214e-6	550.6121	<.0001
Exposure time (s)*Exposure time (s)	1	1	1.90628e-6	264.2447	<.0001

**Response Surface**

<b>Coef</b>	<b>Power (W)(1200,1600)</b>	<b>Exposure time (s)(30,60)</b>	<b>Electrical resistivity (Ohm.cm)</b>
Power (W)(1200,1600)	0.000286	-6.417e-5	-9.167e-6
Exposure time (s)(30,60)	.	0.0002869	0.0002558

**Solution**

<b>Variable</b>	<b>Critical Value</b>
Power (W)(1200,1600)	1393.1159
Exposure time (s)(30,60)	38.254718

Solution is a Minimum,  
 Predicted Value at Solution  
 0.0029843

**Prediction Profiler**

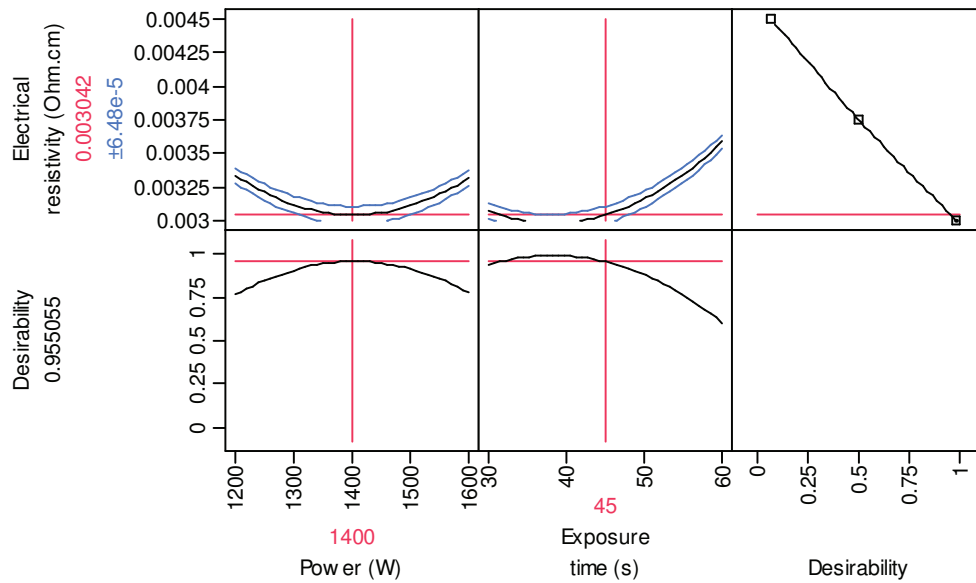
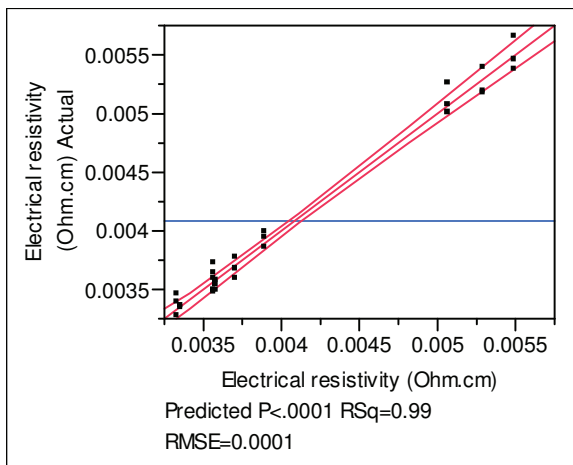


**TABLE 2 Full report of Box-Wilson experimental design for T700/CNT type fibers**

**Response Electrical resistivity (Ohm.cm)  
Actual by Predicted Plot**



**Summary of Fit**

RSquare	0.988085
RSquare Adj	0.985602
Root Mean Square Error	9.871e-5
Mean of Response	0.004081
Observations (or Sum Wgts)	30

**Analysis of Variance**

Source	DF	Sum of Squares	Mean Square	F Ratio
Model	5	0.00001939	3.8783e-6	398.0461
Error	24	0.00000023	9.7434e-9	<b>Prob &gt; F</b>
C. Total	29	0.00001963		<.0001

**Lack Of Fit**

Source	DF	Sum of Squares	Mean Square	F Ratio
Lack Of Fit	3	3.15594e-8	1.052e-8	1.0921
Pure Error	21	2.02283e-7	9.6325e-9	<b>Prob &gt; F</b>
Total Error	24	2.33843e-7		0.3743
				<b>Max RSq</b>
				0.9897

**Parameter Estimates**

Term	Estimate	Std Error	t Ratio	Prob> t
Intercept	0.0035664	3.649e-5	97.74	<.0001
Power (W)(1400,1800)	0.0005353	1.645e-5	32.54	<.0001
Exposure time (s)(30,60)	0.0004449	1.844e-5	24.13	<.0001
Power (W)*Exposure time (s)	0.0002542	2.849e-5	8.92	<.0001
Power (W)*Power (W)	0.0002132	1.416e-5	15.05	<.0001
Exposure time (s)*Exposure time (s)	0.0002712	2.051e-5	13.22	<.0001

**Effect Tests**

Source	Nparm	DF	Sum of Squares	F Ratio	Prob > F
Power (W)(1400,1800)	1	1	0.00001031	1058.640	<.0001
Exposure time (s)(30,60)	1	1	0.00000567	582.3145	<.0001
Power (W)*Exposure time (s)	1	1	0.00000078	79.5620	<.0001
Power (W)*Power (W)	1	1	0.00000221	226.5772	<.0001
Exposure time (s)*Exposure time (s)	1	1	0.00000170	174.7805	<.0001

**Response Surface**

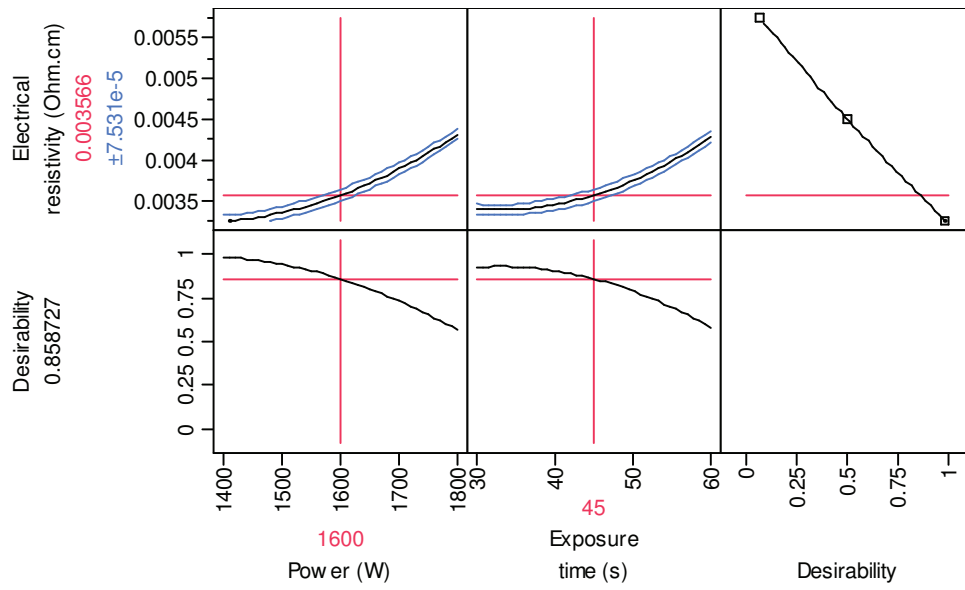
Coef	Power (W)(1400,1800)	Exposure time (s)(30,60)	Electrical resistivity (Ohm.cm)
Power (W)(1400,1800)	0.0002132	0.0002542	0.0005353
Exposure time (s)(30,60)	.	0.0002712	0.0004449

**Solution**

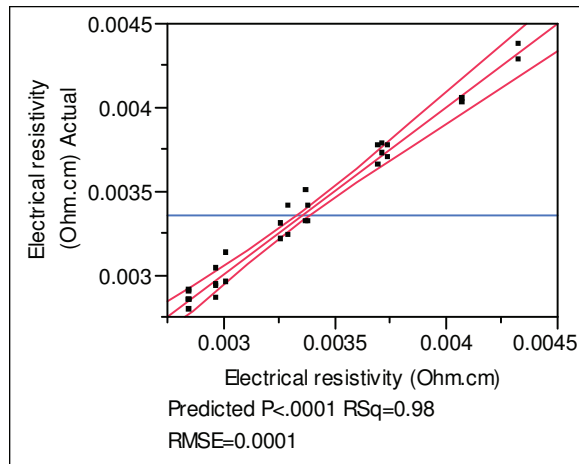
Variable	Critical Value
Power (W)(1400,1800)	1387.325
Exposure time (s)(30,60)	40.170528

Solution is a Minimum  
 Predicted Value at Solution  
 0.0032102

**Prediction Profiler**





**TABLE 3 Full report of Box-Behnken experimental design for AS4 type fibers****Response Electrical resistivity (Ohm.cm)  
Actual by Predicted Plot****Summary of Fit**

RSquare	0.982384
RSquare Adj	0.974457
Root Mean Square Error	7.389e-5
Mean of Response	0.003356
Observations (or Sum Wgts)	30

**Analysis of Variance**

Source	DF	Sum of Squares	Mean Square	F Ratio
Model	9	6.08911e-6	6.7657e-7	123.9277
Error	20	1.09188e-7	5.4594e-9	<b>Prob &gt; F</b>
C. Total	29	6.1983e-6		<.0001

**Lack Of Fit**

Source	DF	Sum of Squares	Mean Square	F Ratio
Lack Of Fit	3	1.49375e-8	4.9792e-9	0.8981
Pure Error	17	9.425e-8	5.5441e-9	<b>Prob &gt; F</b>
Total Error	20	1.09188e-7		0.4624
				<b>Max RSq</b>
				0.9848

**Parameter Estimates**

Term	Estimate	Std Error	t Ratio	Prob> t
Intercept	0.00285	3.016e-5	94.48	<.0001
Power (W)(1200,1600)	0.0002781	1.847e-5	15.06	<.0001
Exposure time (s)(30,60)	9.4375e-5	1.847e-5	5.11	<.0001
Flow ratio of dopant to pyrrole(0,2)	-0.000256	1.847e-5	-13.87	<.0001
Power (W)*Exposure time (s)	7.375e-5	2.612e-5	2.82	0.0105
Power (W)*Flow ratio of dopant to pyrrole	-0.000035	2.612e-5	-1.34	0.1953
Exposure time (s)*	-0.000295	2.612e-5	-11.29	<.0001
Flow ratio of dopant to pyrrole				
Power (W)*Power (W)	0.0003744	2.719e-5	13.77	<.0001
Exposure time (s)*Exposure time (s)	4.4375e-5	2.719e-5	1.63	0.1183
Flow ratio of dopant to pyrrole*	0.0005306	2.719e-5	19.52	<.0001
Flow ratio of dopant to pyrrole				

**Effect Tests**

Source	Nparm	DF	Sum of Squares	F Ratio	Prob > F
Power (W)(1200,1600)	1	1	1.23766e-6	226.7029	<.0001
Exposure time (s)(30,60)	1	1	1.42506e-7	26.1030	<.0001
Flow ratio of dopant to pyrrole(0,2)	1	1	1.05062e-6	192.4442	<.0001
Power (W)*Exposure time (s)	1	1	4.35125e-8	7.9702	0.0105
Power (W)*Flow ratio of dopant to pyrrole	1	1	9.8e-9	1.7951	0.1953
Exposure time (s)*	1	1	6.962e-7	127.5238	<.0001
Flow ratio of dopant to pyrrole					
Power (W)*Power (W)	1	1	1.035e-6	189.5827	<.0001
Exposure time (s)*Exposure time (s)	1	1	1.45413e-8	2.6636	0.1183
Flow ratio of dopant to pyrrole*	1	1	2.07923e-6	380.8556	<.0001
Flow ratio of dopant to pyrrole					

**Response Surface**

Coef	Power (W)(1200,1600)	Exposure time (s)(30,60)	Flow ratio of dopant to pyrrole(0,2)	Electrical resistivity (Ohm.cm)
Power (W)(1200,1600)	0.0003744	7.375e-5	-0.000035	0.0002781
Exposure time (s)(30,60)	.	4.4375e-5	-0.000295	9.4375e-5
Flow ratio of dopant to pyrrole(0,2)	.	.	0.0005306	-0.000256

**Solution**

Variable	Critical Value
Power (W)(1200,1600)	1328.5382
Exposure time (s)(30,60)	44.402222
Flow ratio of dopant to pyrrole(0,2)	1.2185987

Solution is a Minimum  
 Predicted Value at Solution  
 0.0027704

**Prediction Profiler**

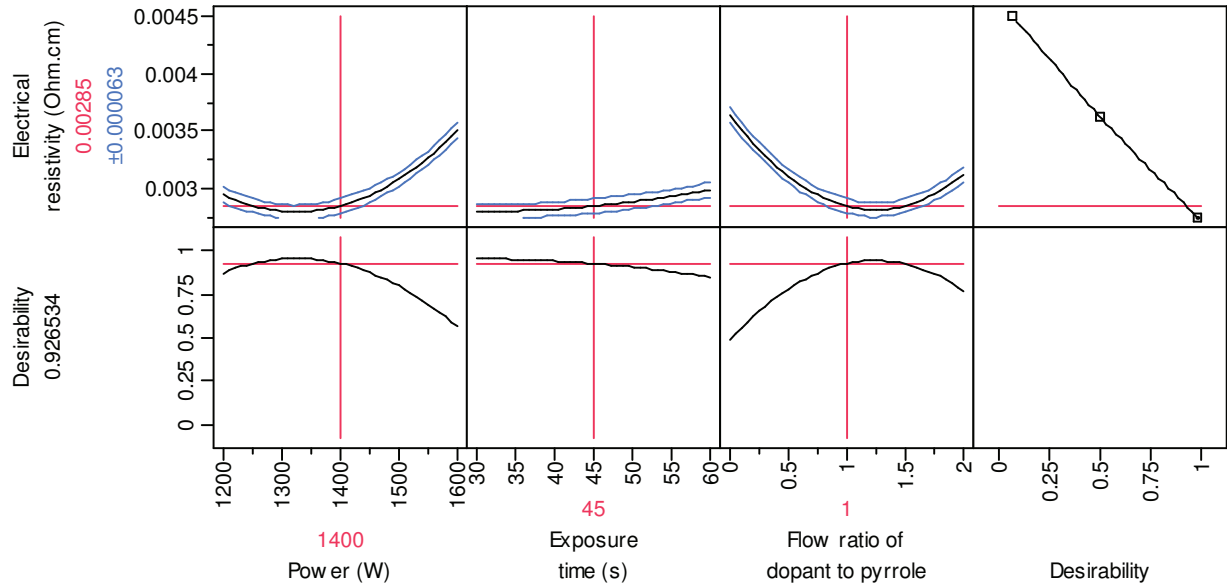
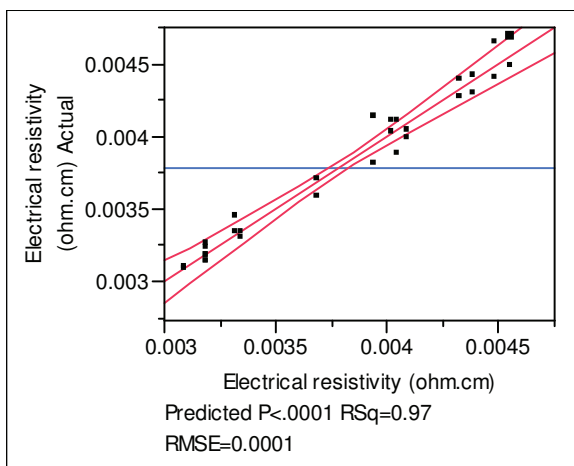


**TABLE 4 Full report of Box-Behnken experimental design for T700/CNT type fibers**

**Response Electrical resistivity (ohm.cm)  
 Actual by Predicted Plot**



**Summary of Fit**

RSquare	0.972539
RSquare Adj	0.960181
Root Mean Square Error	0.000105
Mean of Response	0.003786
Observations (or Sum Wgts)	30

**Analysis of Variance**

Source	DF	Sum of Squares	Mean Square	F Ratio
Model	9	7.8629e-6	8.7366e-7	78.7003
Error	20	2.22021e-7	1.1101e-8	<b>Prob &gt; F</b>
C. Total	29	8.08492e-6		<.0001

**Lack Of Fit**

Source	DF	Sum of Squares	Mean Square	F Ratio
Lack Of Fit	3	4.93875e-8	1.6462e-8	1.6211
Pure Error	17	1.72633e-7	1.0155e-8	<b>Prob &gt; F</b>
Total Error	20	2.22021e-7		0.2216
				<b>Max RSq</b>
				0.9786

**Parameter Estimates**

Term	Estimate	Std Error	t Ratio	Prob> t
Intercept	0.0031833	0.000043	74.01	<.0001
Power (W)(1400,1800)	0.0004994	2.634e-5	18.96	<.0001
Exposure time (s)(30,60)	0.0001169	2.634e-5	4.44	0.0003
Flow ratio of dopant to pyrrole(0,2)	-0.000105	2.634e-5	-3.99	0.0007
Power (W)*Exposure time (s)	0.0000025	3.725e-5	0.07	0.9472
Power (W)*Flow ratio of dopant to pyrrole	6.625e-5	3.725e-5	1.78	0.0905
Exposure time (s)*	-6.625e-5	3.725e-5	-1.78	0.0905
Flow ratio of dopant to pyrrole				
Power (W)*Power (W)	0.0002196	3.877e-5	5.66	<.0001
Exposure time (s)*Exposure time (s)	0.0002996	3.877e-5	7.73	<.0001
Flow ratio of dopant to pyrrole*	0.0006108	3.877e-5	15.75	<.0001
Flow ratio of dopant to pyrrole				

**Effect Tests**

Source	Nparm	DF	Sum of Squares	F Ratio	Prob > F
Power (W)(1400,1800)	1	1	0.00000399	359.4263	<.0001
Exposure time (s)(30,60)	1	1	2.18556e-7	19.6879	0.0003
Flow ratio of dopant to pyrrole(0,2)	1	1	1.764e-7	15.8904	0.0007
Power (W)*Exposure time (s)	1	1	5e-11	0.0045	0.9472
Power (W)*Flow ratio of dopant to pyrrole	1	1	3.51125e-8	3.1630	0.0905
Exposure time (s)*	1	1	3.51125e-8	3.1630	0.0905
Flow ratio of dopant to pyrrole					
Power (W)*Power (W)	1	1	3.56063e-7	32.0747	<.0001
Exposure time (s)*Exposure time (s)	1	1	6.62771e-7	59.7035	<.0001
Flow ratio of dopant to pyrrole*	1	1	2.75533e-6	248.2045	<.0001
Flow ratio of dopant to pyrrole					

**Response Surface**

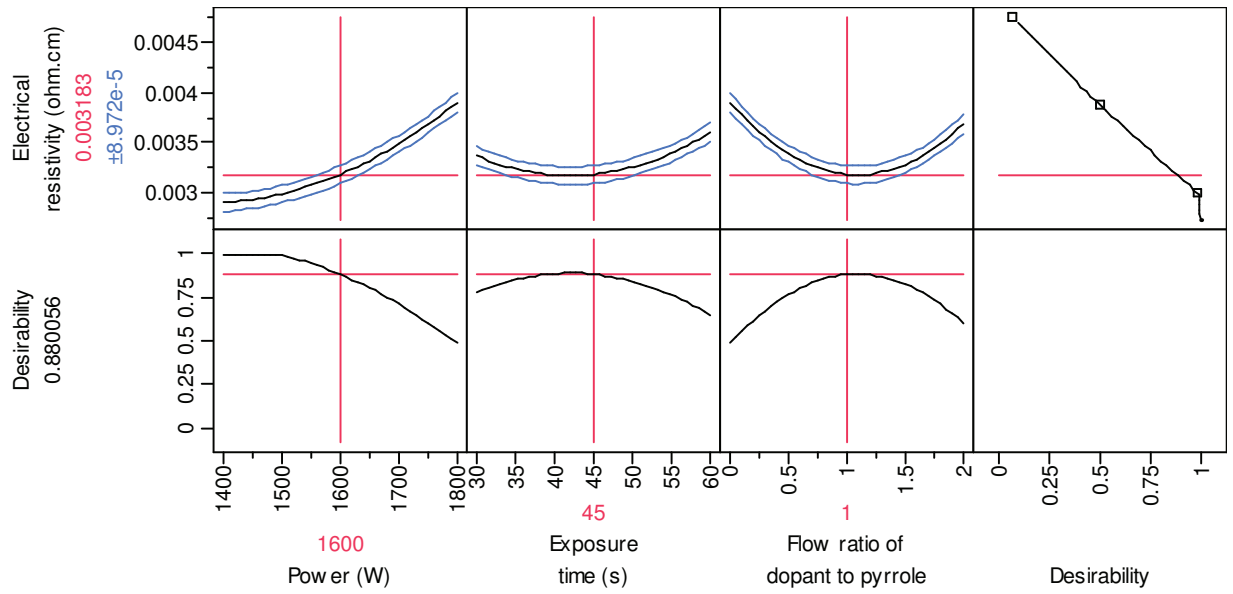
Coef	Power (W)(1400,1800)	Exposure time (s)(30,60)	Flow ratio of dopant to pyrrole(0,2)	Electrical resistivity (ohm.cm)
Power (W)(1400,1800)	0.0002196	0.0000025	6.625e-5	0.0004994
Exposure time (s)(30,60)	.	0.0002996	-6.625e-5	0.0001169
Flow ratio of dopant to pyrrole(0,2)	.	.	0.0006108	-0.000105

**Solution**

Variable	Critical Value
Power (W)(1400,1800)	1368.5795
Exposure time (s)(30,60)	42.377377
Flow ratio of dopant to pyrrole(0,2)	1.1392154

Solution is a Minimum  
Critical values outside data range  
Predicted Value at Solution  
0.0028769

**Prediction Profiler**



## Chapter IV

# Characterization of plasma polypyrrole deposited fibers





## *Introduction*

This chapter deals with the characterization of plasma polypyrrole deposited AS4 and T700/CNT fibers by using several techniques such as XPS (X-ray photoelectron spectroscopy), AFM (atomic force microscopy), SEM (scanning electron microscopy), and TGA (thermogravimetric analysis). Untreated samples (i.e. samples that are not subjected to any plasma treatment) were also analyzed in order to compare the differences between the unmodified and plasma modified samples.

XPS is a favorable material surface analysis technique due to its surface sensitivity, and qualitative/quantitative elemental identification capabilities. It is one of widely applicable technique which often used to identify the chemically bonded functional groups on a material surface. In XPS, monoenergetic soft X-rays are used to irradiate a sample in high vacuum producing photoionization and ejected free electrons. These photoelectrons are collected with an electron lens assembly, energy analyzed, and counted. The resulting spectrum consists of peaks that correspond to the electronic energy states of the sample material. By integrating the area under a given peak and correcting for its ionization cross section, quantitative elemental analysis of the material can be made. A typical quantitative analysis of a material is based on the chemical shift, which is related to the electron density around the nucleus in the atom of interest. Any mechanism that decreases the electron density around the nucleus will increase the binding energy, and any mechanism that increases the electron density will decrease the binding energy of the core electrons. Thus the chemical shift is closely related to the electronegativity of the species to which the atom of interest is. In this study, XPS was used for the investigation of the influence of various plasma parameters (i.e. power, duration, precursor type) on the modification of AS4 and CNT grafted T700 (T700/CNT) carbon fibers.

SEM is a useful technique to produce an image of a specimen by detecting the interactions between electron beam and the sample. The image of a sample can be obtained with two basic types of electrons: secondary electrons and backscattered electrons. Secondary electrons are generated when the electron beam from the SEM strikes the sample and ionizes the atoms of the sample. Secondary electron images

provide images of a sample's surface morphology, because most of the detected secondary electrons originating from very near the surface of the sample. Backscattered electrons are electrons from the SEM beam that strike the atoms of the sample and are ejected back out of the sample. This interaction occurs at deeper depths in the sample than secondary electron generation. In this study, SEM was used to track the morphological changes between the unmodified and plasma modified carbon fibers.

AFM measurements can be performed in contact or non-contact mode. In non-contact mode (tapping-mode) the cantilever is oscillated at its resonant frequency and the force gradient (changes in force) between the tip and the carbon fiber sample can be detected. As the probe gets closer to the carbon fiber surface, the force gradients change both the oscillation amplitude and phase of the vibration. Both of those changes can be used to control the tracking of the probe over the surface of fiber. During AFM scanning of a fiber, the most important challenge is to hold fiber securely under the probe in order to avoid the vibration and the movement of the fibers during the scanning operation. For this purpose, Tempfix (Agar Scientific) was used to fix individual carbon fibers on a glass plates as described in Chapter II. AFM was used to investigate surface topography of unmodified and plasma modified carbon fibers in order to have an idea on the roughness property.

TGA is a principle thermoanalytical method designed to monitor mass loss of a sample during the heating process. Any type of physicochemical process such as dehydration, decomposition, vaporization, and pyrolysis, etc. can be observed by using a thermal analyzer. There are two types of thermal analyzers: vertical and horizontal balance. Vertical balance instruments have a specimen pan hanging from the balance (TA Instruments, etc) or located above the balance on a sample stem (Netzsch). Horizontal balance instruments (TA, Perkin Elmer, etc) normally have two pans (sample and reference) and can perform additional analyses (e.g. DTA and DSC). The measurement is normally carried out in air or in an inert atmosphere, such as nitrogen or argon, and the weight is recorded as a function of increasing temperature. The maximum temperature is selected so that the specimen weight is stable at the end of the experiment, implying that all chemical reactions are completed. TGA was used to compare the thermal stabilities of unmodified and plasma modified carbon fibers.

## *1 Surface properties of plasma treated T700/CNT and AS4 fibers*

### *1.1 Results of XPS*

The changes in the elemental composition of carbon nanotubes grafted carbon fibers (T700/CNT) and AS4 fibers with plasma treatment were studied to examine the surface of these fibers treated at different plasma conditions by using electron spectroscopy for chemical analysis (XPS).

Figures 4.1-4.5 show the low resolution XPS spectra (survey spectra at 187.85 eV) of untreated, 1400 W 45 s, 1400 W 60 s, and 1800 W 45 s pyrrole and 1400 W 45 s pyrrole+dopant (pTSA.H<sub>2</sub>O) plasma treated T700/CNT fibers, respectively. Figure 4.6 shows the low resolution XPS spectra of untreated and 1400 W 45 s pyrrole+dopant (pTSA.H<sub>2</sub>O) plasma treated AS4 fibers. Table 4.1 gives the elemental composition and the N/C and O/C of the surfaces of those fibers. The results of XPS measurements show that the surface composition of both fibers can be changed substantially during the plasma treatment.

Neither the precursor pyrrole nor the carrier gas contains oxygen, but oxygen was detected at a considerable amount in all XPS measurements of plasma treated samples. Since all experiments took place in the open-air configuration (refer to Chapter II, Figure 2.5), the most probable reason of the presence of oxygen peak in each spectrum may be related to the atmospheric oxygen and/or water vapor which might be trapped in the deposited layer during the plasma operation. Besides, it has been known that free radicals remain on the plasma polymer surface and these radicals possess a long half life which are susceptible to react with oxygen in air and further form carbonyl, hydroxyl, and carboxyl groups [94, 95].

Figures 4.7-4.11 demonstrate the high resolution XPS spectra (core level spectra at 29.35 eV) of untreated T700/CNT fibers, 1400 W 45 s, 1400 W 60 s, 1800 W 45 s pyrrole plasma, and 1400 W 45 s pyrrole+dopant plasma treated T700/CNT fibers, respectively. Figures 4.12-4.13 show the high resolution XPS spectra (core level spectra at 29.35 eV) of untreated and 1400 W 45 s pyrrole+dopant plasma treated AS4 fibers, respectively. Tables 4.2-4.4 represent the values of the binding energy (B.E.), the peak assignment (P.A.) and the relative area (R.A.) of each photopeak estimated from the

curve fit of C1s, N1s, and O1s. Carbon to oxygen ratio for only pyrrole plasma treated T700/CNT samples was found around 3.0 while it was equal to 38.4 for the untreated sample. In the case of pyrrole+dopant plasma treated T700/CNT fiber, it was found that carbon to oxygen ratio slightly was increased to ~5.5. It is also not surprising that almost the same C to O ratio (~5.8) was observed in the case of AS4 fiber which was also treated at the same plasma conditions (1400 W 45s pyrrole+dopant plasma). For the pyrrole plasma treated T700/CNT fibers, carbon to nitrogen ratio was ranging between 2 and 15 while it was equal to 64 for untreated T700/CNT fibers (Table 4.1). Increase of oxygen and nitrogen content in all plasma polymers is a proof of plasma polypyrrole deposition (not ideal polypyrrole) which accounts for several advantages such as the improvement of adhesion between matrix and the fiber [96].

In the case of untreated T700/CNT fiber, carbon, nitrogen and oxygen content was 96.0 %, 1.5 %, and 2.5 %, respectively. Survey spectra showed that the surface of untreated T700/CNT fiber contains low concentration of nitrogen (<1.5%) and oxygen (<2.5%) which indicate that few nitrogen and oxygen based functional groups present on the surface of T700/CNT fibers compared to plasma treated fibers. When high resolution spectra were examined (Fig. 4.7) some peaks appeared to be multiple peaks. Carbon gave a major peak at 284.6 eV corresponds to aromatic, graphitic and/or aliphatic carbon (C=C, C-C, C-H) and the others were detected around 286.3, 287.7, and 289.3 corresponds to C-O, C=O, and COO (i.e. carbonyl compounds) in ester and/or anhydrides, respectively [12]. Additionally, the asymmetry of C1s line (between the low and high energy levels) and the presence of  $\pi$ -plasmon at high energy levels (Fig. 4.7, C1s spectrum) may be related to electronic transitions in multi-walled carbon nanotubes due to conductivity electrons that are located at the Fermi level, in the same fashion as in transition metals [106].

The T700/CNT fiber treated at 1400 W 45 s pyrrole plasma, carbon, nitrogen and oxygen content was found about 61%, 21%, and 18%, respectively. Survey spectra shows that the surface of these fibers contains highly nitrogen (>21%) and oxygen (>17%) based functional groups on the surface of these fibers. When high resolution spectra were explored (Fig. 4.8), C 1s, N 1s, and O 1s peaks were most likely to be decomposed into five, three, and two lines, respectively. Carbon gave a major peak at 284.7 eV which may

correspond to  $\alpha$ -carbons in pyrrole ring and/or aromatic, graphitic and aliphatic carbons originated from T700/CNT fiber. The lowest energy component of C 1s peak detected around 283.6 eV may correspond to  $\beta$ -carbons in pyrrole ring [95, 100]. The third line of C 1s located at 286.2 eV might be an overlap of C=N, C-N, C-OH or C-O groups [95] or it could be originated from the presence of polaron species  $=\text{C-NH}^+$  [107]. The fourth line at 287.6 eV may be attributed to C=O, C=N or the excited state of C-N (i.e. C-N\*) in pyrrole ring [82]. The highest energy component of C1s photopeak gave a line around 288.8 eV which indicates the presence of carbonyl and/or ether groups in esters and anhydrides [12]. The major peak of N 1s (399.2 eV) is assigned to -NH- groups of pyrrole [97]. The lowest energy component of N1s peak (~398 eV) may be attributed to N=C whereas the highest energy component (~400.4 eV) may correspond to the nitrogen atoms that are more positively charged than the N atoms of the main pyrrole peak [82, 95, 97]. Decomposition of O 1s peak indicates an overlap of O-N, O-C, and O=C groups at 532.34 eV and the important signal of O 1s around 530.9 eV indicates the surface reaction with oxygen is likely to occur due to the open-air configuration of plasma system and/or the exposure to air after the plasma operation [97].

Survey spectrum of 1400 W 60 s pyrrole plasma treated T700/CNT fiber surface shows that it contains 71 % carbon, 7.2 % nitrogen and ~22 % oxygen. The high resolution C 1s, N 1s and O 1s spectra for this sample are shown in Fig. 4.9. The line shape analysis of C 1s photopeak reveals that it can be decomposed into four lines and symmetric in both high and low binding energy sides. Carbon gave a major peak around 283.8 eV and another important peak at 285.0 eV may correspond to  $\alpha$ -carbons and  $\beta$ -carbons in pyrrole ring, respectively [82, 95]. Similar to 1400 W 45 s treated sample, the third line of C 1s is located at 286.2 eV and it might be an overlap of C=N, C-N, C-OH or C-O groups [95]. The highest energy component of C 1s peak around 287.7 eV is probably due to the overlap of C=O, C=N or the excited state of C-N (i.e. C-N\*) [82]. The main peak of N 1s (399.7 eV) is attributable to -NH- groups of pyrrole [97]. The lowest energy component of N 1s peak (~398 eV) is attributed to N=C whereas the highest energy component (~400.4 eV) may correspond to the nitrogen atoms that are more positively charged than the N atoms of the main pyrrole peak as it was observed in the other plasma treated samples [82, 95, 97]. Decomposition of O 1s peak indicates an

overlap of O-N, O-C, and O=C groups (532.25 eV) and similar to 1400 W 45 s treated T700/CNT fibers. The presence of O 1s signal around 530.9 eV is an indication of the surface reaction with oxygen due to the air exposure [97].

Survey spectra of 1800 W 45 s pyrrole plasma treated T700/CNT fiber surface shows that it contains 75.5 % carbon, 5.2 % nitrogen and ~19 % oxygen. The high resolution C 1s, N 1s and O 1s spectra for this sample are shown in Fig. 4.10. The C 1s high resolution spectrum was resolved in four peaks. Besides, the fifth one (~291.6 eV, 0.5%) could be attributed to the presence of the shake-up satellites ( $\pi$ - $\pi^*$ ) [100]. When the high resolution C 1s photopeak was explored, the increase in binding energies showed that the C 1s orbital assume different conformations. In the case of 1800 W 45 s treated fiber surface, the lowest energy component (~285.2 eV) can be associated with carbon bonds in C <sub>$\beta$</sub> -COOH [7] or  $\alpha$ - carbons in pyrrole ring [82, 95]. Because, it is noted in all components of C 1s peaks the value of FWHM (full-width-half-maximum) was equal to 1.72 eV whereas the FWHM values of the components of C 1s peaks in other samples were varied between 1.44 (for T700/CNT ) and 1.58 eV. Due to the high FWHM value of C1s peak components of 1800 W 45 s treated sample, the components of C 1s peak may be shifted to higher energy levels compared to the other plasma treated samples. Therefore the peak around 285.2 eV might also correspond to  $\alpha$ -carbons in pyrrole ring. The clear shift can be seen in Fig. 4.14 which provides the comparison of C1s curve fit spectrum of 1800 W 45 s plasma treated fiber with the other T700/CNT plasma treated fibers. The peaks recorded around 286.6 eV, 288.0 eV, 289.3 eV may be attributed to the similar functional groups which has already been discussed above. The main peak of N 1s (~400.5 eV) might be assigned to nitrogen atoms that are more positively charged than the atoms of the other components of N 1s peak [82, 95, 97]. The lowest energy component of N 1s peak (~399.3 eV) may correspond to -NH- groups of pyrrole [97]. The highest binding region (~401.8 eV) of N 1s core level may be related to the extra charges that are present on the selected N atoms in the deposited layer. However, this charge does not occur at specific nitrogen sites, involves the whole pyrrole ring unit [95]. The main peak of O 1s (532.2 eV) is assigned to the O-N, O-C or O=C groups. The second line, located at 533.6 eV might correspond to carbonyl compounds, alcohols or ethers [12].

In order to find out the effect of dopant, T700/CNT and AS4 fibers were treated at the same plasma conditions (1400 W 45s) and examined by using XPS spectroscopy. At first, the absence of sulfur atom on their survey spectrum and decrease observed in their oxygen at-% (about 5%) draws attention (Figures 4.5 & 4.6b, Table 4.1 & 4.2). Even though dopant (pTSA.H<sub>2</sub>O) contains sulphur, in none of their XPS spectrum sulphur atom was detected. Therefore, it can be concluded that pTSA.H<sub>2</sub>O was not penetrated inside the plasma polypyrrole as a tosylate ion (dopant ion); it might partly be dissociated into gaseous products (e.g. SO<sub>2</sub>) and lost during the plasma polymerization of pyrrole. During this process, it may affect the structure by creating defectively  $\alpha$ - $\beta$  bonded carbon atoms (around 285.8 eV) [108] which has not been detected in the other plasma treated samples. As evidenced by the highly similar decomposition of C 1s, N 1s and O 1s photopeaks, it can be said that the surface chemistry of those fibers have been changed in the same manner (Figures 4.11 and 4.13). As it was found by XPS curve fit, untreated AS4 has less aromatic and/or graphitic structure than T700/CNT fibers due to the lower C=C and C-C groups (Table 4.2 & 4.3). It was also found that the surface of as-received AS4 fiber includes oxygen based functional at a considerable amount (~10 %) due to the surface oxidation that is carried out by the supplier [12].

The C 1s spectrum was asymmetric on the high binding energy side which could be an indication of crosslinked chain terminating, non- $\alpha$ - $\alpha'$ -bonded carbons or carbons in partially saturated rings in polypyrrole materials [95]. These carbons are usually referred to measures of disorder of the material [95]. In the N 1s spectrum, the asymmetric shape implies the electrostatic interactions that may occur in polypyrrole materials [95, 99]. The explored peak shapes in XPS spectra showed that the pyrrole plasma treated T700/CNT fibers have more symmetrical C 1s and N 1s peaks than that of T700/CNT fibers due to the presence of relatively ordered polymer deposition. It was also shown that the most ordered material among the pyrrole plasma treated samples was belonged to 1400 W 60 s sample due to the obtained somewhat symmetrical peak shape compared to the others. It is also noted that the presence of the shake-up satellites ( $\pi$ - $\pi^*$ ) around 291 eV might be due to electronic transitions in PPy ring [100] and/or electronic transitions (i.e.  $\pi$ -plasmon) in the carbon nanotubes [106].



The surface of untreated T700/CNT fibers were composed mainly of carbon in C-C/C-H and C-O/C-OH or C-N/C=N which were about 81.7 and 9.0 %, respectively. In the case of plasma polypyrrole deposited fibers, the content of both oxygen and nitrogen based functional groups were increased compared to untreated fibers. The increase in the concentration of oxygen and nitrogen based active groups may alter the polarity and the structure of the fiber surface. Therefore, all results obtained showed that not only the plasma polypyrrole (PPPy) deposited on carbon nanotubes, but also to improve the adhesion between matrix and fibers as a result of produced active groups on these fiber surfaces.

TABLE 4.1 XPS results for surface composition of T700/CNT and AS4 fibers treated at different conditions

Fiber	Precursor	Plasma conditions	C at %	N at %	O at %	C/N	C/O
T700/CNT	Untreated		96.0	1.5	2.5	64.0	38.4
	Pyrrole	1400 W 45 s	61.1	21.1	17.8	2.8	3.4
		1400 W 60 s	71.0	7.2	21.8	9.8	3.2
		1800 W 45 s	75.5	5.2	19.3	14.5	3.9
	Pyrrole + pTSA.H <sub>2</sub> O	1400 W 45 s	70.8	16.4	12.8	4.3	5.5
AS4	Untreated		85.4	4.9	9.7	17.4	8.8
	Pyrrole + pTSA.H <sub>2</sub> O	1400 W 45 s	71.7	16.2	12.2	4.4	5.8



TABLE 4.2 XPS C 1s, N1s, and O 1s curve fit results of untreated and plasma treated T700/CNT fibers at different conditions

Sample	Property	C 1s photopeak					N 1s photopeak			O 1s photopeak		
		1	2	3	4	5	1	2	3	1	2	3
T700/CNT untreated	B.E. (eV)	284.6	286.2	287.7	289.3	290.9	398.5	401.1		530.6	532.5	
	R.A (%)	81.66	9.0	3.71	2.39	3.24	33.65	66.35		24.24	76.76	
T700/CNT 1400 W 45 s pyrrole	P.A	C-C, C-H	C-O, C-OH, C-N, C=N	C=N, C=O	CO-O	plasmon	N=C	NH <sub>2</sub> /N <sup>+</sup> H <sub>3</sub>	O 1s	O-N, O-C, O=C		
	B.E. (eV)	283.6	284.7	286.2	287.6	288.8	397.9	399.2	400.4	530.9	532.3	
T700/CNT 1400 W 60 s pyrrole	R.A (%)	7.47	44.7	16.97	19.7	11.16	17.82	58.19	23.99	72.12	27.88	
	P.A	Cβ	Cα and/or C-C, C-H	C-O, C-OH, C-N, C=N Or =C-NH <sup>+</sup>	C-N*, C=N, C=O	CO-O	N=C =N-	-NH-	N <sup>+</sup>	O 1s	O-N, O-C, O=C	
T700/CNT 1800 W 45 s pyrrole	B.E. (eV)	283.8	285	286.1	287.7		398.0	399.7	400.4	530.9	532.3	
	R.A (%)	52.88	22.04	7.22	17.86		25.38	63.1	11.52	54.64	45.36	
T700/CNT 1400 W 45 s pyrrole+ dopant	P.A	Cβ	Cα	C-O, C-OH, C-N, C=N	C-N*, C=N, C=O	plasmon	N=C =N-	-NH-	N <sup>+</sup>	O 1s	O-N, O-C, O=C	
	B.E. (eV)	285.2	286.6	288.0	289.3	291.6	399.3	400.5	401.8	532.2	533.6	
T700/CNT 1400 W 45 s pyrrole+ dopant	R.A (%)	65.8	16.05	8.44	9.16	0.54	35.44	56.25	8.31	58.85	41.15	
	P.A	Cβ-COOH, Cα	C-O, C-OH, C-N, C=N	C-N*, C=N, C=O	CO-O	plasmon	-NH-	N <sup>+</sup>	NH <sub>2</sub> /N <sup>+</sup> H <sub>3</sub>	O-N, O-C, O=C	C-OH, -OH, R-O-R'	
T700/CNT 1400 W 45 s pyrrole+ dopant	B.E. (eV)	284.5	285.8	287.2	288.5	289.9	398.9	399.9	400.9	531.4	532.1	
	R.A (%)	52.94	20.57	11.26	12.99	2.25	22.94	58.77	18.29	42.20	40.89	
T700/CNT 1400 W 45 s pyrrole+ dopant	P.A	C-C, C-H, Cβ	Cα-β	C-N*, C=N, C=O	CO-O	plasmon	N=C =N-	-NH-	N <sup>+</sup>	O=C=	O-N, O-C, O=C	
	B.E. (eV)	284.5	285.8	287.2	288.5	289.9	398.9	399.9	400.9	531.4	532.1	
T700/CNT 1400 W 45 s pyrrole+ dopant	R.A (%)	52.94	20.57	11.26	12.99	2.25	22.94	58.77	18.29	42.20	40.89	
	P.A	C-C, C-H, Cβ	Cα-β	C-N*, C=N, C=O	CO-O	plasmon	N=C =N-	-NH-	N <sup>+</sup>	O=C=	O-N, O-C, O=C	
T700/CNT 1400 W 45 s pyrrole+ dopant	B.E. (eV)	284.5	285.8	287.2	288.5	289.9	398.9	399.9	400.9	531.4	532.1	
	R.A (%)	52.94	20.57	11.26	12.99	2.25	22.94	58.77	18.29	42.20	40.89	
T700/CNT 1400 W 45 s pyrrole+ dopant	P.A	C-C, C-H, Cβ	Cα-β	C-N*, C=N, C=O	CO-O	plasmon	N=C =N-	-NH-	N <sup>+</sup>	O=C=	O-N, O-C, O=C	
	B.E. (eV)	284.5	285.8	287.2	288.5	289.9	398.9	399.9	400.9	531.4	532.1	
T700/CNT 1400 W 45 s pyrrole+ dopant	R.A (%)	52.94	20.57	11.26	12.99	2.25	22.94	58.77	18.29	42.20	40.89	
	P.A	C-C, C-H, Cβ	Cα-β	C-N*, C=N, C=O	CO-O	plasmon	N=C =N-	-NH-	N <sup>+</sup>	O=C=	O-N, O-C, O=C	

TABLE 4.3 XPS C 1s, N1s, and O 1s curve fit results of untreated and plasma treated AS4 fiber

Sample	Property	C 1s photopeak					N 1s photopeak			O 1s photopeak		
		1	2	3	4	5	1	2	3	1	2	3
AS4	B.E. (eV)	284.5	285.8	287.3	288.7		399.2	400.6	402.3	531.1	532.3	533.7
	R.A (%)	73.33	16.45	6.81	3.41		42.74	48.74	8.52	47.08	39.98	12.93
AS4	P.A	C-C, C-H	COR	C=N, C=O	COO		NH <sub>2</sub>	NH <sub>2</sub> /N <sup>+</sup> H <sub>3</sub>	NO <sub>x</sub>	O=C	-OH	R-O-R'
	B.E. (eV)	284.7	286	287.8	288.9	290.9	398.4	399.7	400.7	531	532	533.3
AS4 1400 W 45 s pyrrole + dopant	R.A (%)	63.00	14.55	12.59	8.26	1.50	29.01	54.57	16.42	37.53	42.68	19.79
	P.A	C-C, C-H, C $\beta$	C $\alpha$ - $\beta$	C-N*, C=N, C=O	CO-O	plasmon	N=C =N-	-NH-	N <sup>+</sup>	O=C=	O-N, O-C, O=C	C-OH, -OH, R-O-R'

\*excited states [82]

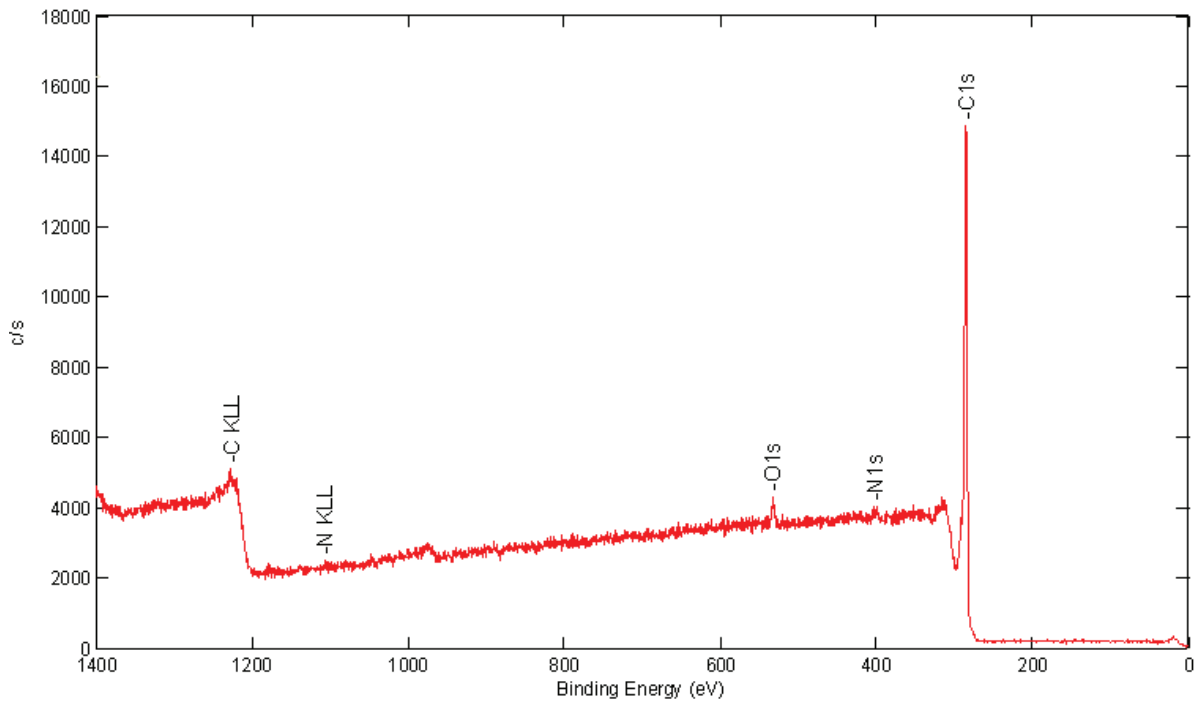


Figure 4.1 XPS spectrum of untreated T700/CNT fiber

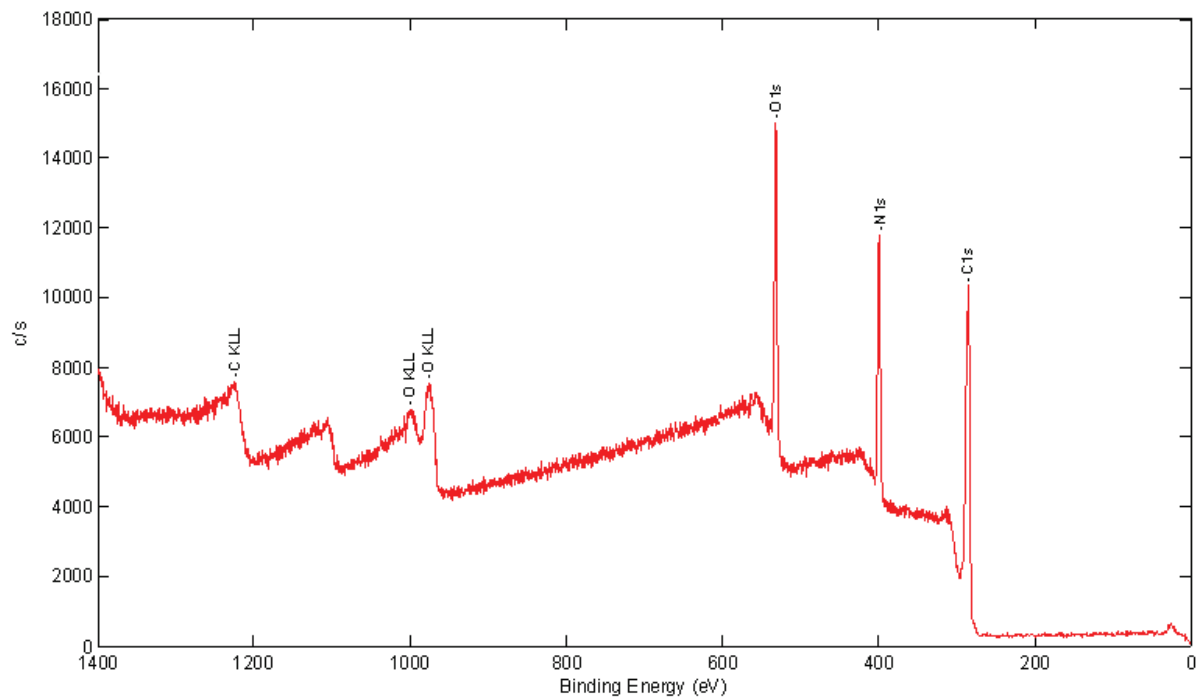


Figure 4.2 XPS spectrum of pyrrole plasma treated (1400 W and 45s) T700/CNT fiber

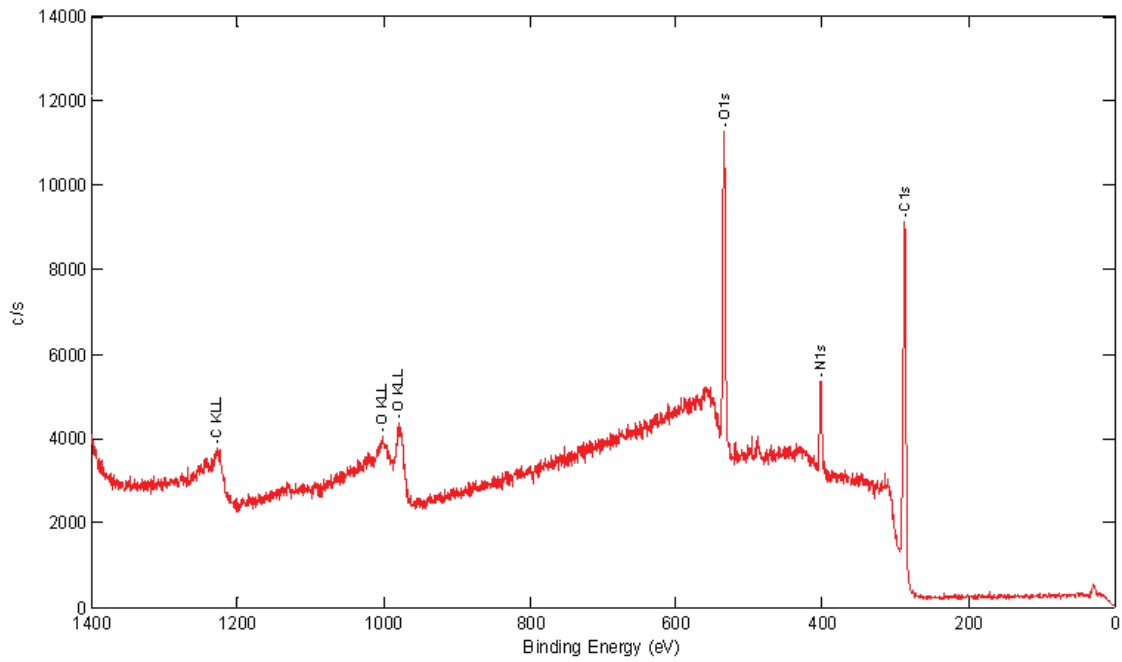


Figure 4.3 XPS spectrum of pyrrole plasma treated (1400 W and 60s) T700/CNT fiber

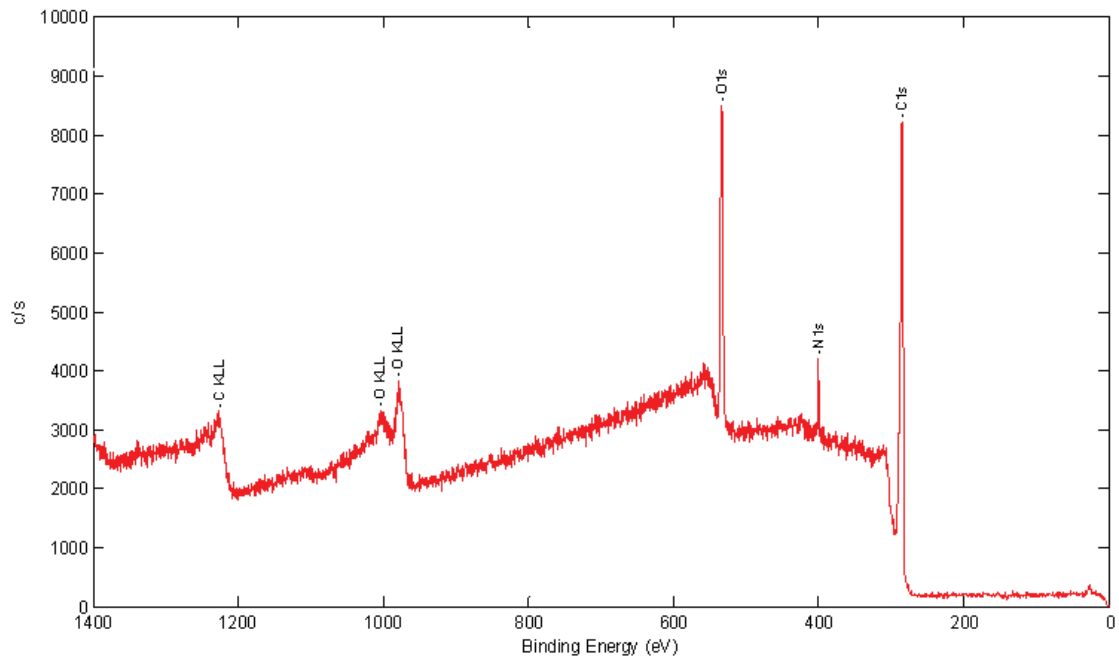


Figure 4.4 XPS spectrum of pyrrole plasma treated (1800 W and 45s) T700/CNT fiber

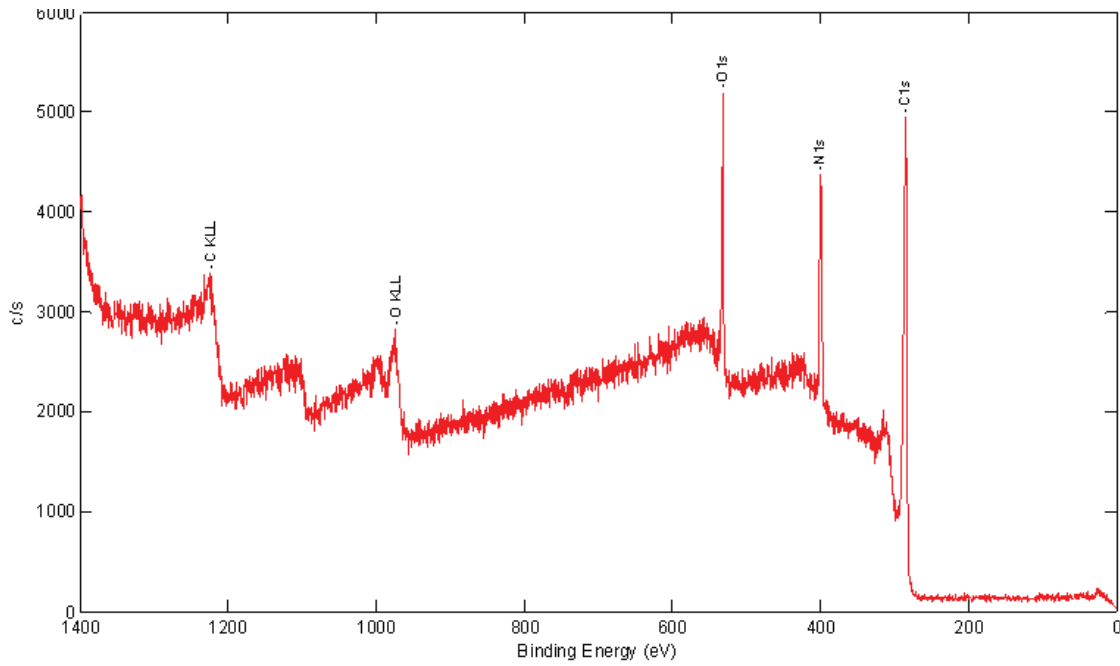


Figure 4.5 XPS spectrum of pyrrole plasma treated (1400 W and 45s+dopant) T700/CNT fiber

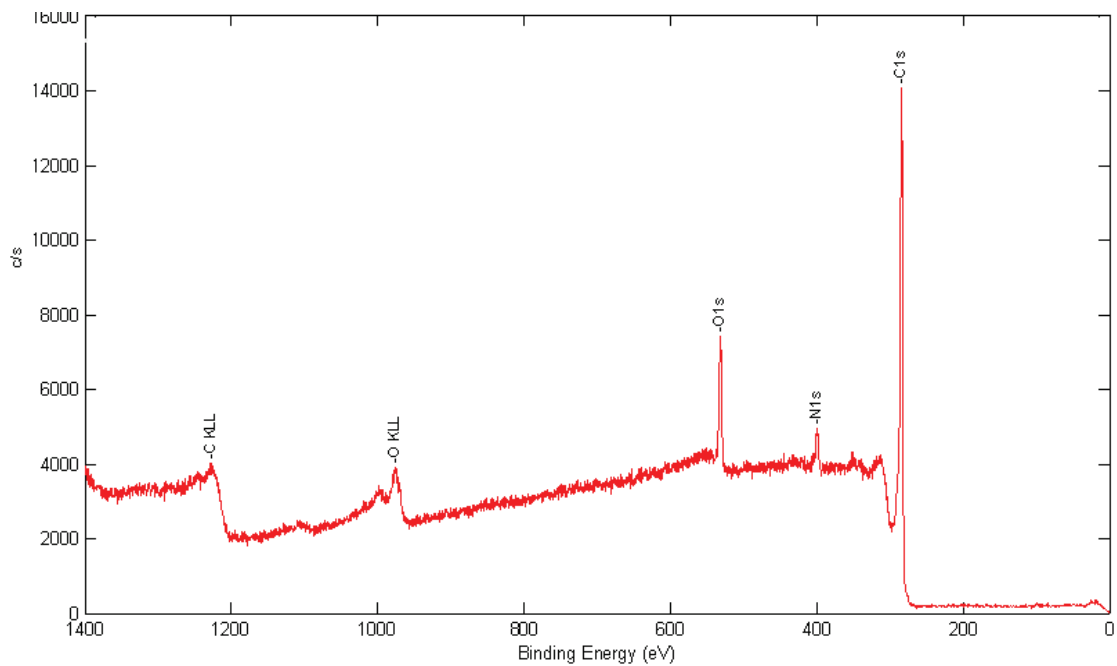


Figure 4.6a XPS spectrum of untreated AS4 fiber

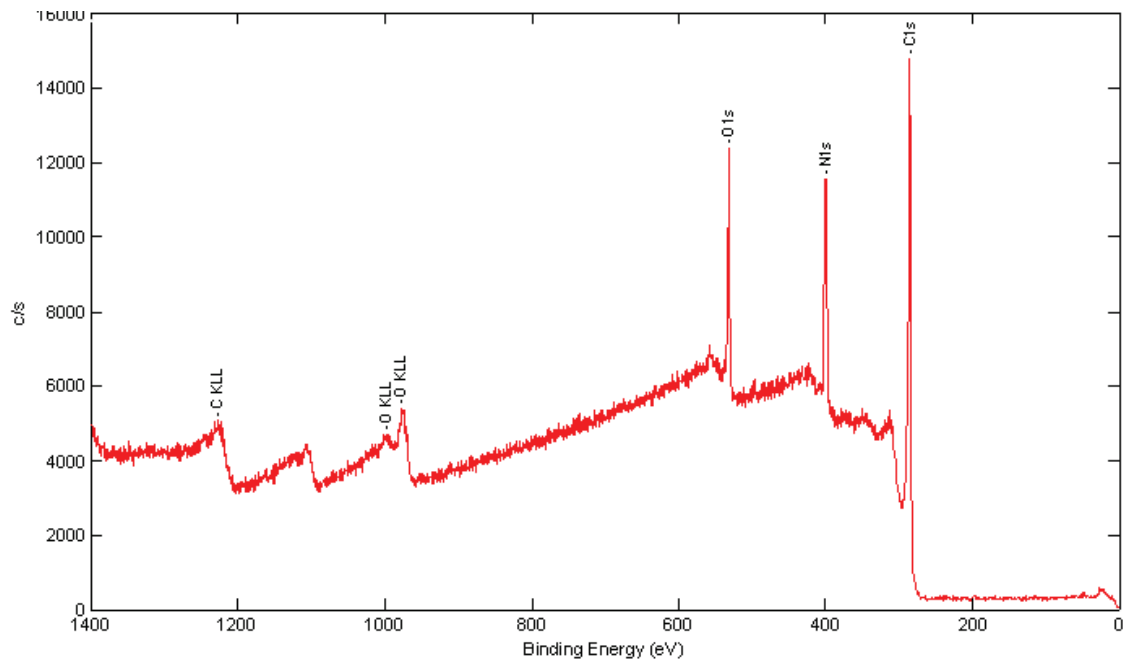


Figure 4.6b XPS spectrum of pyrrole plasma treated (1400 W and 45s+dopant) AS4 fiber

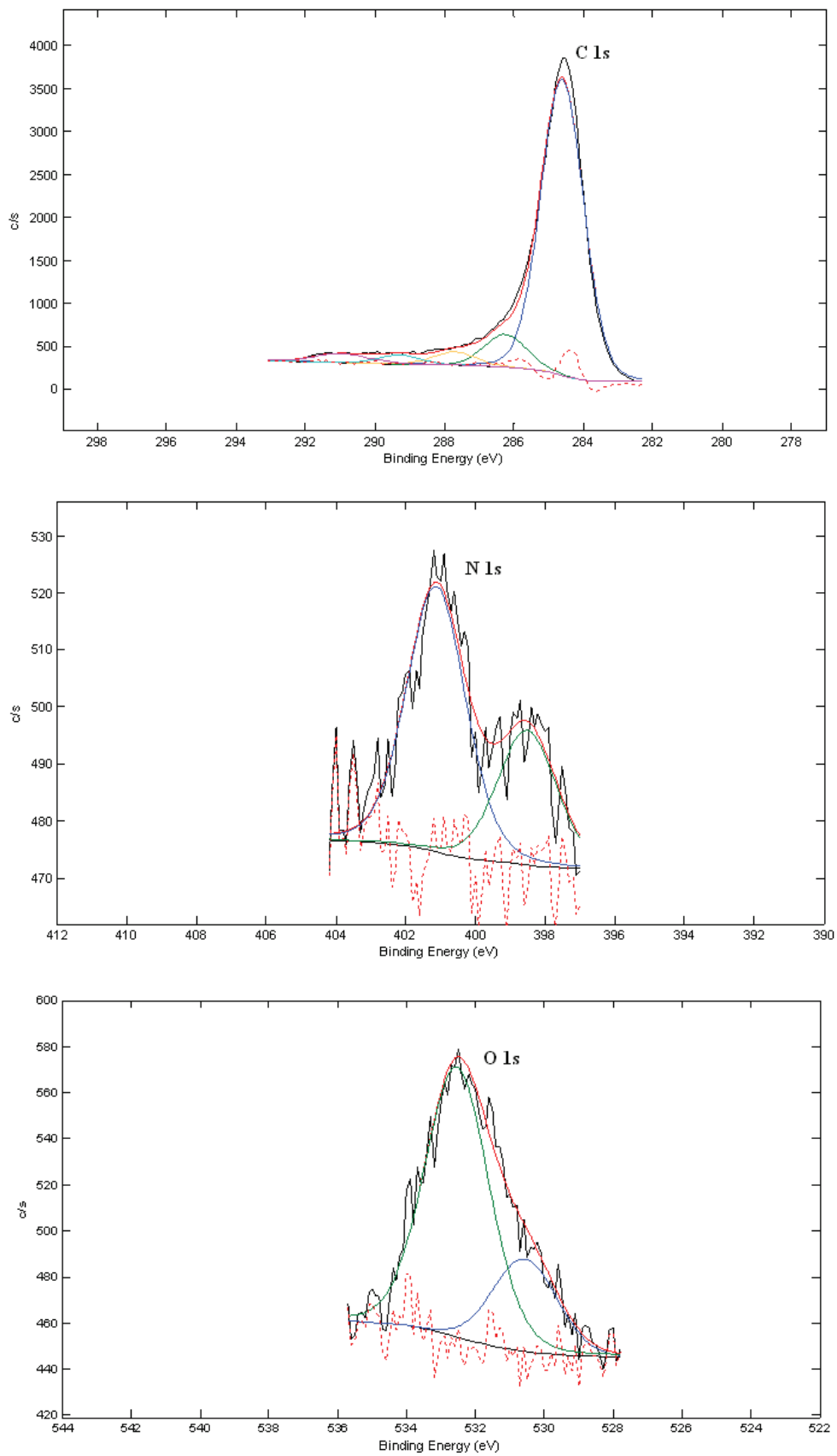


Figure 4.7 High resolution spectra of untreated T700/CNT fiber

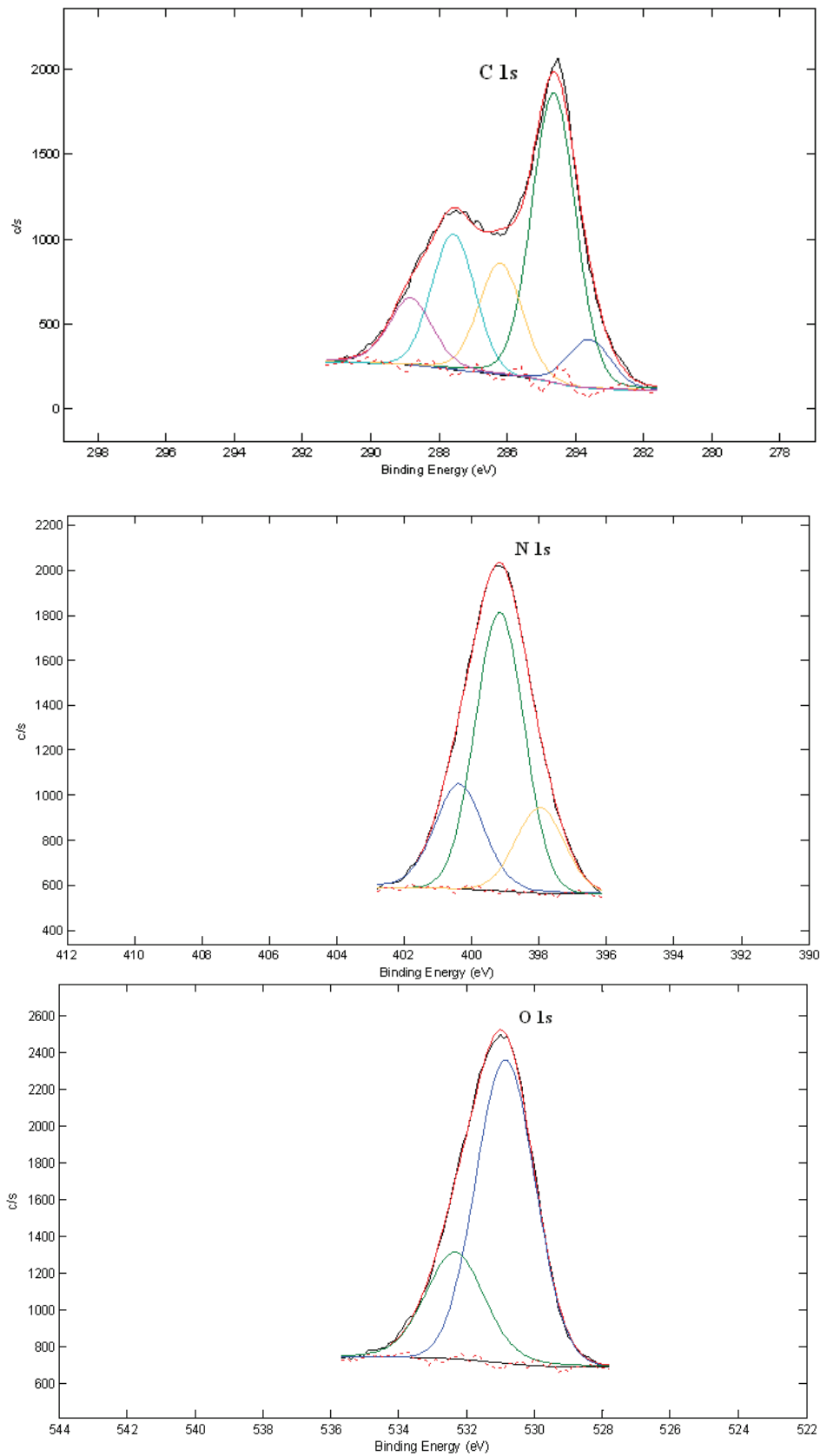


Figure 4.8 High resolution spectra of pyrrole plasma (1400 W 45 s) treated T700/CNT fibers



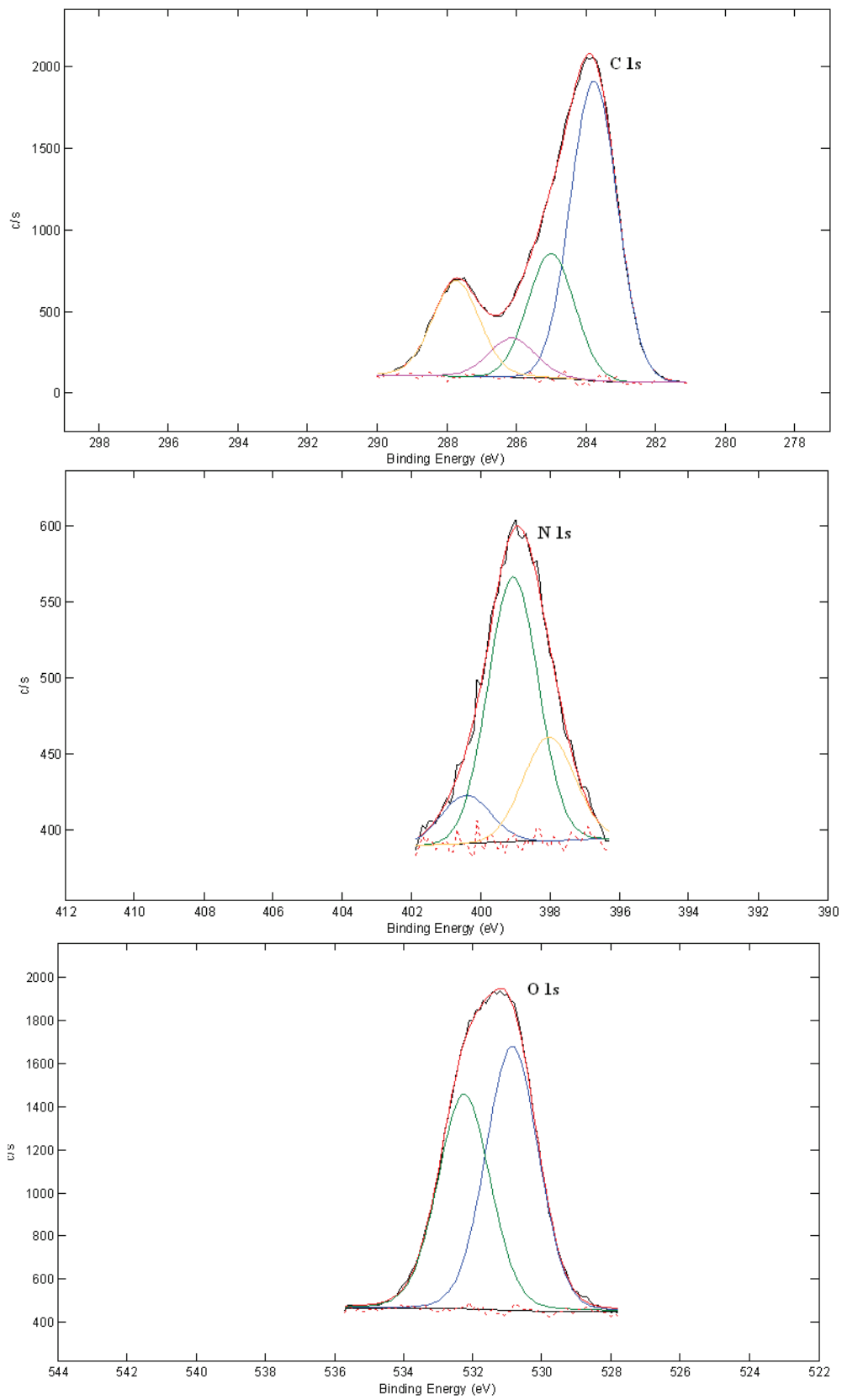


Figure 4.9 High resolution spectra of pyrrole plasma (1400 W 60 s) treated T700/CNT fibers

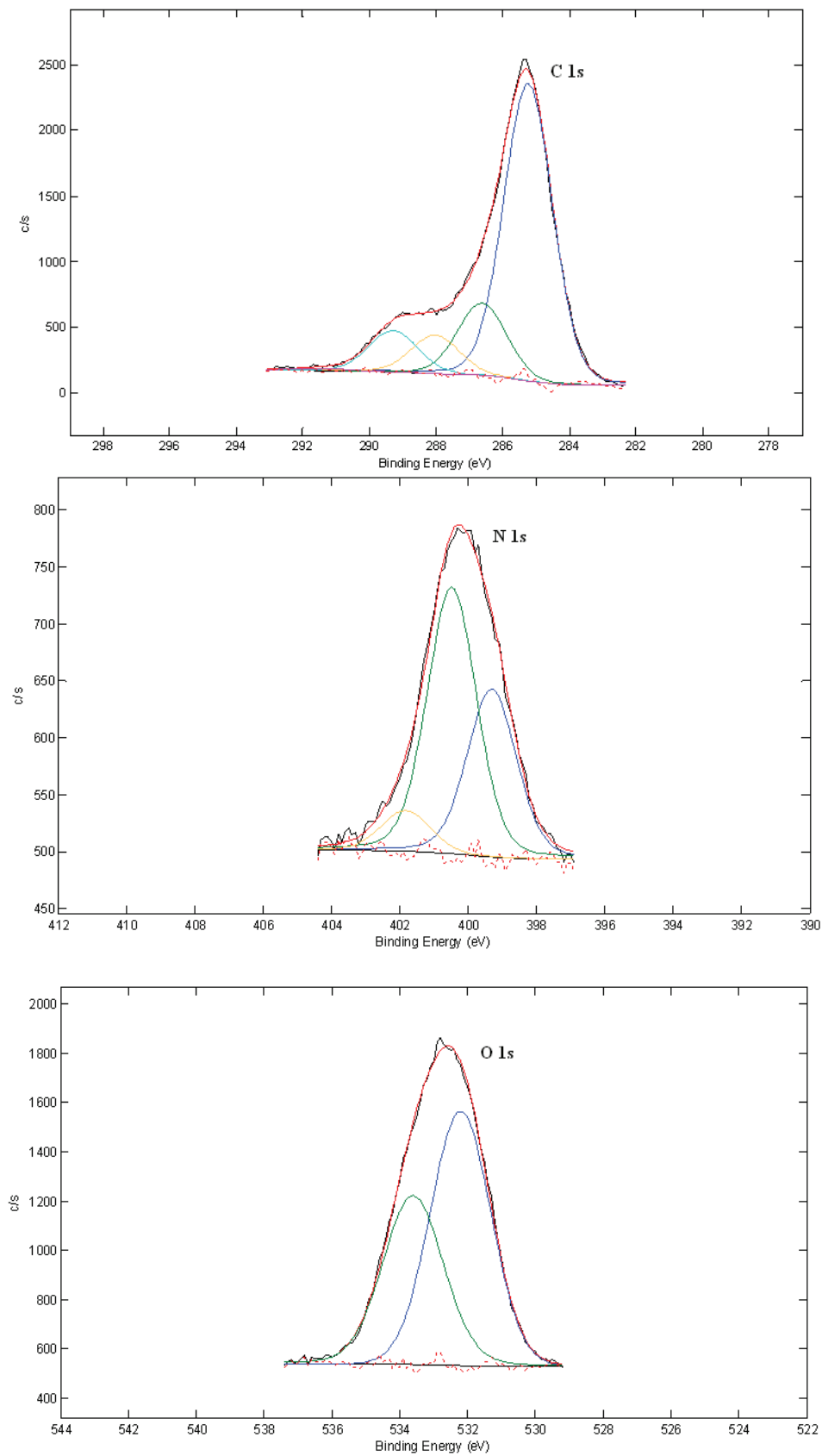


Figure 4.10 High resolution spectra of pyrrole plasma (1800 W 45 s) treated T700/CNT fibers

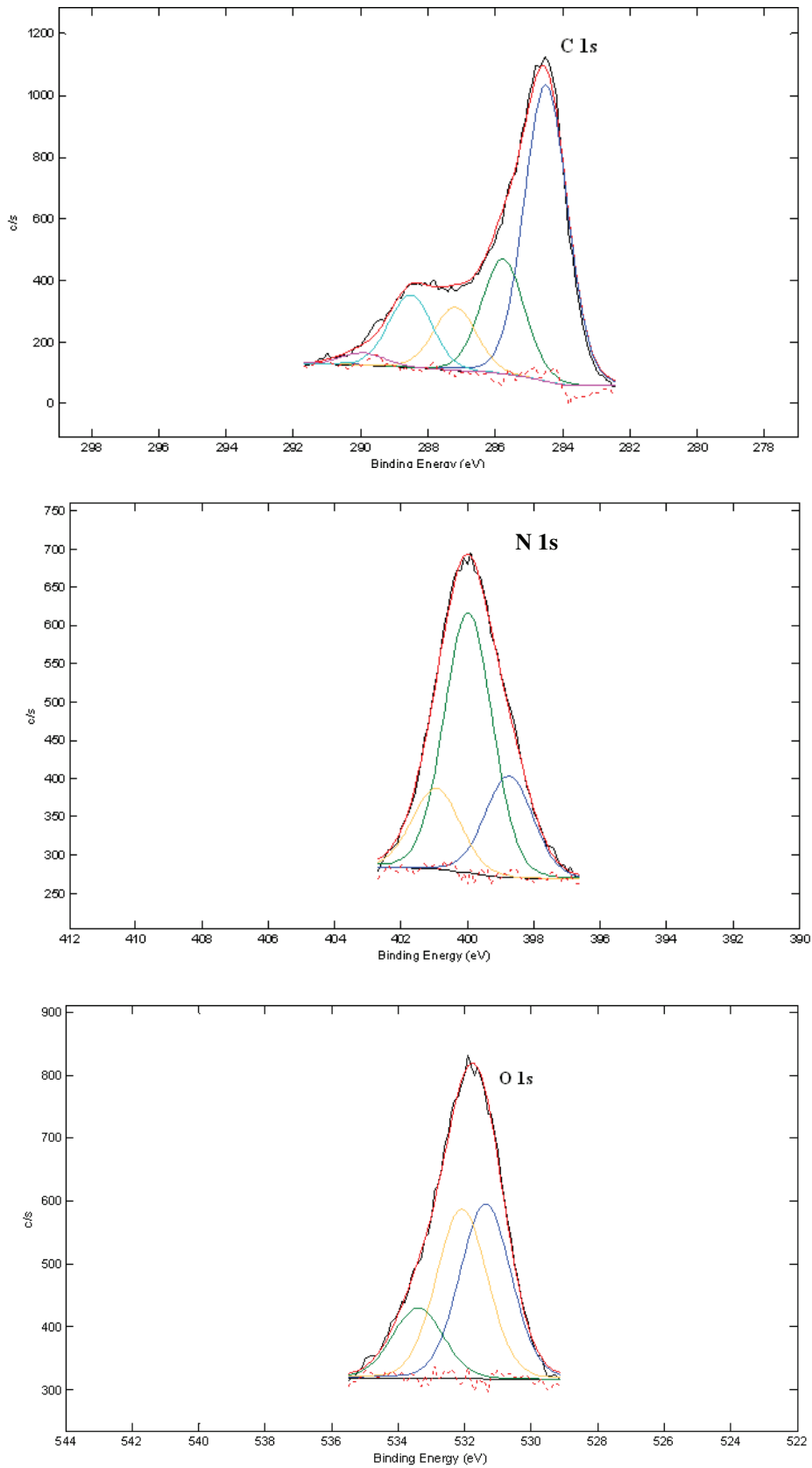


Figure 4.11 High resolution spectra of pyrrole plasma (1400 W 45 s + dopant) treated T700/CNT fibers

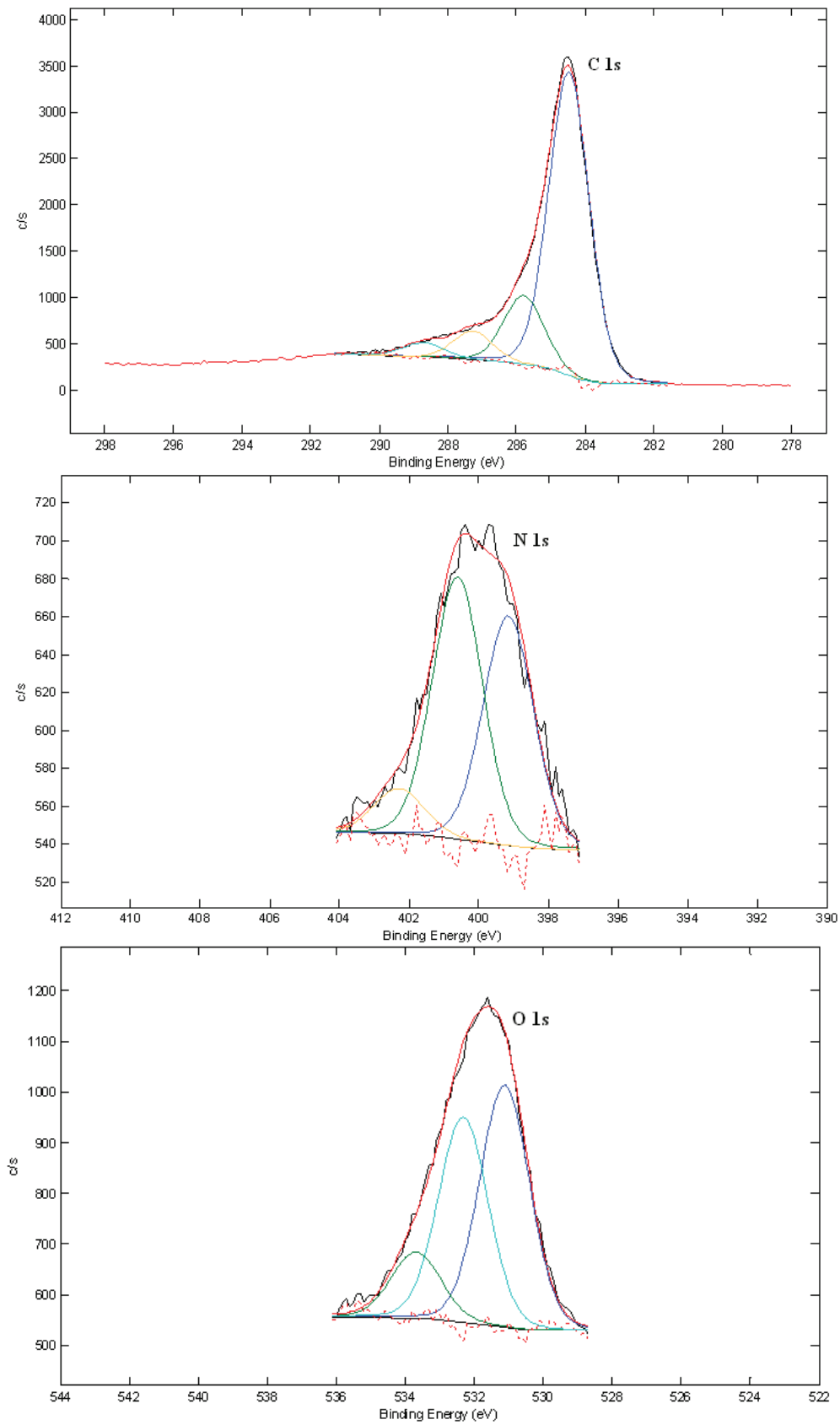


Figure 4.12 High resolution spectra of untreated AS4 fibers

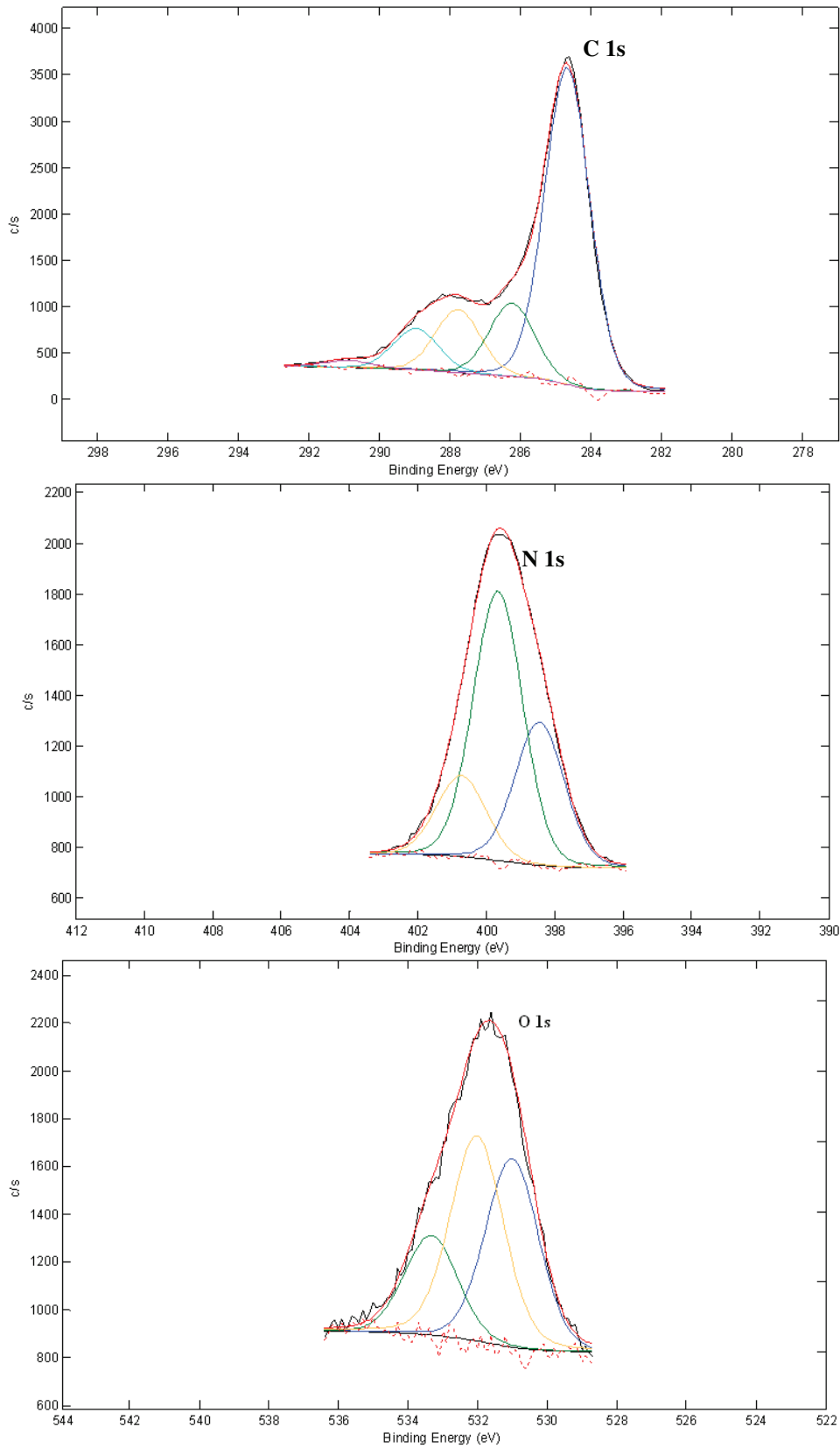


Figure 4.13 High resolution spectra of AS4 fibers treated at 1400 W 45 s + dopant

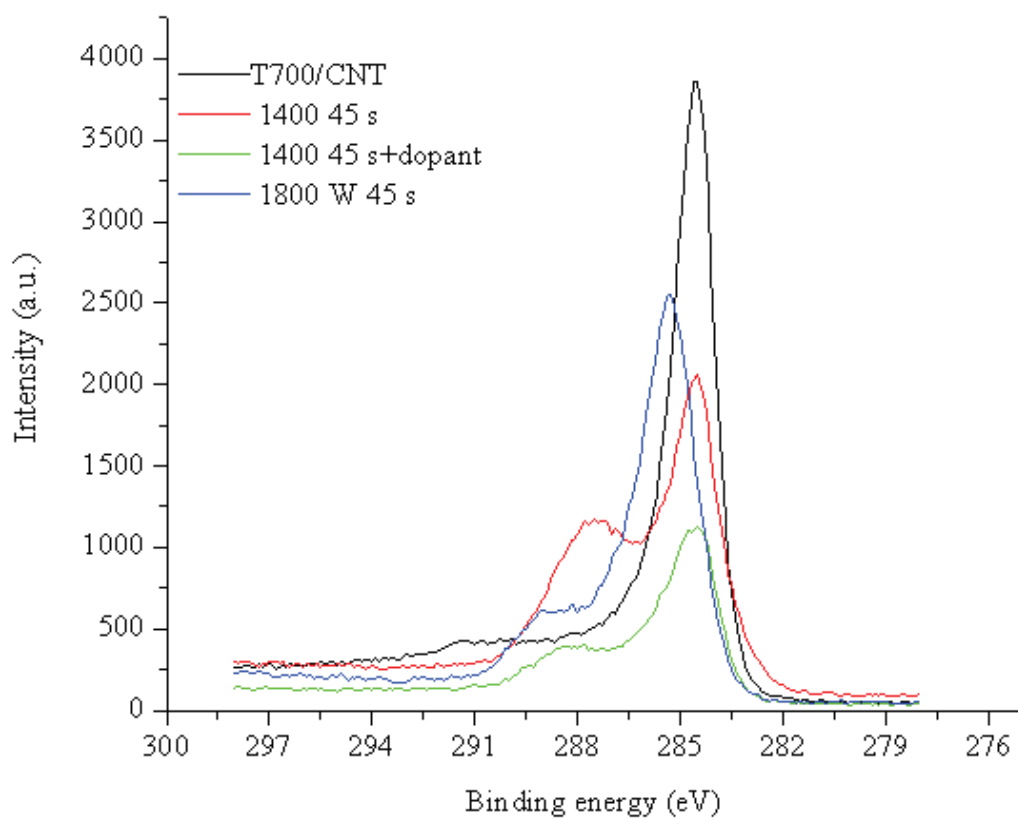


Figure 4.14 Comparison of XPS C 1s core level spectra of plasma treated T700/CNT fibers at different plasma conditions

## *1.2 Results of SEM*

The SEM micrographs of plasma treated T700/CNT fibers vary between 2 kX and 50 kX and are shown in Figures 4.16-4.19. Two different micrographs, one of which corresponds to the highly dense part and the other to loosely covered part of untreated T700/CNT fibers are given in Figure 4.15. It should be noted that these two morphologies are often observed in untreated T700/CNT fibers throughout the study. The difference between the homogeneity of deposited nanotubes also reflects the homogeneity differences in plasma treated T700/CNT fibers. The SEM micrographs presented in Figure 4.19 were taken from the different perspectives in order to show the morphological differences between the plasma polypyrrole deposited and untreated T700/CNT fibers. The diameter of nanotubes on the untreated T700/CNT fibers was ranging between 8-10 nm. The diameter of carbon nanotubes on 1400 W 45s, 1400 W 60s, 1800 W 45s, and 1400 W 45s+dopant pyrrole plasma treated T700/CNT fibers were 12-16 nm, 17-23 nm, 16-19 nm, and 10-16 nm, respectively. Thus, the deposited plasma polymer can be seen on the carbon nanotubes, with thickness ranging from 2-13 nm, clearly covering the surface of carbon nanotubes and its agglomerates. Almost all pyrrole plasma treated T700/CNT samples were exhibited tiny spherulites which is one of the common morphology observed in plasma polymerized [79, 80] and electrochemically polymerized polypyrrole [101]. Since the deposited layer was not as thick as that was reported in literature, the tiny spherical formations of polypyrrole may not be as same as in those micrographs given in literature [79, 80]. On the other hand, the plasma polymerization of pyrrole on AS4 fibers clearly indicates the polypyrrole spherulites (20-180 nm) formed on these fibers (Fig. 4.20a). In the plasma polymerization of pyrrole (+dopant), these tiny spherulites become smaller (20-60 nm) most likely due to the presence of dopant which affect the reactions in the post-discharge and result in different morphology (Fig. 4.20b). Highly different morphology was observed on AS4 fiber which was treated at 1400 W 90s (Fig. 4.21b). The reason of the ablated layer of polypyrrole could be explained by the CAP (competitive ablation polymerization) mechanism [94].

At longer exposure times, whatever the power, the deposited polymer was removed from the fiber surface indicating that the effect of exposure time. AS4 fiber which was also treated for 90 s at 1800 W, in addition to the ablated layer (similar to 1400 w 90 s treated AS4), substantial spherical formations was also observed in place of detached layer probably due to the ongoing plasma exposure (Fig. 4.21c).

The structure of deposited polymer on T700/CNT and AS4 fibers may not be ideal polypyrrole as typically observed in electrochemically polymerized polypyrrole, but it may contain cross-linking as expected from the plasma polymers [102]. The possibility of trapped oligomers in the polymer, the presence of amorphous carbon deposits on carbon nanotubes due to CVD process and the agglomerated carbon nanotubes on T700/CNT fibers might also be contributed to the morphological differences observed on these micrographs. The plasma polypyrrole that was formed under the applied conditions can be explained by the diffusion controlled nucleation growth at the surface of the material [95]. In the case of T700/CNT fibers, the carbon nanotubes on the fiber surface possibly serve as nucleation sites during the pyrrole polymerization on T700/CNT fibers.



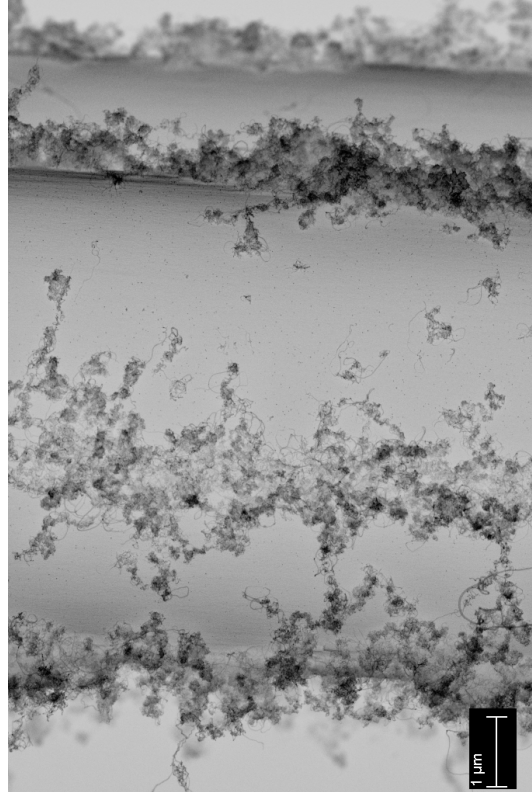
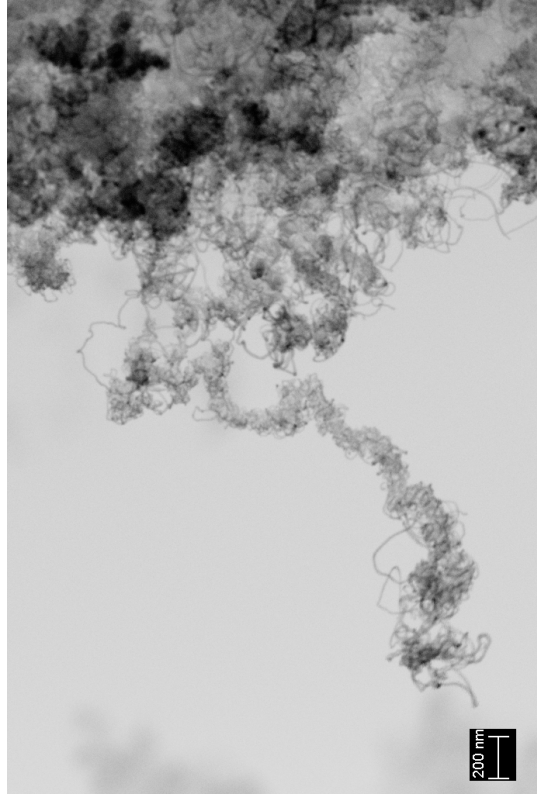
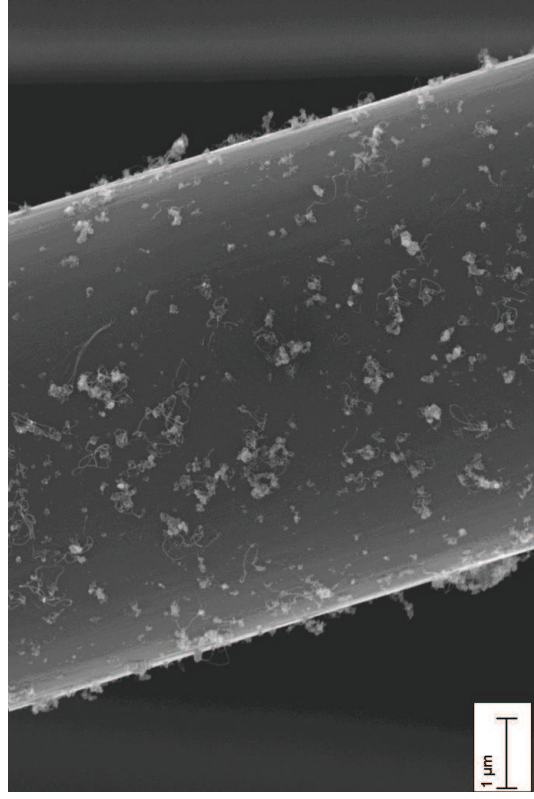
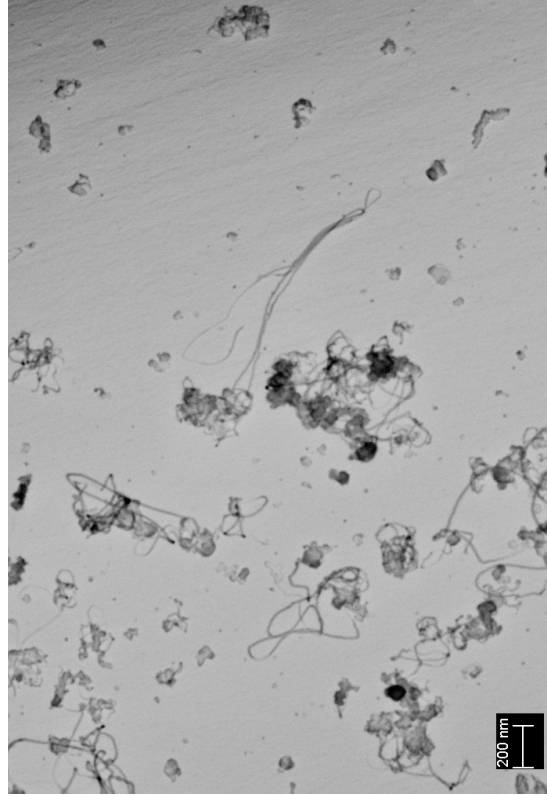


Figure 4.15 SEM micrograph of untreated T700/CNT fibers

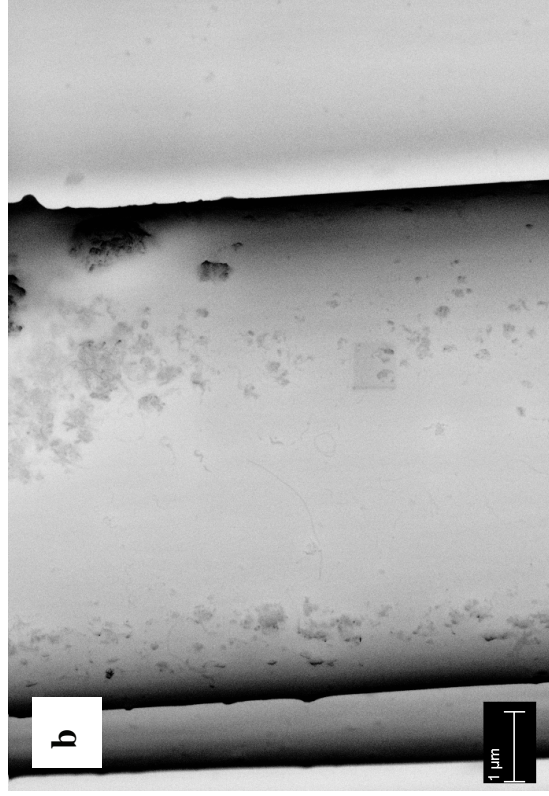
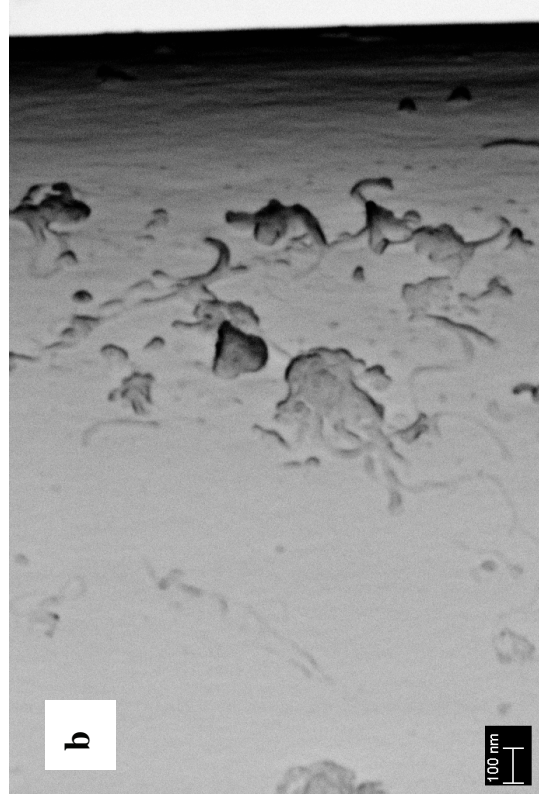
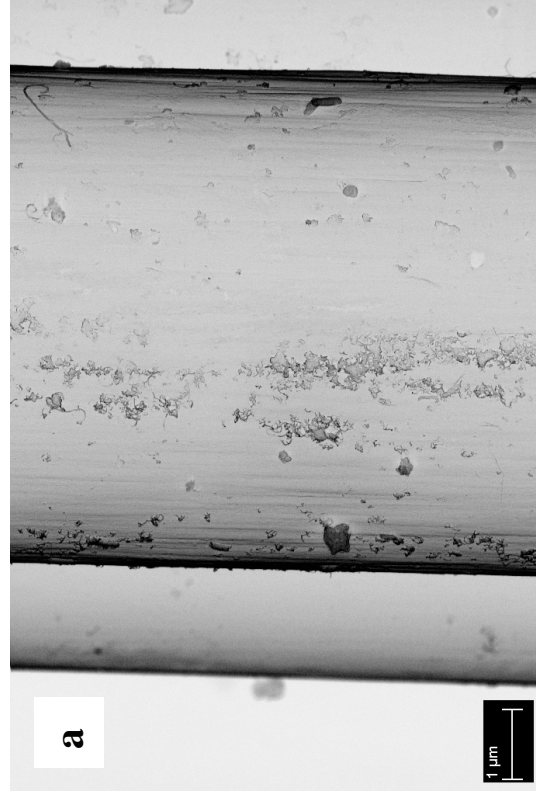
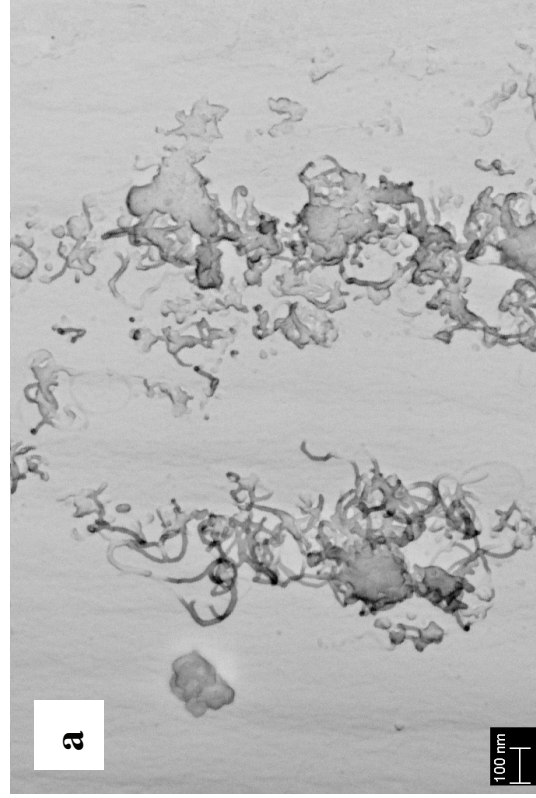


Figure 4.16 SEM micrograph of pyrrole plasma treated T700/CNT fibers, a) 1400 W 45s, b) 1400W 60s



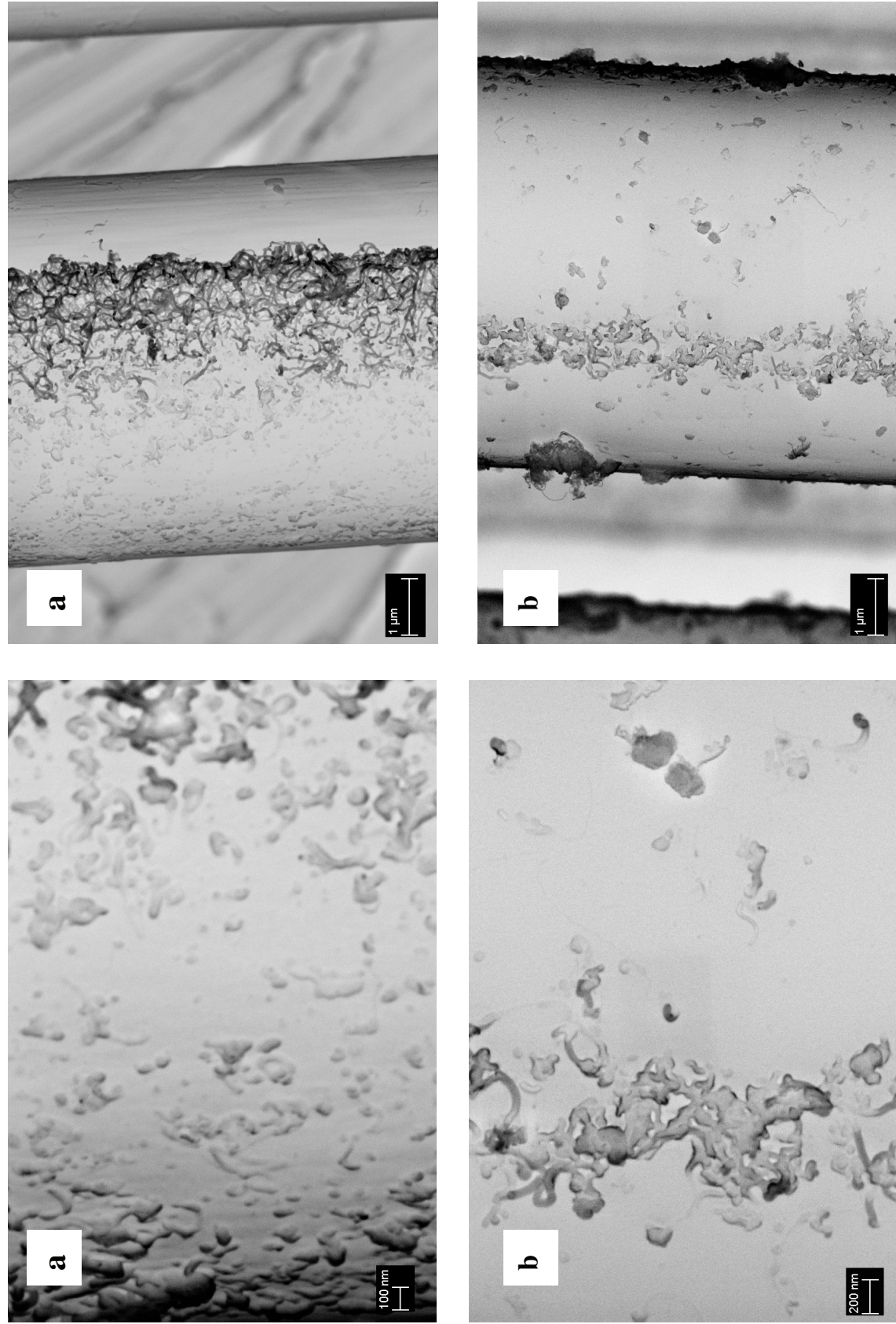


Figure 4.17 SEM micrograph of pyrrole plasma treated T700/CNT fibers, a) 1800 W 45s, b) 1800 W 60s

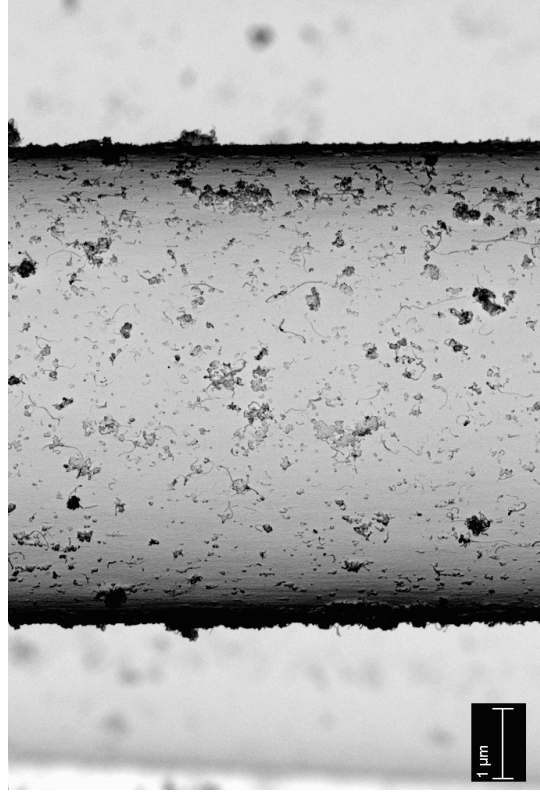
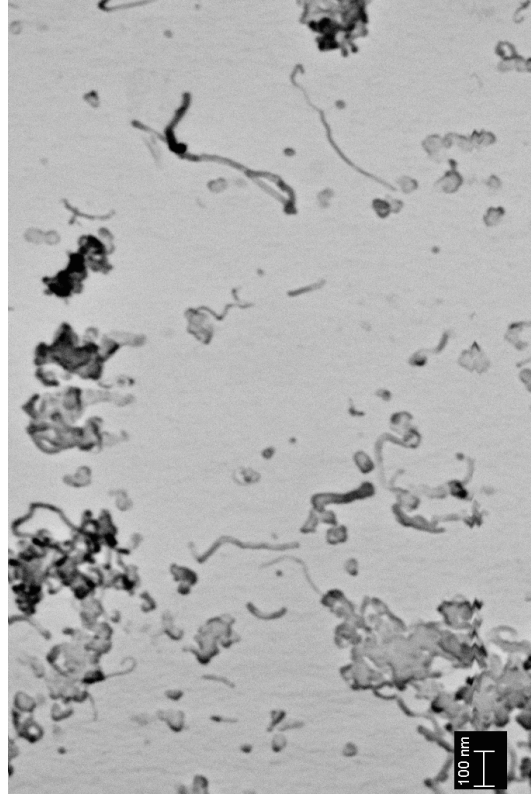


Figure 4.18 SEM micrograph of pyrrole plasma treated T700/CNT fibers at 1400 W 45s +dopant



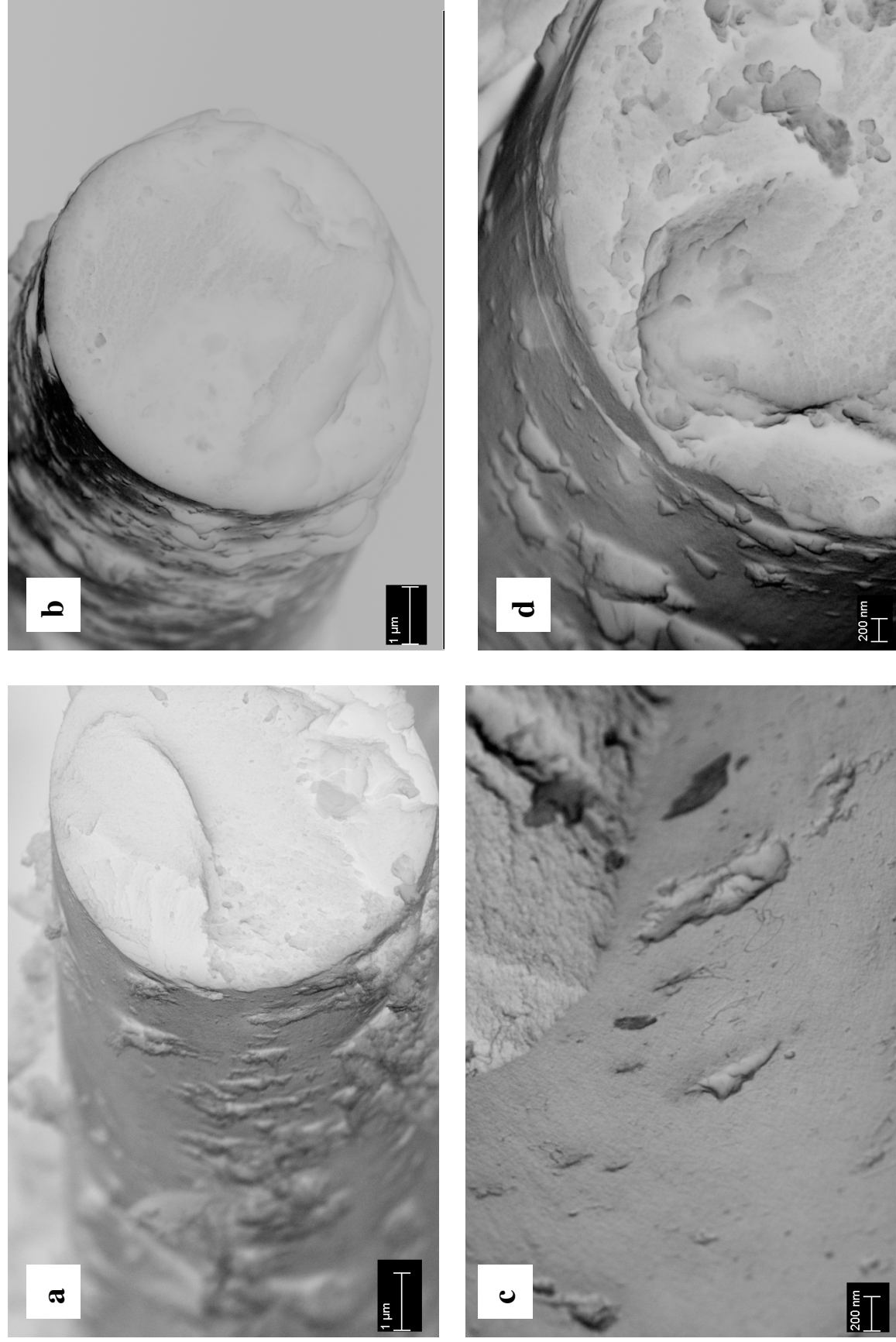


Figure 4.19 SEM micrograph of T700/CNT fibers, a) untreated, b) 1400 W 45 s c) 1400W 45s + dopant, d) 1800 W 45s

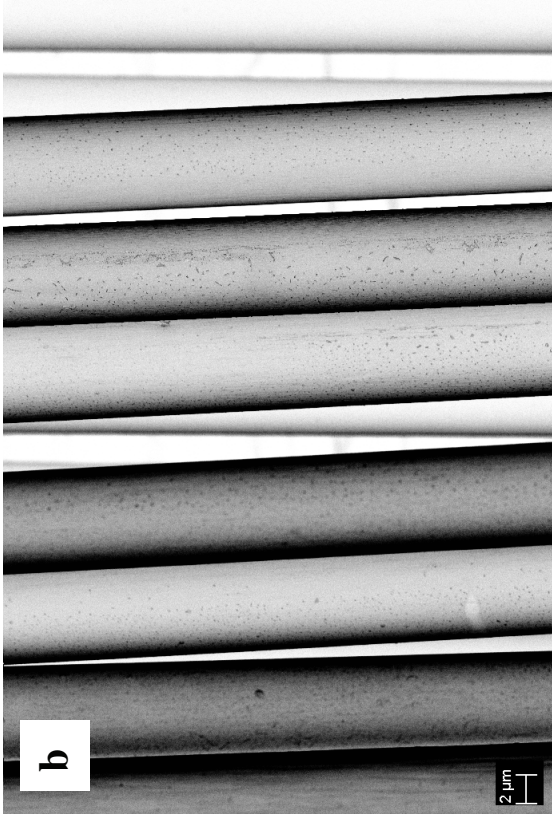
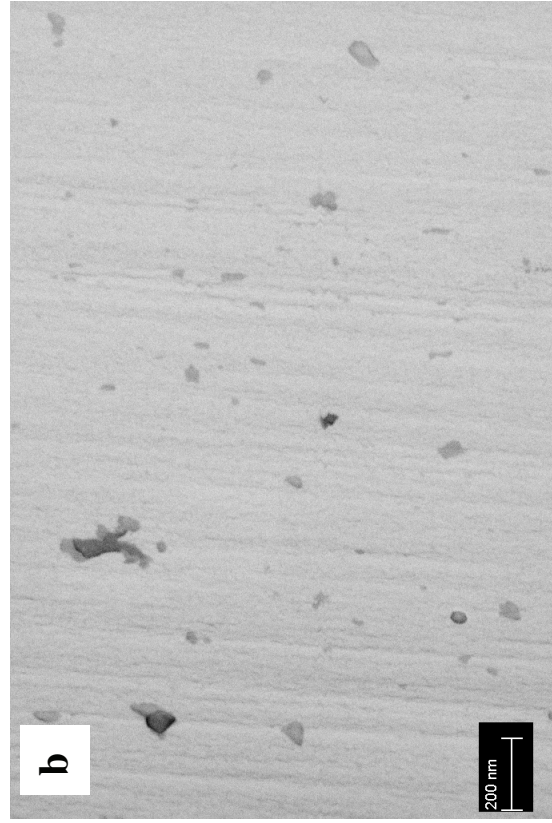
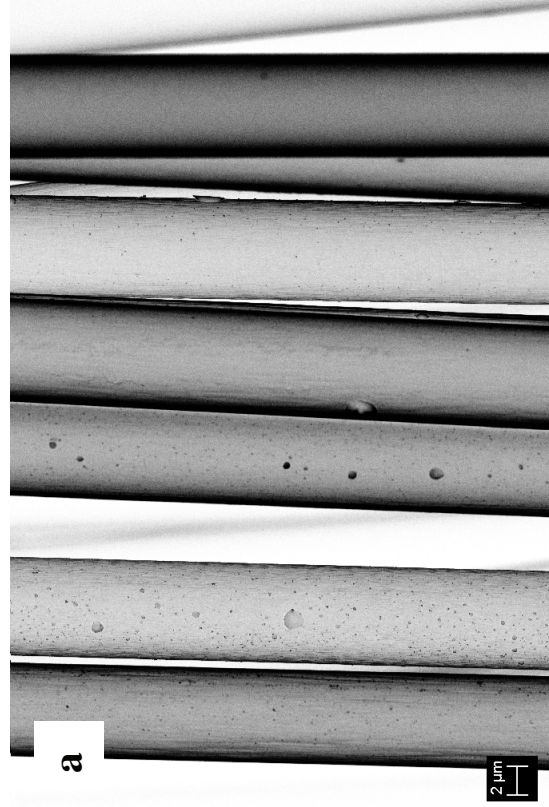
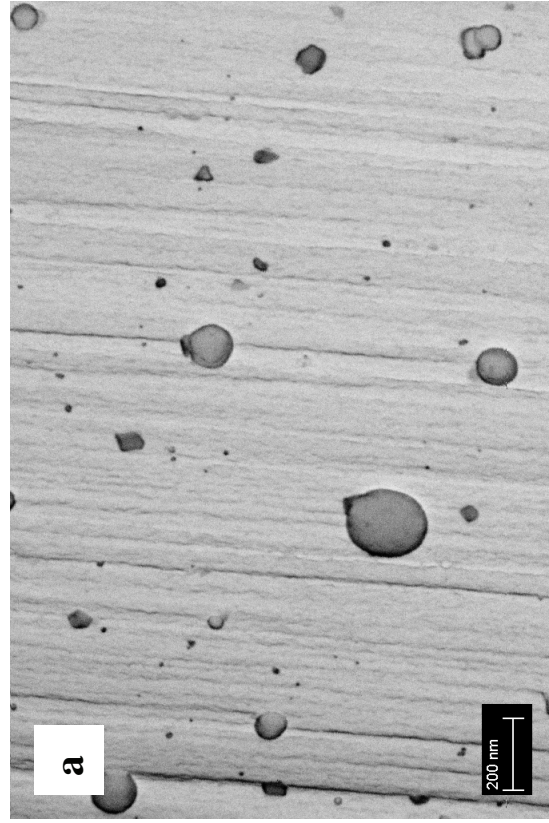


Figure 4.20 SEM micrograph of plasma treated AS4 fiber treated a) 1400 W 45 s (50 kX, 2kX), b) 1400 W 45 s + dopant (50 kX, 2kX)



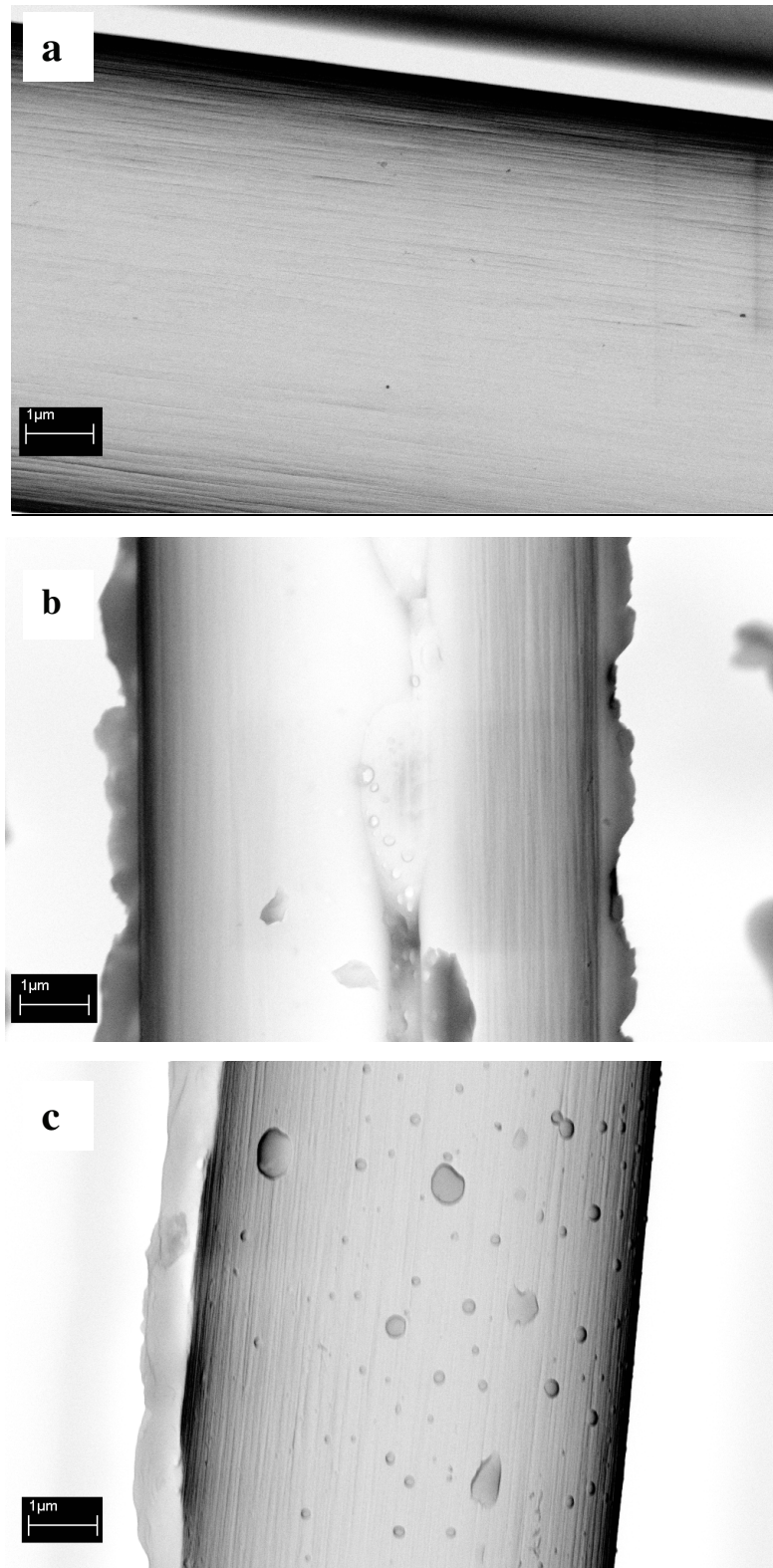


Figure 4.21 SEM micrograph of AS4 fibers, a) untreated, b) 1400 W 90 s, c) 1800 W 90s

### 1.3 Results of AFM

Roughness analysis of T700/CNT was performed by using the partial image rather than the full image of the samples. Partial images were taken from the flat part of the fiber in order to avoid wrong assessment of the roughness value. Hence, neither the fine globular structure of polymer [79, 80] nor the deposits on carbon nanotubes were chosen as a reference point for the measurements. In this respect, three measurements were recorded by positioning small squares (i.e. reference measurements) on totally flat part of each fiber. These measurements were repeated on at least two filaments from each fiber bundle. The increase in surface roughness can be followed in Fig. 4.22. Table 4.4 summarizes the results of the roughness analysis of plasma treated T700/CNT by means of RMS (root-mean-square average) and  $R_a$  (arithmetic average) as obtained from the AFM images. Figures 4.23-4.24 show AFM images of the curved portion of untreated and plasma treated T700/CNT fibers, respectively. Comparison of the AFM images for untreated and plasma treated samples shows that after the subsequent plasma treatments the surface topography may change on a microscopic scale. The results obtained indicated that the  $R_a$  and RMS values were 1.08 and 0.85 for untreated T700/CNT fibers, respectively. The AFM image of 1800 W 45 s treated T700/CNT fiber was shown a significant increase in roughening compared to untreated T700/CNT fiber. Namely, the fiber surface became rougher with ~3.6 times that of the T700/CNT fiber. Besides, the lowest increase (from 1.08 nm to 2.53 nm) was observed for 1400 W 60 s which corresponds to 2.3 times of the T700/CNT fiber roughness. The increase observed in surface roughness compared to untreated T700/CNT fiber may provide more contact points between fiber and matrix due to the increased surface area (i.e. increased roughness). It is believed to be beneficial for their application as reinforcement in composites [96]. In this respect, the mechanical properties were further analyzed by means of ILSS and flexural strength and discussed in Chapter V.



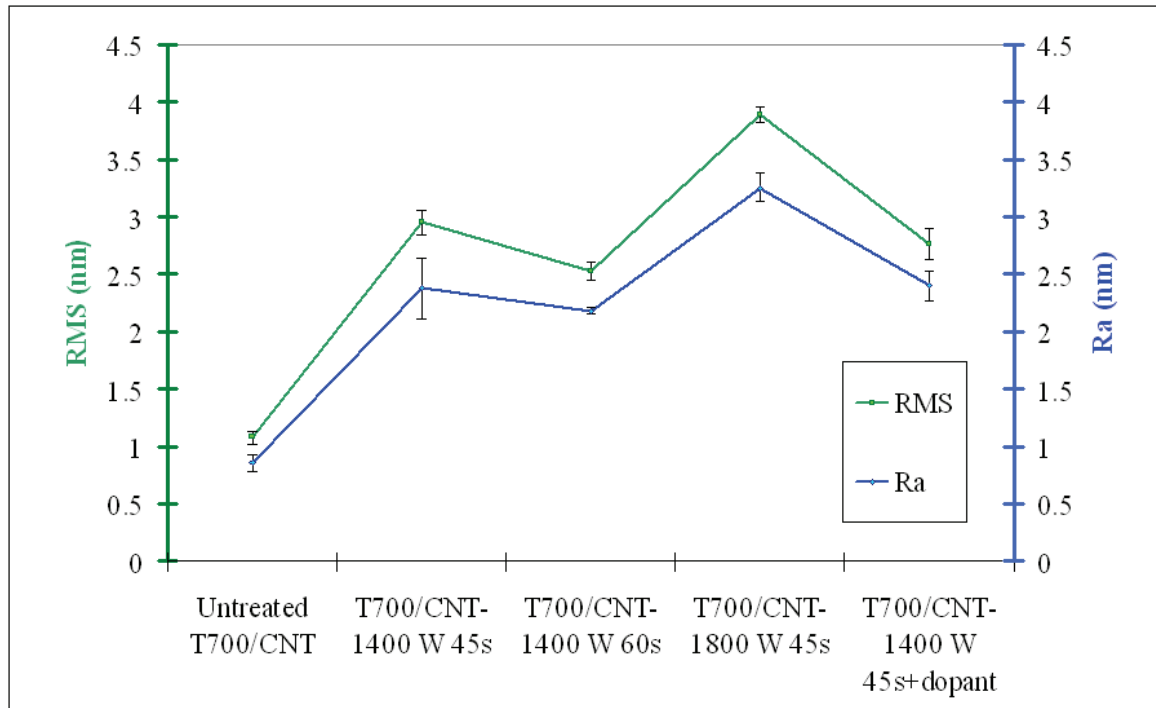


Figure 4.22 Comparison of roughness parameters of T700/CNT fibers treated at different plasma conditions

TABLE 4.4 Roughness values of T700/CNT fibers treated at different plasma conditions

Fiber	Precursor	Plasma conditions	RMS (nm, 2 $\mu\text{m}$ x 2 $\mu\text{m}$ )	Ra (nm, 2 $\mu\text{m}$ x 2 $\mu\text{m}$ )
T700/CNT	Untreated	-	1.0804 $\pm$ 0.0556	0.8582 $\pm$ 0.0697
	Pyrrole	1400 w 45 s	2.9526 $\pm$ 0.1106	2.3775 $\pm$ 0.2682
		1400 w 60 s	2.5297 $\pm$ 0.0795	2.1837 $\pm$ 0.0348
		1800 w 45 s	3.8882 $\pm$ 0.0631	3.2535 $\pm$ 0.1246
		1400 w 45 s	2.7673 $\pm$ 0.1356	2.3994 $\pm$ 0.1286

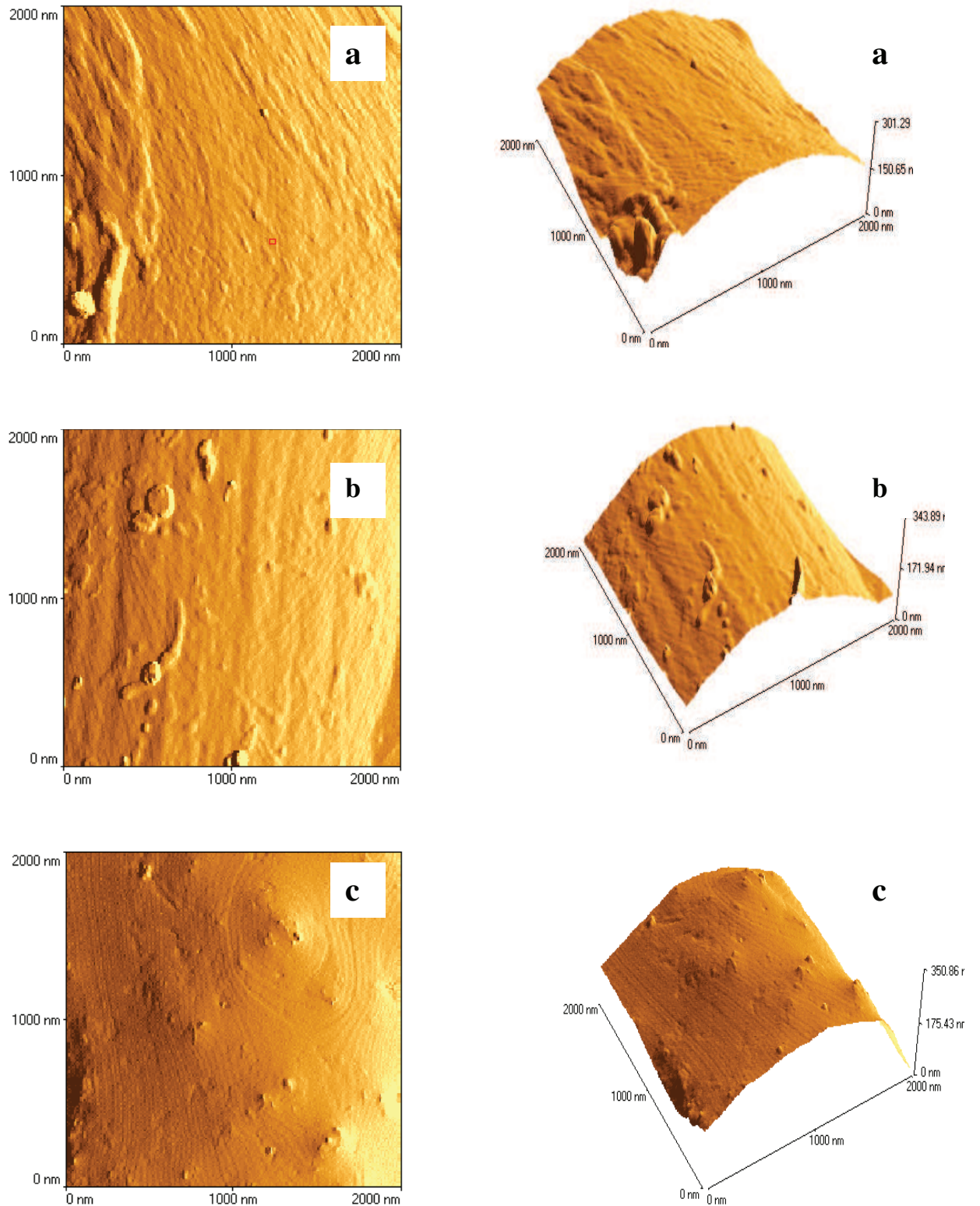


Figure 4.23 2D and 3D AFM image of AS4 fibers, a) Untreated , b) 1400 W 45 s c) 1400 W 60 s

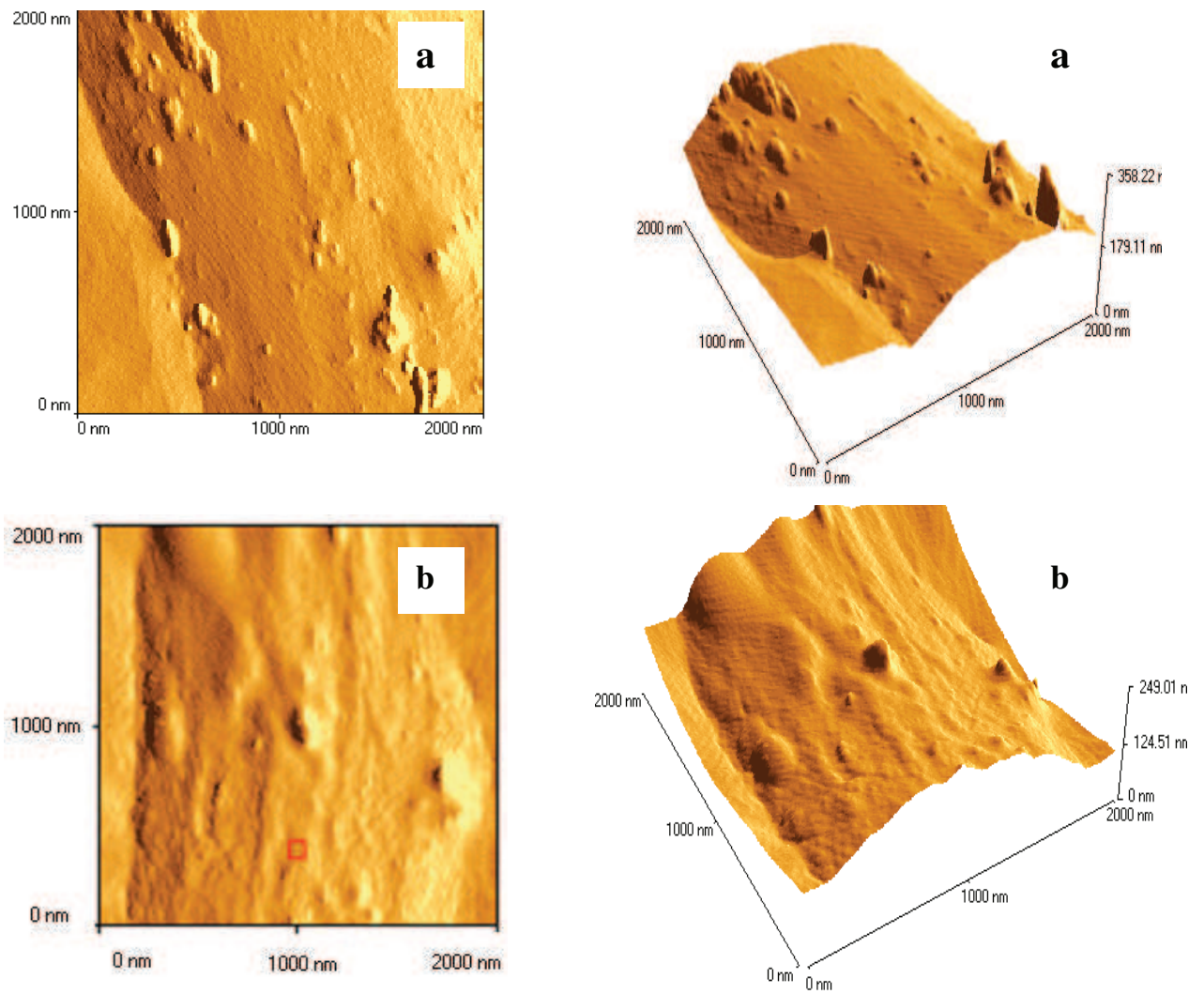


Figure 4.24 2D and 3D AFM image of T700/CNT fibers, a) 1400 W 45 s + dopant, b) 1800 W 45 s

### 1.4 Thermogravimetric analysis (TGA)

TGA was employed to study the thermal properties of the plasma polypyrrole deposited T700/CNT by using a thermal analyzer. In order to study the oxidative modes of thermal change, T700/CNT fibers were analyzed at constant heating rate (10 °C/min) in nitrogen atmosphere. Thermal stabilities of plasma treated fibers are compared in Figure 4.25. The amount of deposited polymer on T700/CNT fibers was calculated by using a simple equation as follows:

$$m_{polymer} = m_{total} (X_1 - X_2)$$

where  $m_{polymer}$  is the amount of deposited polymer (mg)

$m_{total}$  = total amount of sample in the creuse (mg)

$X_2$  = max. weight loss of plasma treated sample (wt.%)

$X_1$  = max. weight loss of untreated sample (wt.%)

TGA results show the trend in the change of decomposition process of deposited polymer on fibers as a function of temperature up to 900 °C. Usually plasma polymers began to lose weight at low temperatures (250-300 °C) [103]. Within the same period of time, compared to untreated T700/CNT fibers, all plasma pyrrole treated samples began to lose weight with relatively fast rate up to 400 °C which suggests the loss of polymeric structures [81, 104]. The weight loss between 300 and 600 °C was attributed to evolution of CO<sub>2</sub> due to decomposition of functional groups (e.g. carboxyl compounds) [105]. With keeping in mind the surface chemical structure, which was identified in XPS spectrum, the higher the amount of carbonyl, alcohols, and ether compounds the lower the stability of deposited polymer. Thus, the highest weigh loss was observed in 1400 W 45 s pyrrole + dopant plasma treated sample probably because of the presence of less stable polymer than that of other plasma treated samples. Besides, 1400 W 45 s, 1400 W 60 s and 1800 W 45 s plasma pyrrole treated samples lose weight almost at the same rate. The weight loss observed between 600 and 900 °C probably corresponds to the carbonyl and hydroxyl groups forming CO [105].

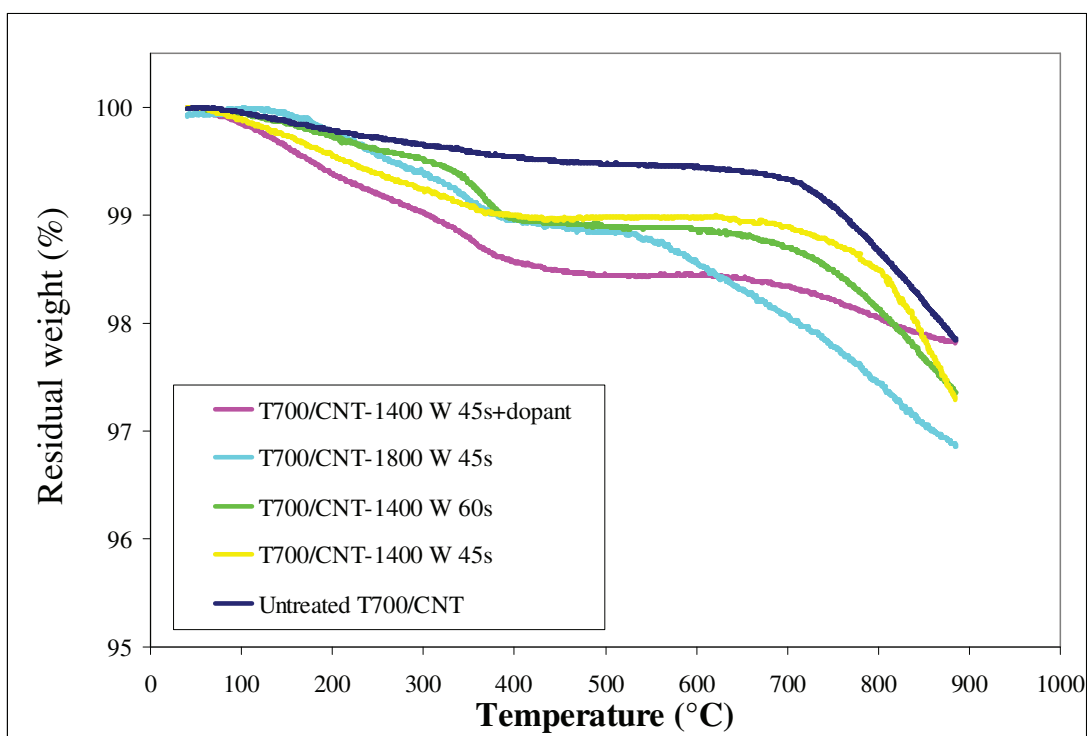


Figure 4.25 TGA thermograms of T700/CNT fibers treated at different plasma conditions

TABLE 4.5 The values of maximum weight loss and calculated amount of polymer on fibers around 900 °C

Fiber	Precursor	Plasma conditions	Weight loss (wt-%)	Amount of deposited polymer (mg)
T700/CNT	Untreated	-	2.155	
	Pyrrole	1400 w 45 s	2.716	$1.75 \times 10^{-2}$
		1400 w 60 s	2.650	$1.91 \times 10^{-2}$
		1800 w 45 s	3.139	$2.11 \times 10^{-2}$
	Pyrrole + pTSA.H <sub>2</sub> O	1400 w 45 s	2.182	$1.27 \times 10^{-3}$

## 2 Conclusion

The polymerization process of pyrrole is based on quite new process (post-discharge DBD, see Chapter II) compared to the conventional plasma polymerization processes (RF, MW, vacuum, etc). Therefore, finding the most suitable conditions for plasma polymerization of pyrrole in post-discharge as well as the characterization of plasma polypyrrole coated fibers are the important aspects of this work.

From low to high powers (1400 W to 1800 W), it has been observed that the plasma polypyrrole polymers tend to lose the memory of its monomeric structure due to the loss of  $\alpha$ - and  $\beta$ -carbons in pyrrole ring. This kind of change might be due to more ring opening reactions and high loss of nitrogen-containing species at higher power levels. Additionally, this sharp change was not observed at low power (independent of exposure time (45 s or 60 s)).

All results, which were gathered from the different characterization techniques, proved the possibility of plasma polypyrrole deposition under the carefully designed conditions (refer to Chapter II, III). Further, compared to unmodified carbon fibers, plasma polypyrrole deposition may also be beneficial for their application as reinforcement in composites (discussed in Chapter V).

## Chapter V

# Characterization of plasma treated carbon fiber/epoxy composites





## *Introduction*

This chapter focuses on the characterization of mechanical and electrical properties of untreated and plasma polypyrrole treated AS4 and T700/CNT/epoxy composites as well as untreated T700GC/epoxy composites. Mechanical properties of composites were determined by three-point bending tests and electrical properties were evaluated by the electrical resistance measurements in three different configurations. In order to test those properties carbon fiber/epoxy (Hexcel M21) prepregs were manufactured by vacuum bag method as described in Chapter II Section 4.

Flexural strength and ILSS tests were conducted to determine the healing effect of plasma surface treatment performed on carbon fibers. ILSS results show the degree of compatibility of fiber to matrix. Flexural strength shows in a way the degree of surface flaws and stress concentration points impregnated during plasma treatment. As it is known, flexural strength of a composite is controlled by the tensile strength of the fiber and by the adhesion between fiber and matrix which is assumed to be describable by ILSS.

The longitudinal and transversal (through-width and through thickness) electrical resistance of carbon fiber/composites (DC,  $\omega=0$ ) were measured in order to calculate the electrical resistivity of composites by using different locations of electrodes. For composites, electrical conductivity is dependable on the orientation of the carbon fibers. In longitudinal direction, current flow along the carbon fibers and it is affected by the number of conducting fibers. In transversal directions, the density of fiber to fiber contact points and percolation effect of filler are the important parameters.

## *1 Mechanical properties of plasma treated carbon fiber/epoxy composites*

Carbon fibers do not have only single crystal nature like graphite whiskers which make them highly flaw sensitive. The flaws on the fiber surface can be eliminated and healed to improve the mechanical properties of fibers by a number of different methods. It is known that fracture in brittle materials initiated by tensile stresses far below the intrinsic strength of the material due to these surface irregularities. These irregularities may be eliminated either by decreasing the volume of the material or by healing including plasma surface modification technique for adhesion promotion in composites [109, 110].

As it was confirmed by XPS analyses, pyrrole and pyrrole/dopant (pTSA.H<sub>2</sub>O) plasma depositions are capable of producing functional groups (e.g. CN, COC) on T700/CNT and AS4 carbon fibers and these functional groups may react with epoxy, resulting in an increase of interfacial bond-strength between fiber and epoxy matrix. Also, the deposited layers may help to fill the surface flaws and micro crazes and cracks that may exist at the surface of those carbon fibers which may provide enhanced adhesion between fiber and epoxy. In order to understand the healing effect of the plasma treatment, ILSS and flexural strength of T700/CNT and AS4 epoxy composites were tested in this study.

It is noted that before the preparation of carbon fiber-reinforced composites, plasma treatment speed of carbon fibers was adjusted to 0.2 m/min. At that plasma treatment speed, each 12 cm-long fiber bundles were able to be treated continuously at the optimum exposure time (~40 seconds, see Chapter III). ILSS and flexural strength results obtained as a function of power input (1400 W and 1800 W) and precursor type (pyrrole or pyrrole/dopant) are presented in Figures 5.1 and 5.2. In the first group (black-white bar graphs), an increase was observed in both ILSS and flexural strength of plasma treated T700/CNT/epoxy composites with any plasma treatment compared to untreated T700/CNT/epoxy composites. The maximum improvement in ILSS and flexural strength of plasma treated T700/CNT/epoxy composites was found roughly 14% and 17%, respectively over untreated T700/CNT/epoxy composites. Also, an increase in ILSS and

flexural strength of 1800 W pyrrole plasma treated T700/CNT fibers were about 1% and 6% over untreated T700GC/epoxy composites. The fiber surface become increasingly rougher when the input power was increased to 1800 W as it was presented in AFM and SEM results (see Chapter IV). Increase in surface roughness should promote mechanical interlocking between the fiber and the matrix [111, 112]. Better resin-fiber contact (wettability) and formation of stronger Van der Waals forces by the removal of surface contaminants might also provide better mechanical properties [113]. On the other hand, the rest of the plasma treated T700/CNT/epoxy composites exhibited lower flexural and ILSS values than 1800 W pyrrole plasma treated T700/CNT fiber composites. This result can be due to the loss of oxygen-based functional groups at lower plasma powers (this result is confirmed by XPS) and the formation of a weak boundary layer between fiber surface and the matrix.

In the second group (grey-black bar graphs), a decrease in ILSS was observed in pyrrole+dopant plasma treated AS4 fiber composite compared to pyrrole plasma treated one. The same trend was also observed in T700/CNT/epoxy composites which were treated at the same plasma conditions (i.e.1400 W pyrrole and pyrrole/dopant). Due to change in chemical composition of the deposited thin film, larger surface flaws might not be healed extensively and interfacial contact between the plasma polymer and epoxy matrix may not be sufficient enough to provide better mechanical properties in pyrrole+dopant treated fiber composites. A slight increase was observed in flexural strength of 1400 W pyrrole plasma treated AS4 fiber/epoxy composites over 1400 W pyrrole+dopant plasma treated ones (from 1126 to 1230 MPa). Obviously, without dopant, pyrrole plasma treatment at 1400 W was provided better mechanical properties probably due to improved resin-fiber contact and stronger Van der Waals forces.

Finally, plasma treated T700/CNT composites (i.e. except dopant) are exhibited an increase in the ILSS and flexural strength which may be due to enhanced mechanical, chemical and/or reaction bonding [112] that formed better fiber-matrix interface. Increase in surface roughness may form improved mechanical interlocking, removal of surface contamination, existence of crosslinkings on the polymer surface, introduction of polar compounds on fibers and presence of reactive species (e.g. carboxylic functionalities)

which reacted with the matrix and increased the bond strength [113] and created a matrix-compatible structure on fiber surface.

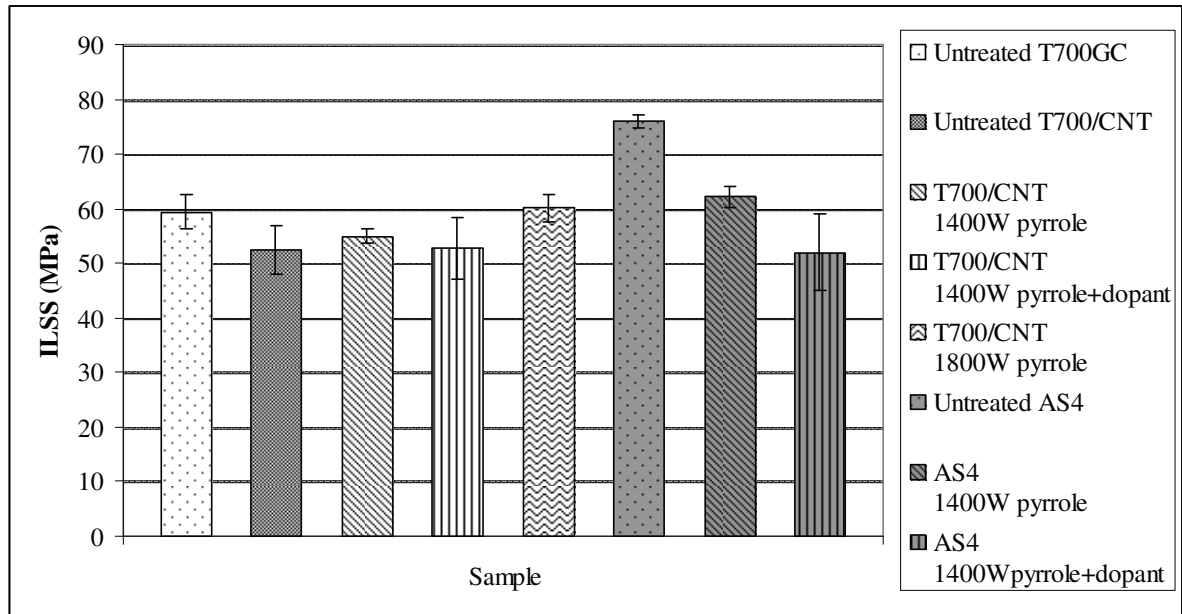


Figure 5.1 ILSS of plasma treated T700/CNT fiber/epoxy and AS4/epoxy composites (with illustrated monomers by plasma)

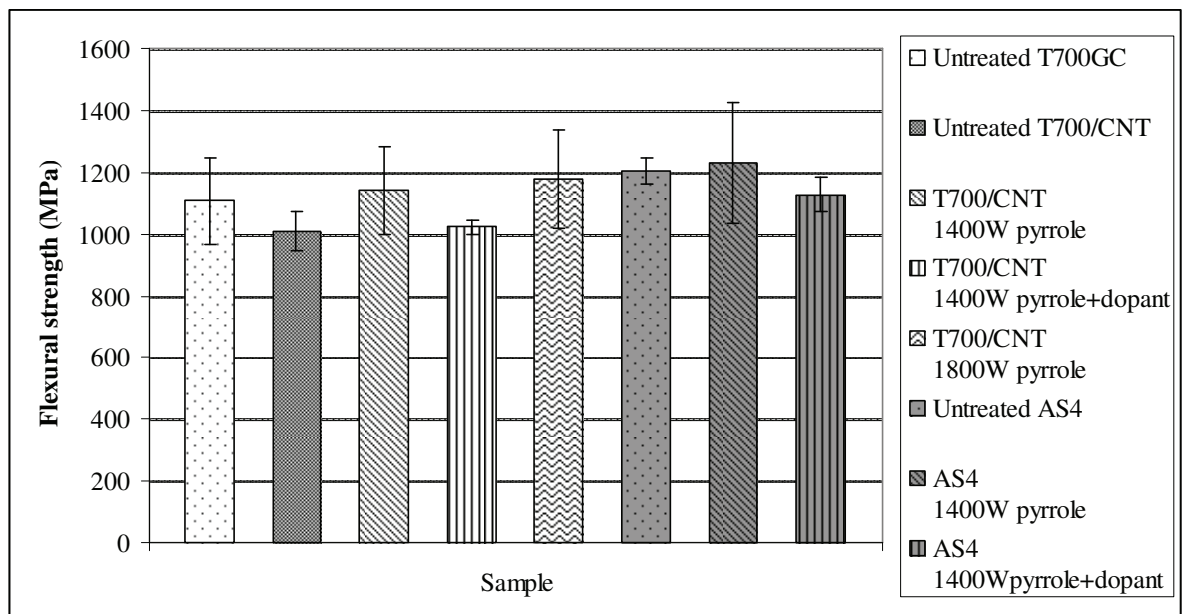


Figure 5.2 Flexural strength of plasma treated T700/CNT fiber/epoxy and AS4/epoxy composites (with illustrated monomers by plasma)

## *2 Results of SEM*

The topography of flexure surfaces of T700/CNT/epoxy and AS4/epoxy composites before and after plasma treatment was examined by Scanning Electron Microscopy (SEM) studies. SEM micrographs of T700GC/epoxy flexure surfaces were also taken to compare the effect of CNT grafting on T700 carbon fibers.

The whole fracture surfaces of each type of fiber/epoxy composites are shown at low magnifications (50-100 kX) in Figures 5.3-5.9. Fiber matrix interface in tension areas and fracture surfaces from compression areas are shown in Figures 5.10-5.15 and Figures 5.16-5.21, respectively. Those figures are also helpful in detecting how the fracture occurred containing both tensile and compressive failure among AS4/epoxy, T700GC/epoxy, and T700/CNT/epoxy composites. Through these micrographs, the boundary areas between compression-tension region and tensile and compressive failure regions as well as fiber buckling on the compressive side and delaminations in the interface layers can be seen as a result of flexural failure [114]. In general, it can be said that the failure starts in compression face, because the compressive strength of the material usually lower than the tensile strength [115-117], then it may be followed by delaminations between fiber/epoxy layers due to the shear and normal stresses [118].

The plasma pyrrole treated AS4 fiber/epoxy composites (Figs. 5.7, 5.13) showed less fiber pull out and somewhat good wetting of fiber compared to untreated AS4/epoxy (Figs. 5.5, 5.11) and pyrrole+dopant treated AS4/epoxy composites (5.14a and 5.14b). The fiber tips from those areas are the characteristic features of carbon fiber failing under tension. It can be said that the first fiber ruptures for those fibers appeared in the compression region followed by the delaminations occurred in the interface layers then reached to the tensile rupture of fibers.

Except plasma pyrrole+dopant treated T700/CNT/epoxy composites, all other T700GC and T700/CNT epoxy specimens in which the fibers submitted to tensile stresses did not break completely (Figures 5.3, 5.4, 5.6, 5.9). Therefore, it can be concluded that the main failure in those specimens occurs in compression. Increased fiber roughness of 1800 W pyrrole plasma treated T700/CNT fiber/epoxy composites



(confirmed by AFM) may promote mechanical interlocking (keying) mechanism between the fiber and matrix.

It can be suggested that by using pyrrole monomer without any feed of dopant may enhance the interfacial bond strength between T700/CNT fiber and epoxy due to the diffuse of atoms or molecules of treated fiber into the matrix at the interface [112]. For plasma pyrrole+dopant treated T700/CNT/epoxy composites, the brush-like appearance of the fracture surface and the fibers which pulled out of the resin are some of the signs of poor interfacial bonding (Figs. 5.8 and 5.15). It should also be noted that the voids in the matrix (air pockets) have an adverse effect on flexural properties and one cause of failure [112].



Figure 5.3 SEM micrograph of whole fracture surface of untreated T700/CNT fiber composite

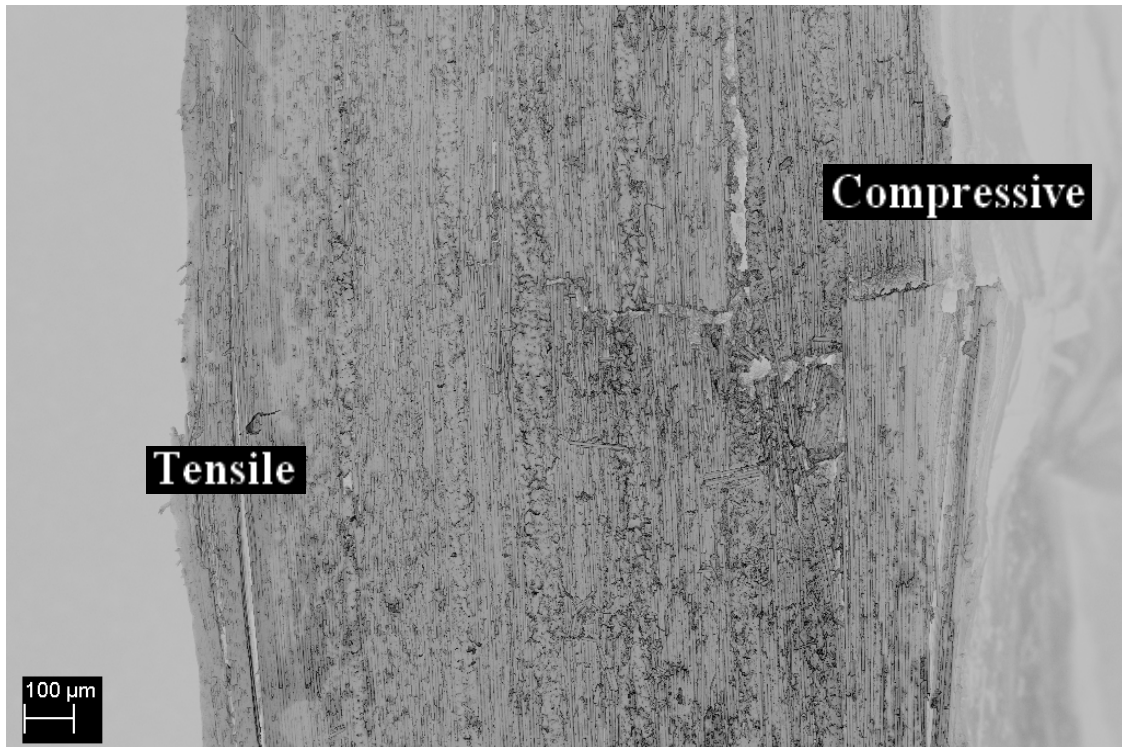


Figure 5.4 SEM micrograph of whole fracture surface of untreated T700GC fiber composite

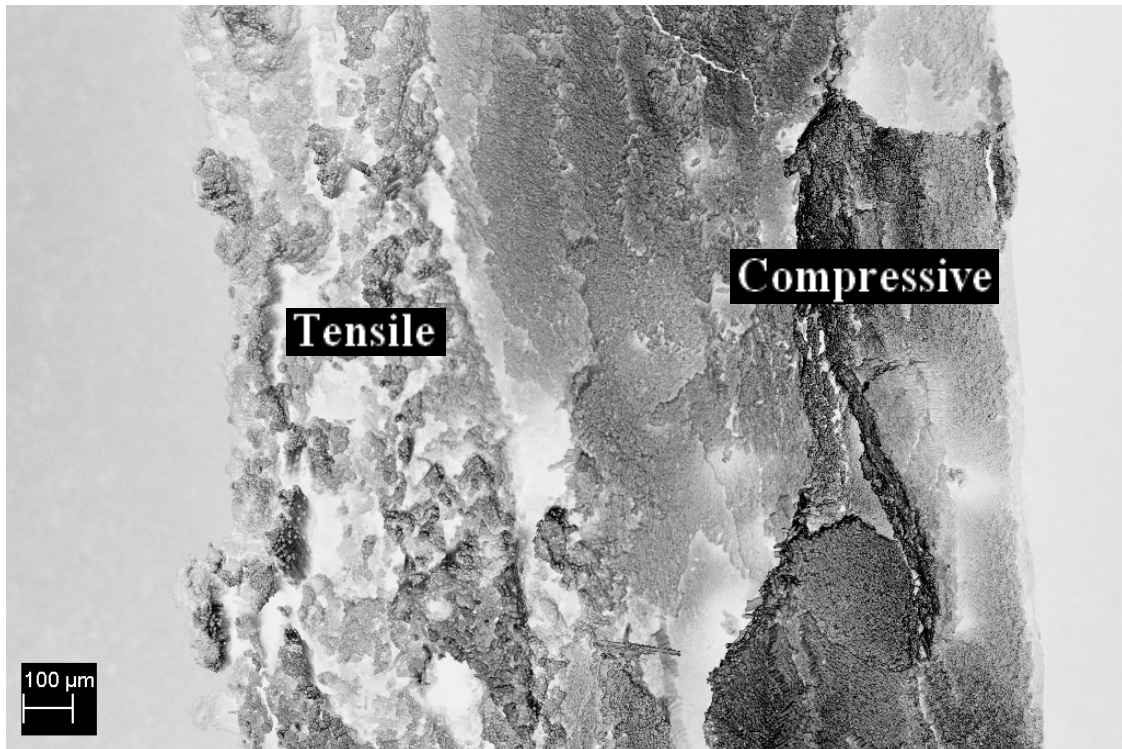


Figure 5.5 SEM micrograph of whole fracture surface of untreated AS4 fiber composite



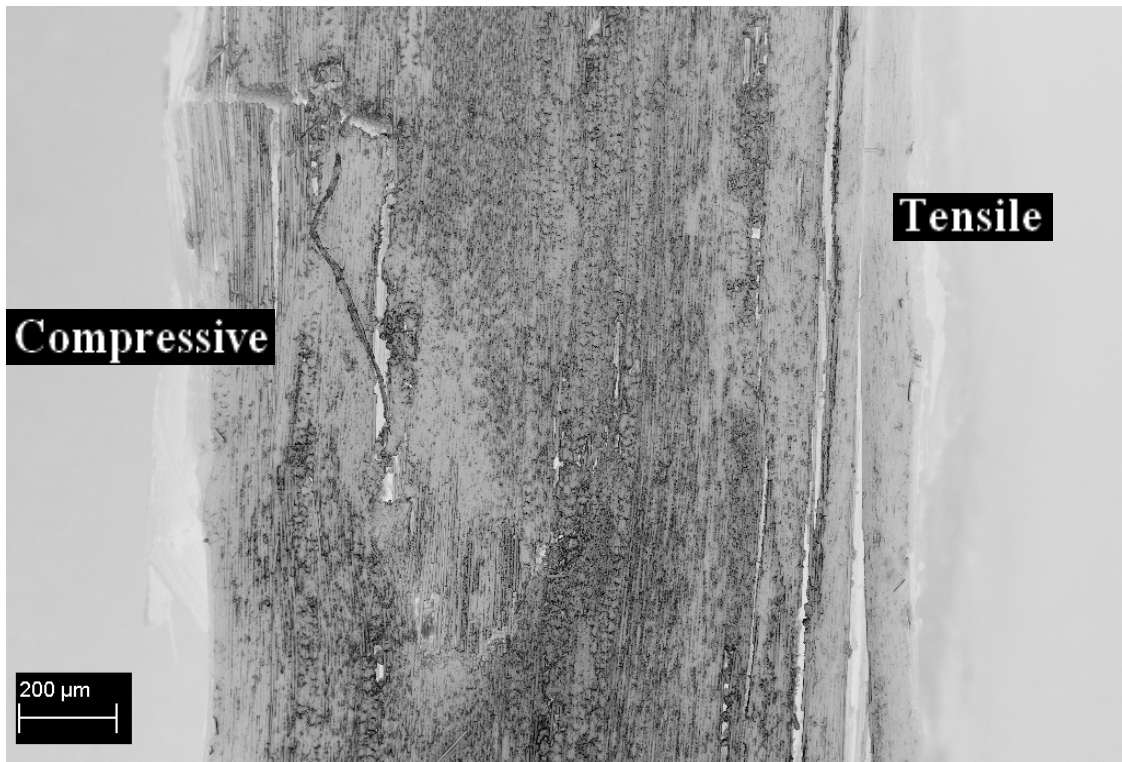


Figure 5.6 SEM micrograph of whole fracture surface of pyrrole (1400 W) treated T700/CNT fiber composite

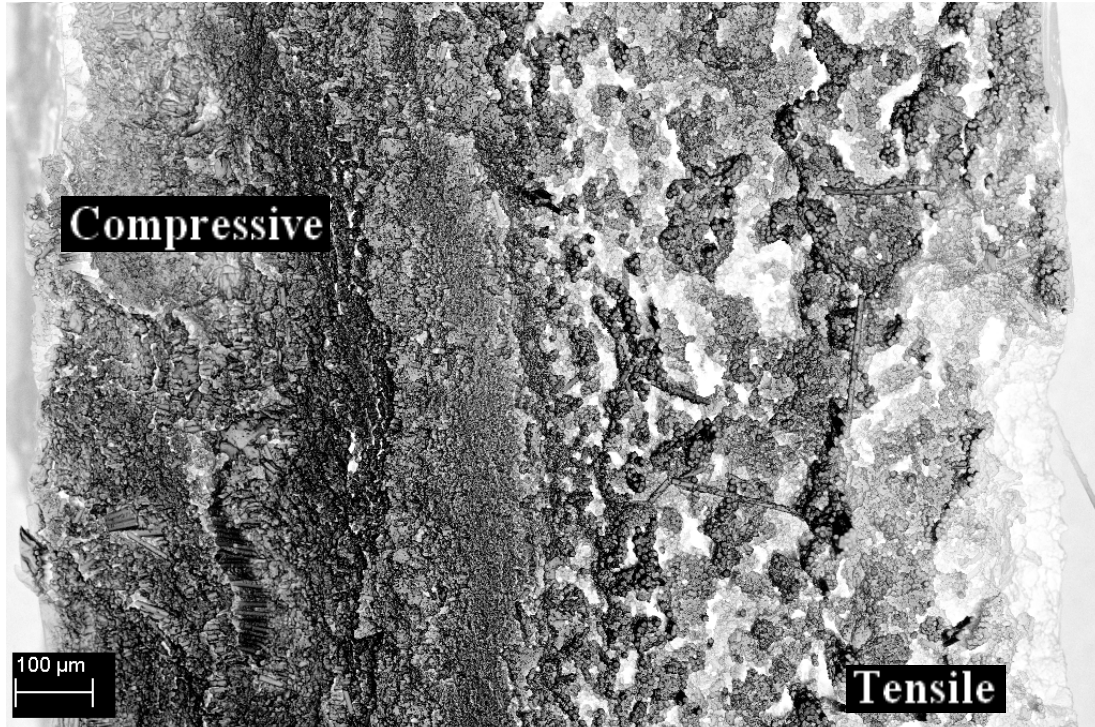


Figure 5.7 SEM micrograph of whole fracture surface of pyrrole (1400 W) treated AS4 fiber composite



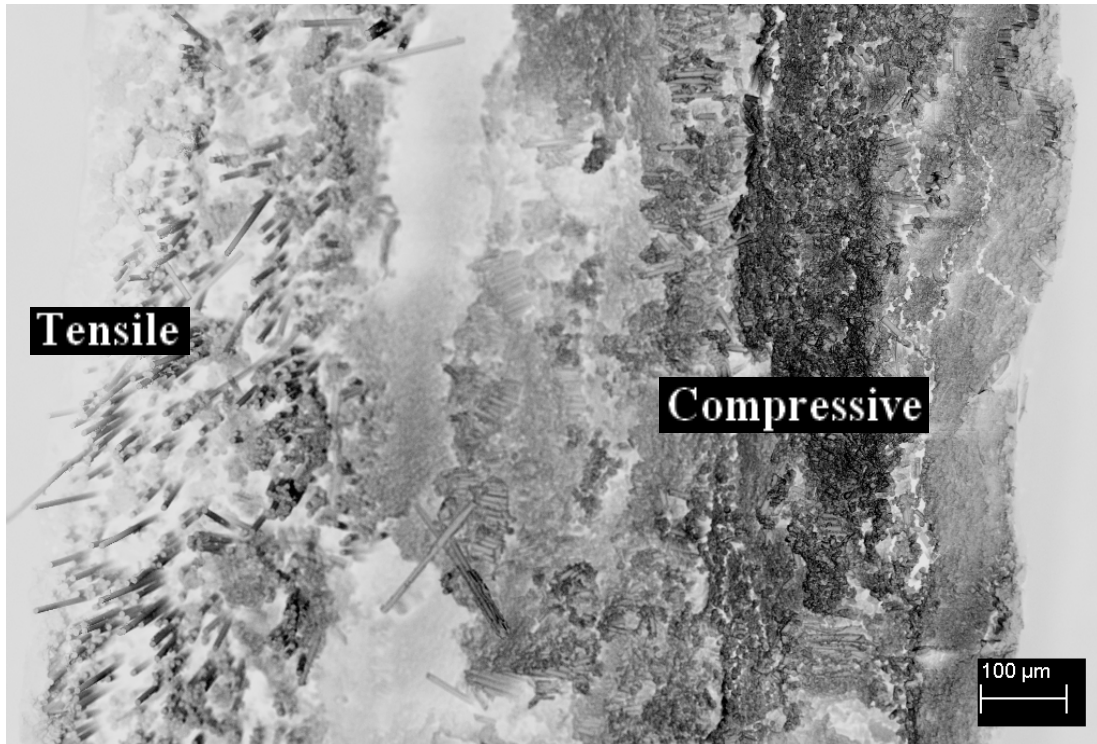


Figure 5.8 SEM micrograph of whole fracture surface of pyrrole+dopant (1400 W) treated T700/CNT fiber composite



Figure 5.9 SEM micrograph of whole fracture surface of pyrrole (1800 W) treated T700/CNT fiber composite

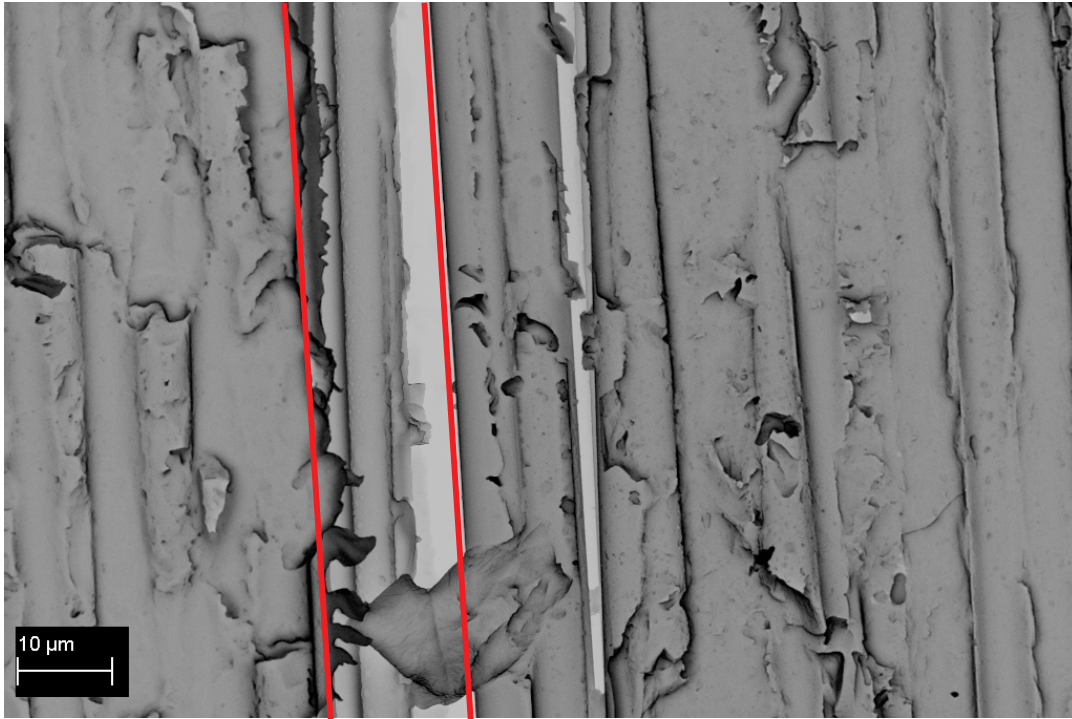


Figure 5.10 SEM micrograph of fiber matrix interface under tension for untreated T700 fiber epoxy composite (between two red lines)

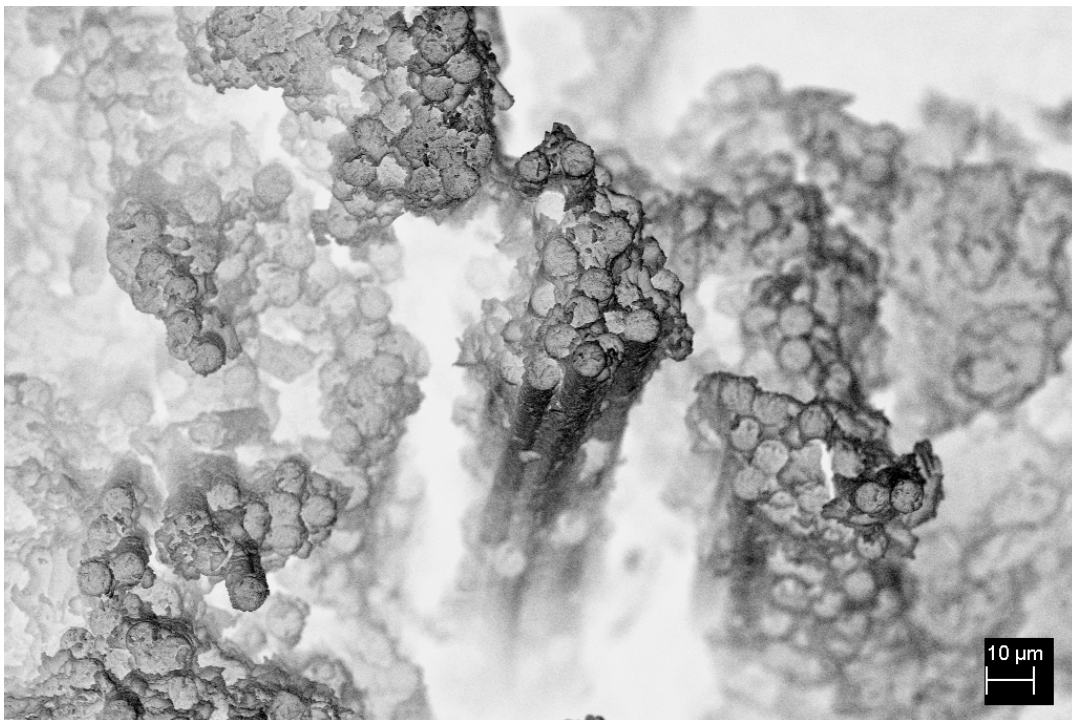


Figure 5.11 SEM micrograph of fiber matrix interface and fiber tips under tension for untreated AS4 fiber epoxy composite



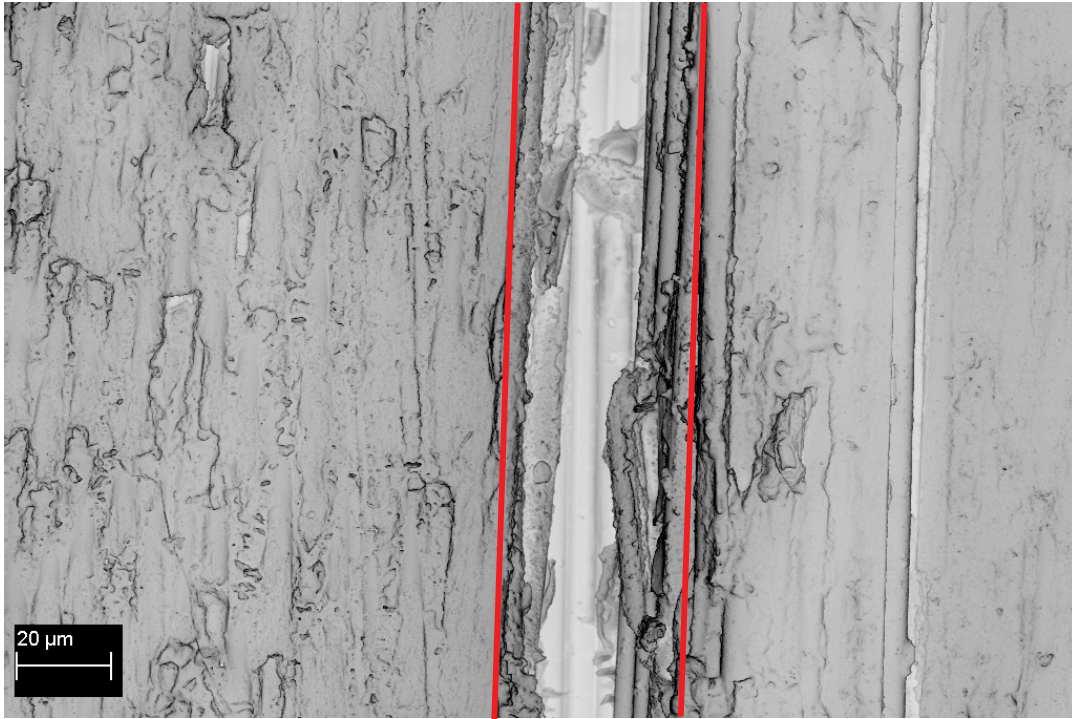


Figure 5.12 SEM micrograph of fiber matrix interface under tension for pyrrole (1400W) treated T700/CNT fiber epoxy composite (between two red lines)

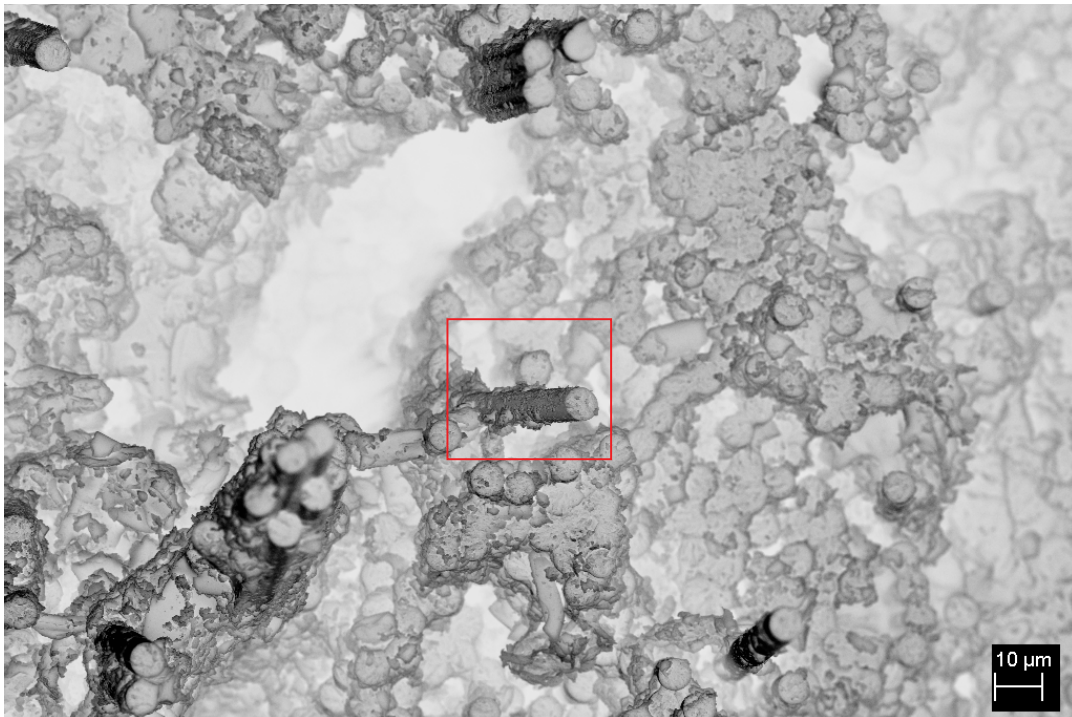


Figure 5.13a SEM micrograph of fiber matrix interface and fiber tips under tension for pyrrole (1400W) treated AS4 fiber epoxy composite (500X)

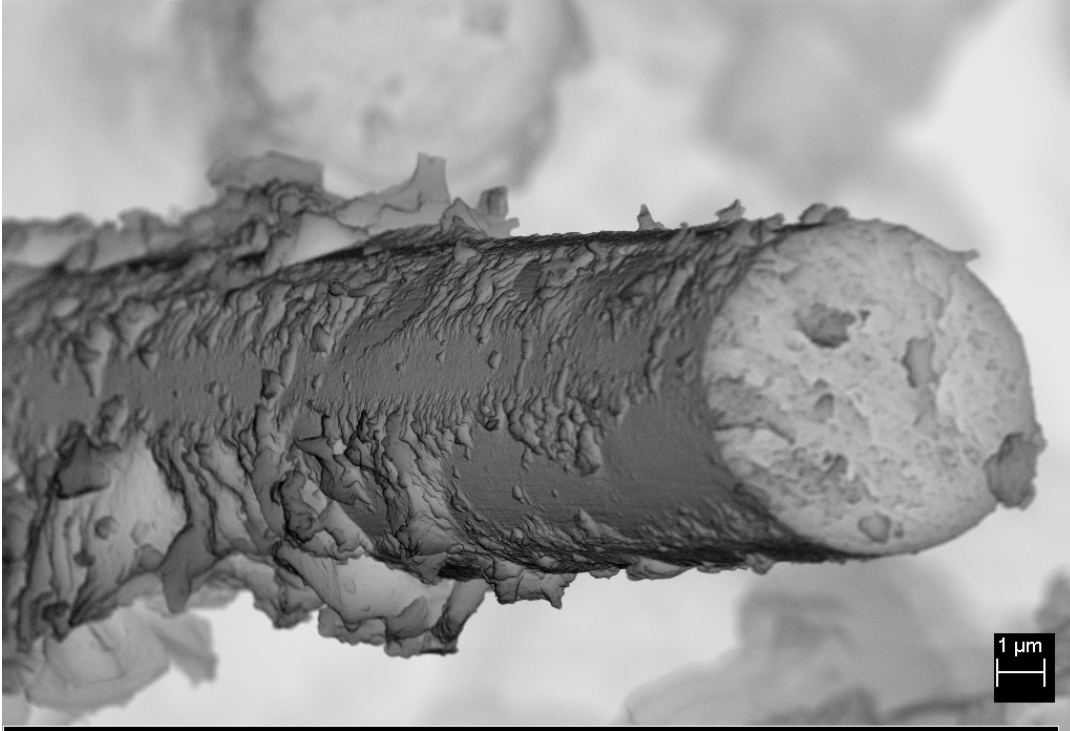


Figure 5.13b SEM micrograph of fiber tip with epoxy matrix from tension area of pyrrole (1400W) treated AS4 fiber epoxy composite (5kX)

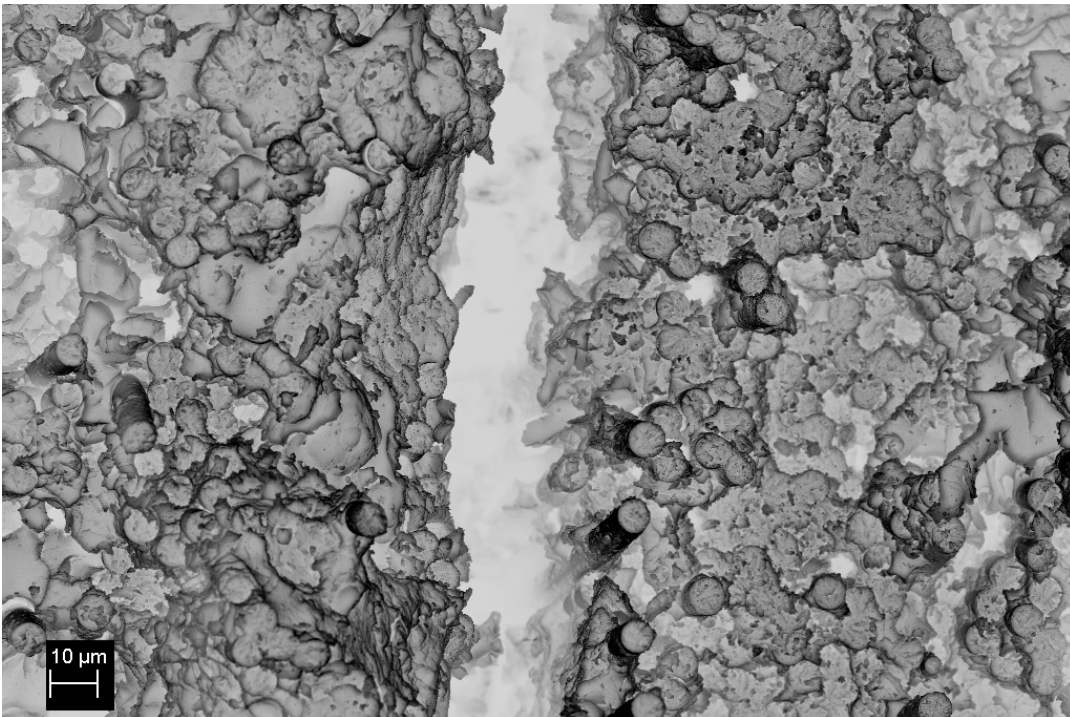


Figure 5.14a SEM micrograph of fiber matrix interface and fiber tips under tension for pyrrole+dopant (1400W) treated AS4 fiber epoxy composite (500X)



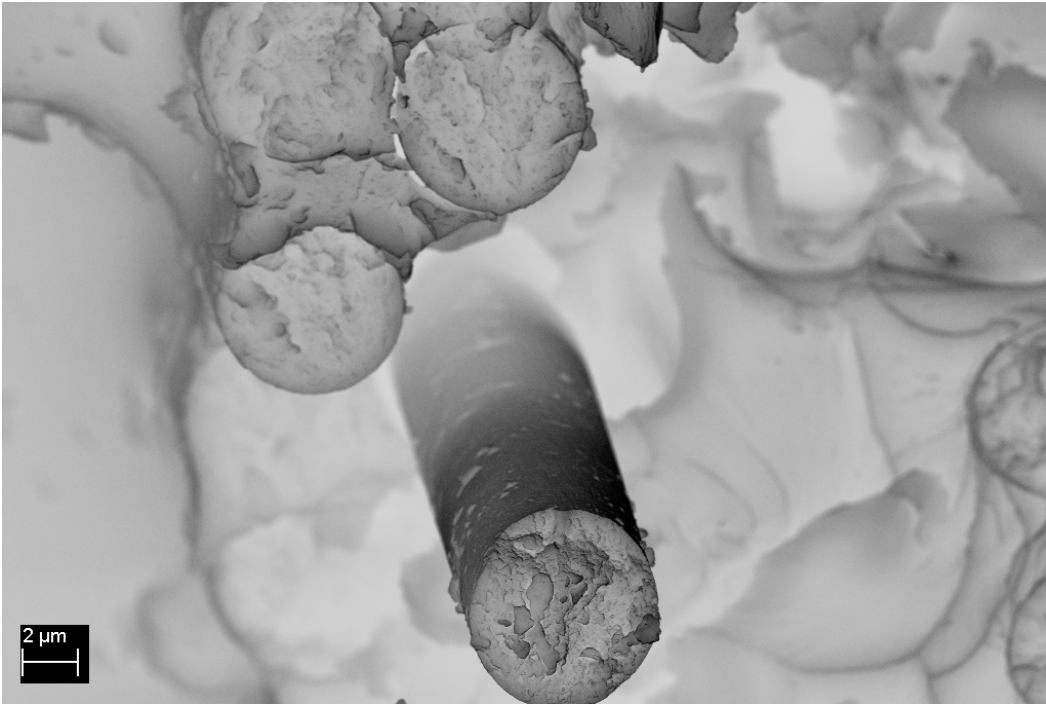


Figure 5.14b SEM micrograph of fiber matrix interface and fiber tips under tension for pyrrole+dopant (1400W) treated AS4 fiber epoxy composite (3kX)

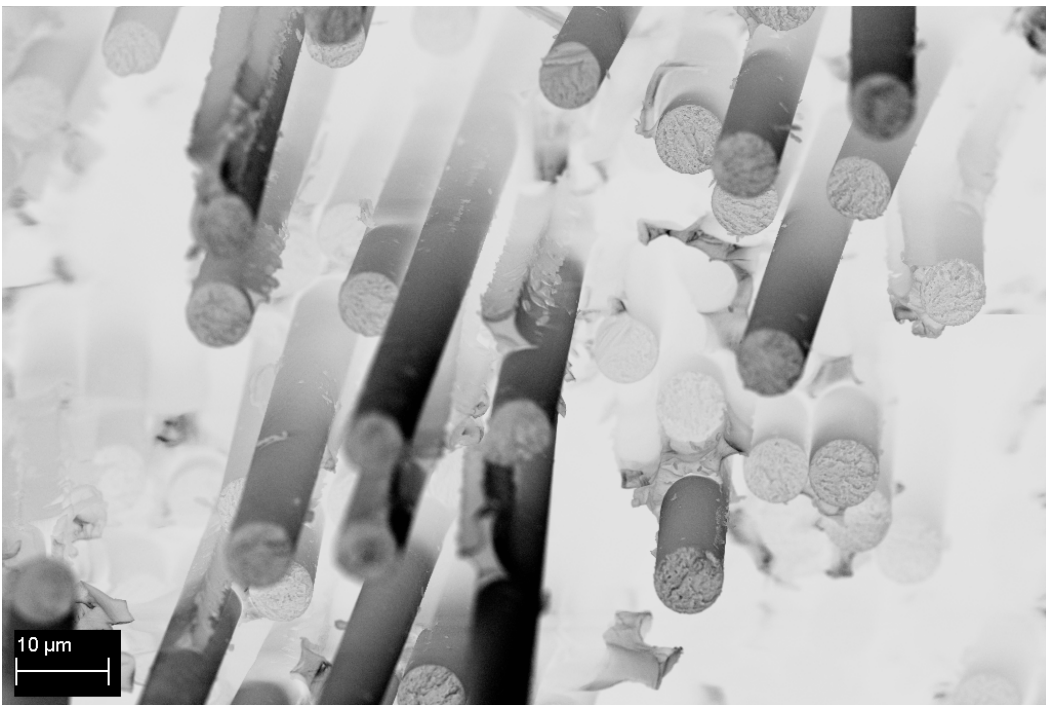


Figure 5.15 SEM micrograph of fiber matrix interface and fiber tips under tension for pyrrole+dopant (1400W) treated T700/CNT fiber epoxy composite

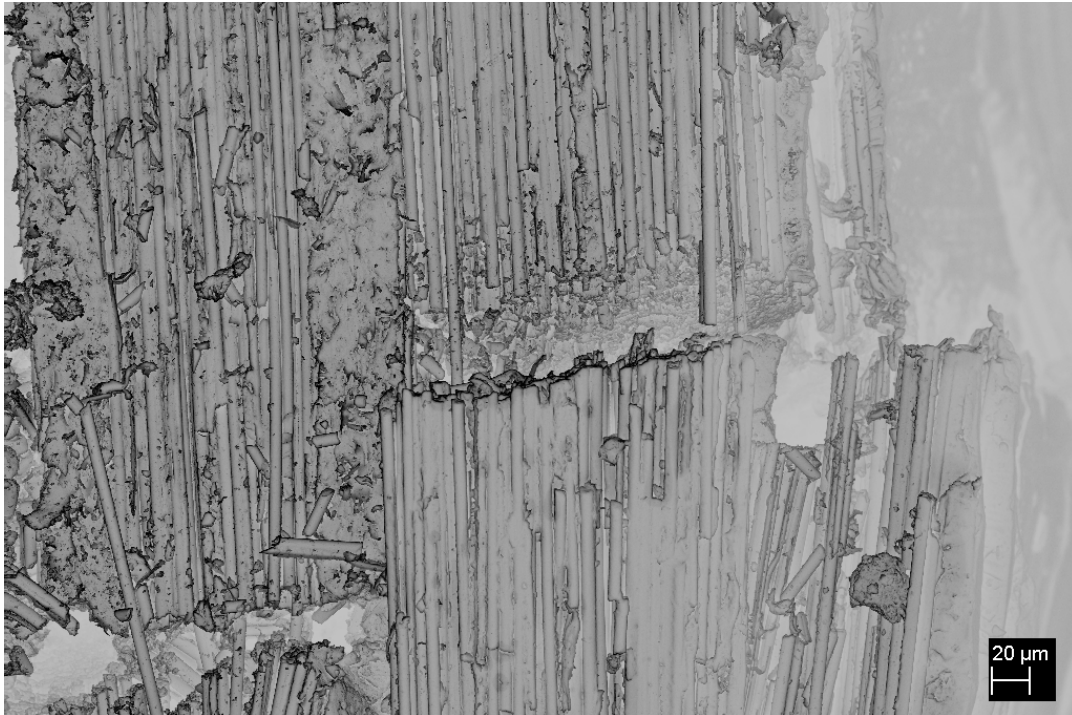


Figure 5.16 SEM micrograph of fiber matrix interface from compression area for untreated T700GC fiber composite

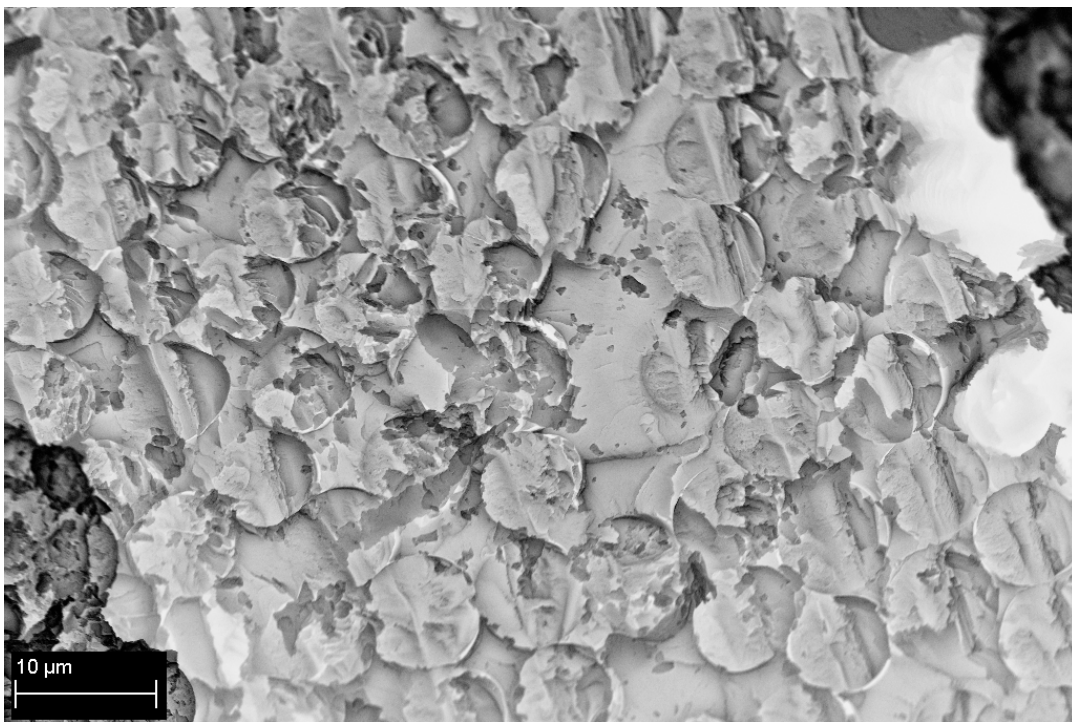


Figure 5.17 SEM micrograph of fiber matrix interface from compression area for untreated AS4 fiber composite





Figure 5.18 SEM micrograph of fiber matrix interface from compression area for pyrrole (1400 W) treated T700/CNT fiber composite

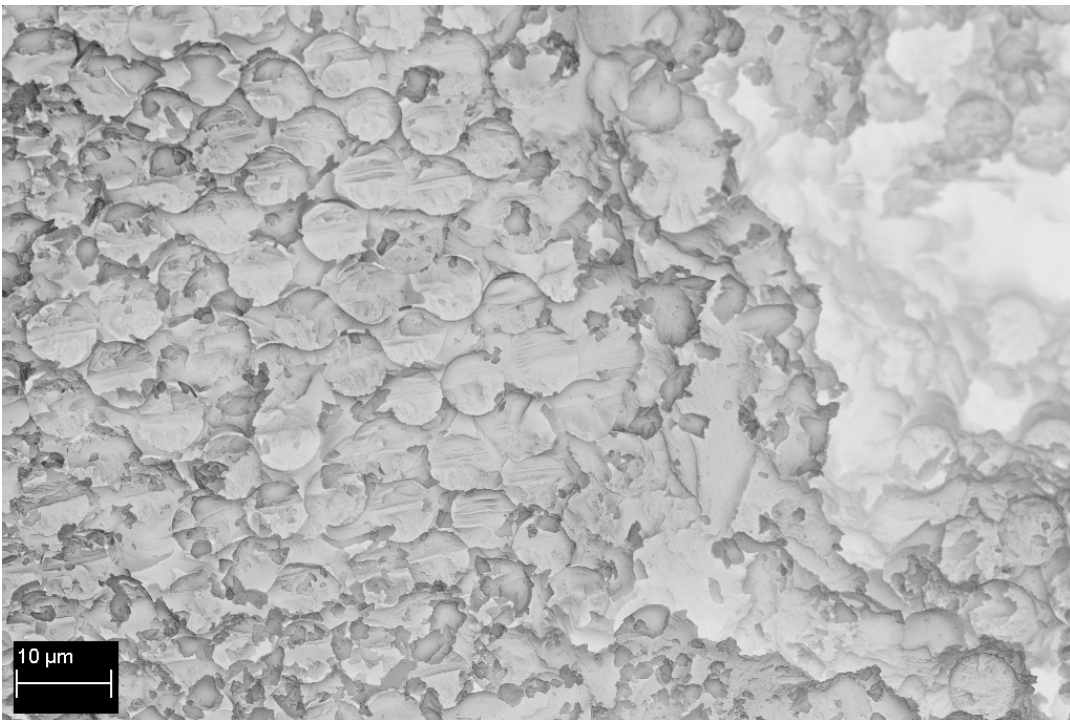


Figure 5.19 SEM micrograph of fiber matrix interface from compression area for pyrrole (1400 W) treated AS4 fiber composite





Figure 5.20 SEM micrograph of fiber matrix interface from compression area for pyrrole+dopant (1400 W) treated T700/CNT fiber composite

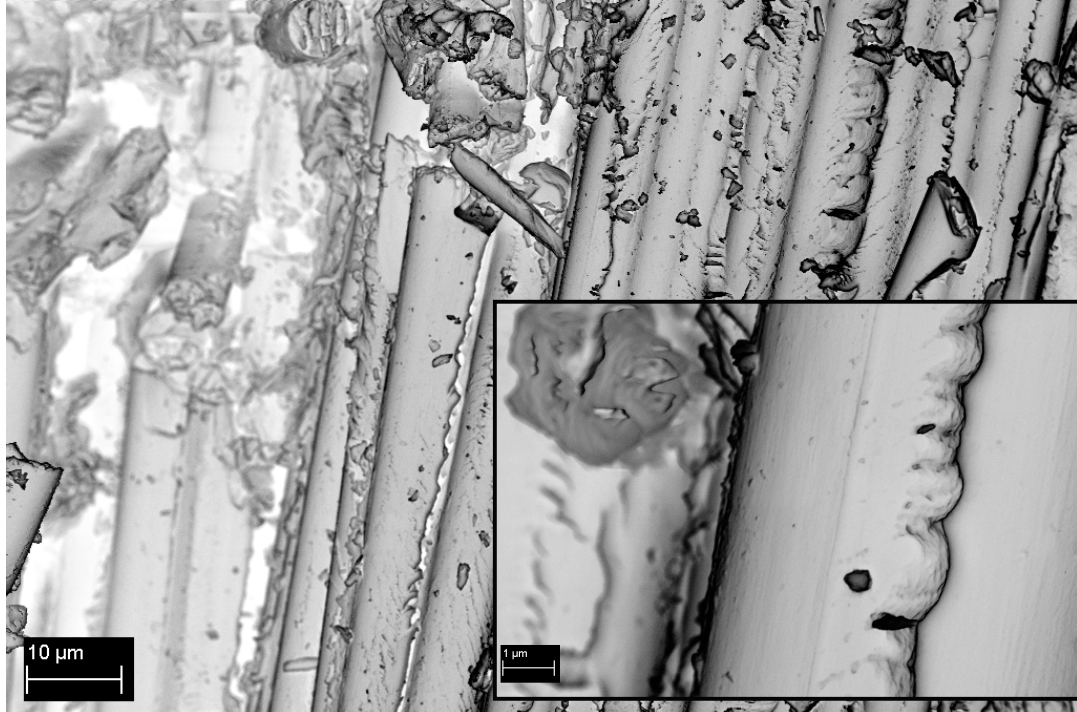


Figure 5.21 SEM micrograph of fiber matrix interface from compression area for pyrrole (1800 W) treated T700/CNT fiber composite)



### *3 Electrical properties of plasma treated carbon fiber/epoxy composites*

The longitudinal and transversal (through-width and through thickness) electrical resistance of carbon fiber/composites (DC,  $\omega=0$ ) were measured in order to calculate the electrical resistivity of AS4/epoxy, T700GC/epoxy, and T700/CNT/epoxy composites by using different locations of electrodes. In longitudinal direction, current flow along the carbon fibers and it is assumed to be proportional to the number of conducting fibers. In transversal directions, the density of fiber to fiber contact points and percolation effects are considered as dominant processes [90]. For those composites, conductivity is not isotropic but depends on the orientation of the carbon fibers [119]. In order to demonstrate the possible conduction pathways in a composite, a schema is shown in Fig. 5.22.

As information, the electric resistivity of plasma treated AS4 fibers was ranging from  $2.8 \times 10^{-3} \Omega \cdot \text{cm}$  to  $4.38 \times 10^{-3} \Omega \cdot \text{cm}$  whereas plasma treated T700/CNT fibers was changing between  $3.08 \times 10^{-3} \Omega \cdot \text{cm}$  and  $5.65 \times 10^{-3} \Omega \cdot \text{cm}$ . All those results can also be predicted from the variability charts (Figs. 5.23 and 5.24). The electrical resistivity of fibers which were used to prepare fiber/epoxy composites, were changing roughly between  $2.8 \times 10^{-3}$  and  $4.58 \times 10^{-3} \Omega \cdot \text{cm}$  (Figs. 5.25 and 5.26) and untreated AS4, T700/CNT and T700GC fibers were  $2.75 \times 10^{-3} \Omega \cdot \text{cm}$ ,  $2.79 \times 10^{-3} \Omega \cdot \text{cm}$  and  $3.58 \times 10^{-3} \Omega \cdot \text{cm}$ , respectively.

Neither in longitudinal nor in transversal resistance measurements, contact resistance between electrodes and a composite sample can be omitted. Therefore, the contact resistance which includes resistance of wires, resistance between the wires and electrodes, resistance between electrodes and sample is measured by extrapolation of the experimental data as shown in Fig. 5.25 [90]. In this graph, composite samples of various lengths were used to assess the linearity of the electrical resistance in the longitudinal direction. In transversal directions same approach was applied by changing the placement of electrodes [90]. The results of electrical resistivity of composite samples in comparison with carbon fibers excluding contact resistance are demonstrated in Figures 5.26 and 5.27.

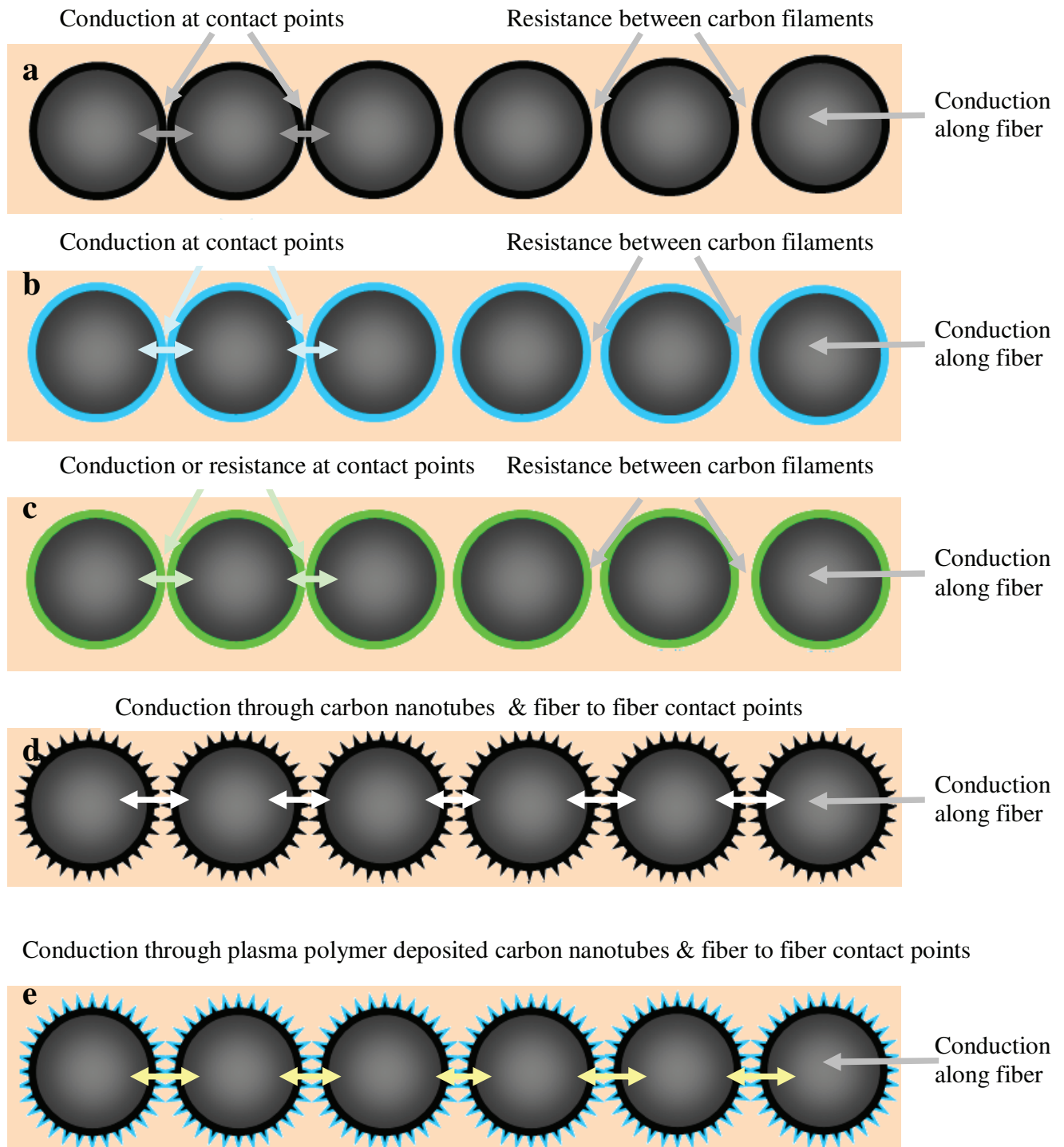


Figure 5.22 Illustration of electric conduction in a fiber reinforced composite sample (front-view), a) untreated AS4/epoxy sample, b) plasma treated AS4/epoxy sample, c) untreated T700GC/epoxy sample, d) untreated T700/CNT/epoxy sample, e) plasma treated T700/CNT/epoxy sample (  Epoxy,  Plasma polymer,  sizing on T700GC fiber,  CNTs,  CNTs covered with plasma polymer)

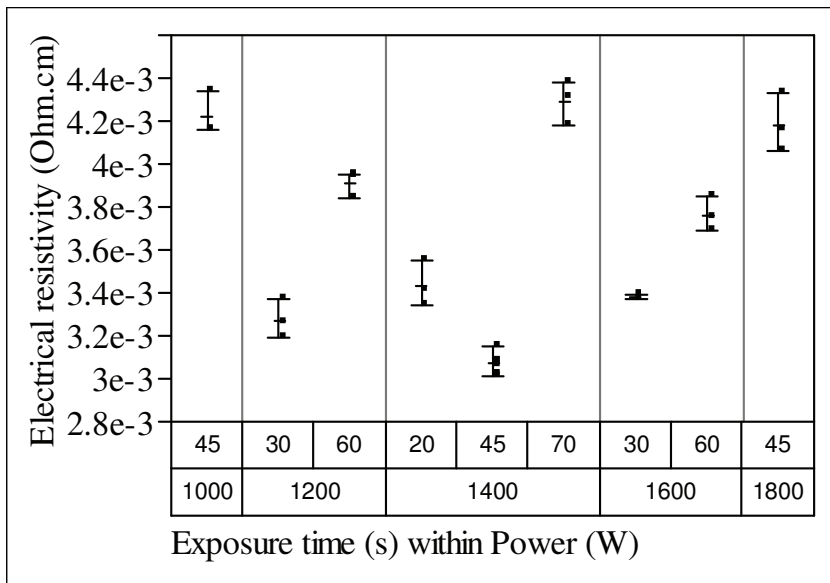


Figure 5.23a Variability chart for electrical resistivity of plasma pyrrole treated AS4 fibers

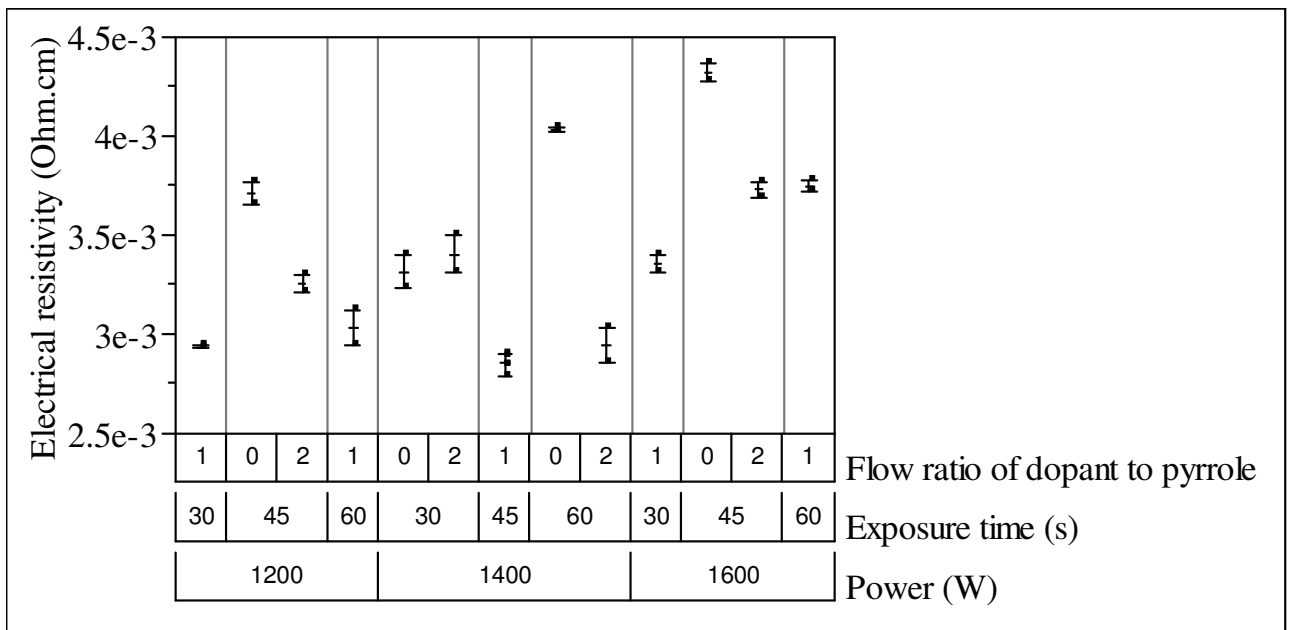


Figure 5.23b Variability chart for electrical resistivity of plasma pyrrole and/or pyrrole+dopant treated AS4 fibers

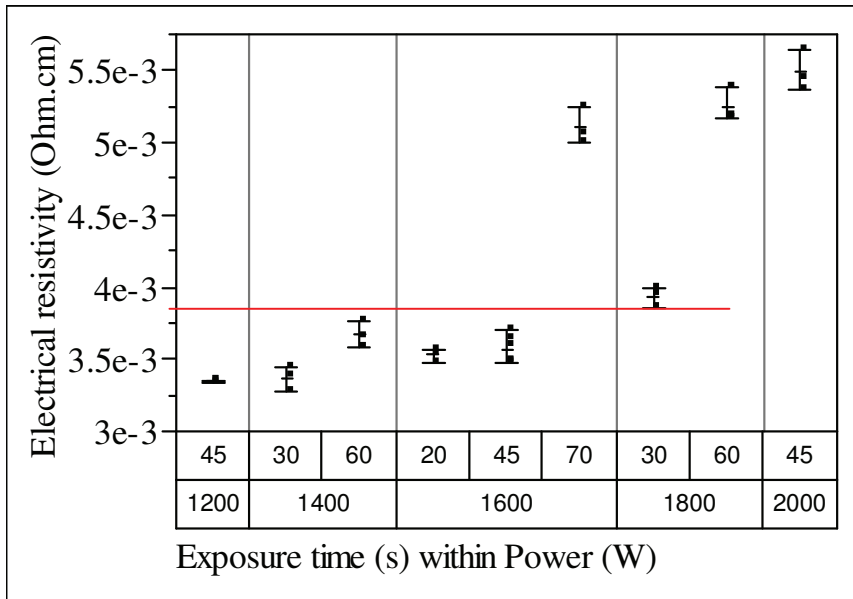


Figure 5.24a Variability chart for electrical resistivity of plasma pyrrole treated T700/CNT fibers (Note: Red line shows the electrical resistivity of untreated T700GC fiber)

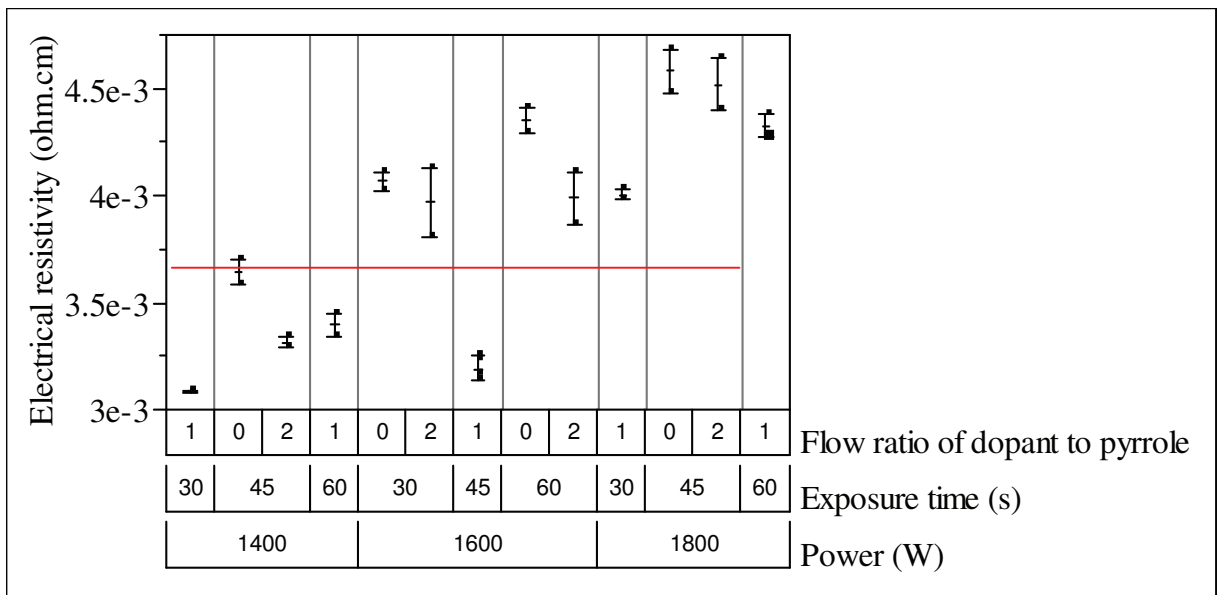


Figure 5.24b Variability chart for electrical resistivity of plasma pyrrole and/or pyrrole+dopant treated T700/CNT fibers (Note: Red line shows the electrical resistivity of untreated T700GC fiber)

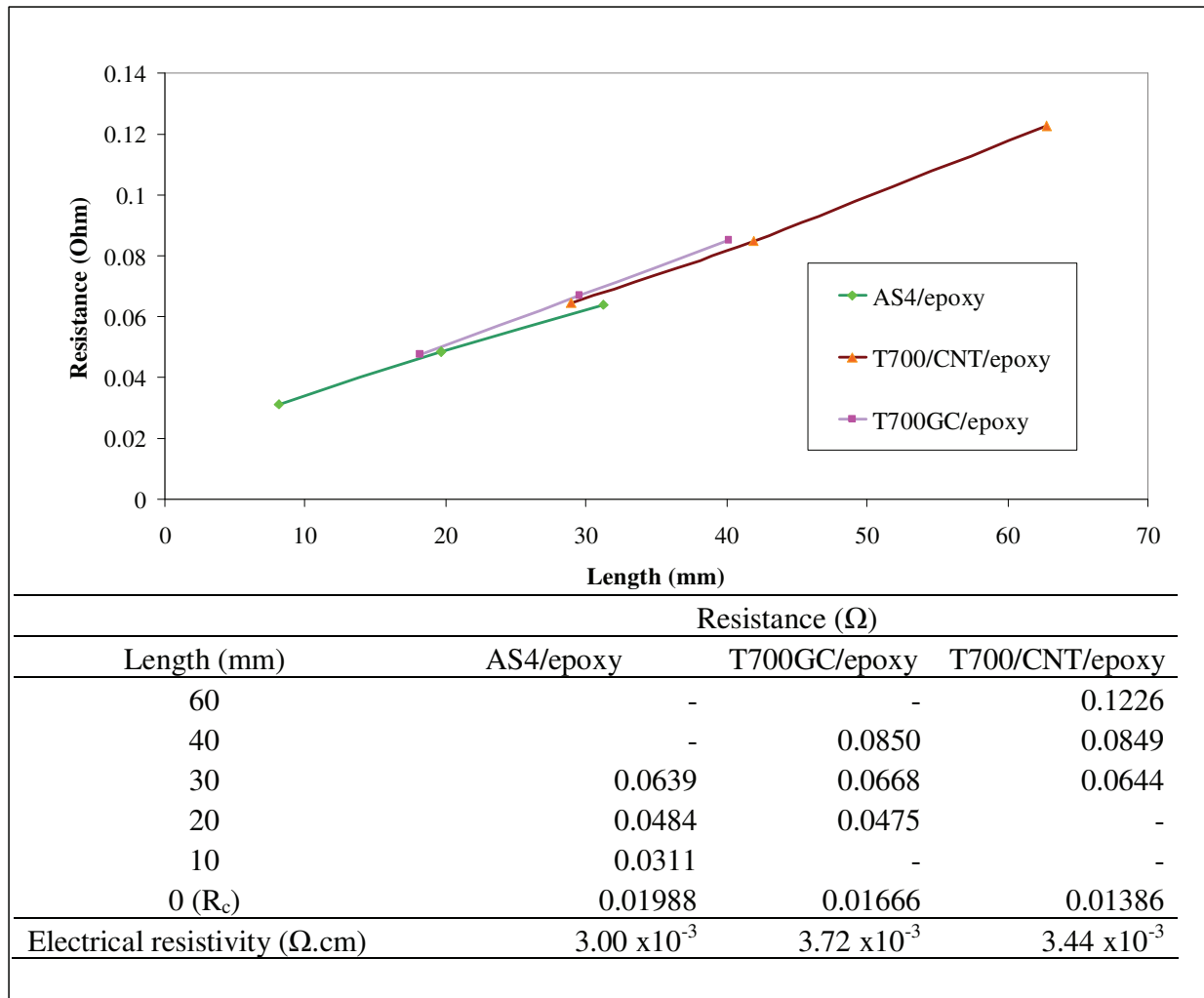


Figure 5.25 Longitudinal resistance versus composite sample length

According to the resistance measurements, contact resistance of composites samples were found roughly  $0.0167 \Omega$  as shown in Figure 5.25 (interception with resistance axis). According to the parallel resistance approach [119], electrical resistivity of AS4/epoxy, T700GC/epoxy and T700/CNT composite samples were calculated as  $3.00 \times 10^{-3}$ ,  $3.72 \times 10^{-3}$  and  $3.44 \times 10^{-3} \Omega.cm$ , respectively whereas the plasma treated samples were ranging between  $3.11 \times 10^{-3}$  and  $4.60 \times 10^{-3} \Omega.cm$  (Figure 5.25) (equations are given in Chapter II). These results indicated that the electrical resistivity of composite samples were roughly at the same order of magnitude in the longitudinal direction. It could be due to the current flow along nearly the same number of conducting fibers [90, 119].

In the case of transversal electrical resistance measurements, it is known that the density of fiber-to-fiber contact points as well as the percolation threshold of the filler (e.g. CNTs) plays important role to transfer the composite from insulative state into conductive state [90, 119, 120]. It has been stated that often at percolation threshold (i.e. critical concentration of filler) the electrical conductivity of the composite increases by several orders of magnitude. The most likely reason is that the filler forms a continuous network inside the polymer matrix [120].

According to the electrical resistivity of untreated and plasma treated T700/CNT/epoxy composites, it can be said that the percolation threshold cannot be reached completely in T700/CNT/epoxy composites. Namely, grafted CNTs on T700 fibers cannot form highly continuous network inside the epoxy matrix. Moreover, it is understood that the electrical conductance of CNTs the in transversal directions were partly hindered by the deposited plasma polypyrrole (Figure 5.27). However, the electrical resistivity of untreated T700/CNT/epoxy and 1400 W plasma treated T700/CNT/epoxy composites roughly four and two times lower than that of T700GC/epoxy composites. Therefore, it is assumed that T700/CNT fiber/epoxy composites were exhibited better electric conductance compared to T700GC/epoxy composites due to the filler effect of CNTs in the epoxy interlayers.

The transversal electrical resistivity of untreated T700GC/epoxy and AS4/epoxy composites were nearly 5.0  $\Omega$ .cm. Whatever the type of fiber, the electrical resistivity remains higher than that of untreated and plasma treated T700/CNT/epoxy composites. The decrease in transversal electrical resistivity shows that the number of contact points between adjacent fibers can be rendered by grafting CNTs on carbon fibers (e.g. T700/CNT).

In order to decrease the electrical resistivity in transversal directions, it may be useful to research the critical filler loading in the case of T700/CNT/epoxy composites. It is thought that increase in the density of fiber-to-fiber contact points may be ensured with the good amount of CNTs grafting on the carbon fibers. Afterwards, such composites might provide lower electrical resistivity in transversal directions (normal to fiber axis for unidirectional composites).

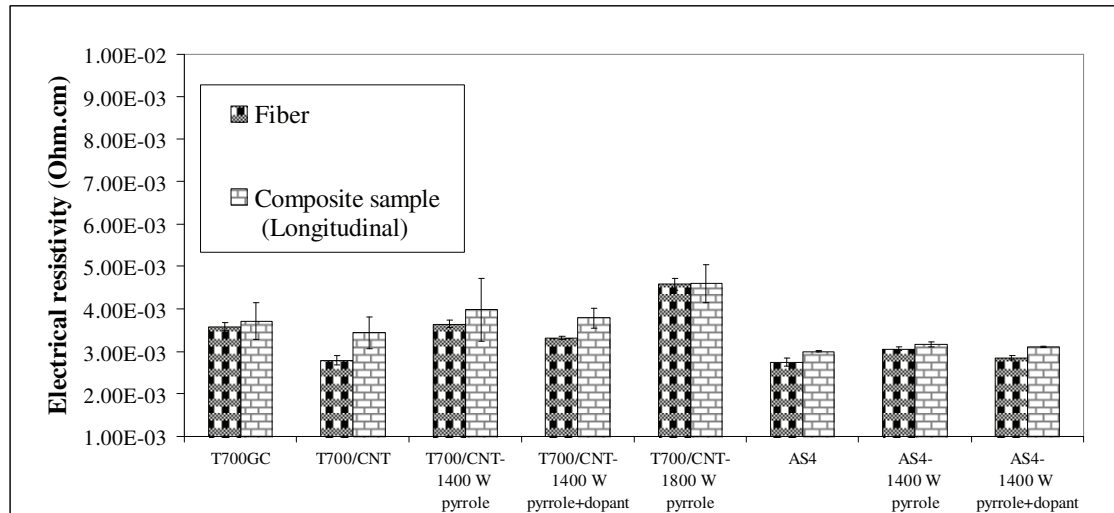


Figure 5.26 Comparison of electrical resistivity of carbon fibers and their composites (in longitudinal direction)

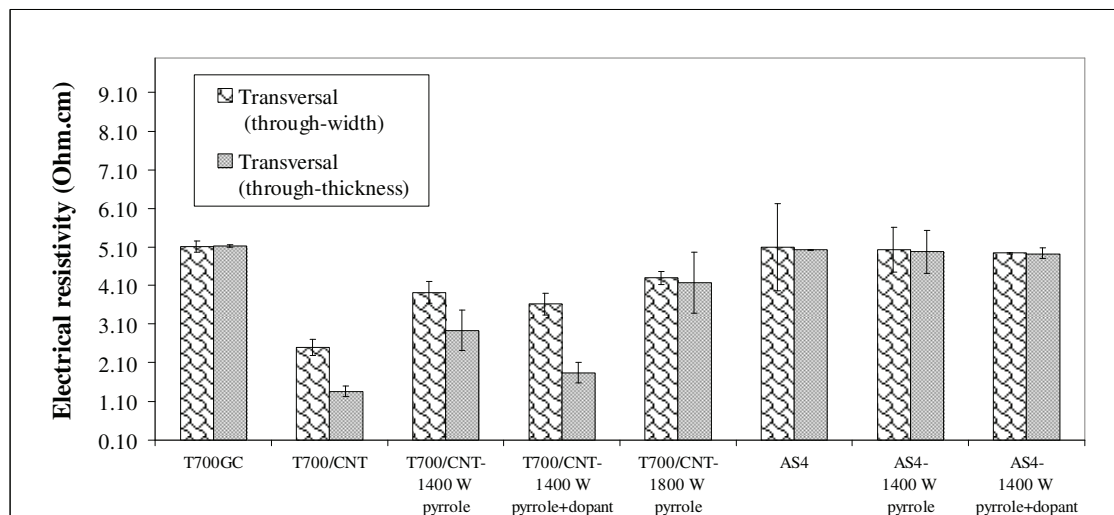


Figure 5.27 Comparison of transversal electrical resistivity of composites



## *4 Conclusion*

This chapter was devoted to the characterization of mechanical and electrical properties of AS4/M21 and T700GC/M21 and T700/CNT/M21 epoxy composites. For this purpose, ILSS, flexural strength and longitudinal and transversal electrical resistivities of composites were studied experimentally.

According to the results, carbon fibers showed different dependencies on plasma conditions (precursor type and plasma power input), though electrical and mechanical properties of composites varied from one sample to another. Among the plasma treated fiber composites, higher plasma power treated fiber composites (1800 W pyrrole) exhibited the maximum ILSS, flexural strength, and electrical resistivity. However, lower plasma power treated composites (1400 W pyrrole+ dopant) exhibited the lowest ILSS, flexural strength and electrical resistivity. It can be concluded that the higher the plasma power the lower the electrical conductivity and the higher the mechanical properties.

## General conclusion

## *General conclusion and perspectives*

In the frame of this work, we adapted a dielectric barrier discharge technique for continuous plasma polypyrrole deposition on the surface CFs and CNTs-CF. The aim of this study was to enhance the interfacial properties of CF and CNTs-CF composites and to retain the intrinsic properties of those materials as well as to provide valuable alternatives to previous polymer deposition methods existed in the literature.

In the first chapter, we reviewed the fundamental properties of the composites, CFs, CNTs and the principles of adhesion between fiber and matrix in order to provide necessary background for the study. Additionally, plasma processes including different types of plasma discharges, and their effect on CFs and CNTs were discussed in detail.

In the second chapter, we presented the experimental set-up of the plasma treatment and the procedures of several sorts of characterization studies (e.g. chemical, electrical, and mechanical).

In the third chapter, we dealt with the statistical analysis of experiments by response surface methodology. We evaluated the effect of double and triple varied process parameters (i.e. plasma power, exposure time and precursors) on electrical resistivity of CFs and CNTs-CF. The electrical resistivity of plasma deposited fibers was found strongly dependent on process parameters such as power, duration of the experiment, and combination of precursor to dopant. A relatively low plasma power input and a moderate exposure time were found required to obtain minimum electrical resistivity.

In the fourth chapter, we focused on the characterization of plasma polypyrrole deposited CFs and CNTs-CF fibers by using several techniques such as XPS (X-ray photoelectron spectroscopy), AFM (atomic force microscopy), SEM (scanning electron microscopy), and TGA (thermogravimetric analysis). We also analyzed untreated samples (i.e. samples that are not subjected to any plasma treatment) in order to compare the effect of plasma treatment on such samples. We found that from low to high powers (1400 W to 1800 W), deposited polymer tend to lose the memory of its monomeric structure probably due to the loss of  $\alpha$  and  $\beta$ -carbons in pyrrole ring. This kind of change might be due to more ring opening reactions and high loss of nitrogen-containing species

at higher power levels. Regardless of exposure time, this sharp change was not observed at low powers. We found that p-toluene sulfonic acid monohydrate (pTSA. H<sub>2</sub>O) was not acted as a dopant in the form of tosylate ion. In our case, we believed that the reason of low electrical resistivity values originated from the less amount of deposited plasma polymer in the presence of pTSA.H<sub>2</sub>O vapor.

In the fifth chapter, we characterized the mechanical and electrical properties of untreated, plasma polypyrrole treated CFs and CNTs-CF experimentally. We performed three-point bending test and longitudinal and transversal electrical resistivity measurements for CNTs-CF and CFs composites in order to determine the healing effect of plasma surface treatment on carbon fibers. We concluded that the higher the plasma power the lower the electrical conductivity and the higher the mechanical properties.

In this PhD study, we showed that the plasma polypyrrole can be deposited on carbon fibers at atmospheric pressure DBD. We found that response surface methodology (Box designs) can be applicable in modeling to evaluate the effects of important variables on electrical resistivity of carbon fibers. We also diminished the risk to inhale free carbon nanotubes by encapsulating them into plasma polypyrrole and epoxy resin successfully.

For further studies, in order to decrease the electrical resistivity in transversal directions, it would be useful to research the critical filler loading in the case of T700/CNT/epoxy composites. It is thought that increase in the density of fiber-to-fiber contact points may be ensured with the higher amount of CNTs grafting on the carbon fibers. Afterwards, such composites might provide lower electrical resistivity in transversal directions (normal to fiber axis for unidirectional composites).



## References

## References

- [1] Carl Zweben, Myer Kutz (Ed.), in Handbook of Materials Selection, Chapter 12 Composite Materials , John-Wiley and Sons, New York, USA, 2002.
- [2] V. I Biryuk, T. G. Sorina, Advisory group for aerospace research and development (AGARD), Advanced polymeric and metallic composite materials for space and aerospace vehicle structures and strength optimization of composite structures and their certification, Canada Communication Group, Quebec, Canada, 1995.
- [3] Daniel Gay, Suong V. Hoa, Stephen W. Tsai, Composite materials design and applications, CRC Press LLC, Florida, USA, 2003.
- [4] Autar K. Kaw, Mechanics of composite materials, CRC Press LLC, Florida, USA, 1997.
- [5] Prepregs-Raw material for high performance composites, *Reinforced plastics* **October 2002**, pp. 24-28.
- [6] P. C. Wu, Greg Jones, Chris Shelley, Bert Woelfli, Novel microporous films and their composites, *Journal of engineered fibers and fabrics* **2007**, (2), 49-59.
- [7] Deborah D. L. Chung, Carbon fiber composites, Butterworth-Heinemann, MA, USA, 1994.
- [8] J. B Donnet, R. Y. Qin, Study of carbon fiber surfaces by scanning tunneling microscopy Part I. Carbon fibers from different precursors and after various heat treatment temperatures, *Carbon* **1992**, (30), 787-796.
- [9] Hugh O. Pierson, Handbook of carbon, graphite, diamond, fullerenes, Noyes Publication, NJ, USA, 1993.
- [10] D. D Edie, The effect of processing on the structure and properties of carbon fibers, *Carbon* **1998**, (36), 345-362.
- [11] Suter-kunststoffe ag, Composite materials, Internet version: 16/06/2011.
- [12] U. Zielke, K. J. Hüttinger, W.P. Hoffman, Surface oxidized carbon fibers: I. Surface structure and chemistry, *Carbon* **1996**, (34), 983-998.
- [13] Erik T. Thostenson, Chunyu Li, Tsu-Wei Chou, Nanocomposites in context (Review), *Composites Science and Technology* **2005**, (65), 491-516.



- [14] K. Tanaka, Y. Yamabe, K. Fukui (Eds.), The science and technology of carbon nanotubes, Elsevier, Oxford, UK, 1999.
- [15] H. S. Nalwa, Handbook of Nanostructured Materials and Nanotechnology, Vol. 5: Organics, Polymers, and Biological Materials, Chapter 6: Carbon Nanotubes (edited by Ajayan, P.M.), pp. 375 – 403, Academic Press, USA, 2000.
- [16] A. Allaoui, S. V. Hoa, P. Evesque, J. Bai, Electronic transport in carbon nanotube tangles under compression: The role of contact resistance, *Scripta Materialia* **2009**, (61), 628–631.
- [17] J. Baker-Jarvis, M. D. Janezic, J. H. Lehman, Dielectric resonator method for measuring the electrical conductivity of carbon nanotubes from microwave to millimeter frequencies, *J. of Nanomaterials* **2007**, (2007), 1-4.
- [18] H. Dai, E.W. Wong, C. M. Lieber, Probing Electrical Transport in Nanomaterials: Conductivity of Individual Carbon Nanotubes, *Science* **1996**, (272), 523-526.
- [19] X. L. Xie, Y. W. Mai, X. P. Zhou, Dispersion and alignment of carbon nanotubes in polymer matrix: A review *Materials Science and Engineering R* **2005**, (49), 89–112.
- [20] M. Meyyappan, Nanotechnology and mechanical engineering, A workshop on redefining mechanical engineering, FL, USA, 25-27 January 2002.
- [21] J. H. Du, J. Bai, H. M. Cheng, The present status and key problems of carbon nanotube based polymer composites *eXPRESS Pol. Letters* **2007**, (1), 253–273.
- [22] M. Pasquali, Single-walled carbon nanotubes in liquids: basic science and applications to processing, EMCC - 5th Chemical Engineering Conference for Collaborative Research in Eastern Mediterranean Countries, 24-29 May 2008, Cetraro (CS), Italy.
- [23] R. Ionescu, E. H. Espinosa, E. Sotter, E. Llobet, X. Vilanova, X. Correig, A. Felten, C. Bittencourt, G. Van Lier, J. C. Charlier, J. J. Pireaux, Oxygen functionalisation of MWNT and their use as gas sensitive thick-film layers *Sensors and Actuators B* **2006**, (113), 36–46.
- [24] T. Xu, J. Yang, J. Liu, Q. Fu, Surface modification of multi-walled carbon nanotubes by O<sub>2</sub> plasma *Applied Surface Science* **2007**, (253), 8945–8951.

- [25] J. A. Kim, D. G. Seong, T. J. Kang, J. R. Youn, Effects of surface modification on rheological and mechanical properties of CNT/epoxy composites *Carbon* **2006**, (44), 1898–1905.
- [26] H. Bubert, S. Haiber, W. Brandl, G. Marginean, M. Heintze, V. Brüser, Characterization of the uppermost layer of plasma-treated carbon nanotubes *Diamond and Related Materials* **2003**, (12), 811–815.
- [27] G. Kalita, S. Adhikari, H. R. Aryal, R. Afre, T. Soga, M. Sharon, M. Umeno, Functionalization of multi-walled carbon nanotubes (MWCNTs) with nitrogen plasma for photovoltaic device application *Current Applied Physics* **2009**, (9), 346–351.
- [28] N. O. V. Plank, R. Cheung, Functionalisation of carbon nanotubes for molecular electronics *Microelectronic Engineering* **2004**, (73–74), 578–582.
- [29] Y. W. Zhu, F.C. Cheong, T. Yu, X. J. Xu, C. T. Lim, J.T.L. Thong, Z. X. Shen, C.K. Ong, Y.J. Liu, A.T.S. Wee, C. H. Sow, Effects of CF<sub>4</sub> plasma on the field emission properties of aligned multi-wall carbon nanotube films *Carbon* **2005**, (43), 395–400.
- [30] Y. C. Hong, D. H. Shin, H. S. Uhm, Super-hydrophobicity of multi-walled carbon nanotubes treated by a glow discharge *Surface & Coatings Technology* **2007**, (201), 5025–5029.
- [31] A. Felten, J. Ghijsen, J. J. Pireaux, R. L. Johnson, C. M. Whelan, D. Liang, G. Van Tendeloo, C. Bittencourt, Photoemission study of CF<sub>4</sub> RF-Plasma treated multi-wall carbon nanotubes *Carbon* **2008**, (46), 1271–1275.
- [32] L. Valentini, D. Puglia, F. Carniato, E. Boccaleri, L. Marchese, J. M. Kenny, Use of plasma fluorinated single-walled carbon nanotubes for the preparation of nanocomposites with epoxy matrix *Composites Science and Technology* **2008**, (68), 1008–1014.
- [33] W. J. Chou, C. C. Wang, C. Y. Chen, Characteristics of polyimide-based nanocomposites containing plasma-modified multi-walled carbon nanotubes *Composites Science and Technology* **2008**, (68), 2208–2213.

- [34] Donglu Shi, Jie Lian, Peng He, L. M. Wang, Win J. van Ooij, Mark Schulz, Yijun Liu, David B. Mast, Plasma deposition of ultrathin polymer films on carbon nanotubes *Applied Physics Letter* **2002**, (81), 1-3.
- [35] K. Yua, Z. Zhu, Y. Zhang, Q. Li, W. Wang, L. Luo, X. Yu, H. Ma, Z. Li, T. Feng, Change of surface morphology and field emission property of carbon nanotube films treated using a hydrogen plasma *Applied Surface Science* **2004**, (225), 380–388.
- [36] Mel Schwartz, Encyclopedia of Materials, Parts and Finishes, CRC Press LLC, Florida, USA, 2000.
- [37] B. K. Fink, R. L. McCullough, Interphase research issues *Composites Part A: Applied science and manufacturing* **1999**, (30), 1-2.
- [38] C. Baillie, J. Emanuelsson, F. Marton, Building knowledge about the interface *Composites Part A: Applied science and manufacturing* **2001**, (32), 305-312.
- [39] John C. Berg, An introduction to interfaces and colloids: the bridge to nanoscience, World Scientific Publishing, Singapore, 2010.
- [40] R. L. Sierakowski, G. M. Newaz, Damage tolerance in advanced composites, Technomic Publishing, Pennsylvania, USA, 1995.
- [41] Jang-Kyo Kim, Y. W. Mai, Engineered interfaces in fiber reinforced composites, Elsevier, Oxford, UK, 1998.
- [42] L. T. Drzal, K. Dusek (Ed.), in Epoxy resins and composites II, Springer-Verlag, Berlin, 1986.
- [43] Composites lift off in primary aerostructures, *Reinforced plastics* **April 2004**, pp. 22-27.
- [44] Duelling with composites, *Reinforced plastics* **June 2006**, pp. 18-23.
- [45] R. P. Taylor, Fibre composite aircraft: capability and safety, Australian Government-Australian Transport Safety Bureau, Australia, 2008.
- [46] Internet:<http://www.airbus.com/aircraftfamilies/passengeraircraft/a350xwbfamily/a350-900/> (Accessed on 01/11/2011).
- [47] Charles A. Harper, Handbook of plastics, elastomers, and composites, 4<sup>th</sup> Ed., Mc-Graw Hill, USA, 2002.

- [48] M.A. Uman, V.A. Rakov, The interaction of lightning with airborne vehicles *Progress in Aerospace Sciences* **2003**, (39), 61–81.
- [49] Anders Larsson, The interaction between a lightning flash and an aircraft in flight *C.R. Physique 3* **2002**, (3), 1423-1444.
- [50] Alexander A. Fridman, Lawrence A. Kennedy, Plasma Physics and Engineering, Taylor and Francis Group, New York, USA, 2004.
- [51] Thomas C. Corke, Martiqua L. Post, Dmitriy M. Orlov, Single dielectric barrier discharge plasma enhanced aerodynamics: physics, modeling and applications, *Plasma Enhanced Aerodynamics* (Review Article: Experiments in Fluids), University of Notre Dame, Center for Flow Physics and Control (accessed on 25/10/2010).
- [52] Internet: <http://universe-review.ca/F13-atom.htm#plasma> (accessed on 01/11/2011).
- [53] A. Grill, Cold Plasma in Materials Fabrication, Institute of Electrical and Electronics Engineers (IEEE) Inc., New York, USA, 1994.
- [54] Claire Tendero, Christelle Tixier, Pascal Tristant, Jean Desmaison, Philippe Leprince, Atmospheric pressure plasmas: A review *Spectrochimica Acta Part B* **2006**, (61), 2 – 30.
- [55] H. Conrads, M. Schmidt, Plasma generation and plasma sources *Plasma Sources Sci. Technol.* **2000**, (9), 441–454.
- [56] U. Kogelschatz, B. Eliasson, W. Egli, Dielectric barrier discharges: principles and applications *Journal de Physique IV* **1997**, (7), 47-66.
- [57] Lamia Braci, Stephanie Ognier, and Simeon Cavadias, Modeling of a DBD Reactor for the Treatment of VOC, Excerpt from the Proceedings of the COMSOL Conference, Milan, 2009.
- [58] Rudiger Foest, Frank Adler, Florian Sigener, Martin Schmidt, Study of an atmospheric pressure glow discharge (APG) for thin film deposition *Surface and Coatings Technology* **2003**, (163 –164), 323–330.
- [59] Jürgen Salge, Plasma assisted deposition at atmospheric pressure *Surface and Coatings Technology* **1996**, (80), 1-7.

- [60] Fiorenza Fanelli, Thin film deposition and surface modification with atmospheric pressure dielectric barrier discharges *Surface & Coatings Technology* **2010**, (205), 1536–1543.
- [61] Françoise Massines, Nicolas Gherardi, Antonella Fornelli, Steve Martin, Atmospheric pressure plasma deposition of thin films by Townsend dielectric barrier discharge *Surface & Coatings Technology* **2005**, (200), 1855 – 1861.
- [62] M. M. Kuraica, B. M. Obradović, D. Manojlović, D. R. Ostojić, J. Purić, Application of coaxial dielectric barrier discharge for potable and waste water treatment (Accessed on 25/10/2010).
- [63] Ferencz S. Denes, Sorin Manolache, Macromolecular plasma-chemistry: an emerging field of polymer science *Prog. Polym. Sci.* **2004**, (29), 815–885.
- [64] V. Brüser, M. Heintze, W. Brandl, G. Marginean, H. Bubert, Surface modification of carbon nanofibres in low temperature plasmas *Diamond and Related Materials* **2004**, (13), 1177–1181.
- [65] G. Bogojeva-Gaceva, E. Mader, L. Häußler, A. Dekanski, Characterization of the surface and interphase of plasma-treated HM carbon fibres *Composites Part A* **1997**, (28A), 445-452.
- [66] A. P. Kettle, A. J. Beck, L. O’Toole, F. R. Jones, R. D. Short, Plasma polymerization for molecular engineering of carbon fibre surfaces for optimized composites *Composites Science and Technology* **1997**, (57), 1023-1032.
- [67] Kingsley K.C. Ho, Adam F. Lee, Steven Lamoriniere, Alexander Bismarck, Continuous atmospheric plasma fluorination of carbon fibres *Composites: Part A* **2008**, (39), 364–373.
- [68] Alan J. Heeger, Semiconducting and metallic polymers Nobel Lecture **2000**, 380-417.
- [69] Terje A. Skotheim, John R. Reynolds, Conjugated Polymers-Theory Synthesis Properties and Characterization, CRC Press Taylor and Francis Group, FL, USA, 2007.
- [70] Alan G. MacDiarmid, Synthetic metals: a novel role for organic polymers, Nobel Lecture *Current Applied Physics* **2001**, (1), 269-279.

- [71] T. F. Otero, I. J. Cantero, Conducting polymers as positive electrodes in rechargeable lithium-ion batteries *J. Power Sources* **1999**, (81-82), 838-841.
- [72] J. Anand, S. Palaniappan, D.N. Sathyanarayana, Conducting polyaniline blends and composites *Prog. Polym. Sci.* **1998**, (23), 993-1018.
- [73] G. Kumar, A. Sivashanmugan, N. Muniyandi, S.K. Dhava, D.C. Trivedi, Polyaniline as an electrode material for magnesium reserve battery *Synthetic Metals* **1996** (80), 279-282.
- [74] V. G. Kulkarni, W. R. Mathew, J. C. Campbell, C. J. Dinkins, P. J. Durbin, In the 49th ANTEC Conference Proceedings, Society of Plastic Engineers and Plastic Engineering, Montreal, Canada, 5-9 May 1991.
- [75] S. Maiti, Recent trends in conducting polymers: problems and promises *Ind. J. Chem.* **1994**, (33A), 524-539.
- [76] M. Morita, Effects of solvent and electrolyte on the electrochromic behavior and degradation of chemically prepared polyaniline-poly(vinyl alcohol) composite films *J. Polym. Sci. Part B: Polym. Phys.* **1994**, (32), 231-242.
- [77] B. Sarı, Lecture notes: conductive polymers, Gazi University, Ankara, Turkey, 2009-2010.
- [78] Yu Iriyama, Plasma polymerization of heteroatomic compounds *Journal of Photopolymer Science and Technology* **2001**, (14), 105-110.
- [79] Kouta Hosono, Ichiro Matsubara, Norimitsu Murayama, Woosuck Shin, Noriya Izu, Shuzo Kanzaki, Structure and properties of plasma polymerized and 4-ethylbenzenesulfonic acid-doped polypyrrole films *Thin Solid Films* **2003**, (441), 72-75.
- [80] Kouta Hosono, Ichiro Matsubara, Norimitsu Murayama, Woosuck Shin, Noriya Izu, Effects of discharge power on the structure and electrical properties of plasma polymerized polypyrrole films *Materials Letters* **2004**, (58), 1371-1374.
- [81] G. J. Cruz, J. Morales, R. Olayo, Films obtained by plasma polymerization of pyrrole *Thin Solid Films* **1999**, (342), 119-126.
- [82] M. Vasquez, G.J. Cruz, M.G. Olayo, T. Timoshina, J. Morales, R. Olayo, Chlorine dopants in plasma synthesized heteroaromatic polymers *Polymer* **2006**, (47), 7864-7870.

- [83] W. J. van Ooij, S. Eufinger, and T. H. Ridgway, DC-Plasma polymerization of pyrrole *Plasmas and Polymers* **1996**, (1) No.3.
- [84] F. Fally, J. Riga, J.J. Verbist, Plasma polymerization of pyrrole, ISPC-10, Bochum, August 1991, pp. 1-6.
- [85] Pieter Heyse, Roel Dams, Sabine Paulussen, Kristof Houthoof, Kris Janssen, Pierre A. Jacobs, Bert F. Sels, Dielectric barrier discharge at atmospheric pressure as a tool to deposit versatile organic coatings at moderate power input *Plasma Processes and Polymers* **2007**, (4), 145-157.
- [86] KS Sree Harsha, Principles of physical vapor deposition of thin films, Elsevier Ltd., Great Britain, 2006.
- [87] Ricardo d'Agustino, Pietro Favia, Francesco Fracassi, Plasma processing of polymers, Kluwer Academic Publishers, Netherlands, 1997.
- [88] Cristina Canal, Freddy Gaboriau, Alex Vilchez, Pilar Erra, M<sup>a</sup>Jose Garcia-Celma, Jordi Esquena, Topographical and Wettability Effects of Post-Discharge Plasma Treatments on Macroporous Polystyrene-Divinylbenzene Solid Foams *Plasma Processes and Polymers* **2009**, (6), 686–692.
- [89] Acxys Technologies, ULD Plasma Brochure, Version 0.2, Saint-Martin le Vinoux, France, 2009.
- [90] J. C. Abry, S. Bochard, A. Chateauminois, M. Salvia, G. Giraud, In situ detection of damage in CFRP laminates by electrical resistance measurements *Composites Science and Technology* **1999**, (59), 925-935.
- [91] Yunus A. Çengel, Thermodynamics: An engineering approach, 5<sup>th</sup> Edition, McGraw Hill, Boston, USA, 2006.
- [92] George E. P. Box, William Gordon Hunter, J. Stuart Hunter, Statistics for Experimenters: Design, Innovation, and Discovery, John Wiley&Sons, 2005.
- [93] JMP, User's Guide, Version 7.0, SAS Institute Inc., 2007.
- [94] H. Yasuda, in Plasma chemistry of polymers, Ed., M. Shen, Marcell Dekker Inc., New York, 1976.
- [95] Jie Zhou and Ellen R. Fisher, Properties of PPPy/Au Composite Nanofibers *Journal of Nanoscience and Technology* **2004**, (4), 539-547.



- [96] Xuezhong Zhang, Yudong Huang, Tianyu Wang, Surface analysis of plasma grafted carbon fiber *Applied Surface Science* **2006**, (253), 2885-2892.
- [97] Jinggong Wang, K. G. Neoh, E. T. Kang, Comparative study of chemically synthesized and plasma-polymerized pyrrole and thiophene thin films *Thin Solid Films* **2004**, (446), 205-217.
- [98] Nora Graf, Eda Yegen, Thomas Gross, Andreas Lippitz, Wilfried Weigel, Simone Krakert, Andreas Terfort, Wolfgang E.S. Unger, XPS and NEXAFS studies of aliphatic and aromatic amine species on functionalized surfaces *Surface Science* **2009**, (603), 2849-2860.
- [99] E. Benseddik, M. Makhlouki, J. C. Bernede, S. Lefrant, A. Pron, XPS studies of environmental stability of polypyrrole-poly(vinyl alcohol) composites *Synthetic Metals* **1995**, (72), 237-242.
- [100] P. Lisboa, G. Gilliland, G. Ceccone, A. Valsesia, F. Rossi, Surface functionalization of polypyrrole films using UV-light induced radical activation *Applied Surface Science* **2006**, (252), 4397-4401.
- [101] Bin Lin, R. Sureshkumar, J. L. Kardos, Electropolymerization of pyrrole on PAN-based carbon fibers: experimental observations and a multiscale modeling approach *Chemical Engineering Science* **2001**, (56), 6563–6575.
- [102] H. Biederman D. Slavínská, Plasma polymer films and their future prospects *Surface and Coatings Technology* **2000**, (125), 371-37
- [103] W. Weisweiler, K. Schlitter, Surface modification of carbon fibers by plasma polymerization *Thin Solid Films* **1992**, (207), 158-165.
- [104] T. Uyar, L. Toppare, J. Hacaloğlu, Characterization of electrochemically synthesized p-toluene sulfonic acid doped polypyrrole by direct insertion probe pyrolysis mass spectrometry *J. of Analytical and Applied Pyrolysis* **2002**, (64), 1-13.
- [105] J. Brandrup , E. H. Immergut , E. A. Grulke, Polymer Handbook, 4<sup>th</sup> Ed., John Wiley & Sons Inc. USA, 1999.

- [106] Y. M. Shulga, Ta-Chang Tien, Chi-Chen Huang, Shen-Chuan Lo, V. E. Muradyan, N. V. Polyakova, Yong-Chien Ling, R. O. Loutfy, A. P. Moravsky, XPS study of fluorinated carbon multi-walled nanotubes *J. of Electron Spectroscopy and Related Phenomena* **2007**, (160), 22-28.
- [107] Ladawan Ruangchuay, Johannes Schwank, Anuvat Sirivat, Surface degradation of a-naphthalene sulfonate-doped polypyrrole during XPS characterization *Applied Surface Science* **2002**, (199), 128–137.
- [108] E. Pigois-Landureau, Y. F. Nicolau, M. Delamar, XPS study of layer-by-layer deposited polypyrrole thin films *Synthetic Metals* **1995**, (72), 111-119.
- [109] D. J. Marks, F. R. Jones, Plasma polymerised coatings for engineered interfaces for enhanced composite performance *Composites: Part A* **2002**, (33), 1293–1302.
- [110] T. J. Swait, T. Whittle, C. Soutis, F. R. Jones, Identification of interfacial and interphasal failure in composites of plasma polymer coated fibres *Composites: Part A* **2010**, (41), 1047-1055.
- [111] W. Kowbel and C. H. Shan, Mechanical behaviour of carbon-carbon composites made with cold plasma treated carbon fibres *Composites* **1995**, (26), 791-797.
- [112] M.A. Montes-Moran, F.W.J. van Hattum, J.P. Nunes, A. Martinez-Alonso, J.M.D. Tascon, C.A. Bernardo, A study of the effect of plasma treatment on the interfacial properties of carbon fibre–thermoplastic composites *Carbon* **2005**, (43), 1778–1814.
- [113] P. Kettlet, F. R. Jones, M. R. Alexander, R. D. Short, M. Stollenwerk, J. Zabold, W. Michaeli, W. Wu, E. Jacobs and I. Verpoest, Experimental evaluation of the interphase region in carbon fibre composites with plasma polymerised coatings *Composites Part A* **1998**, (29A), 241-250.
- [114] Chensong Dong, Heshan A. Ranaweera-Jayawardena, Ian J. Davies, Flexural properties of hybrid composites reinforced by S-2 glass and T700S carbon fibres *Composites: Part B* **2011**.
- [115] N. Carbajal, F. Mujika, Determination of compressive strength of unidirectional composites by three-point bending tests *Polymer Testing* **2009**, (28), 150–156.

- [116] Carl R. Schultheisz and Anthony M. Waas, Compressive failure of composites Part I: Testing and micromechanical theories *Prog. Aerospace Sci.* **1996**, (32), 1-42.
- [117] Glenn C. Grimes, Composite materials: testing and design, 10<sup>th</sup> edition, ASTM, Philadelphia, USA, 1992.
- [118] P. N. B. Reis, J. A. M. Ferreira, F. V. Antunes, J. D. M. Costa, Flexural behaviour of hybrid laminated composites *Composites: Part A* **2007**, (38), 1612–1620.
- [119] O. Ceysson, M. Salvia, and L. Vincent, Damage mechanisms characterisation of carbon fibre/epoxy composite laminates by both electrical resistance measurements and acoustic emission *Scripta Materialia* **1996**, (34), 1273-1280.
- [120] Mohammed H. Al-Saleh, Uttandaraman Sundararaj, A review of vapor grown carbon nanofiber/polymer conductive composites *Carbon* **2009**, (47), 2-22.



## *Résumé*

L'incorporation de fibres de carbone greffées avec des nanotubes de carbone (CNTs-CF) dans une matrice polymère permet d'obtenir des matériaux avec des propriétés mécaniques, des propriétés de conductivité électrique et de conductivité thermique notamment améliorées. Ces matériaux sont des candidats idéaux pour être intégrés dans des applications fonctionnelles et même structurales dans les domaines de l'industrie aéronautique, de l'industrie automobile, de la défense et de l'industrie des produits pour le sport. L'objectif (des travaux menés au cours) de cette thèse de Doctorat est d'établir une technique efficace de production de matériaux composites possédant des propriétés multifonctionnelles. Nous étudions l'adaptation d'une technique de dépôt de polymère par plasma sur la surface de fibres de carbone (CFs) puis sur la surface de CNT-CFs. Le dépôt de polymère par plasma sur la surface CNT-CFs est ici recherché non pour des raisons de sécurité, certainement avantageuses, mais pour conférer les propriétés des nanotubes de carbone à l'ensemble du matériau composite.

Dans le premier chapitre, nous proposons un tour d'horizon des 2 sujets majeurs de notre étude : (1) les matériaux composites et leurs applications (2) les applications des plasmas pour procédés de traitement des matériaux.

Dans le deuxième chapitre, nous présentons la procédure expérimentale du traitement plasma des fibres, ainsi que le schéma détaillé du mécanisme permettant de manipuler les échantillons. Nous précisons aussi les procédures suivies pour la caractérisation chimique, électrique et mécanique des fibres et des matériaux composites.

Dans le troisième chapitre, nous évaluons les effets des variations de 2 et de 3 paramètres (par exemple la puissance plasma utilisée, la durée d'exposition et la nature des précurseurs) sur la résistivité électrique des fibres de carbone (CFs) et des fibres de carbone greffées de nanotubes de carbone (CNTs-CF) par la méthodologie des surfaces de réponse. D'après cette étude pour l'optimisation du procédé, nous étudions les principaux facteurs et les interactions entre les différents paramètres. Nous montrons les variables (ou facteurs) qui ont la plus grande influence sur la résistivité électrique sur les 2 types de fibres de carbone.

Dans le quatrième chapitre, nous traitons des études de caractérisations des fibres de carbone par XPS (composition chimique), MEB (microstructure), AFM (topologie, rugosité) et TGA (stabilité thermique, cinétique de dégradation). Il s'agit de fournir une meilleure compréhension des structures obtenues sur de telles fibres dans des domaines allant du macroscopique jusqu'au niveau de l'atome. Nous analysons aussi des échantillons avant traitement pour comparer les différences morphologiques et chimiques avec les échantillons traités par plasma.

Finalement, dans le cinquième chapitre, nous étudions les propriétés mécaniques et électriques des échantillons de matériaux composites élaborés à partir de fibres non-traitées et des fibres traitées par dépôt plasma de polypyrrole (sur CFs et CNTs-CF). A partir des essais mécaniques et des mesures électriques, nous concluons sur les améliorations apportées par le traitement plasma.

**Mot-clés** : plasma, dépôt polymère par plasma, fibre de carbone, fibre de carbone greffées avec des nanotubes de carbone

## *Abstract*

The incorporation of carbon nanotubes grafted carbon fibers (CNTs-CF) into polymer matrices provides highly-enhanced mechanical, electrical, and thermal properties to the materials. They are ideal candidates to be integrated into structural and functional applications in the fields of aerospace, automobile, defense, and sport industries. The aim of this PhD thesis is to establish an efficient technique to produce carbon fiber composites with multifunctional properties. We study the adaptation of a plasma technique for polymer deposition on the surface of carbon fibers (CFs) and carbon nanotubes grafted carbon fibers (CNTs-CF). The plasma polymer deposition on CNTs-CF is not performed only to keep nanotubes on the carbon fiber surface for safety reasons, but it is also applied to retain the bulk properties of those materials.

In the first chapter, we give an overview of the two major subjects of the study: (1) composites and their applications, (2) plasma application for materials processing.

In the second chapter, we present the experimental procedure of the plasma treatment process of fibers including the detailed design of the plasma system for the treatment of these samples. Then we explain the procedures of several sorts of characterization studies of fibers and composites (e.g. chemical, electrical, and mechanical).

In the third chapter, we evaluate the effect of double and triple varied process parameters (i.e. plasma power, exposure time and precursors) on electrical resistivity of CFs and CNTs-CF by response surface methodology. According to the optimization studies we investigate the main factors and the interactions between the different process parameters and we demonstrate which variable (or factor) has the greatest effect on the electrical resistivity of both types of the treated carbon fibers.

In the fourth chapter, we deal with the characterization studies of the plasma treated CFs and CNTs-CF by using XPS (chemical structure), SEM (microstructure), AFM (topography, roughness), and TGA (thermal stability, degradation kinetics) in order to provide better understanding of the obtained structures on such fibers in a domain ranging from macroscopic to atomic scales. We also analyze the untreated samples to compare mainly the chemical and morphological differences between unmodified and plasma modified fibers.

Finally, in the fifth chapter, we study the mechanical and electrical properties of untreated and plasma polypyrrole treated CFs and CNTs-CF reinforced composites experimentally. According to the electrical and mechanical tests, we determine the healing effect of plasma surface treatment performed on CFs and CNTs-CF.

**Keywords:** plasma, polymer deposition by plasma, carbon fiber, carbon nanotube grafted carbon fiber